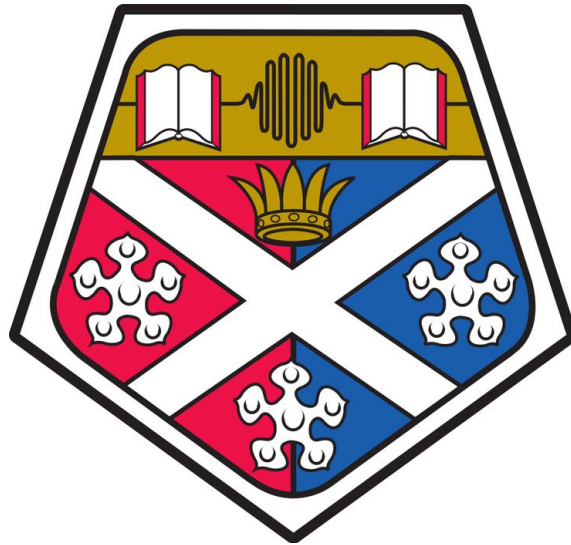


# Coherent control of Rydberg atoms using sub-kHz linewidth excitation lasers

Rémy Legaie

---



Experimental Quantum Optics and Photonics Group  
Department of Physics and SUPA

University of Strathclyde

A thesis presented in the fulfilment of the requirements for the  
degree of

*Doctor of Philosophy*

2019

# Coherent control of Rydberg atoms using sub-kHz linewidth excitation lasers

Rémy Legaie

---

## Abstract

This thesis presents the development of a new experimental apparatus for neutral atom quantum computing with Rydberg atoms. We describe the construction and characterisation of three continuous wave lasers stabilised simultaneously on a ultra-high finesse Ultra-low-expansion (ULE) cavity, providing long-term stability and sub-kHz linewidth lasers with a tunable offset-lock frequency as required for high fidelity quantum operations. High-resolution spectroscopy on a cloud of cold Cs atoms was achieved using electromagnetically induced transparency (EIT), in order to calibrate absolute cavity mode frequencies with respect to Rydberg transitions and determine the cavity long-term drift of  $\sim 1$  Hz/s.

We have demonstrated trapping of single Cs atoms in optical tweezers and developed a high-resolution imaging system capable of sub- $\mu\text{m}$  spatial resolution in the atom plane. Coherent control of atomic qubits has been achieved via fast rotations between long-lived hyperfine ground states as well as coherent Rydberg excitations towards the states  $50S_{1/2}$ ,  $69S_{1/2}$  and  $81D_{5/2}$ . The experiment allows us to control the atoms electric field environment and minimise stray electric fields with  $\sim 1$  mV/cm sensitivity, in order to keep long ground-Rydberg coherence times.

We have observed Rydberg blockade between two atoms separated by  $6 \mu\text{m}$  for both states  $69S_{1/2}$  and  $81D_{5/2}$ , showing an almost complete suppression of the doubly excited state probability. The creation of an entangled state is deduced from the  $\sqrt{2}$  collective-enhancement of the Rabi oscillations with respect to the single atom case. Our ability to perform double-atom experiment offers the opportunity to implement a proof of a principle of a cNOT mesoscopic gate based on EIT, using the Rydberg state  $81D_{5/2}$  for high-fidelity operations.

# Contents

	Page
<b>Contents</b>	<b>i</b>
<b>List of Figures</b>	<b>v</b>
<b>List of Tables</b>	<b>viii</b>
<b>Declaration</b>	<b>ix</b>
<b>Acknowledgements</b>	<b>x</b>
<b>Dedication</b>	<b>xii</b>
<b>1 Introduction</b>	<b>1</b>
1.1 Qubit representation . . . . .	2
1.2 Quantum gates and quantum circuits . . . . .	3
1.3 The rise of QIP . . . . .	5
1.3.1 Trapped ions . . . . .	6
1.3.2 Superconducting circuits . . . . .	7
1.3.3 Neutral atoms . . . . .	7
1.4 The choice of Rydberg atoms . . . . .	8
1.5 QIP with Rydberg atoms . . . . .	9
1.6 Longer term hybrid system . . . . .	10
1.7 Outline of the thesis . . . . .	13
1.8 Publications arising from this work . . . . .	15
<b>I Theoretical Requirements</b>	<b>16</b>
<b>2 Rydberg Atom Properties</b>	<b>17</b>
2.1 Rydberg atom properties . . . . .	17
2.1.1 Rydberg state lifetimes . . . . .	19
2.2 Dipolar interactions . . . . .	20
2.2.1 Two regimes of interaction . . . . .	21
2.2.2 Angular dependence and interaction strength . . . . .	23
2.3 Dipole blockade . . . . .	25
2.4 Summary . . . . .	28

<b>3</b>	<b>Atom-Light Interactions</b>	<b>29</b>
3.1	The two-level atom . . . . .	29
3.1.1	Wavefunctions and Hamiltonian approaches . . . . .	31
3.1.2	The density matrix . . . . .	32
3.1.3	Ramsey fringes . . . . .	35
3.1.4	The dressed atom picture . . . . .	36
3.1.5	Optical dipole trap . . . . .	37
3.2	Three-level atom . . . . .	37
3.2.1	EIT . . . . .	39
3.2.2	Two-photon Raman transitions . . . . .	42
3.2.3	Important features of three-level $\Lambda$ system . . . . .	43
3.2.4	Optimised parameters estimation . . . . .	44
3.3	Summary . . . . .	47
<b>II</b>	<b>Experimental Realisations</b>	<b>48</b>
<b>4</b>	<b>ULE Cavity</b>	<b>49</b>
4.1	Qubit and Rydberg lasers . . . . .	50
4.1.1	Qubit A laser . . . . .	51
4.1.2	Rydberg A and B lasers . . . . .	52
4.2	Fabry-Perot cavity theory . . . . .	56
4.3	Horizontal reference cavity experiment . . . . .	60
4.4	Laser stabilisation . . . . .	64
4.4.1	Pound-Drever-Hall locking . . . . .	66
4.4.2	Experimental implementation and frequency offset locking . . . . .	70
4.5	Cavity characterisation . . . . .	77
4.5.1	Determination of the zero-CTE temperature . . . . .	77
4.5.2	Determination of the FSR of the cavity . . . . .	80
4.5.3	Ringdown-measurements and cavity parameters . . . . .	81
4.6	Laser characterisation . . . . .	84
4.6.1	Beatnote measurement at 509 nm . . . . .	84
4.6.2	Analysis of the lasers performances . . . . .	86
4.7	Summary . . . . .	88
<b>5</b>	<b>Cold Atom Experiment Setup</b>	<b>89</b>
5.1	Vacuum system . . . . .	89
5.1.1	Aspheric lenses . . . . .	92
5.1.2	Passive and active control of the electric field . . . . .	93
5.2	Laser cooling . . . . .	93
5.2.1	Working principle of the magneto-optical trap (MOT) . . . . .	94
5.2.2	Experimental implementation . . . . .	95
5.3	Imaging system . . . . .	100
5.3.1	MOT chamber imaging . . . . .	100
5.3.2	Science chamber imaging . . . . .	102
5.4	MOT characterisation . . . . .	104
5.4.1	MOT loading rate . . . . .	104
5.4.2	MOT temperature . . . . .	106
5.5	Optical transport . . . . .	106

5.6	Single atom trapping . . . . .	109
5.6.1	Light assisted collisions . . . . .	110
5.6.2	Single atom loading . . . . .	110
5.6.3	Single atom readout . . . . .	112
5.6.4	Characterisation of the single atoms in the ODT . . . . .	113
5.7	Qubit state preparation . . . . .	115
5.7.1	Stretched state pumping . . . . .	116
5.7.2	Clock state pumping . . . . .	117
5.8	Summary . . . . .	117
<b>6</b>	<b>Cavity Frequencies Calibration</b>	<b>118</b>
6.1	Vapour cell EIT . . . . .	119
6.1.1	Qubit A detuning with respect to the probe laser using $67D_{5/2}$ Rydberg state . . . . .	119
6.1.2	Determination of accessible Rydberg states . . . . .	124
6.1.3	Experimental verification of Rydberg state frequencies . . . . .	125
6.2	Cold atoms EIT . . . . .	126
6.2.1	Optical pumping optimisation . . . . .	126
6.2.2	EIT alignment procedure . . . . .	129
6.2.3	EIT experiment . . . . .	131
6.3	Data analysis . . . . .	132
6.3.1	EIT experiment on $68D_{5/2}$ and $69S_{1/2}$ . . . . .	132
6.3.2	$50S_{1/2}$ : EIT and ULE cavity drift calibration . . . . .	135
6.4	Summary . . . . .	138
<b>III</b>	<b>Manipulation of Single and Two Qubits</b>	<b>139</b>
<b>7</b>	<b>Coherent Control</b>	<b>140</b>
7.1	Ground state manipulation . . . . .	141
7.1.1	Hyperfine state detection . . . . .	141
7.1.2	Two-Photon Raman spectroscopy . . . . .	143
7.1.3	Ground state coherence . . . . .	146
7.2	Rydberg state manipulation . . . . .	149
7.2.1	Rydberg state detection . . . . .	149
7.2.2	Rydberg excitation setup . . . . .	150
7.2.3	Rydberg excitation beams parameters . . . . .	151
7.2.4	Rydberg excitation sequence . . . . .	153
7.2.5	Control of the electric field . . . . .	156
7.2.6	Coherent excitation to Rydberg states $69S_{1/2}$ and $81D_{5/2}$ . . . . .	161
7.2.7	Rydberg excitation limitations . . . . .	164
7.3	Rydberg Blockade . . . . .	165
7.3.1	Entanglement . . . . .	170
7.4	Summary . . . . .	171
<b>8</b>	<b>Mesoscopic Rydberg EIT Gate</b>	<b>172</b>
8.1	Rydberg EIT Gate . . . . .	173
8.2	Expected fidelities . . . . .	176
8.3	Possible improvements . . . . .	179

---

8.4 Summary . . . . .	180
<b>IV Conclusion and Outlook</b>	<b>181</b>
9 Conclusion	182
<b>V Appendices</b>	<b>185</b>
A Calculating Rabi frequencies on dipole transitions	186
B Homebuilt photodiodes	190
B.1 High bandwidth photodiode . . . . .	190
B.2 High gain photodiode . . . . .	191
<b>Bibliography</b>	<b>194</b>

# List of Figures

1.1	Bloch sphere representation of a qubit state . . . . .	2
1.2	Circuit representation for the creation of the Bell State $ \Psi^+\rangle$ . . . . .	4
1.3	Ensembles of atoms trapped above a CPW resonator . . . . .	12
2.1	Dipole-dipole interactions . . . . .	21
2.2	Angular dependence of the $C_6$ coefficient . . . . .	23
2.3	Dipole blockade between Rydberg atoms . . . . .	26
3.1	Two-level atom . . . . .	30
3.2	Ramsey fringes . . . . .	35
3.3	Dressed atom approach . . . . .	36
3.4	Excitation schemes for a three-level atom . . . . .	38
3.5	Three-level atom susceptibility . . . . .	40
3.6	Optimised parameters for two-photon excitation of $81D_{5/2}$ Rydberg state . . . . .	44
4.1	ECDL picture . . . . .	51
4.2	Rydberg SHG schematic . . . . .	53
4.3	Rydberg SHG Photograph . . . . .	55
4.4	Fabry-Perot cavity . . . . .	57
4.5	Theoretical cavity transmission . . . . .	58
4.6	Side view schematic of the cylindrical high-finesse ULE cavity within the stainless steel vacuum can . . . . .	61
4.7	Experimental cavity locking setup . . . . .	62
4.8	Hermitte-Gauss cavity modes . . . . .	63
4.9	Cavity reflection coefficient . . . . .	65
4.10	Imaginary part of the cavity reflection coefficient . . . . .	66
4.11	Imaginary and real parts of the demodulated reflected signal . . . . .	69
4.12	Experimental PDH error signal . . . . .	70
4.13	Schematic of the cavity locking setup . . . . .	71
4.14	Schematic of the lasers setup and locking electronics . . . . .	73
4.15	Photograph of the electronics for PDH feedback . . . . .	74
4.16	Schematic of the fast-feedback branch applied to the diode laser current . . . . .	74
4.17	In-loop error signal of Qubit A laser . . . . .	75
4.18	Illustration of the sideband locking technique . . . . .	77
4.19	Determination of the zero-CTE temperature . . . . .	78
4.20	Free-spectral range determination . . . . .	81
4.21	Cavity ringdown . . . . .	82
4.22	Beatnote measurement at 509 nm . . . . .	85

5.1	Overview of the vacuum system . . . . .	90
5.2	High-NA aspheric lenses and electrodes for electric field control . . . . .	91
5.3	Energy level structure of the $D_2$ transition for caesium atom . . . . .	95
5.4	Overview of the cooling laser system . . . . .	96
5.5	Experimental layout for polarisation spectroscopy and error signal . . . . .	99
5.6	MOT chamber camera calibration . . . . .	102
5.7	Science chamber optics to image atoms trapped into microscopic optical dipole traps . . . . .	103
5.8	MOT loading curve . . . . .	105
5.9	Schematic of light assisted collisions in a microscopic dipole trap . . . . .	109
5.10	Optical layout for the creation of two microscopic ODT and fluorescence imaging . . . . .	111
5.11	Single atom readout . . . . .	112
5.12	Single atom temperature using release-recapture technique . . . . .	114
5.13	Optical pumping schemes . . . . .	116
6.1	Schematic of EIT in vapour cell . . . . .	119
6.2	vapour cell EIT for $67D_{3/2}$ and $67D_{5/2}$ states . . . . .	121
6.3	EIT spectroscopy on $67D_{5/2}$ Rydberg state . . . . .	122
6.4	Detunings and fundamental cavity mode for Qubit A laser . . . . .	123
6.5	Schematic of the experimental cold atoms EIT setup . . . . .	128
6.6	Optical pumping optimisation into the $ F = 4, m_F = 4\rangle$ stretched state . . . . .	129
6.7	Alignment procedure for the observation of EIT in cold atoms . . . . .	130
6.8	EIT on $68D_{5/2}$ Rydberg state in cold atoms . . . . .	133
6.9	EIT on $69S_{1/2}$ Rydberg state in cold atoms . . . . .	134
6.10	EIT $50S_{1/2}$ in cold atoms . . . . .	136
6.11	Spectroscopy of the $50S_{1/2}$ Rydberg state . . . . .	137
6.12	Evaluation of the cavity drift . . . . .	137
7.1	Timing sequence for single atom ground state rotations . . . . .	142
7.2	Schematic of the ground state rotations experimental setup . . . . .	143
7.3	Setup of Qubit B laser . . . . .	144
7.4	Two-photon spectroscopy and Rabi oscillations between clock states . . . . .	145
7.5	Ground states coherence . . . . .	147
7.6	Setup for Rydberg state excitation to $50S_{1/2}$ . . . . .	150
7.7	Single atom Rydberg excitation timing sequence . . . . .	152
7.8	Two-photon spectroscopy and Rabi oscillations for $ 4, 0\rangle \rightarrow 50S_{1/2}$ . . . . .	154
7.9	Active electric field compensation using electrodes . . . . .	157
7.10	Stark maps of $50S_{1/2}$ Rydberg state . . . . .	159
7.11	Rabi oscillations from $ 4, 0\rangle$ and $ 4, 4\rangle$ to the Rydberg state $50S_{1/2}$ . . . . .	160
7.12	Ramsey spectroscopy for the $ 4, 4\rangle \rightarrow 50S_{1/2}$ Rydberg excitation . . . . .	161
7.13	Two-photon spectroscopy and Rabi oscillations of the $ 4, 4\rangle \rightarrow 69S_{1/2}$ transition . . . . .	162
7.14	Spectroscopy and Rabi flopping on the $ 4, 4\rangle \rightarrow 81D_{5/2}$ transition . . . . .	163
7.15	Rydberg blockade and collective excitation for the Rydberg state $ r\rangle = 69S_{1/2}$ . . . . .	167
7.16	Rydberg blockade and collective excitation for the Rydberg state $ r\rangle = 81D_{5/2}$ . . . . .	169

---

8.1	Schematic of the EIT gate . . . . .	173
8.2	Fidelities in the blockaded and non-blockaded regime . . . . .	177
8.3	Evolution of the populations during the smooth $\pi$ -pulse . . . . .	178
B.1	photodiode board . . . . .	190
B.2	Circuit of the high bandwidth photodiode . . . . .	191
B.3	Circuit of the high gain photodiode . . . . .	192
B.4	Calibration of the high gain photodiode . . . . .	192

# List of Tables

1.1	Performance of different kind of qubits . . . . .	11
2.1	Quantum defect values . . . . .	18
2.2	Scaling laws for properties of the Rydberg states . . . . .	19
3.1	Optimised parameters for the two-photon excitation $ 4, 4\rangle \rightarrow 81D_{5/2}$ .	46
4.1	SHG cavity mirrors reflectivity . . . . .	54
4.2	Optimised parameters of the fast-feedback LRC filter . . . . .	76
4.3	Cavity parameters summary . . . . .	83
7.1	Residual electric fields . . . . .	158

# Declaration

I confirm that no part of the material offered has previously been submitted by myself for a degree in this or any other University. Where material has been generated through joint work, the work of others has been indicated.

Rémy Legaie  
Glasgow, March 10, 2020

The copyright of this thesis rests with the author. No quotation from it should be published without their prior written consent and information derived from it should be acknowledged.

# Acknowledgements

First and foremost, I would like to thank my supervisor Jonathan Pritchard for giving me the opportunity to be part of this exciting adventure. From my first day in the lab, you always encouraged me with patience and helped me to improve my independence. It has been an amazing experience to work under your guidance. All your experimentalist, programming and management skills have always been fascinating for me.

A special thanks go to Craig Picken, my labmate from the beginning, with whom I shared bad power outage days like the best when we saw the first Rydberg Rabi oscillations in the lab. The Hybrid team has been growing with Katie in my last year. You have always been optimistic and always kept the smile even if I was moaning about the unlocked cavity. For sure, you will take the experiment to exciting new challenges. Finally, Aurélien and Lindsey arrived when I was writing up, but again a big thanks to all of you for proofreading of my thesis.

I must also thank the past and present members of the Strathclyde Experimental Quantum Optics and Photonics group for making this PhD journey stimulating and enjoyable. First the higher staff Erling Riis, Stefan Kuhr, Thorsten Ackemann, Aidan Arnold, Paul Griffin and Elmar Haller for their experimental advices and for always have their office door open, whatever can be the question. I have been fortunate to work with many talented Postdocs or PhD students including Stuart Ingleby, Rachel Offer, Oliver Burrow, Craig Colqhoun, Andrea Di Carli, Rachel Elvin, Rudy Romain, Matthew Johnson, Carolyn O'Dwyer, James McGilligan, Ivor Kresic, Calum Mac Rae and I want to thank all of them. Finally, a special big thanks to the french team Dylan Cotta, Manuel Andia and Bruno Peaudecerf.

Because going from an empty lab to a cold atoms experiment requires lots of mechanical and electronics hard work, it would have been impossible without the help of highly skilled technicians. I would like to deeply thank Ewan MacLagan and Robert Wylie in the machine workshop and Ken Gibson, John Broadfoot and Mark Hutcheon in the electronics workshop.

I also had the wonderful opportunity to be part of the organising committee of YAO 2018 conference, thanks to all of you Araceli, Jorge, Jennifer and Rosaria.

Finally, I would like to express my deepest gratitude to people who have trusted me since my resumption of studies after teaching, who are Jean-Baptiste Fournier, Sara Ducci, Thomas Bourdel and Caroline Champenois.

None of this would have been possible if my friends Gaël, Benjamin, Julien and Thomas hadn't always encouraged me. Moreover, I'm lucky to have the support of my whole family. I would especially thank my aunt H el ene as well as my uncles Stanislas and Bernard.

Finally, I would like to thank my mother for always pushing me to realise my dreams and being there when I need it. I would never have gotten this far without her belief in me.

*This thesis is dedicated to my mum,  
for your endless love and support,  
and my beloved grandparents Jan and Waleria.*

# Chapter 1

## Introduction

The birth of quantum physics has been one of the major intellectual adventures of the twentieth century, that has still not revealed its boundaries. After the first half of this century, which led to the mathematical foundations of the theory, quantum physics has quickly left fundamental questions for applications. This has generated a large amount of the new devices such as the laser [1] or the remarkable invention of the semiconductor transistor [2]. The latter is closely connected to the emergence of the digital computer, arising from the synergy between quantum physics and computer science, which has revolutionized our every day life. The progress of computational power was made possible due to the miniaturisation of the chips containing the transistors, that has been quantified according to “Moore’s law”. The paper of Gordon Moore [3] published in 1965, indicates that the number of transistors on a chip should double every two years and this prediction has gradually been verified over the years. However, the rate of progress is now approaching saturation where the size of the transistor is comparable to the atomic size. Nowadays, classical computers reach their limitations, facing intractable problems such as simulating quantum systems like molecules or materials, as well as solving hard problems ranging from factorisation to optimisation problems.

An alternative approach had already been suggested by Richard Feynman in 1982. In his famous paper [4], he pointed out that if one wants to simulate complex quantum mechanical system, it should be done by another quantum system. In parallel, Yuri Manin [5, 6] and Paul Benioff [7, 8] proposed to develop a quantum

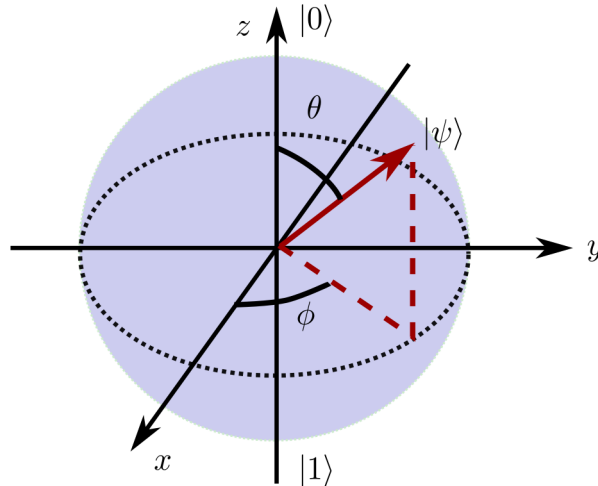


Figure 1.1: Bloch sphere representation of a qubit state  $|\psi\rangle = \cos\left(\frac{\theta}{2}\right)|0\rangle + e^{i\phi}\sin\left(\frac{\theta}{2}\right)|1\rangle$ . The state is fully described by its two spherical coordinates  $\theta$  and  $\phi$ . Pure quantum states lie at the surface of the Bloch sphere, whereas quantum mixed states lie inside the sphere. A single-qubit gate corresponds to the rotation of the state  $|\psi\rangle$  on the Bloch sphere.

computer, followed by David Deutsch [9, 10] who further expanded the model of quantum computation. Born from the association of quantum phenomena and the progress made by classical computations, a new research field has been established, known as *quantum information science*.

## 1.1 Qubit representation

The elementary bricks of quantum information processing (QIP) are called *quantum bits* or *qubits*, having two orthogonal quantum states  $|0\rangle$  and  $|1\rangle$ . In contrast to digital information processing where information is encoded in a *bit* with two logical values 0 or 1, a qubit is a quantum-mechanical two-level system that can be put in any superposition in the form of

$$|\Psi\rangle = \alpha|0\rangle + \beta|1\rangle, \quad (1.1)$$

where  $\alpha$  and  $\beta$  are complex numbers. The superposition principle [11] is one of the foundations of the theory which, much like waves in classical physics, considers that the addition of two states will be another valid quantum state. Each measurement on the qubit finds state  $|0\rangle$  with a probability  $|\alpha|^2$  and state  $|1\rangle$  with a probability  $|\beta|^2$ .

A useful and intuitive representation of such a single-qubit state is the Bloch sphere, depicted in Fig. 1.1. Indeed, as the probabilities have to sum up to 1 ( $|\alpha|^2 + |\beta|^2 = 1$ ), it is equivalent to picture the qubit state on a sphere of unit radius, such that each point on the surface of the sphere corresponds to a pure state. Thus the qubit can be written as [12]

$$|\psi\rangle = \cos\left(\frac{\theta}{2}\right) |0\rangle + e^{i\phi} \sin\left(\frac{\theta}{2}\right) |1\rangle, \quad (1.2)$$

where  $\theta$  and  $\phi$  represent spherical coordinates on this three dimensional sphere represented by the Bloch vector  $(\cos\phi \sin\theta, \sin\phi \sin\theta, \cos\theta)$ . It is worth noticing that a mixed state, given by a statistical ensemble of pure states, would be described by a vector whose length lies inside the Bloch sphere.

## 1.2 Quantum gates and quantum circuits

There are few implementations possible for QIP but the most useful for our work is the “quantum circuit” model, which consists of a concatenation of quantum gates allowing information to be processed. We ignore other approaches introduced more recently such as one-way quantum computing [13, 14], adiabatic quantum computing [15] or topological quantum computing [16].

In analogy with classical information processing based on logic gates, quantum gates act on single-qubit or multi-qubit with the requirement of being unitary operators [12]. While an infinite number of quantum gates would be required in order to build all quantum operations, it has been shown [17, 18] that we can perform any multi-qubit unitary transformation if one can realise arbitrary single-qubit rotations on the Bloch sphere combined with two-qubit gates. The set of gates that allows for implementing any quantum computation is called a *universal gate set*. A common example [19] consists of two single-qubit gates called Hadamard ( $H$ ) and  $T$  gates, in combination with the two-qubit controlled-NOT (cNOT) gate. The matrix representations of  $H$  and  $T$  in the basis  $\{|0\rangle, |1\rangle\}$  are given by [12]

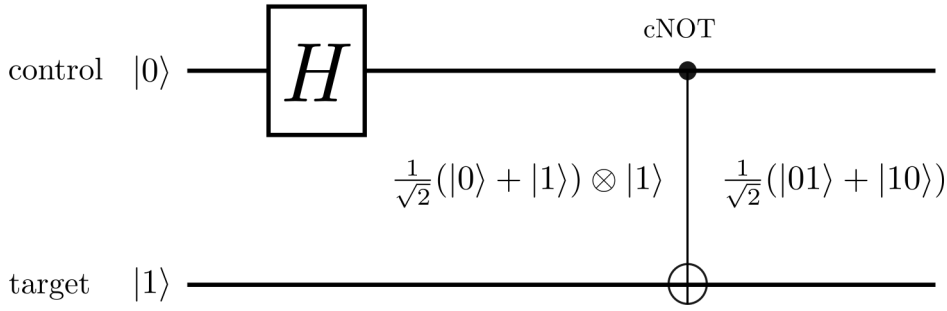


Figure 1.2: Circuit representation for the creation of the Bell State  $|\Psi^+\rangle$ . The single-qubit Hadamard gate  $H$  is applied to the control qubit, initially prepared in the state  $|0\rangle$ , and creates the superposition state  $1/\sqrt{2}(|0\rangle + |1\rangle)$ . Applying a subsequent cNOT gate allows to create the maximally entangled Bell state  $|\Psi^+\rangle = 1/\sqrt{2}(|01\rangle + |10\rangle)$  by flipping the spin of the target qubit depending on the state of the control qubit.

$$\hat{U}_H = \frac{1}{\sqrt{2}} \begin{pmatrix} 1 & 1 \\ 1 & -1 \end{pmatrix} \quad \text{and} \quad \hat{U}_T = \begin{pmatrix} 1 & 0 \\ 0 & e^{i\frac{\pi}{4}} \end{pmatrix}. \quad (1.3)$$

The universal two-qubit gate we are interested in implementing is the cNOT gate, which acts on two qubits known as “control qubit” and “target qubit”. The action of the cNOT gate is to change the state of the target qubit depending on the state of the control qubit. If the control qubit is in state  $|0\rangle$  the target is left unchanged, while if it is in state  $|1\rangle$  the state of the target qubit is flipped. The matrix representation of the cNOT gate in the basis  $\{|00\rangle, |01\rangle, |10\rangle, |11\rangle\}$  is given by [12]

$$\hat{U}_{\text{cNOT}} = \begin{pmatrix} 1 & 0 & 0 & 0 \\ 0 & 1 & 0 & 0 \\ 0 & 0 & 0 & 1 \\ 0 & 0 & 1 & 0 \end{pmatrix}. \quad (1.4)$$

Finally, a last requirement for implementing quantum computation lies in the possibility to create entanglement between qubits. This is a phenomenon that has no classical counterpart, where the quantum state of each qubit can not be described independently [20, 21]. This correlation between qubits can be implemented using quantum circuits. For instance, any two-qubit maximally entangled Bell states [12] can be derived from the association of a single-qubit gate such as an Hadamard gate followed by a cNOT gate, as represented in Fig. 1.2.

## 1.3 The rise of QIP

Quantum information science has really become rapidly attractive after Peter Shor wrote his 1994 paper [22] on the efficient prime-factorisation problem based on a quantum algorithm. This problem consists in decomposing a given positive integer number into product of prime factors. For arbitrary input size  $N$ , the quantum algorithm takes a number of time steps that is polynomial in  $N$  whilst the classical analog grows exponentially. Public key-encryption systems such as RSA-cryptosystem [23] depends on the difficulty to realise such a factorisation and would be broken via quantum computers. This has awakened a real opportunity for developing secure communication via quantum cryptography [24–26]. Moreover, there has been an expanding range of possible quantum computer applications, including unsorted database search [27], quantum image processing [28], quantum simulation [29–32] or machine learning [33].

Various architectures have been implemented to create a scalable quantum computer. Among them, trapped ions, superconducting qubits and Rydberg atoms, which must all satisfy a set of criteria referred to as *DiVincenzo criteria* [18] and given by

- a scalable physical system with well-characterised qubits,
- the ability to initialise the qubit in a given quantum state,
- long coherence times, much longer than the gate operation time,
- a universal set of quantum gates,
- the ability to measure the qubit's state.

Nevertheless, two major challenges are related to the creation of the universal quantum computer. The first one lies in the scalability of the chosen platform. Indeed, the minimum number of qubits that would be needed to realise classically intractable calculation varies from hundreds to thousands and beyond [34]. The second one emerges from perturbation of the quantum states by the environment, leading to decoherence which introduces errors. While performing a quantum operation, the

error is defined as  $\epsilon = 1 - \mathcal{F}$ , where  $\mathcal{F}$  is called the fidelity [12] (See Sec. 8.2) and quantifies the overlap between an expected state and the experimental one. Errors can be circumvented using error correction procedures [35], at the cost of stringent conditions on the error threshold. Indeed, achieving fault-tolerant quantum error correction codes requires an error threshold between  $10^{-2}$  and  $10^{-4}$ .

### 1.3.1 Trapped ions

Laser cooled ions in Paul traps are among the most precisely controlled quantum systems available [36]. The ion trap community has a wide combination of attributes for QIP that has grown rapidly since the proposal from Ignacio Cirac and Peter Zoller in 1995 [37]. In the same year, It was followed by the first implementation of the cNOT gate based on the Cirac-Zoller idea with a single ion [38].

Trapped ion qubits have demonstrated high-fidelity state preparation and read-out [39]. Some other milestones are the first realisation of deterministic quantum teleportation of atomic qubits [40, 41], the creation of deterministic multi-particle entangled states between 2 [42], 4 [43] and 14 qubits [44].

Moreover, single-qubit and two-qubit gates have been achieved with high-fidelities [45, 46], entering into the regime of fault-tolerant error correction with gate errors of  $\sim 10^{-4}$  and  $\sim 10^{-3}$  respectively. Rather large operation time of quantum gates in the order of 10-100  $\mu\text{s}$  are compensated by their incredibly long coherence time of  $\sim 50\text{ s}$  [47]. Recently, the duration of quantum logic gates has been reduced by an order of magnitude to 1.6  $\mu\text{s}$  [48] while maintaining high gate fidelity. Furthermore, unprecedented large coherence time up to 10 minutes [49] has been demonstrated.

Finally, multi-qubit algorithms [36] have allowed for the demonstration of a scalable Shor algorithm [50] and complete 3-qubit Grover search algorithm [51]. The last challenge consists of creating a platform that could handle more than 11 ions [52] to overcome decoherence arising from Coulomb interactions. A promising way to tackle scalability comes from the development of microfabricated segmented ion traps [53, 54].

### 1.3.2 Superconducting circuits

Superconducting circuits based on Josephson junctions are promising candidates for quantum computing. Indeed, these artificial atoms can be designed according to specific characteristics [55]. Moreover, they allow for scalability due to the possibility of being routinely made on a chip using standard lithographic techniques. A universal set of logic gates have been demonstrated with single-qubit gate fidelity of 99.92 % and two-qubit gate fidelity up to 99.4 % [56], in the path for fault-tolerant error-correction. Moreover, 10-qubit entanglement [57] as well as 20-qubit Schrödinger cat states [58, 59] have been realised recently, opening the way to efficient multi-qubit quantum algorithms. This attractive result has opened the way for commercial applications such as the company Rigetti which proposes a quantum cloud service or companies such as IBM, D-Wave or Google for private applications. However, even if quantum gates can be achieved with very short time of  $\sim 10$ 's ns, superconducting qubits are still limited by very low coherence time of  $20 - 40 \mu\text{s}$  [56].

### 1.3.3 Neutral atoms

Due to manufacturing limitations, the fabrication of large number of artificial atoms can't claim full uniformity over the large range of qubits required for implementing scalable QIP protocols. This can be overcome by atoms which, for the same species and isotopes, are identical. Another key feature of cold atoms for QIP is the long-coherence times of their ground state hyperfine levels, ideal candidates for optical memories, with similar intrinsic performance to ions and demonstrated storage times on the order of minutes [60, 61]. Moreover, although the previous platforms have their own strengths and limitations, atoms provide a clear advantage of scalability with the possibility to cool and trap large number of identical atomic qubits [62]. This can be achieved using microscopic arrays of dipole traps [63] or optical lattices [64]. Single atoms can be trapped in two-dimensional (2D) atomic arrays with single site resolution using spatial light modulator (SLM) [65–67] showing demonstration of quantum gate [68–70] and quantum simulation [67]. However, this method suffers from the drawback of the optical tweezers being stochastically

loaded [71]. Even if methods have been developed to obtain 90 % loading [72–74], the probability to load multiple traps in a single run becomes exponentially small for extension to large atomic arrays. This challenge has been overcome with dynamic reconfigurable traps using an acousto-optic deflector (AOD) [75] or SLM [76]. Another possibility consists of real-time movable optical tweezers for the creation of defect-free 2D optical arrays of atoms [77], with the opportunity to extend to 3D architectures of up to 72 atoms [78]. Optical tweezers traps turn out to create 3D atom architectures with experimental duty-cycles 2 orders of magnitude [62] smaller than conventional 3D atom trapping in optical lattice, loaded from a Mott-insulator [79]. This technique has been extended from alkali-atoms to both divalent atoms [80–83] and molecules [84].

## 1.4 The choice of Rydberg atoms

Efficient implementation of entanglement and quantum gates require strong interaction between atoms. However, neutral atoms in their ground states interact mostly through negligible magnetic dipole interactions. Highly entangled states have been engineered through controlled collisions between individual neighbouring neutral atoms trapped in an optical lattice [85–87]. Moreover, two-atom entanglement based on local spin-exchange has been demonstrated using mobile optical tweezers [88].

Whilst previous entanglement methods are taking place at short distances  $< 1 \mu\text{m}$ , highly excited Rydberg atoms (atoms with high principal quantum number  $n$ ) are a promising alternative candidate for QIP. Rydberg states have very long lifetimes, typically of  $\sim 150 \mu\text{s}$  in our experiment, with extension to  $\sim 350 \mu\text{s}$  under future cryogenic temperatures. This exceeds the  $\mu\text{s}$ -timescale for quantum gate operations. Another key property of Rydberg atoms comes from their large dipole moments  $\propto n^2$ , leading to strong and long-range dipolar interactions that can be switched on or off over 12 orders of magnitude [89].

The first proposal to use dipole-dipole interactions for implementing fast quantum gates between two neutral atoms, is based on the central feature of Rydberg dipole blockade [90], as detailed later in Chap 2. This effect arises from strong dipole-dipole interactions, shifting the doubly excited states out of resonance, within a sphere of

a few  $\mu\text{m}$  surrounding one atom promoted to a Rydberg state. This has been followed by a second proposal establishing that dipole blockade can be extended to a mesoscopic ensemble of  $N$  atoms for quantum information processing [91]. The evidence of Rydberg blockade has been first demonstrated in cold atomic ensembles through suppression of Rydberg excitation [92–94] or its manifestation via sub-Poissonian counting statistics [95]. Since then, a large range of applications based on Rydberg blockade has been suggested, such as single atom and single-photon sources [96], quantum non-linear optics [97], many-particle entanglement [89, 98–101] or quantum simulation [102, 103].

## 1.5 QIP with Rydberg atoms

The first step towards the realisation of QIP protocols with Rydberg atoms [89] has been the demonstration of sub-Poissonian loading of single atoms into microscopic dipole traps by Schlosser *et al.* [71, 104] in 2001. Single atom manipulation in optical tweezers has paved the way towards the experimental implementation of single and two-qubit gates. In 2004, ground state manipulation of single atoms has been demonstrated with MHz rates [105]. This was followed, in 2008, by the first coherent excitations between ground and Rydberg states in a large ensemble of 100 atoms [106] and microscopic samples of 1-10 atoms [107]. Shortly afterwards, in 2009, Rydberg blockade between two nearby trapped atoms was simultaneously implemented in two groups [108, 109]. In the same year of 2010, two major breakthroughs were achieved, corresponding to the entanglement between two Rydberg atoms mapped onto the long-lived ground states [110, 111] as well as the implementation of a cNOT gate [112, 113] using Rydberg blockade.

Furthermore, Rydberg states allow for controlled and versatile interactions either between different atomic isotopes [114] or atomic species [115]. This is a major advantage for embedding ancilla qubits that can be read out without perturbing the logical qubits for quantum error correction. Moreover, taking advantage of Rydberg long-range interactions allows for the realisation of multi-qubit gate operations such as Toffoli [116, 117] and Deutsch gates [118], without decomposition into multiple two-qubit gates. This makes it possible to implement Grover’s search algorithm [119,

[120] and should enable fault-tolerant quantum computing using surface code [121].

Over the last decade, the generation of two-qubit entangled state using Rydberg interactions has been one of the major experimental concerns. Their low-fidelities [68, 110, 113, 114] have only reached a maximum value of 81% either using Rydberg dressing [122] or Rydberg blockade [123], after post-selection, and still far from the fault-tolerant error threshold.

Recent experiments have overcome barriers to high fidelity gate operations by engineering the laser systems to overcome a major technical limitation of previous experiments arising from laser phase noise coupling to qubit evolution [124]. By careful filtering of the laser light, it has been possible to perform ground-Rydberg operations with  $\mathcal{F} > 0.97$  fidelity [125] and more recently [117] high fidelity two-qubit and multi-qubit operations with  $\mathcal{F} > 0.95$ , making them competitive against performance of large scale trapped ion and superconducting qubit platforms but without the challenges to scaling of large numbers of qubits.

## 1.6 Longer term hybrid system

Achieving a high-fidelity universal set of gates combined with a scalable number of qubits remains the most challenging issue for the future of quantum computing, with each platform experiencing strengths and weaknesses, as shown in Tab. 1.1. Another step will require to develop a quantum network [126] in order to distribute entanglement and information between distant nodes.

For now, superconducting qubits are leading, due to the maturity in the field of superconducting devices and the possibility to engineer strong coupling between qubits through microwave coplanar waveguide resonator (CPW) [127, 128]. However, as mentioned earlier in Sec. 1.3.2, superconducting qubits suffer from poor coherence times and make challenging to operate error corrections codes for developing fault-tolerant quantum computation [129–131]. Nevertheless, one can consider their coupling with another quantum system that would store the information, namely a *quantum memory*, allowing to preserve a long coherence time while maintaining fast processing with superconducting qubits. This *hybrid system* would combine the

Qubit	single/two-qubit gate error	single/two-qubit gate duration	coherence time
Trapped ions	$1.0(3) \times 10^{-6}$ [47] / $8(4) \times 10^{-4}$ [45]	$12 \mu\text{s}$ [47] / $30 \mu\text{s}$ [45]	$T_2^* = 50 \text{ s}$ [47]
Superconducting	$6.0(5) \times 10^{-4}$ [56] / $5.6(5) \times 10^{-3}$ [56]	$15 \text{ ns}$ [56] / $43 \text{ ns}$ [56]	$T_2^* = 10 \mu\text{s}$ [56]
Atoms	Neutral atoms $3.8(2) \times 10^{-5}$ [132] / Rydberg atoms $2.4(8) \times 10^{-2}$ [117]	$266 \text{ ns}$ [105] / $285 \text{ ns}$ [117]	Ground-Ground $T_2^* = 10 \text{ ms}$ [123] Ground-Rydberg $T_2^* = 17(2) \mu\text{s}$ [123]

Table 1.1: Performance of different kind of qubits

best properties of each technologies and offers an alternative route to fulfilling the requirements for QIP.

The bridge between a quantum memory and the superconducting qubits can be performed via a CPW resonator that acts as a quantum bus for transferring the information from one to the other. Several quantum memories have been investigated to couple with a superconducting resonator such as Nitrogen Vacancy (NV)-centers [133, 134], polar molecules [135] or the spin of ions in solid states [136] as well as neutral atoms with 3D microwave cavity [137]. Nevertheless, the best results for the coupling between a quantum memory and a superconducting CPW resonator has been achieved with atoms magnetically trapped  $14 \mu\text{m}$  above a CPW resonator at liquid helium temperature, taking advantage of the long coherence time of  $\sim 7 \text{ s}$  [138] offered by their hyperfine ground states and separated by  $6.8 \text{ GHz}$  [139].

However, although hyperfine ground states are ideal memory candidates, their coupling with microwave photons from the CPW resonator is made via weak magnetic dipole interactions. An alternative to achieve strong coupling between atoms and the CPW resonator can be reached via the huge electric dipole moments of atomic Rydberg states [120, 140, 141].

Our experiment seeks to develop such a coupling between atomic Rydberg ensembles with superconducting CPW [120, 141–144]. Using atoms as a quantum memory allows to take advantage of the long coherence time and strong optical transitions offered by their hyperfine ground states. On the other hand, Rydberg atoms experience strong and long-range interactions as well as transitions between neighbouring

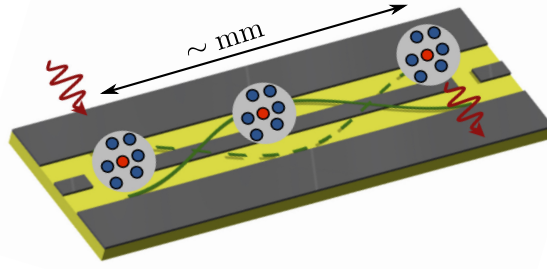


Figure 1.3: Ensembles of atoms trapped above a CPW resonator within antinodes of the standing wave of the field. Red arrows represent optical photons. Atoms are excited in the Rydberg states (red spheres) and entangled at the  $\sim$ mm scale via the microwave cavity field (green).

Rydberg states in the microwave regime, making them ideal for a hybrid system involving superconducting circuits.

Trapping ensembles of atoms above the anti-node of superconducting coplanar waveguide (CPW), as shown in Fig. 1.3, will allow to enter in the strong coupling regime, providing the opportunity to couple ensembles of atoms for quantum memory with superconducting qubits for quantum processing as well as realising long-range entanglement between atomic ensembles using a cavity mediated long-range interaction ( $\sim$ mm scale).

The long term objectives for our project require design choices motivated by future upgrades to cryogenic operation. This hybrid quantum device would offer the potential to unlock a large panel of applications such as microwave-to-optical conversion [145], scalable long range interactions for mm-scale entanglement between atomic ensembles [141, 146] and cavity cooling [147], offering a new platform for scalable quantum information processing.

## 1.7 Outline of the thesis

This thesis is separated into four parts and is structured as follows : an introduction compares different experimental platforms for the implementation of QIP protocols and explains our motivation to realise an hybrid experiment based on the coupling of Rydberg atomic ensembles to superconducting resonators. Part **I** gives an overview of the exaggerated properties of Rydberg atoms and the theoretical background to understand two-photon transitions. Part **II** describes the construction of the experiment, the methods for trapping and imaging single atoms in optical tweezers, along with the development of cooling lasers and excitation lasers stabilised on a high finesse cavity. This is followed by the calibration of the excitation lasers with respect to Rydberg transitions using EIT. Part **III** demonstrates coherent control of atomic qubits either during ground state rotations or ground-Rydberg excitations, shows evidence of Rydberg blockade between two nearby atoms and describes the potential of our experiment to realise a mesoscopic cNOT gate based on EIT, with high-fidelity. Finally, part **IV** outlines the future steps we intend to conduct.

### Part **I** : Theoretical Requirements

- Chapter 2 gives a brief introduction on Rydberg atoms and the scaling laws relative to their properties. Particular attention is given to the dipole-dipole interactions between Rydberg atoms and their consequences such as dipole blockade.
- Chapter 3 reviews fundamental results from the interaction of a two-level atom with a monochromatic light, allowing to develop three-level atom theory to describe two-photon transitions and understand quantum interference effect such as electromagnetically induced transparency (EIT).

### Part **II** : Experimental Realisations

- Chapter 4 covers the narrow-linewidth laser system, built to perform Rydberg two-photon excitations detuned from the intermediate state, as well as its characterisation.

- Chapter 5 describes the experimental apparatus used to trap single atoms with optical tweezers. This chapter also discusses about the imaging system performances along with single atom characterisation and atom's state preparation using optical pumping.
- Chapter 6 presents the spectroscopy of Rydberg states using EIT, both in vapour cell and cold atoms, allowing to calibrate cavity frequencies with respect to Rydberg transitions and determine long-term cavity frequency drift due to material aging.

### **Part III : Manipulation of Single and Two Qubits**

- Chapter 7 presents the realisation of single-qubit rotations between hyperfine ground states as well as coherent excitation from ground to Rydberg states. The chapter describes the experimental implementation of Rydberg blockade between two trapped atoms.
- Chapter 8 investigates the possibility to implement a mesoscopic cNOT gate, based on EIT, using our experiment.

### **Part IV : Conclusion and Outlook**

- Chapter 9 gives a summary of the achieved results and provides an outlook into the near future of the experiment.

## 1.8 Publications arising from this work

- C. J. Picken, R. Legaie, K. Macdonnell and J. D. Pritchard, *Entanglement of neutral-atom qubits with long ground-Rydberg coherence times*, [Quantum Sci. Technol.](#) **4**, 015011 (2019)
- R. Legaie, C. J. Picken and J. D. Pritchard, *Sub-kHz excitation lasers for Quantum Information Processing with Rydberg atoms*, [J. Opt. Soc. Am. B](#) **35**, 892 (2018).
- C. J. Picken, R. Legaie and J. D. Pritchard, *Single atom imaging with an sCMOS camera*, [App. Phys. Lett.](#) **111**, 164102 (2017).

# Part I

## Theoretical Requirements

# Chapter 2

## Rydberg Atom Properties

Rydberg atoms are atoms with at least one electron in a highly excited state [148]. In our experiment, the range of principal quantum number we will deal with is between  $n = 50$  to  $n = 81$  of  $^{133}\text{Cs}$ . In this chapter, we will give a flavour of the most important features of Rydberg atoms required to interpret the results presented in this thesis. After presenting an overview of the exaggerated atomic properties of alkali Rydberg atoms in Sec. 2.1, we will describe the strong and long-range Rydberg-Rydberg interactions in Sec. 2.2. Finally in Sec. 2.3, we will explain the concept of Rydberg blockade arising from dipole-dipole interactions and motivate its use for creating entanglement and quantum gate operations. A more detailed presentation of Rydberg atoms can be found in [148] or [149].

### 2.1 Rydberg atom properties

Below we consider the case of a single valence electron, as it is the case for alkali Rydberg atoms. This enables Rydberg atoms to be approximated as hydrogen atoms whose binding energy  $\mathcal{E}_n$  in the Bohr model of atom [150] is given by

$$\mathcal{E}_n = -hc\frac{R_{\text{H}}}{n^2}, \quad (2.1)$$

where  $h$  is the Planck constant,  $c$  the speed of light,  $n$  the principal quantum number and  $R_{\text{H}}$  the Rydberg constant for hydrogen atom.

We often treat the Rydberg atom as hydrogenic, whose valence electron orbits a positively charged core with a  $-1/r$  Coulomb potential. However, we neglect the fact that for low orbital angular momentum states with  $\ell \leq 3$ , the valence electron has a high probability density in the core. The screening from the inner electrons is decreased and the valence electron feels a deeper potential than the Coulomb potential. The inner electrons can also be polarised by the valence electron. These two interactions with the core combine to increase the binding energy of the low- $\ell$  Rydberg states with respect to hydrogenic states. A phenomenological approach called quantum defect theory allows calculation of the binding energies. This consists of replacing the principal quantum number with an effective quantum number  $n^*$  characterised by the quantum defects  $\delta_{n,\ell,j}$  in the Rydberg formula, such that

$$\mathcal{E}_{n,\ell,j} = -hc \frac{R_{Cs}}{(n^*)^2}. \quad (2.2)$$

Here, the Rydberg constant  $R_\infty = \frac{m_e e^4}{8\pi\epsilon_0^2 h^3}$  [151] is weighted by the mass of  $^{133}\text{Cs}$  to give an effective Rydberg constant  $R_{Cs} = R_\infty / (1 + \frac{m_e}{m_{Cs}}) = 109\,736.862\,7339 \text{ cm}^{-1}$  [152] and  $n^* = n - \delta_{n,\ell,j}$  is the effective principal quantum number.

The quantum defects  $\delta_{n,\ell,j}$  depend on the element and the angular momentum quantum numbers. Indeed, for Rydberg states, the coupling between the core and the valence electron is so small ( $\ll 1 \text{ MHz}$ ) that we can neglect the hyperfine structure. The quantum defects can be calculated using the Rydberg-Ritz formula [140]

$$\delta_{n,\ell,j} = \delta_0 + \frac{\delta_2}{(n - \delta_0)^2} + \frac{\delta_4}{(n - \delta_0)^4} + \dots \quad (2.3)$$

The values of  $\delta_0, \delta_2 \dots$  have been experimentally determined by spectroscopic measurements [152–155] and Tab. 2.1 shows different values that we have used for pre-

State	$\delta_0$	$\delta_2$
$n S_{1/2}$	4.0493532	0.2391
$n P_{3/2}$	3.5590676	0.37469
$n D_{5/2}$	2.4663144	0.01381

Table 2.1: Quantum defect values taken from [152, 153] to calculate Rydberg transitions used in the experiment.

Property	$(n^*)$ -scaling
Binding Energy $\mathcal{E}_{n,\ell,j}$	$(n^*)^{-2}$
Level Spacing	$(n^*)^{-3}$
Orbital Radius	$(n^*)^2$
Radiative Lifetime $\tau$	$(n^*)^3$
Polarisability $\alpha$	$(n^*)^7$
VdW coefficient $C_6$	$(n^*)^{11}$

Table 2.2: Scaling laws for properties of the Rydberg states [148].

dicting our Rydberg transitions (see Chap. 6).

Similarly to the hydrogen atom [150, 156], general properties of Rydberg atoms can be derived from scaling laws dependent on the effective quantum number  $n^*$ . Table 2.2 shows an overview of important properties and their scaling behavior. For our range of principal quantum numbers, the electron radius defined as  $\langle r \rangle = 0.5[3(n^*)^2 - \ell(\ell + 1)]$  can be as large as 400 nm and so loosely bound that it results in exaggerated properties, arising from extremely large dipole moments  $\propto (n^*)^2$ . The extreme sensitivity of the Rydberg states to an electric field, which scales as  $\propto (n^*)^7$ , highlights the necessity to control the electric field environment of our experiment to perform coherent excitation from ground to Rydberg states (see Sec. 7.2.5). Additionally, the long lifetime  $\propto (n^*)^3$  and the control over the magnitude of the interactions  $\propto (n^*)^{11}$  make them convenient for developing coherent quantum gates [89, 91, 157, 158] as will be shown in Chap. 8.

### 2.1.1 Rydberg state lifetimes

Rydberg atoms are suitable candidates for quantum information processing due to their long lifetime ( $> 100 \mu\text{s}$ ) which can be derived from two contributions. Firstly, the inverse of the radiative lifetime  $\tau_0$  is given by the sum over the Einstein- $A_{n\ell \rightarrow n'\ell'}$  coefficient when decaying from a state  $|n\ell\rangle$  to lower energy states  $|n'\ell'\rangle$  [159] with

$$\Gamma_0 = \frac{1}{\tau_0} = \sum_{\mathcal{E}_{n\ell} > \mathcal{E}_{n'\ell'}} A_{n\ell \rightarrow n'\ell'}, \quad (2.4)$$

where the Einstein- $A_{n\ell \rightarrow n'\ell'}$  coefficient is proportional to the cube of the resonance

frequency of the transition  $\omega_{n\ell, n'\ell'}$  and the square of the dipole matrix element  $|\langle n'\ell' | er | n\ell \rangle|^2$ , which means the dominant radiant decay path is still decay to the lowest lying state despite the weak dipole matrix element.

Secondly, at finite temperature, the effect of black-body relaxation (BBR) must be considered which occurs at a rate [159]

$$\Gamma_{\text{BBR}} = \sum_{n'} A_{n\ell \rightarrow n'\ell'} \frac{1}{e^{\hbar\omega_{nn'}/k_B T} - 1}, \quad (2.5)$$

resulting in a total decay rate of

$$\Gamma_{\text{eff}} = \frac{1}{\tau_{\text{eff}}} = \Gamma_0 + \Gamma_{\text{BBR}}. \quad (2.6)$$

Unlike the radiative decay that couples to low-lying states, the BBR causes a dominant decay to close-lying states with strong electric dipole transitions.

In our experiment, we will realise Rydberg coherent excitation towards the states  $69S_{1/2}$  and  $81D_{5/2}$  (see Chap. 7) which have an effective lifetime of  $134 \mu\text{s}$  and  $163 \mu\text{s}$  at 300 K respectively, while future work in a cryogenic environment at 4 K will allow to further increase their values to  $349 \mu\text{s}$  and  $310 \mu\text{s}$ . This is four order of magnitude bigger than the typical lifetime of the low lying state  $6P_{3/2}$  of 30 ns [160], representing an ideal platform to perform quantum gates while minimising decoherence.

## 2.2 Rydberg atom interactions

In addition to the atomic properties discussed above which show Rydberg atoms as good candidates for quantum information processing applications, another key property lies in the ability to turn on and off the strong and long-range interactions between two Rydberg atoms by 12 order of magnitudes [89]. At a separation distance on the order of  $R \sim 1 \mu\text{m} \gg (n^*)^2 \times a_0$ , with  $a_0$  the Bohr radius, the dipole-dipole interactions can become predominant over the excitation bandwidth of the lasers and play an important role in our experiment.

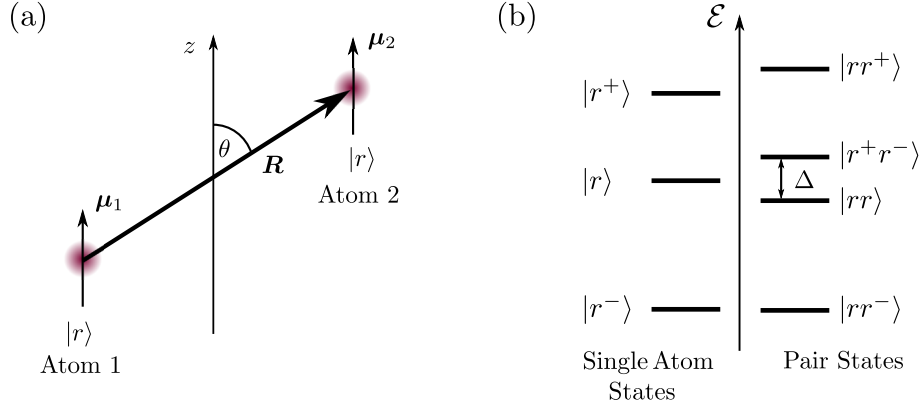


Figure 2.1: (a) Dipole-dipole interactions between two atoms separated by a distance  $\mathbf{R}$ , making an angle  $\theta$  with respect to the quantisation axis  $z$ . (b) Transformation from the single atom states space constituted from three Rydberg states  $|r^+\rangle$ ,  $|r\rangle$  and  $|r^-\rangle$  to the subsystem where the pair state  $|rr\rangle$  is nearly degenerate with the state  $|r^+r^-\rangle$ , separated by an energy defect  $\Delta$ .

### 2.2.1 Two regimes of interaction

If we limit our discussion to the case where both atoms are initially excited to the same Rydberg state  $|r\rangle = |n\ell j\rangle$ , the atom pair state can be written as  $|\psi_{\text{pair}}\rangle = |n\ell j, n\ell j\rangle = |rr\rangle$ . The electrostatic dipole-dipole interaction between two Rydberg atoms separated by a distance  $\mathbf{R}$  along the quantisation axis  $z$  with  $\theta = 0$ , as shown schematically in Fig. 2.1 (a), can be written in atomic units as [89]

$$V_{dd}(\mathbf{R}) = \frac{\boldsymbol{\mu}_1 \cdot \boldsymbol{\mu}_2}{R^3} - \frac{3(\boldsymbol{\mu}_1 \cdot \mathbf{R})(\boldsymbol{\mu}_2 \cdot \mathbf{R})}{R^5}. \quad (2.7)$$

The dipole moments  $\boldsymbol{\mu}_{1,2}$  being associated with transitions from the state  $|r\rangle$  to other Rydberg states  $|r^+\rangle$  and  $|r^-\rangle$ , having higher and lower energy respectively, as shown in Fig. 2.1 (b). The electric dipole selection rules induces transitions to other pair states with  $\Delta\ell = \ell \pm 1$ . One finds that the interaction is dominated by transitions to adjacent two-atom pair states with opposite parity [161].

Considering a single significant contribution from the pair state  $|r^+r^-\rangle$ , the pair-states  $|rr\rangle$  and  $|r^+r^-\rangle$  are coupled by  $V_{dd}(R)$  with the energy defect  $\Delta$  defined as

$$\Delta = \mathcal{E}_{|r^+\rangle} + \mathcal{E}_{|r^-\rangle} - 2\mathcal{E}_{|r\rangle}, \quad (2.8)$$

which represents the energy difference of the pair states at infinite separation. In the basis  $\{|rr\rangle, |r^+r^-\rangle\}$ , the Hamiltonian describing the dipole-dipole interaction is

$$\mathcal{H} = \begin{pmatrix} 0 & V_{dd}(R) \\ V_{dd}(R) & \Delta \end{pmatrix}. \quad (2.9)$$

Its diagonalisation leads to the eigenvalues

$$\mathcal{E}_{\pm} = \frac{\Delta}{2} \pm \sqrt{\frac{\Delta^2}{4} + V_{dd}(R)^2}, \quad (2.10)$$

noting that each pair state's eigenenergies are dependent upon the separation of the two atoms. The interaction energies show different forms depending on the distance between the atoms.

**(i) For long range interactions such that  $V_{dd}(R) \ll \Delta$**

$$\Delta\mathcal{E}_{\text{vdW}} \approx -\frac{V_{dd}(R)^2}{\Delta} = -\frac{1}{\Delta} \left(\frac{C_3}{R^3}\right)^2 = -\frac{C_6}{R^6}. \quad (2.11)$$

In this regime, the van der Waals (vdW) interaction dominates and scales as  $1/R^6$ . The effect of the interaction is to shift the state  $|rr\rangle$  by an amount  $\Delta\mathcal{E}_{\text{vdW}}$  that depends only on the sign of the energy defect  $\Delta$ . The strength of the interaction is given by the coefficient  $C_6$  which scales proportional to  $n^{*11}$  as  $V_{dd}(R) \propto \mu^2 \propto n^{*4}$  and the energy defect  $\Delta \propto n^{*-3}$ .

**(ii) For short range interactions such that  $V_{dd}(R) \gg \Delta$**

$$\Delta\mathcal{E}_{dd} \approx \pm V_{dd}(R) = \pm \frac{C_3}{R^3}. \quad (2.12)$$

This is the resonant dipole-dipole interaction regime for short interatomic distance  $R$ , which scales as  $1/R^3$ , with the coefficient  $C_3 \propto \mu^2 \propto n^{*4}$ . Using external electric field it is also possible to tune  $\Delta \approx 0$  to realise a Förster resonance [162–164], allowing to acquire a long-range interaction behavior with a  $1/R^3$  dependence.

The transition between the  $1/R^3$  and  $1/R^6$  regimes occurs at the van der Waals

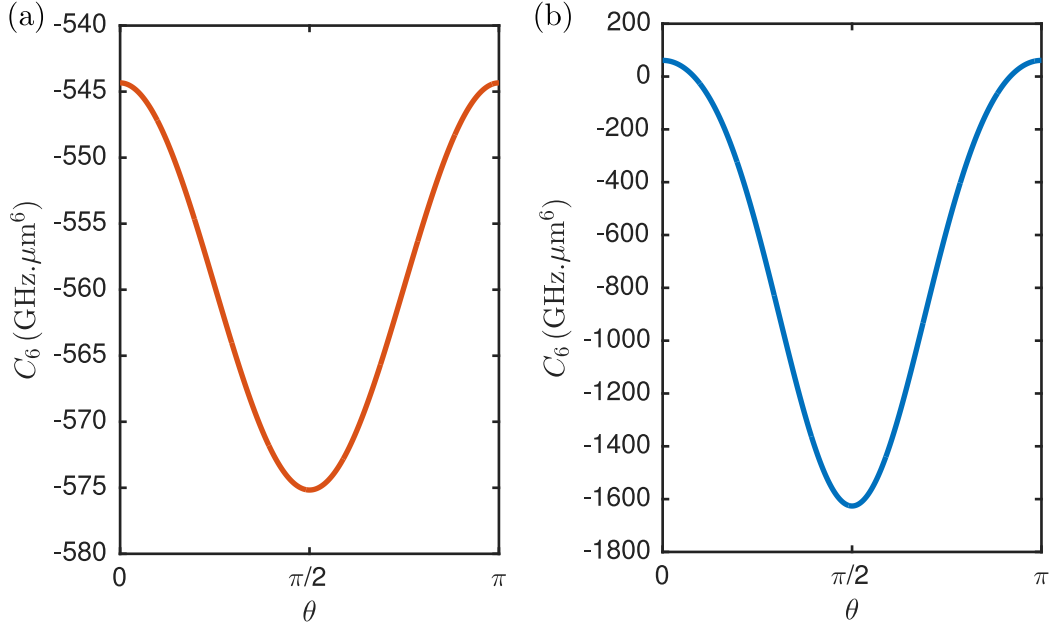


Figure 2.2: Angular dependence of  $C_6$  on  $\theta$  for atom-pair states (a)  $|69S_{1/2}, 69S_{1/2}\rangle$  and (b)  $|81D_{5/2}, 81D_{5/2}\rangle$  with  $m_j = 1/2$  and  $m_j = 5/2$  respectively. This shows that  $S_{1/2}$ -states are almost isotropic whilst  $D_{5/2}$ -states shows pronounced anisotropic interaction.

radius when  $V_{dd}(R_{\text{vdW}}) = |\Delta|$ , where  $R_{\text{vdW}} = \sqrt[6]{|C_6/\Delta|} \propto n^{*7/3}$ .

### 2.2.2 Angular dependence and interaction strength

In the discussion above it was assumed that the internuclear axis was aligned with the quantisation axis  $z$  ( $\theta = 0$ ). Transforming the interaction energy of Eq. 2.7 in the spherical basis allows to reveal the angular dependence of the dipole-dipole interaction.

The dipole operator is defined as  $\mu = -e\mathbf{r} \cdot \hat{\boldsymbol{\epsilon}}$ , where  $\hat{\boldsymbol{\epsilon}}$  is the electric field polarisation unit vector, allowing to introduce the spherical dipole operators

$$\mu_{-1} = \frac{1}{\sqrt{2}}(\mu_x - i\mu_y), \quad (2.13a)$$

$$\mu_0 = \mu_z, \quad (2.13b)$$

$$\mu_{+1} = -\frac{1}{\sqrt{2}}(\mu_x + i\mu_y). \quad (2.13c)$$

The operator  $\mu_{-1}$  drives transitions that change the magnetic quantum number by

$\Delta m_j = -1$  associated to  $\sigma^-$ - transitions, the operator  $\mu_0$  conserves the magnetic quantum number such that  $\Delta m_j = 0$  associated to  $\pi$ -transitions, while the operator  $\mu_{+1}$  drives transitions that change the magnetic quantum number by  $\Delta m_j = +1$  associated to  $\sigma^+$ - transitions. Thus the dipole-dipole operator can be written as a function of both  $\theta$  and  $R$  [165]

$$\begin{aligned}
V(R, \theta) = & \frac{(1 - 3 \cos^2 \theta) (\mu_{1-} \mu_{2+} + \mu_{1+} \mu_{2-} + 2 \mu_{1z} \mu_{2z})}{2 R^3} \\
& + \frac{3 \sin \theta \cos \theta (\mu_{1+} \mu_{2z} - \mu_{1-} \mu_{2z} + \mu_{1z} \mu_{2+} - \mu_{1z} \mu_{2-})}{\sqrt{2} R^3} \\
& - \frac{3 \sin^2 \theta (\mu_{1+} \mu_{2+} + \mu_{1-} \mu_{2-})}{2 R^3},
\end{aligned} \tag{2.14}$$

with  $\mu_{iq}$  corresponding to atom  $i = \{1, 2\}$  and the spherical operator  $q = \{-1, 0, +1\}$ . The dipole-dipole interaction of Eq. 2.14 can be decomposed in three parts that govern the change of the total magnetic quantum number  $M_j = m_{j1} + m_{j2}$ , for which  $\Delta M_j = 0, 1$  and  $2$  respectively. For  $\theta \neq 0$ , atom-pair states with different  $M_j$  can thus be coupled together.

Looking at our state of interest  $69S_{1/2}$  and  $81D_{5/2}$ , we expect two different interaction strengths arising from the anisotropy of the dipole-dipole interaction [164, 166, 167].

For a pair of atoms in the  $69S_{1/2}$  Rydberg state, Fig. 2.2 shows that the van der Waals interaction is almost isotropic due to the spherical symmetry distribution of S states. The atom-pair state  $|rr\rangle = |69S_{1/2}, 69S_{1/2}\rangle$  experiences an interaction dominated with the pair state  $|r^+r^-\rangle = |69P_{3/2}, 68P_{3/2}\rangle$  [166] corresponding to the smallest energy defect of  $\Delta/2\pi = 0.75$  GHz. In order to calculate the magnitude of the interaction we need to take into account all of the possible pair states dipole coupled to the initial pair state  $|69S_{1/2}, 69S_{1/2}\rangle$ . We have used second-order perturbation theory [168] in the uncoupled basis, with a restricted basis built from a range of principal quantum number  $\Delta n = 10$  and a maximum pair state detuning of  $|\Delta|/2\pi < 50$  GHz. The  $C_6$  coefficient is computed using a radial matrix element calculated with the Numerov method [169, 170]. The coefficient  $C_6 = -575 \text{ GHz} \cdot \mu\text{m}^6$  is negative, leading to repulsive interactions with a van der

Waals radius of  $R_{\text{vdW}} \sim 3 \mu\text{m}$ .

In the case of the  $81D_{5/2}$  Rydberg state, the orbital angular momentum of the initial pair state is 4. However, the configuration of our experiment leads to an angle of  $\theta = \pi/2$ , showing a significantly anisotropic interaction and much larger compared to the value aligned along  $z$  ( $\theta = 0$ ), as illustrated in Fig. 2.2. Besides its angular dependence, the interaction strength exhibits a strong dependence on the magnetic quantum number  $m_j$ . We have chosen the state  $m_j = 5/2$  because it has the strongest coupling to the ground state, which is used to obtain a large Rabi frequency for coherent Rydberg excitation in Sec. 7.2.6.

For the atom-pair state  $|rr\rangle = |81D_{5/2}, 81D_{5/2}\rangle$ , the major contribution to the magnitude of the interactions will come from the pair state  $|r^+r^-\rangle = |85P_{3/2}, 76F\rangle$ . The corresponding energy defect is  $\Delta/2\pi = 0.74 \text{ GHz}$  and the coefficient  $C_6 = -1626 \text{ GHz}\cdot\mu\text{m}^6$  is three times higher compared to the  $C_6$  coefficient of the state  $69 S_{1/2}$ . This atom-pair state generates strong repulsive interactions with larger van der Waals radius of  $R_{\text{vdW}} \sim 3.6 \mu\text{m}$ .

## 2.3 Dipole blockade

In our experiment, we will be working on coherent excitation of two single atoms from the ground state  $|g\rangle$  to Rydberg states  $|r\rangle$ . Due to technical implementation (see Sec. 7.3), the minimum experimental interatomic distance is  $6 \mu\text{m}$ , thereby satisfying the condition  $R \gg R_{\text{vdW}}$  where the van der Waals interaction dominates. The effect of the van der Waals interaction on the Rydberg excitation of the pair state  $|gg\rangle$  as a function of the separation  $R$  is illustrated in Fig. 2.3.

The dipole-dipole interaction on the two atoms ground state  $|gg\rangle$  and the singly excited Rydberg state is negligible, hence independent of the separation  $R$ . An excitation laser with Rabi frequency  $\Omega$  in resonance with the transition  $|g\rangle \rightarrow |r\rangle$  can excite the singly Rydberg excited states  $|gr\rangle$  or  $|rg\rangle$ . In the same way, the doubly excited state  $|rr\rangle$  will be populated at large interatomic separation. As the atoms are moved closer together, the van der Waals interaction leads to a progressive energy shift of the doubly excited state  $|rr\rangle$ , until the double excitation to the state

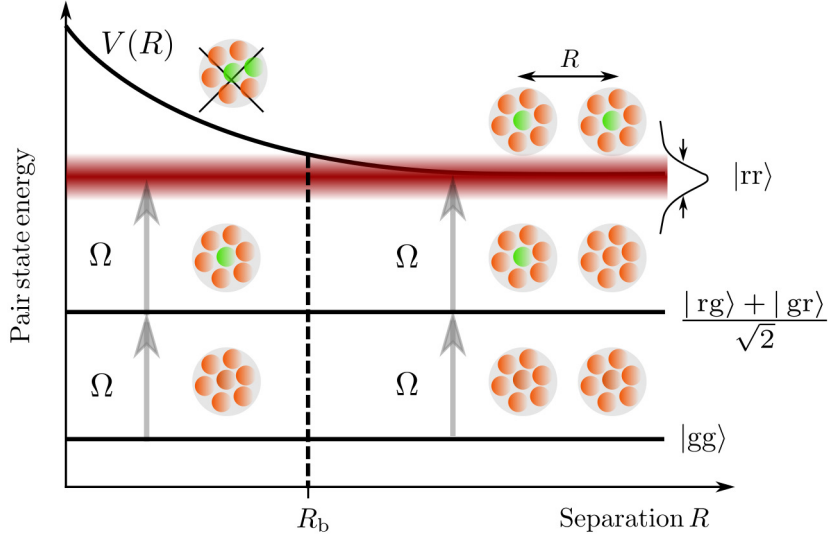


Figure 2.3: Rydberg dipole blockade. At long interatomic separation  $R$ , two atoms can be excited simultaneously to the pair state  $|rr\rangle$ , with red and green spheres standing for unexcited versus excited atoms respectively. Below the blockade radius  $R_b$ , the dipole-dipole interaction shifts the doubly excited state  $|rr\rangle$  out of the excitation bandwidth  $\Omega$ . The blockade prevents multiple excitations, leading to a single excitation collectively shared and the creation of an entangled state  $|\mathcal{W}\rangle = (|rg\rangle + |gr\rangle)/\sqrt{2}$ .

$|rr\rangle$  was shifted out of resonance with the driving field. This phenomenon is called the *dipole blockade* [91] and requires the interaction shift of the doubly excited state  $|rr\rangle$  to be larger than the excitation bandwidth

$$|V_{dd}(R)| > \hbar \times \max(\Omega, \Gamma_r), \quad (2.15)$$

where  $\Gamma_r$  represents the natural linewidth of the Rydberg state  $|r\rangle$  and  $\Omega$  is the excitation linewidth. Experimentally, the excitation linewidth  $\Omega/2\pi \sim 1$  MHz is far bigger than typical values of  $\Gamma_r/2\pi \sim 10$  kHz for our range of Rydberg states.

The volume in which only one atom can be excited to a Rydberg state is a sphere whose limits are defined by the following equality  $V_{dd}(R_b) = \hbar\Omega$ . In the van der Waals regime, the expression of the blockade radius takes the form

$$R_b = \sqrt[6]{\frac{C_6}{\hbar\Omega}}. \quad (2.16)$$

The blockade radius  $R_b$  sets the minimum distance from which two Rydberg excited atoms can be separated from each other, as illustrated in Fig. 2.3. One can deduce

the scaling of the blockade radius knowing that the coefficient  $C_6 \propto (n^*)^{11}$ , such that  $R_b \propto \sqrt[6]{C_6} \propto (n^*)^{11/6}$ .

Therefore, if the excitation of two atoms is done within the blockade sphere such that the interatomic separation verifies  $R < R_b$ , it is impossible to tell which atom gets excited to the Rydberg state due to the fact that they are indistinguishable. It is thus equally probable to obtain the states  $|rg\rangle$  or  $|gr\rangle$ , creating an effective superposition of both states

$$|\mathcal{W}\rangle = \frac{|rg\rangle + |gr\rangle}{\sqrt{2}}. \quad (2.17)$$

This is a way to create a symmetric maximally entangled state whose coupling with the light field is enhanced by a factor  $\sqrt{2}$ , resulting in a collective Rabi frequency of  $\sqrt{2}\Omega$  [91, 108, 109, 123], instead of the single atom excitation at a rate  $\Omega$ .

Generalising to an ensemble of  $N$ -atoms within a blockaded volume  $V = 4/3\pi R_b^3$ , a single excitation is collectively shared amongst the  $N$ -atoms to create an effective two-level atom called a *super-atom* between the collective ground state  $|G\rangle = |g_1, g_2, g_3, \dots, g_i, \dots, g_N\rangle$  and an entangled collective state

$$|\mathcal{W}\rangle = \frac{1}{\sqrt{N}} \sum_{j=1}^N \exp(-i\mathbf{k} \cdot \mathbf{r}_j) |g_1, g_2, g_3, \dots, r_j, \dots, g_N\rangle. \quad (2.18)$$

The phase factor  $\exp(-i\mathbf{k} \cdot \mathbf{r}_j)$  is inherent to the phase of the excitation laser at the position of  $j$ -th atom excited to the Rydberg state and can be used to generate single photons with directional emission [96].

The collective Rabi frequency coupling the many body states  $|G\rangle$  and  $|\mathcal{W}\rangle$  by driving the system with an electric field  $\mathbf{E}$  becomes

$$\begin{aligned}
\Omega_{coll} &= -\frac{e\mathbf{E}}{\hbar} \langle G|\mathbf{r}|\mathcal{W}\rangle, \\
&= -\frac{e\mathbf{E}}{\hbar} \frac{1}{\sqrt{N}} \sum_{j=1}^N \langle g_1, g_2, g_3, \dots, g_N | \mathbf{r} | g_1, g_2, g_3, \dots, r_j, \dots, g_N \rangle, \quad (2.19) \\
&= \frac{1}{\sqrt{N}} \sum_{j=1}^N \Omega = \sqrt{N} \Omega,
\end{aligned}$$

where  $\Omega = -\frac{e\mathbf{E}}{\hbar} \langle g|\mathbf{r}|r\rangle$  is the single atom Rabi frequency between the ground state  $|g\rangle$  and the Rydberg state  $|r\rangle$ . The collective Rabi frequency is enhanced by a factor  $\sqrt{N}$ , showing the accessibility to high degree of entanglement from many-body systems [94, 107, 109, 164, 171].

## 2.4 Summary

Rydberg atoms are a convenient source to encode a qubit due to the ability to make them interact through strong short-range dipole-dipole and long-range van der Waals interactions whilst maintaining long lifetimes ( $> 100 \mu\text{s}$ ) with respect to single atom excitation rate ( $\sim \text{MHz}$ ). This is an important prerequisite for quantum information [89–91, 110, 112, 157]. Moreover, collective Rydberg excitation shared over the blockade sphere offers a practical route to implement a many-body entangled state [172] as we will see in Chap. 8.

# Chapter 3

## Atom-Light Interactions

The simplest model of the interaction between atoms and light is that of a two-level atom driven by a coherent optical field. This system has been exhaustively studied [21, 173, 174] and will allow us to analyse coherent effects such as Rabi oscillations [175] and atom trapping due to the optical dipole force [176, 177] in a first section. Thereafter, we will introduce the concept of the density matrix [21] as well as revealing a useful representation of the two-level system in terms of dressed states [178]. The second section is focused on the physics of the two-photon transition in a three-level atom. We will develop the theoretical framework for understanding two-photon excitation, either from ground to Rydberg states or between ground states. In particular, we will explain the occurrence of Electromagnetically Induced Transparency (EIT) on the two-photon resonance while we will study the possibility to describe off-resonant excitation by an effective two-level atom.

### 3.1 The two-level atom

Consider an atom consisting of two levels  $|g\rangle$  and  $|e\rangle$  separated in energy by  $\hbar\omega_0$ , as depicted in Fig 3.1 (a). The ground state  $|g\rangle$  has a long lifetime such that there is no decay out of the ground state. The interaction between the two-level atom and a monochromatic electromagnetic wave, characterised by a detuning  $\Delta = \omega - \omega_0$  with respect to the atomic transition and a polarisation vector  $\epsilon$ , is given by the

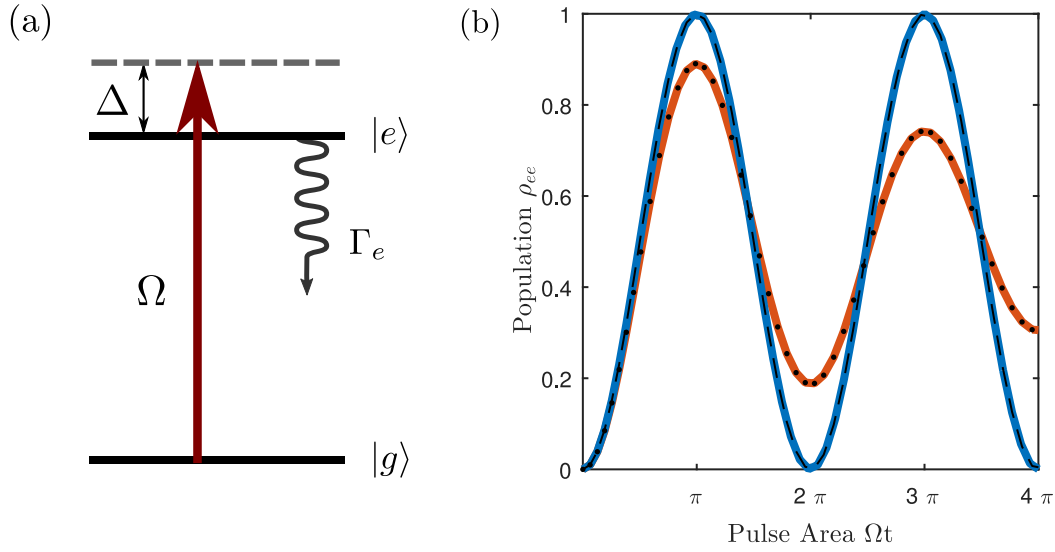


Figure 3.1: (a) Two-level atom with a ground state  $|g\rangle$  and an excited state  $|e\rangle$  driven at the Rabi frequency  $\Omega$  with a detuning  $\Delta = \omega - \omega_0$  with respect to the atomic transition. The excited state being characterised by the spontaneous emission rate  $\Gamma_e$ . (b) Rabi oscillations of the excited state population  $\rho_{ee}$  on resonance ( $\Delta = 0$ ) and without spontaneous emission (blue), obtained by solving numerically the TDSE and its corresponding fit (dashed line) with Eq. 3.6. Including dissipation leads to an exponential damping (orange), which is well interpreted via Eq. 3.15 (dotted line).

Hamiltonian  $\hat{\mathcal{H}} = \hat{\mathcal{H}}_0 + \hat{\mathcal{H}}_{\text{AL}}$  where  $\hat{\mathcal{H}}_0 = \mathbf{p}^2/2m + \hbar\omega_0|e\rangle\langle e|$  is the Hamiltonian for the bare atom and  $\hat{\mathcal{H}}_{\text{AL}} = -\boldsymbol{\mu} \cdot \boldsymbol{\mathcal{E}}$  is the Hamiltonian describing the interaction between an electric dipole  $\boldsymbol{\mu} = -e \hat{\mathbf{r}}$  and the electric field  $\boldsymbol{\mathcal{E}}$ . Using ultracold atoms, we neglect the kinetic energy from the bare atom Hamiltonian  $\hat{\mathcal{H}}_0$ . Moreover, working in a semi-classical picture allows to treat the electric field as a plane wave  $\boldsymbol{\mathcal{E}} = \boldsymbol{\epsilon}(\mathcal{E}_0/2e^{i(\mathbf{k} \cdot \mathbf{r} - \omega t)} + c.c.)$ . We make the dipole approximation  $e^{i\mathbf{k} \cdot \mathbf{r}} \simeq 1$  which is valid in the limit that the spatial extent of the atom is small compared to the wavelength ( $\langle r \rangle \ll \lambda$ ), resulting in

$$\hat{\mathcal{H}}_{\text{AL}} = \frac{\hbar\Omega}{2}e^{-i\omega t}(|e\rangle\langle g| + |g\rangle\langle e|) + c.c., \quad (3.1)$$

where we have introduced the Rabi frequency

$$\Omega = \frac{-\boldsymbol{\mu} \cdot \boldsymbol{\mathcal{E}}}{\hbar} = \frac{\mathcal{E}_0}{\hbar} \langle e | e \mathbf{r} \cdot \boldsymbol{\epsilon} | g \rangle = \frac{\mathcal{E}_0}{\hbar} \langle e | \mu_q | g \rangle, \quad (3.2)$$

and  $\mu_{q=\{-1,0,+1\}}$  the spherical dipole operators defined in Sec. 2.2.2. Applying the *Rotating Wave Approximation (RWA)*, which consists of neglecting fast oscillating

terms at the frequency  $\omega + \omega_0$  [177], the atom-light Hamiltonian is given as

$$\hat{\mathcal{H}}_{\text{AL}}^{\text{RWA}} = \frac{\hbar\Omega}{2} e^{-i\omega t} |e\rangle\langle g| + \frac{\hbar\Omega^*}{2} e^{i\omega t} |g\rangle\langle e|. \quad (3.3)$$

### 3.1.1 Wavefunctions and Hamiltonian approaches

Following the derivation above, we can evaluate the time evolution of any wavefunction of the form  $|\psi(t)\rangle = c_g(t)|g\rangle + c_e(t)|e\rangle$  using the time-dependent Schrödinger equation (TDSE)

$$i\hbar \frac{\partial}{\partial t} |\psi\rangle = \hat{\mathcal{H}} |\psi\rangle. \quad (3.4)$$

Injecting  $|\psi\rangle$  in the TDSE enables us to obtain a set of coupled equations for the complex amplitudes  $c_g$  and  $c_e$ . To remove the exponential time dependence it is convenient to perform a frame rotation, introducing parameters  $\tilde{c}_g = c_g e^{-i\Delta t/2}$  and  $\tilde{c}_e = c_e e^{-i(\Delta/2 + \omega_0)t}$ , resulting in new equations whose integration yields to the solutions [21]

$$\tilde{c}_g(t) = \left[ \cos\left(\frac{\Omega't}{2}\right) - i\frac{\Delta}{\Omega'} \sin\left(\frac{\Omega't}{2}\right) \right] \tilde{c}_g(0) - i\frac{\Omega^*}{\Omega'} \sin\left(\frac{\Omega't}{2}\right) \tilde{c}_e(0), \quad (3.5a)$$

$$\tilde{c}_e(t) = -i\frac{\Omega}{\Omega'} \sin\left(\frac{\Omega't}{2}\right) \tilde{c}_g(0) + \left[ \cos\left(\frac{\Omega't}{2}\right) + i\frac{\Delta}{\Omega'} \sin\left(\frac{\Omega't}{2}\right) \right] \tilde{c}_e(0), \quad (3.5b)$$

where  $\Omega' = \sqrt{|\Omega|^2 + \Delta^2}$  is the generalised Rabi frequency.

For an atom initially in state  $|g\rangle$  ( $\tilde{c}_g(0) = 1$ ), the excited state probability becomes

$$|\tilde{c}_e(t)|^2 = \frac{\Omega^2}{|\Omega|^2 + \Delta^2} \sin^2\left(\sqrt{|\Omega|^2 + \Delta^2} \cdot \frac{t}{2}\right). \quad (3.6)$$

This is also known as Rabi oscillations or single qubit rotations because the atomic evolution can be described by rotations on the Bloch sphere [21]. One can drive full population transfer to the excited state for a pulse area  $\Omega'\tau = \pi$ , called a  $\pi$ -pulse, on-resonance ( $\Delta = 0$ ) as shown in Fig. 3.1 (b). This will be used extensively for

controlling coherent evolution between ground states, and ground to Rydberg states in Chap. 7.

However, to calculate the time evolution of a large system like an ensemble of atoms, we use an alternative approach based on the eigenstates of the Hamiltonian. By making an expansion of the wavefunction on the complete set of eigenstates  $|n\rangle$  with eigenenergies  $\hbar\omega_n$ , the time evolution from the TDSE is simply given by [21]

$$|\psi(t)\rangle = \sum_n c_n(0)e^{-i\omega_n t}|n\rangle. \quad (3.7)$$

Inspection of the coupled equations resulting from the TDSE reveals that in the rotated frame the two-level atom can be described by the Hamiltonian [21]

$$\tilde{\mathcal{H}} = \frac{\hbar}{2} \begin{pmatrix} \Delta & \Omega^* \\ \Omega & -\Delta \end{pmatrix}, \quad (3.8)$$

which we can diagonalise to find the eigenvalues and corresponding eigenstates of the system.

### 3.1.2 The density matrix

So far we have considered the system evolution in terms of the state vectors, solving evolution using the TDSE. This treatment is ideal for isolated systems, but for systems coupled to the environment it is not possible to ascribe a unitary operator to account for dissipative effects of spontaneous emission or dephasing. Moreover, due to the dissipation, the system is often in a statistical mixture  $\{|\psi_i\rangle\}$  instead of a pure state  $|\psi\rangle$  and can not be described by a state vector.

Considering a pure state  $|\psi\rangle$ , the density matrix is the  $2 \times 2$  matrix given by

$$\hat{\rho} = |\psi\rangle\langle\psi| = \begin{pmatrix} \rho_{gg} & \rho_{ge} \\ \rho_{eg} & \rho_{ee} \end{pmatrix}. \quad (3.9)$$

where the diagonal elements  $\rho_{gg}$  and  $\rho_{ee}$  are called known as the populations, and represent the probability of finding the system in state  $|g\rangle$  or  $|e\rangle$  respectively, such

that  $\rho_{gg} + \rho_{ee} = 1$  and  $\dot{\rho}_{gg} = -\dot{\rho}_{ee}$ . Off-diagonal terms  $\rho_{ge}$  and  $\rho_{eg}$  are known as the coherences, dependent upon the relative phase between states  $|g\rangle$  and  $|e\rangle$  and have the properties  $\rho_{ge} = \rho_{eg}^\dagger$ .

The density matrix dynamics is governed by the Liouville-Von Neumann or master equation, the direct analog of the Schrödinger equation, given by

$$\dot{\rho} = \frac{i}{\hbar} [\rho, \hat{\mathcal{H}}]. \quad (3.10)$$

Using the density matrix formalism allows spontaneous emission of the excited states arising from the coupling with the bath of vacuum electric field modes to be taken into account. The resulting time evolution is non-unitary and leads to the evolution of an initially pure state into a mixed state. The coupling to the bath is described by the Lindblad superoperator  $\mathcal{L}(\rho)$  [179]

$$\mathcal{L}(\rho) = -\frac{1}{2} \sum_m (C_m^\dagger C_m \rho + \rho C_m^\dagger C_m) + \sum_m C_m \rho C_m^\dagger, \quad (3.11)$$

where the sum is over all decay modes  $m$ . For a given decay channel from  $|i\rangle$  to  $|j\rangle$ , the first summation describes loss of population from state  $|i\rangle$  due to emission of a photon, and the corresponding decay in the coherence terms  $\rho_{ji,ij}$ , whilst the final term describes population being restored into state  $|j\rangle$ , ensuring  $\text{Tr}\{\rho\} = 1$  for all times [180].

For the two-level atom there is a single decay mode for spontaneous emission from  $|e\rangle$  to  $|g\rangle$  at rate  $\Gamma_e$  which is described by the operator  $C_e = \sqrt{\Gamma_e}|g\rangle\langle e|$ . Inserting this into Eq. 3.11, the Lindblad operator for the two-level atom is

$$\mathcal{L}(\rho) = \begin{pmatrix} \Gamma_e \rho_{ee} & -\frac{1}{2} \Gamma_e \rho_{ge} \\ -\frac{1}{2} \Gamma_e \rho_{eg} & -\Gamma_e \rho_{ee} \end{pmatrix}. \quad (3.12)$$

For a real driving field, the source is never purely monochromatic but instead has a Lorentzian linewidth  $\gamma_p$  [21]. The linewidth leads to enhanced dephasing of the off-diagonal coherences associated with the excited state but leaves the populations unchanged. The linewidth induced dephasing can be included by adding an addi-

tional term to the off-diagonal dephasing rate such that  $\gamma_{eg} \rightarrow \gamma_{eg} + \gamma_p$  [181]. This can be included in the master equation by adding a dephasing term at a rate  $\gamma_p$  to the coherences. Whilst this cannot be expressed in the general Lindblad form of Eq. 3.11, the additional dephasing contribution  $\mathcal{L}_d(\rho)$  can be expressed as

$$\mathcal{L}_d(\rho) = \begin{pmatrix} 0 & -\gamma_p \rho_{ge} \\ -\gamma_p \rho_{ge} & 0 \end{pmatrix}. \quad (3.13)$$

The master equation for the time evolution of the density matrix is now modified to the Lindblad master equation

$$\dot{\rho} = \frac{i}{\hbar} [\rho, \mathcal{H}] + \mathcal{L}(\rho) + \mathcal{L}_d(\rho), \quad (3.14)$$

which returns a set of four coupled equations called Optical Bloch Equations (OBE). For the limiting case of  $\Delta = 0$ , an analytic solution can be found and yields to the excited state probability given by [11]

$$\rho_{ee} = \frac{\Omega^2}{2\Omega^2 + \Gamma_e^2} \left[ 1 - e^{-3\Gamma_e t/4} \left( \cos(\tilde{\Omega}t) + \frac{3\Gamma_e}{4\tilde{\Omega}} \sin(\tilde{\Omega}t) \right) \right], \quad (3.15)$$

where  $\tilde{\Omega} = \sqrt{\Omega^2 + \Gamma_e^2/16}$ . This shows that the role of the excited state spontaneous decay is to cause an exponential damping of the Rabi oscillations into a *steady-state*  $\rho_{ss}$  with a  $1/e$  timescale of  $\tau = 2/(3\pi\Gamma_e)$ , as plotted Fig. 3.1 (b).

In general, for the case of both finite  $\Delta$  and  $\Gamma_e$  there is no simple analytic solution for the system dynamics and instead numerical integration is performed to model the system. However, the asymptotic steady-state can be determined from the condition  $\dot{\rho}_{ss} = 0$ . Introducing a transformation of the OBE to the slow variables  $\tilde{\rho}_{ge} = e^{-i\omega t} \rho_{ge}$  and  $\tilde{\rho}_{eg} = e^{i\omega t} \rho_{eg}$  yields to the solutions

$$\rho_{ee}^{ss} = \frac{|\Omega|^2/4}{(|\Omega|^2/2 + \Gamma^2/4 + \Delta^2)}, \quad (3.16a)$$

$$\tilde{\rho}_{eg}^{ss} = \frac{\Omega}{2} \frac{(\Delta - i\Gamma/2)}{(|\Omega|^2/2 + \Gamma^2/4 + \Delta^2)}. \quad (3.16b)$$

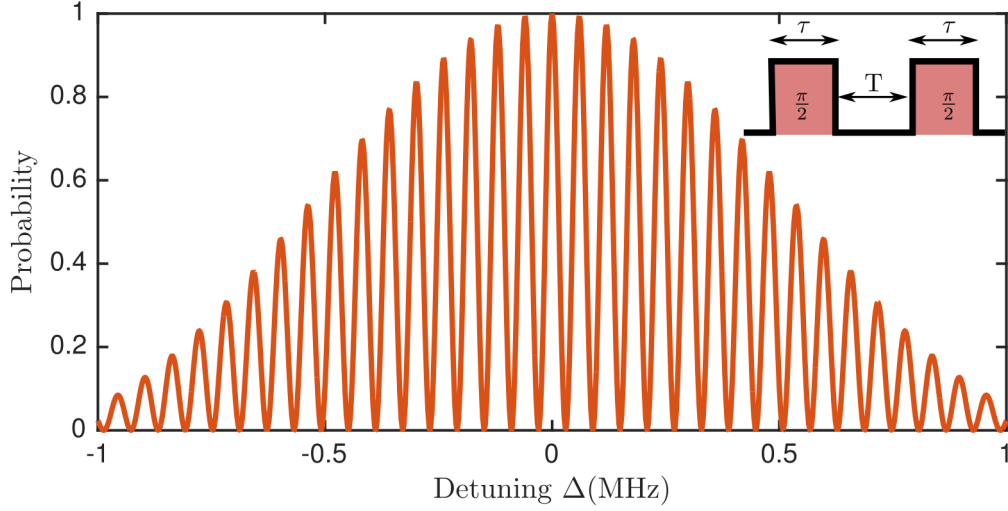


Figure 3.2: Ramsey pulse sequence (top right) and oscillatory pattern of the probability  $P_e(t)$ , obtained by varying the detuning  $\Delta$  for a  $\pi/2$ -pulse duration of  $\tau = 500$  ns, a Rabi frequency of  $\Omega'/2\pi = 1$  MHz and a fixed free evolution time of  $10 \mu\text{s}$ .

### 3.1.3 Ramsey fringes

In order to give an estimation of the coherence time related to quantum information protocols, the experimental benchmark method is the realisation of the so-called Ramsey fringes. After initialisation of the state in  $|g\rangle$ , this protocol requires to first apply a  $\pi/2$ -pulse with duration  $\tau$  to create a superposition state. This is followed by a fixed evolution time  $T$  where the qubit state can precess freely in the Bloch sphere for varying two-photon detuning  $\Delta$ , accumulating a phase  $\phi = \Delta T$ . Finally, a second  $\pi/2$ -pulse with the same interaction time  $\tau$  detects the final state. As shown in Fig. 3.2, the probability of transferring the population in state  $|e\rangle$  exhibits an oscillatory pattern given by [21]

$$P_e(t) = 4 \frac{\Omega^2}{\Omega'^2} \sin^2 \left( \frac{\Omega' \tau}{2} \right) \left[ \cos \left( \frac{\Delta T}{2} \right) \cos \left( \frac{\Omega' T}{2} \right) - \frac{\Delta}{\Omega'} \sin \left( \frac{\Delta T}{2} \right) \sin \left( \frac{\Omega' T}{2} \right) \right]^2, \quad (3.17)$$

which allows for extreme sensitivity to detect the phase  $\phi$  accumulated during the free evolution time. This provides a protocol to test the coherence of the created state during coherent ground state Raman transfer (see Sec. 7.1) as well as coherent Rydberg excitation (see Sec. 7.2).

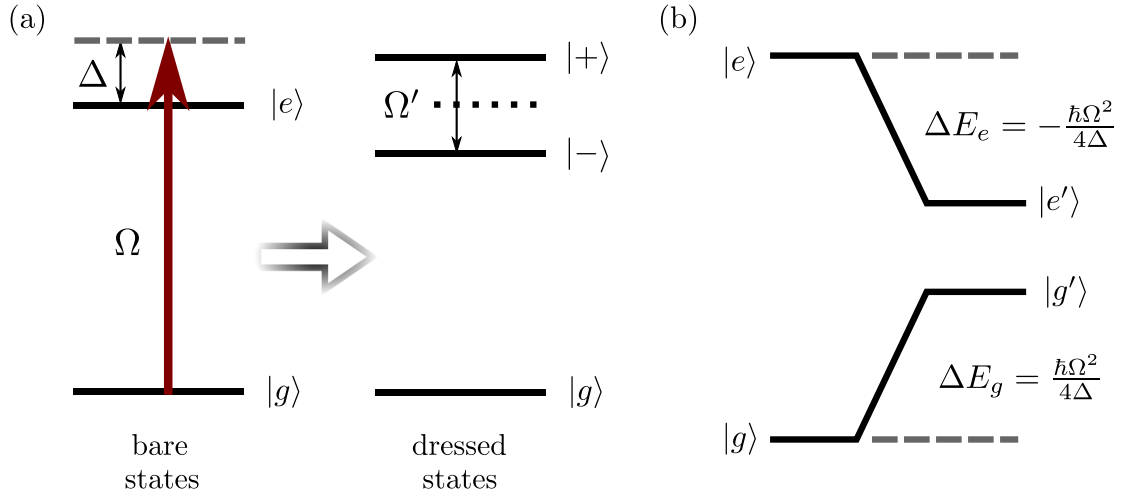


Figure 3.3: (a) Dressed atom picture for a two-level atom where the coupling  $\Omega$  leads to the creation of two new eigenstates  $|\pm\rangle$ , separated by an energy  $\hbar\Omega'$ , such that it results in an avoiding energy anti-crossing on resonance. (b) For large detuning  $\Delta \gg \Omega$ , ground and excited states are shifted due to AC Stark shift or light shift.

### 3.1.4 The dressed atom picture

From the Hamiltonian of the two-level atom described in Eq. 3.8, one can diagonalise the matrix to obtain the corresponding eigenenergies

$$\epsilon_{\pm} = \pm \frac{\hbar}{2} \Omega', \quad (3.18)$$

defining two new eigenstates  $|\pm\rangle$ , called the *dressed states* [178], given by

$$\begin{cases} |+\rangle = \cos\left(\frac{\theta}{2}\right) |e\rangle + \sin\left(\frac{\theta}{2}\right) |g\rangle \\ |-\rangle = \cos\left(\frac{\theta}{2}\right) |g\rangle - \sin\left(\frac{\theta}{2}\right) |e\rangle \end{cases}$$

with the angle  $\theta = \arctan(-\Omega/\Delta)$  describing the admixture between the bare states and the dressed states.

On resonance ( $\Delta = 0$ ) and in the absence of the coupling term  $\Omega$ , the two eigenstates  $|\pm\rangle$  are degenerate. The effect of the coupling  $\Omega$  is to lift the energies, as shown in Fig 3.3 (a), in order to create an anti-crossing on resonance. The higher the coupling Rabi frequency  $\Omega$ , the higher the energy splitting. Moreover, the new eigenstates  $|\pm\rangle$  are an equal mixture of the bare atomic states  $|g\rangle$  and  $|e\rangle$  on resonance, yielding to an energy splitting of the states by  $\pm \hbar\Omega/2$ , called Autler-Townes splitting [182, 183]

### 3.1.5 Optical dipole trap

For large detunings ( $\Delta \gg \Omega$ ), one can make a Taylor expansion of Eq. 3.18 such that

$$\epsilon_{\pm} \approx \pm \frac{\hbar}{2} \left( \Delta + \frac{|\Omega|^2}{2\Delta} \right), \quad (3.19)$$

which results in energy shifts of the ground and excited states of  $\Delta E_g = \hbar\Omega^2/4\Delta$  and  $\Delta E_e = -\hbar\Omega^2/4\Delta$  known as the AC Stark shift, or light shift, as represented in Fig. 3.3 (b).

The AC Stark shift depends on the intensity of the laser as well as on the sign of the detuning, and can be used to trap atoms in optical fields. For  $\Delta < 0$ , red frequency detuning, the atoms will be trapped to regions of high intensity. However, for blue frequency detuning corresponding to  $\Delta > 0$ , the atoms will be expelled from the regions of highest intensity.

In our experiment, we trap atoms using a Nd:YAG laser beam ( $\lambda = 1064$  nm) with high power ( $\sim 10$  W), which corresponds to very large negative detuning from the cesium  $D_2$ -transition, as discussed in Chap. 5.

## 3.2 Three-level atom

Much of atom-light interactions physics can be understood from the two-level atom, however our experiment does need to be modeled by a three-level system. Consider a three-level atom with ground  $|g\rangle$ , excited  $|e\rangle$  and Rydberg  $|r\rangle$  states separated by energy  $\hbar\omega_{eg}$  and  $\hbar\omega_{re}$  respectively, as shown in Fig. 3.4 (a), in a ladder configuration. The atomic levels are driven by two monochromatic laser fields. The first laser field  $\mathcal{E}_1$  at frequency  $\omega_1$  drives the transition from  $|g\rangle$  to  $|e\rangle$  with detuning  $\Delta_1 = \omega_1 - \omega_{eg}$  while the second laser field  $\mathcal{E}_2$  at frequency  $\omega_2$  drives the transition from  $|e\rangle$  to  $|r\rangle$  with detuning  $\Delta_2 = \omega_2 - \omega_{re}$ . Similarly to Sec. 3.1, the magnitude of the electric dipole coupling is described by both Rabi frequencies  $\Omega_1 = -\boldsymbol{\mu}_{eg} \cdot \mathcal{E}_1/\hbar$  and  $\Omega_2 = -\boldsymbol{\mu}_{re} \cdot \mathcal{E}_2/\hbar$ .

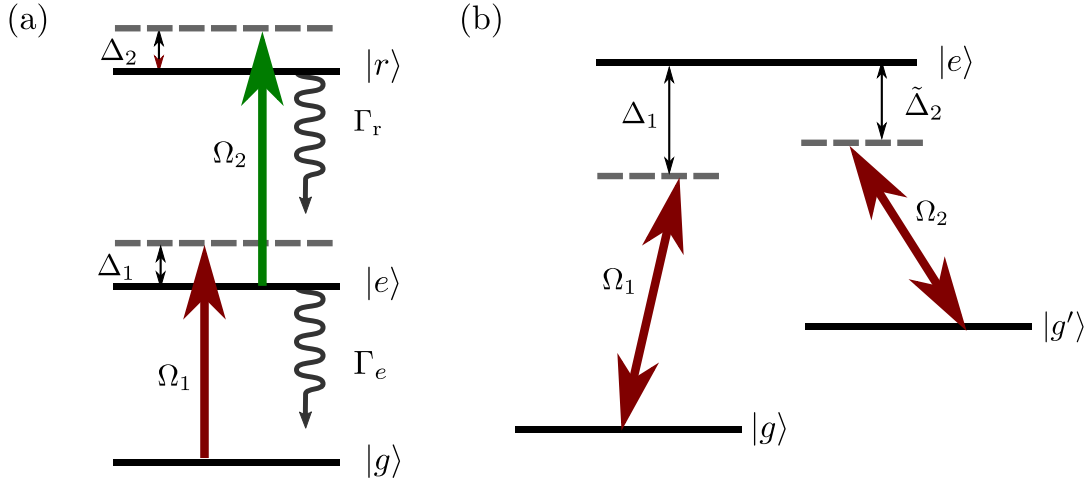


Figure 3.4: (a) Three-level atom in a ladder configuration with a ground state  $|g\rangle$ , a short lived intermediate state  $|e\rangle$  and a Rydberg state  $|r\rangle$  driven by two Rabi frequencies  $\Omega_1$  and  $\Omega_2$  with their corresponding detunings  $\Delta_1$  and  $\Delta_2$  respectively. (b)  $\Lambda$ -system configuration where in this case two ground states  $|g\rangle$  and  $|g'\rangle$  are coupled off-resonantly to the intermediate state  $|e\rangle$ .

The Hamiltonian for the system in the rotating wave approximation is given by  $\mathcal{H} = \mathcal{H}_0 + \mathcal{H}_{al}$  where

$$\mathcal{H}_0 = \hbar\omega_g|g\rangle\langle g| + \hbar\omega_e|e\rangle\langle e| + \hbar\omega_r|r\rangle\langle r|, \quad (3.20)$$

and

$$\mathcal{H}_{al} = \hbar\frac{\Omega_1}{2}(e^{-i\omega_1 t}|e\rangle\langle g| + e^{i\omega_1 t}|g\rangle\langle e|) + \hbar\frac{\Omega_2}{2}(e^{-i\omega_2 t}|r\rangle\langle e| + e^{i\omega_2 t}|e\rangle\langle r|). \quad (3.21)$$

The states  $|g\rangle$ ,  $|e\rangle$  and  $|r\rangle$  can be expressed as orthogonal normalised column vectors  $|g\rangle = (1, 0, 0)^t$ ,  $|e\rangle = (0, 1, 0)^t$  and  $|r\rangle = (0, 0, 1)^t$ .

Moving into the rotating frame results in a Hamiltonian matrix of the form [184]

$$\mathcal{H} = \hbar \begin{pmatrix} 0 & \Omega_1/2 & 0 \\ \Omega_1/2 & -\Delta_1 & \Omega_2/2 \\ 0 & \Omega_2/2 & -(\Delta_1 + \Delta_2) \end{pmatrix}. \quad (3.22)$$

The time evolution of a single atom is given by the density matrix which follows the Lindblad master equation

$$\dot{\rho} = \frac{i}{\hbar} [\rho, \mathcal{H}] + \mathcal{L}(\rho). \quad (3.23)$$

For the three-level atom there are two decay modes for spontaneous emission, one from  $|e\rangle$  at rate  $\Gamma_e$  and another from  $|r\rangle$  at rate  $\Gamma_r$ , which are described by the collapse operators [185]

$$C_e = \sqrt{\Gamma_e}|g\rangle\langle e|, \quad (3.24a)$$

$$C_r = \sqrt{\Gamma_r}|e\rangle\langle r|. \quad (3.24b)$$

### 3.2.1 Electromagnetically induced transparency (EIT)

In this section, we will focus on the regime of *Electromagnetically Induced Transparency (EIT)*. In the literature [149, 184], the first laser field  $\mathcal{E}_1$  is referred as the *probe laser* with Rabi frequency  $\Omega_p$  and detuning  $\Delta_p$  while the second laser field  $\mathcal{E}_2$  is referred as the *coupling laser* with Rabi frequency  $\Omega_c$  and detuning  $\Delta_c$ . The finite-linewidth of the probe and coupling lasers are  $\gamma_p$  and  $\gamma_c$  respectively and  $\gamma_{\text{rel}} = \gamma_p + \gamma_c$  corresponds to the linewidth relative to the two-photon resonance.

In the absence of the coupling laser, we are dealing with the simple case of a two-level system studied in Sec. 3.1, driven by the probe laser field.

The optical response of a medium is determined by its susceptibility [11, 149, 184] which, at the probe laser frequency  $\omega_p$  and for a uniform atomic density of  $\rho_0$  atoms per unit volume, is related to the density matrix by [181]

$$\chi(\omega_p) = -\frac{2\rho_0\mu_{eg}^2}{\varepsilon_0\hbar\Omega_p}\tilde{\rho}_{eg}. \quad (3.25)$$

$\chi$  is the complex susceptibility, and can be resolved into the real and imaginary components,  $\chi = \chi_R + i\chi_I$ . The imaginary part of  $\chi$  will govern the intensity transmission of the beam  $T$  such that

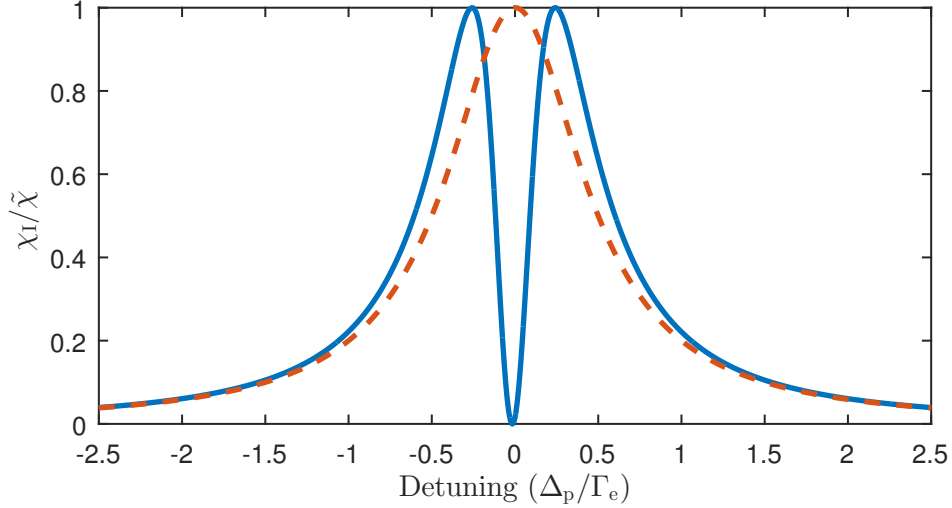


Figure 3.5: Comparison between the imaginary part of the susceptibility  $\chi_I$  of the two-level atom (dashed line) and the three-level atom in the EIT condition (solid line), showing the narrow transparency window on resonance. The curves have been calculated for  $\Omega_p = \Gamma_e/10$  and  $\Omega_c = \Gamma_e/2$  without taking into account effect of finite laser-linewidth ( $\gamma_{gr} = 0$ ), and scaled with respect to  $\tilde{\chi} = 2\rho_0\mu_{eg}^2/\epsilon_0\hbar\Gamma_e$ .

$$T = \frac{I}{I_0} = \exp(-k_p\chi_I\ell), \quad (3.26)$$

where  $I_0$  is the light intensity in the vacuum,  $\ell$  is the length of the medium and  $k_p = 2\pi/\lambda_p$  the wavevector of the probe laser. Injecting the steady states solution found for  $\tilde{\rho}_{eg}^{ss}$  in Eq. 3.16b provides a Lorentzian absorption profile of the probe laser in the absence of any homogeneous line-broadening. The absorption profile is represented by the imaginary part of the susceptibility  $\chi_I$  in Fig. 3.5.

In the case of the three-level system it is not possible to solve the master equation analytically. Instead, for the case  $\Omega_p \ll \Gamma_e, \Omega_c$ , the population can be assumed to remain in the ground-state for all times  $\rho_{gg}^{ss} = 1$ . Using this assumption, the steady-state coherence for the probe transition can be evaluated, yielding to the expression of  $\chi$  in the weak probe limit given by [149, 181]

$$\chi(\Delta_p) = \frac{i\rho_0\mu_{eg}^2/\epsilon_0\hbar}{\gamma_{ge} - i\Delta_p + \frac{\Omega_c^2/4}{\gamma_{gr} - i(\Delta_p + \Delta_c)}}, \quad (3.27)$$

with  $\gamma_{ge} = \Gamma_e/2 + \gamma_p$  and  $\gamma_{gr} = \Gamma_r/2 + \gamma_{rel}$  in analogy with Eq. 3.12 and Eq. 3.13.

The imaginary part of  $\chi(\Delta_p)$  is plotted in Fig. 3.5. In comparison with the two-level atom,  $\chi_I$  is now vanishing in resonance at  $\Delta_p = \Delta_c = 0$ , hence exhibits a full transmission of the probe laser for  $\gamma_{gr} = 0$ . This narrow transparency window arising from the coupling to a third level is called *Electromagnetically Induced Transparency (EIT)*, with a full width at half maximum proportional to  $\Omega_c^2$  [184]. We could equally see that  $\chi_R$  shows a steep slope [184] which allows for reduction of the group velocity of the probe field and the potential to stop a light pulse [186].

### Dressed states picture

The emergence of the probe field transparency in the absorption spectrum can be understood intuitively using the dressed states picture [187]. The diagonalisation of the Hamiltonian of Eq. 3.22 provides the new eigenstates of the three-level atom which, at the two-photon resonance  $\Delta_p + \Delta_c = 0$  and for  $\gamma_{gr} = 0$ , are given by [149, 184]

$$|D\rangle = \cos\theta|g\rangle - \sin\theta|r\rangle, \quad (3.28a)$$

$$|+\rangle = \sin\theta \sin\phi|g\rangle + \cos\phi|e\rangle + \cos\theta \sin\phi|r\rangle, \quad (3.28b)$$

$$|-\rangle = \sin\theta \cos\phi|g\rangle - \sin\phi|e\rangle + \cos\theta \cos\phi|r\rangle, \quad (3.28c)$$

where  $\theta$  and  $\phi$  are the mixing angles defined as

$$\tan\theta = \frac{\Omega_p}{\Omega_c}, \quad \tan 2\phi = \frac{\sqrt{\Omega_p^2 + \Omega_c^2}}{\Delta_p}. \quad (3.29)$$

The corresponding eigenenergies are

$$\mathcal{E}_D = 0 \quad \text{and} \quad \mathcal{E}_{\pm} = \frac{\hbar}{2} (\Delta_p \pm \sqrt{\Delta_p^2 + \Delta_c^2 + \Omega_c^2}). \quad (3.30)$$

In the weak probe limit ( $\Omega_p \ll \Omega_c, \Gamma_e$ ) and on resonance ( $\Delta_p = 0$ ), one obtains

the eigenstates

$$|\pm\rangle = \frac{|r\rangle \pm |e\rangle}{\sqrt{2}}, \quad (3.31a)$$

$$|D\rangle = |g\rangle. \quad (3.31b)$$

The state  $|D\rangle$  with zero-energy is the ground state and does not couple to the probe field, which is why it is referred to as a *dark-state*. Inversely, the two eigenstates  $|\pm\rangle$  are known as *bright-states* where the excitation probability amplitudes with respect to the state  $|e\rangle$  are equal but with opposite signs. This gives rise to destructive interference of the excitation pathways which makes the probe laser transparent to the atomic medium and leading to the system staying in the dark state  $|D\rangle$ .

### 3.2.2 Two-photon Raman transitions

Rather than working on resonance in a three-level ladder configuration for EIT, coherent two-photon excitation to a Rydberg state requires large detuning  $\Delta_1$  from the intermediate state  $|e\rangle$  as shown in Fig. 3.4 (a), to minimise spontaneous emission during the excitation process that would lead to decoherence. We aim to determine for which range of parameters this excitation scheme can be reduced to an effective two-level system.

Rotating into the frame of averaged frequencies, we can transform the Hamiltonian of Eq. 3.22 into an effective Hamiltonian [188] given by

$$\mathcal{H} = \frac{\hbar}{2} \begin{pmatrix} \delta & \Omega_1 & 0 \\ \Omega_1 & -2\Delta & \Omega_2 \\ 0 & \Omega_2 & -\delta \end{pmatrix}, \quad (3.32)$$

where  $\delta = \Delta_1 + \Delta_2$  and  $\Delta = \frac{\Delta_1 - \Delta_2}{2}$ .

Working at large detuning from the intermediate state  $|e\rangle$  is a necessity to minimise spontaneous emission. In the case where the detuning is large relative to the Rabi frequencies ( $|\Delta_{1,2}| \gg \Omega_{1,2}$ ), the state  $|e\rangle$  can be adiabatically eliminated due to fast

variation in the population  $\rho_{ee}$  such that  $\dot{\rho}_{ee} = 0$  [188].

The Hamiltonian can then be re-arranged in an effective two-level Hamiltonian similar to Eq. 3.8 in the basis  $\{|g\rangle, |r\rangle\}$

$$\mathcal{H}^{eff} = \frac{\hbar}{2} \begin{pmatrix} \Delta_{eff} & \Omega_R \\ \Omega_R & -\Delta_{eff} \end{pmatrix}, \quad (3.33)$$

where the effective detuning  $\Delta_{eff} = \delta + \Delta_{AC}^g - \Delta_{AC}^r$  has new terms corresponding to the differential AC Stark shift  $\Delta_{AC}^g = \frac{|\Omega_1|^2}{4\Delta}$  and  $\Delta_{AC}^r = \frac{|\Omega_2|^2}{4\Delta}$  for the states  $|g\rangle$  and  $|r\rangle$  respectively, while the effective two-photon Rabi frequency between  $|g\rangle$  and  $|r\rangle$  is given by

$$\Omega_R = \frac{\Omega_1 \Omega_2}{2\Delta}. \quad (3.34)$$

According to Sec. 3.1.1, the system will undergo Rabi oscillations between ground and Rydberg states at the rate  $\Omega' = \sqrt{\Omega_R^2 + \Delta_{eff}^2}$  with full population transfer for  $\Delta_{eff} = 0$ , corresponding to  $\delta = \Delta_{AC}^r - \Delta_{AC}^g = \frac{|\Omega_2|^2}{4\Delta} - \frac{|\Omega_1|^2}{4\Delta}$ , due to AC Stark shift. One can notice the difference with EIT conditions where  $\delta = 0$  ( $\Delta_1 = -\Delta_2$ ).

### 3.2.3 Important features of three-level $\Lambda$ system

As shown in Fig 3.4 (b), we will perform coherent transfer between two hyperfine ground states  $|g\rangle$  and  $|g'\rangle$  coupled to the intermediate state  $|e\rangle$ , with the Rabi frequencies  $\Omega_1$  and  $\Omega_2$  respectively, in a  $\Lambda$  configuration. Such excitation scheme can be described by the Hamiltonian in Eq. 3.32 by defining a new detuning  $\tilde{\Delta}_2 = \omega_2 - (\omega_e - \omega_{g'})$  such that  $\delta = \Delta_1 - \tilde{\Delta}_2$  and  $\Delta = (\Delta_1 + \tilde{\Delta}_2)/2$ .

Therefore, the  $\Lambda$ -configuration can be described by a two-level system between the states  $|g\rangle$  and  $|g'\rangle$  with the effective Hamiltonian given by Eq. 3.33. The notable difference with the ladder configuration arises from the fact that both states are close together, inducing another contribution to the AC Stark shift such that the new effective detuning  $\Delta_{eff} = \Delta_1 - \tilde{\Delta}_2 + \Delta_{AC}^{g,TOT} - \Delta_{AC}^{g',TOT}$  with,

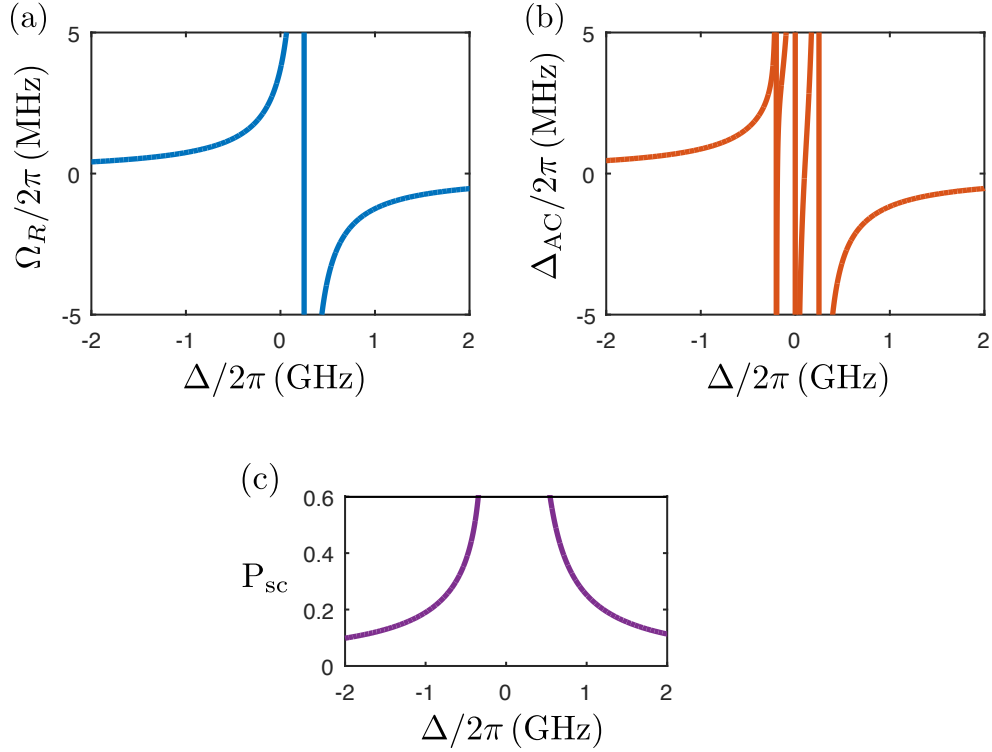


Figure 3.6: Theoretical predictions of (a) Rabi frequencies  $\Omega_R$ , (b) differential AC Stark shifts between ground and Rydberg state  $\Delta_{AC}$  as well as (c) scattering probabilities  $P_{sc}$  for the transition  $|4, 4\rangle \rightarrow 81D_{5/2}$  as a function of the detuning  $\Delta$  from the intermediate state  $|e\rangle$ .

$$\Delta_{AC}^{g,TOT} = \frac{|\Omega_1|^2}{4\Delta} + \frac{|\Omega_2|^2}{4(\Delta - \omega_{HFS})}, \quad (3.35)$$

$$\Delta_{AC}^{g',TOT} = \frac{|\Omega_1|^2}{4(\Delta + \omega_{HFS})} + \frac{|\Omega_2|^2}{4\Delta}. \quad (3.36)$$

and where  $\omega_{HFS}$  corresponds to the hyperfine splitting between the ground states.

### 3.2.4 Optimised parameters estimation

The ability to perform accurate Rydberg excitation and ground-state rotations using two-photon excitation schemes is critical in developing quantum gates. We have seen that both excitations can be reduced to a two-level system with Rabi frequencies  $\Omega_R = \frac{\Omega_1\Omega_2}{2\Delta}$ , where  $\Omega_{1,2}$  represents dipole allowed Rabi frequencies. It is important to recall that this expression for the Rabi frequency is accurate for  $|\Delta| \gg \Delta_{hf}$  [68], where  $\Delta_{hf}$  is the width of the hyperfine structure of the intermediate level

$|e\rangle = |6P_{3/2}\rangle$  in our experiment. Appendix A gives an overview of the way to calculate the single photon Rabi frequency for a dipole allowed transition using the Wigner-Eckart theorem. This allows us to predict the best set of parameters to obtain fast Rabi oscillations and preserve quantum states from decoherence.

Two-photon excitation suffers from two drawbacks that need to be reduced. The dominant source of error in such an excitation is due to spontaneous emission from the intermediate level  $|e\rangle$ . This can be evaluated from calculation of the probability to scatter a photon during a  $\pi$ -pulse which for Rydberg and ground state two-photon excitation, are given by [68]

$$P_{\text{sc,Ryd}} = \frac{\gamma_e t_\pi}{2} \left( \frac{|\Omega_2|^2}{2\Delta^2} + \frac{|\Omega_1|^2}{2\Delta^2} \right) \quad (3.37)$$

and

$$P_{\text{sc,Ground}} = \frac{\gamma_e t_\pi}{2} \left( \frac{|\Omega_1|^2}{2\Delta^2} + \frac{|\Omega_2|^2}{2(\Delta - \omega_{\text{HFS}})^2} + \frac{|\Omega_1|^2}{2(\Delta + \omega_{\text{HFS}})^2} + \frac{|\Omega_2|^2}{2\Delta^2} \right), \quad (3.38)$$

where  $t_\pi = \pi/\Omega_R$  and  $\gamma_e = 1/\tau_e$  is the radiative decay rate from the intermediate state  $|e\rangle$ . The factor  $\frac{1}{2}$  accounts for half of the population being in state  $|g\rangle$  and the other half being in state  $|r\rangle$  during the  $\pi$ -pulse [68] corresponding to the Rydberg excitation or the states  $|g\rangle$  and  $|g'\rangle$  for the case of a ground state rotation. The second source of error is the differential AC Stark shift  $\Delta_{\text{AC}}$  arising from the effective two-photon detuning  $\Delta_{\text{eff}}$ . Due to possible variation in Rabi frequency coming from intensity noise or shift of the detuning, it needs to be minimised to obtain high-fidelity Rabi oscillations and maximise population transfer.

However, to make accurate theoretical predictions of two-photon Rabi frequencies, Stark shifts and scattering probabilities, one needs to take into account the hyperfine structure of the intermediate state  $|e\rangle$ . This is obtained by modifying Eq. 3.34 and summing over all dipole allowed excitation pathways via the intermediate state  $f_e$ , such that the two photon Rabi frequency is given by

Parameter	Value
$\Delta/2\pi$	+ 1.03 GHz
$\Omega_R/2\pi$	+ 1.05 MHz
$\Delta_{AC}/2\pi$	+1.13 MHz
$P_{sc}$	0.24

Table 3.1: Optimised parameters for the two-photon excitation  $|4, 4\rangle \rightarrow 81D_{5/2}$  with a detuning of  $\Delta/2\pi = +1.03$  GHz from the centre of mass of the intermediate state  $6P_{3/2}$ .

$$\Omega_R = \sum_{f_e} \frac{\Omega_{f, m_f \rightarrow f_e, m_{f_e}} \Omega_{f_e, m_{f_e} \rightarrow j, m_j}}{2(\Delta + \Delta_{f_e})} \quad (3.39)$$

where  $\Delta_{f_e}$  is the relevant hyperfine level detuning from the centre of mass of the intermediate state.

Calculations for the two-photon excitation from the ground state  $|4, 4\rangle$  to the Rydberg state  $81D_{5/2}$  are represented in Fig. 3.6 with a detuning  $\Delta/2\pi = +1.03$  GHz from the center of mass of the intermediate state  $|e\rangle$ . The first and the second photon are both  $\sigma^+$ -polarised. The set of parameters are taken from Sec. 7.2.6. They consist of a first photon of 852 nm with a laser beam power of 453 nW and a beam waist of 14  $\mu\text{m}$  coupled to a second photon from a laser beam at 509 nm with a power of 74 mW focused down to a beam waist of 18  $\mu\text{m}$ .

From Fig. 3.6, one observes that keeping the detuning  $|\Delta|/2\pi > 1$  GHz allows to minimise both the scattering probability and the differential AC Stark shift whilst achieving a Rabi frequency  $|\Omega_R|/2\pi > 1$  MHz. We summarise in Tab. 3.1 the range of optimal parameters that we plan to obtain for coherent excitation implemented in Sec. 7.2.6.

### 3.3 Summary

Studying the evolution of the simple two-level system allows to derive the principal insight of atom-light interactions. Adding a third level unlocks rich physics phenomena such as quantum interferences leading to a narrow transparency window in the absorption feature of the excited states  $|e\rangle$ , where this process is referred to as EIT. Observing this phenomena requires the two-photon resonance  $\Delta_p = \Delta_c = 0$  to be exactly met, which will be useful to calibrate our narrow excitation lasers in Chap. 6. Moreover, it is possible to drive two-photon excitation for Rydberg excitation or ground state rotations detuned from the excited state  $|e\rangle$ . Compared to the single photon excitation case, one can perform excitation towards  $S$  and  $D$  states which are dipole forbidden for direct excitation from the ground state. Secondly, it is possible to engineer large two-photon Rabi frequency  $\Omega_R$  on the order of the  $\sim$  MHz rate, while minimising decoherence mechanisms such as spontaneous emission and differential AC Stark shift.

## Part II

# Experimental Realisations

# Chapter 4

## Rydberg excitation lasers stabilisation

In our experiment, we perform two-photon excitation to Rydberg states to overcome the challenges of the weak dipole matrix elements of the UV wavelength for single-photon transition [107]. Two-photon excitation to Rydberg states requires large detuning from the intermediate state to minimise spontaneous emission during the excitation process, as detailed in Sec. 3.2.4. This means it is not possible to use an atomic reference cell for frequency stabilisation. In addition, high-fidelity excitation requires the laser linewidth to be narrowed to minimise laser induced dephasing [67, 124].

Typically, stabilisation to an atomic reference results in laser linewidths of order 10-100 kHz [21]. However, to achieve a laser linewidth that is narrow compared to the Rydberg state lifetime (generally 10-100 kHz) we require a frequency reference capable of sub-kHz linewidth and offering excellent long-term stability. A solution to this problem is to utilise a high-finesse reference cavity [189], exploiting the technological developments driven by the atomic clock community using optimal material and geometry choices [190]. This enables laser stabilisation with sub-Hz linewidths and absolute drifts below mHz/hour for state-of-the-art optical clock experiments [191–197].

In this chapter we describe the stabilisation of our Rydberg excitation lasers to a high-finesse reference cavity and the characterisation of both the reference cavity and the lasers themselves. The work reported in this chapter and chapter 6 has been published in [198].

## 4.1 Qubit and Rydberg lasers

Our goal is to perform two-photon Rydberg excitation via the caesium D<sub>2</sub>-line using lasers at 852 nm with a detuning  $\Delta_p$  from the excited state  $|e\rangle = 6P_{3/2}$  and 509 nm with a detuning  $\Delta_c$  from a Rydberg state  $|r\rangle$ , as illustrated in Fig. 3.4 (a). The first step of the excitation from  $6s\ ^2S_{1/2} \rightarrow 6p\ ^2P_{3/2}$  is performed using an extended cavity diode laser (ECDL) at 852 nm. For the second step, light at 509 nm is required which is generated from a pair of homebuilt second harmonic generation (SHG) systems, Rydberg A & B, which double light from a pair of master lasers operating at 1018 nm.

Commercial laser diodes are available at the convenient wavelengths of 852 nm and 1018 nm, with powers of  $\sim 40$  mW and a tuning range of a few nanometers by adjusting the temperature of the diode. The high-reflectivity (HR) of the laser diode rear facet combined with the low-reflectivity of the front facet act as a cavity and provides optical feedback for lasing at a given frequency. However, the laser linewidth is rather large  $\sim 10$ -100 MHz in free running mode compared to typical atomic transition linewidth of  $\sim 1$  MHz, besides being unstable. Increasing the length of the cavity allows to reduce the laser linewidth as well as increasing the stability. This is achieved using an external cavity (ECDL) made of the laser diode rear facet and a diffraction grating at the other end.

Our ECDL design uses laser diodes mounted in a solid aluminium body with frequency control achieved using holographic gratings operated in a Littrow configuration [199], as shown in Fig. 4.1 (a). The first diffraction order of the grating is reflected back to the diode while the output laser beam is made of the 0<sup>th</sup> order. The grating mount is doubly hinged to provide decoupling of horizontal and vertical adjustment. Coarse frequency tuning of the grating angle is performed using a precision 170 TPI screw, with fine tuning achieved using a piezoelectric actuator

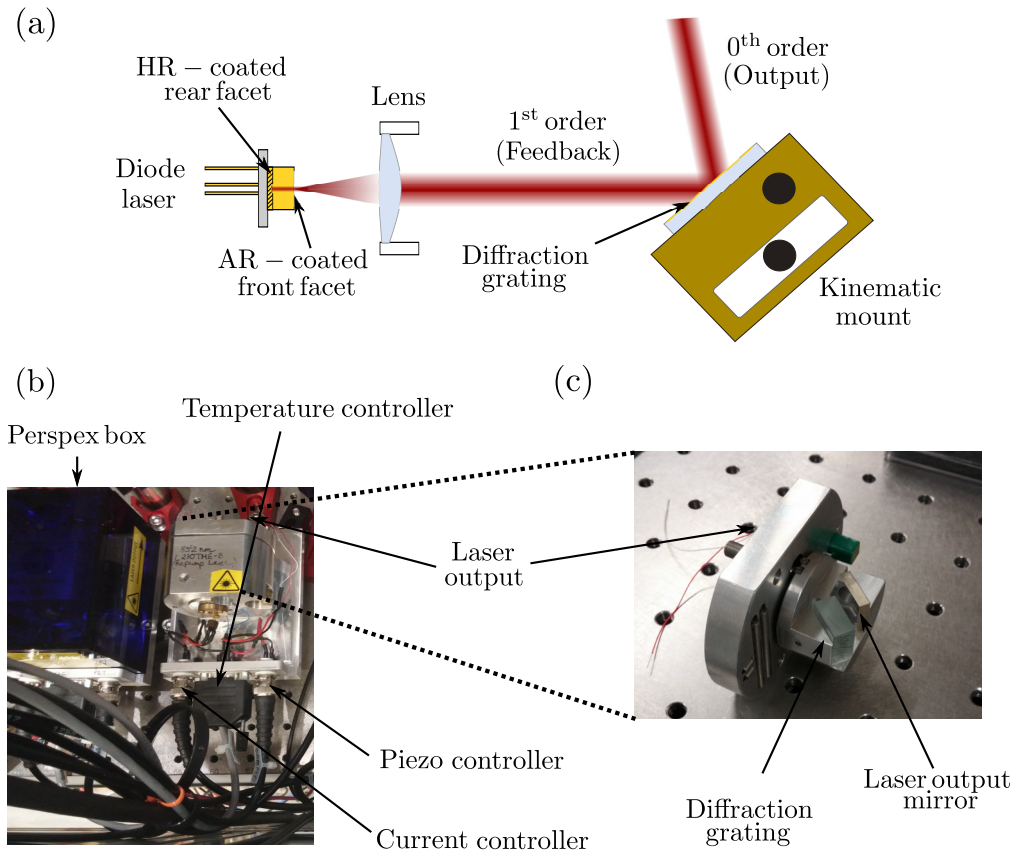


Figure 4.1: (a) A laser diode in a Littrow configuration. The first order reflection from a grating is fed back into the laser diode creating an external cavity. The output beam is the direct reflection ( $0^{\text{th}}$  order) from the grating. (b) Photograph of the different components of the ECDL. (c) Zoom on the central part of the ECDL with the diffraction grating as well as an output mirror. The mirror is always parallel to the grating in order to keep the beam angle constant as the grating is turned.

(Thorlabs AE0505D08F). All the lasers are temperature stabilised to  $< 0.1^{\circ}\text{C}$  using a commercial Arroyo 5240 PID controller driving a Peltier cooler and placed in a perspex box with an anti-reflection (AR) coated window to provide thermal and mechanical insulation, see Fig. 4.1 (b).

#### 4.1.1 Qubit A laser

The first step laser, Qubit A, uses a standard Fabry-Perot laser diode (Thorlabs L852P150) with 30 % optical feedback from a grating with 1800 lines/mm (Thorlabs GH13-18V), as shown in Fig. 4.1 (c), giving a mode-hop free tuning range of 5 GHz. We manage to obtain roughly 40 mW of output power for a current of 70 mA. After an isolator to avoid back reflections into the diode and due to the elliptical

shape of the output beam, we use a set of anamorphic prisms with a ratio 3:1 to render it circular. Finally, light passes through a double-pass 80 MHz acousto-optic modulator (AOM) for control of frequency and intensity before being delivered to the experiment via a polarisation-maintaining (PM) single mode optical fibre, see Fig. 4.14.

### 4.1.2 Rydberg A and B lasers

As shown in Fig. 4.2 and Fig. 4.3, the master lasers for Rydberg A & B, are generated from AR coated infrared laser diodes at 1018 nm (Toptica LD-1020-0400-2 and Sacher SAL-1030-060 respectively) combined with a 1200 lines/mm visible grating (Thorlabs GH13-12V) tunable from 1010-1025 nm with no realignment of the vertical feedback. After the isolator, the output beams are passing through a set of anamorphic prisms with a ratio 2:1 to render them circular. High power is achieved using a commercial Tapered-Amplifier (TA) (M2K TA-1010-2000-DHP) for each laser, contained in a homebuilt copper mount. We obtain 1.36 W output TA power for 22 mW seed power at a TA input current of 4 A.

However, the tapered region generates a large beam divergence in the vertical direction compared to the horizontal one. To compensate for astigmatism, the beam is passing through a series of spherical and cylindrical lenses in order to obtain a round-shaped collimated beam.

### Second Harmonic Generation (SHG) cavity

To generate light at 509 nm, the Rydberg lasers are doubled via cavity-enhanced second harmonic generation (SHG) [200] using an AR coated quasi-phase matched periodically poled KTP crystal from Raicol Crystal Ltd. with dimensions of 1x2x20 mm and a poling period of  $\Lambda = 7.725 \mu\text{m}$ . An additional singlet with focal length  $f = 400 \text{ mm}$  is placed before the SHG cavity to ensure mode matching with the incoming beam, resulting in an input beam waist radius of  $100 \mu\text{m}$ . The non-linear crystal is placed into a brass heating block at the centre of a symmetrical bow-tie cavity, with temperature control provided using a Peltier device allowing tempera-

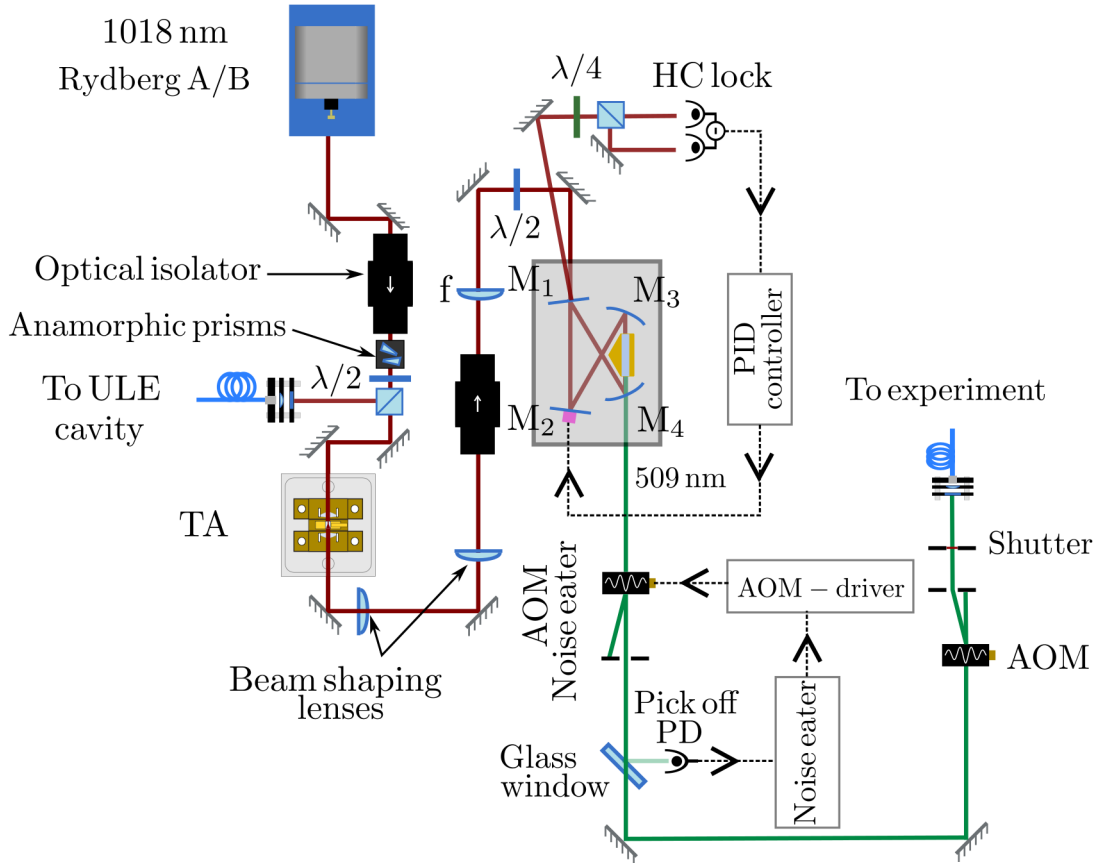


Figure 4.2: Rydberg SHG system. The laser light at 1018 nm is passing through a TA for increasing the power before to create the 509nm beam using the SHG bow-tie cavity. The 509 nm beam power is then stabilised using an AOM-based noise-eater. This followed by an AOM for frequency and intensity control at the experiment and a shutter for extinguishing the light if necessary, before being coupled to a PM-fibre. The cavity is stabilised using the Hänsch-Couillaud (HC) lock detector made of a  $\lambda/4$  waveplate, a PBS and a differential photodiode.

ture tuning from 15-95°C. This corresponds to peak doubling efficiencies from 1020-1015 nm to enable excitation of Rydberg states with principal quantum number from  $n \geq 45$  to ionization.

Figure 4.2 shows a schematic of the bow-tie cavity which consists of two plane mirrors ( $M_1$  and  $M_2$ ) and two concave focusing mirrors ( $M_3$  and  $M_4$ ) with - 30 mm radius of curvature. All the mirrors are dual coated for the pump beam at 1018 nm and the second harmonic beam at 509 nm, with their reflectivities given in Tab. 4.1.

The expression of the second harmonic power  $P_{2\omega}$  [201] built up in the SHG cavity is proportional to the length of the crystal  $L$  as well as the square of the incident power  $P_{\omega}^2$ . Although it could be attractive to reduce the waist size of the fundamental

Mirror	Configuration	ROC (mm)	Reflectivity R at 1018 nm (%)	Reflectivity R at 509 nm (%)
M <sub>1</sub>	plane	inf	89.0	-
M <sub>2</sub>	plane	inf	> 99.8	< 5
M <sub>3</sub>	concave	- 30	> 99.8	< 5
M <sub>4</sub>	concave	- 30	> 99.8	< 5

Table 4.1: Table referencing the different mirrors of the SHG cavity with ROC standing for radius of curvature. The mirrors have been purchased at Layertec with the references in parenthesis : input coupler mirror M<sub>1</sub> (110 252), the plane pump mirror M<sub>2</sub> (101 041) and 2 pump concave mirrors M<sub>3</sub> and M<sub>4</sub> (102 289).

beam in the crystal to increase its intensity, this would be detrimentally reflected on the length of the interaction between the pump beam and the crystal. Thus, an optimisation between pump beam focusing and interaction length has been achieved based on the article of Boyd and Kleinman [201], leading to an optimal waist radius of 25  $\mu\text{m}$  in the middle of the crystal. Finally, the cavity has a 1.25 GHz free spectral range (FSR) and a finesse of  $\mathcal{F} \sim 50$  (See Sec. 4.2), to which we achieve an optimised 95 % modematching for an input beam power of 1 W.

The cavity length is stabilised to give peak SHG output power using the Hänsch-Couillaud technique [202], which is quite inexpensive and frequency modulation free. This locking scheme is based on the polarisation analysis of the reflected beam from the cavity, which contains a birefringent element, e.g. the nonlinear crystal. As illustrated in Fig. 4.2, it only requires a polarisation analysing assembly made of a quarter-waveplate ( $\lambda/4$ ), a polarisation beam splitter (PBS) and a differential photodiode. The polarisation of the incoming pump beam is controlled using a half-waveplate ( $\lambda/2$ ) in order to get  $\sim 5^\circ$  with the horizontal plane. The incident light can be decomposed in terms of two orthogonal, linearly polarised components, that are parallel or perpendicular to the horizontal plane. According to the paper of Hänsch and Couillaud [202], the horizontal component of the reflected field component acquires a phase shift depending on its detuning from the cavity resonance (see Sec. 4.2). However, the vertical component is directly reflected and used as a phase reference. At resonance, the reflected field components are in phase. Out of resonance, the phase shift accumulated by the horizontal component leads to an elliptically polarised of the overall reflected field, whose ellipticity depends on the

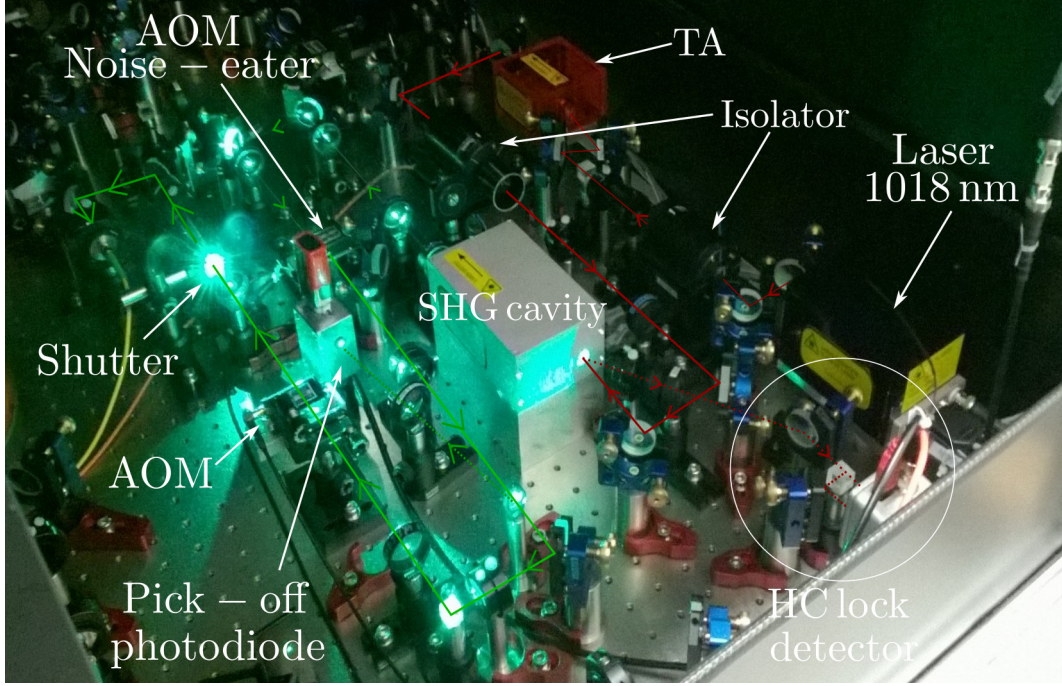


Figure 4.3: Photograph of the Rydberg SHG system showing the Rydberg laser at 1018 nm, followed by the TA and the SHG cavity. The light is also passing through the a first AOM for noise eating before going through a second AOM to control its frequency and amplitude at the experiment.

sign of the detuning. The  $\lambda/4$  plate converts the reflected beam in linearly polarised components with equal intensity at resonance or different amplitudes otherwise, that are separated using a PBS. A differential photodiode generates an error signal which exhibits a dispersion shape with zero crossing when the cavity is at resonance. The error signal is fed into a PID controller which controls the voltage applied to a piezo-electric transducer (PZT) mounted on the plane mirror  $M_2$ , controlling the length of the SHG cavity to maintain it at resonance.

Following optimisation of the alignment and crystal temperature, we typically obtain 370 mW at 509 nm for 650 mW infrared power, achieving  $\sim 57\%$  conversion efficiency at a TA current of 3.0 A. At higher infrared input powers ( $> 1\text{W}$ ), we observe power clamping arising from a competing  $\chi^{(2)}$  - non linearity whereby the intracavity second harmonic beam acts as a pump for non-degenerate optical parametric oscillation [203]. This can be overcome using a lower input coupler reflectivity [204] or by adjusting the cavity geometry to increase the waist in the crystal [205].

### Noise eater

An important requirement for quantum gates is to ensure constant pulse area. Intensity noise leads to change in the two-photon Rabi frequency  $\Omega_R$ , which will turn up into rotation errors and affects the detuning due to variable AC-Stark shift. Thus, we have implemented an AOM based noise eater to minimise slow noise which is related to long term drift of the intensity.

As illustrated in Fig. 4.2, a fraction of the SHG output beam ( $\sim 1$  mW) at 509 nm is picked off using a glass window and collected with a photodiode (Thorlabs PD36A-EC, gain 10 dB). The output signal from the photodiode is compared to a set voltage using an analog noise eater electronics box, whose output voltage is connected to an AOM-driver. The input of the AOM-driver is mixed with a voltage control oscillator (VCO) and amplified before being delivered to an 80 MHz AOM. This allows to regulate the diffraction efficiency into the 1<sup>st</sup>-order in order to maintain the intensity of the 0<sup>th</sup>-order stabilised. We are able to eliminate intensity noise with less than 1 % amplitude variation over one hour.

Finally, the beam passes through an 80 MHz AOM to provide frequency and intensity control in the experiment before being coupled into a single mode PM fibre, which leads to  $\sim 160$  mW available at the cold atoms. AOM frequencies for all lasers are derived from a common direct digital synthesis (DDS) evaluation board (AD9959) device to provide controllable relative phase between the lasers.

## 4.2 Fabry-Perot cavity theory

We consider a lossless cavity in a plano-concave configuration consisting of one plane mirror and one concave mirror as shown in Fig. 4.4 (a). We assume that light travelling in the cavity is made of plane waves, such that the incident light can be described as a monochromatic plane wave of frequency  $\nu$  :  $\mathcal{E}_{\text{in}} = \mathcal{E}_0 e^{2i\pi\nu t}$ . The two mirrors, separated by a distance  $L$ , are characterised by two amplitude coefficients of reflection  $r$  and transmission  $t$ . Without any cavity loss, one obtains the relation  $r^2 + t^2 = 1$  or  $R + T = 1$ , when using the intensity coefficients of reflection  $R = r^2$  and transmission  $T = t^2$ .

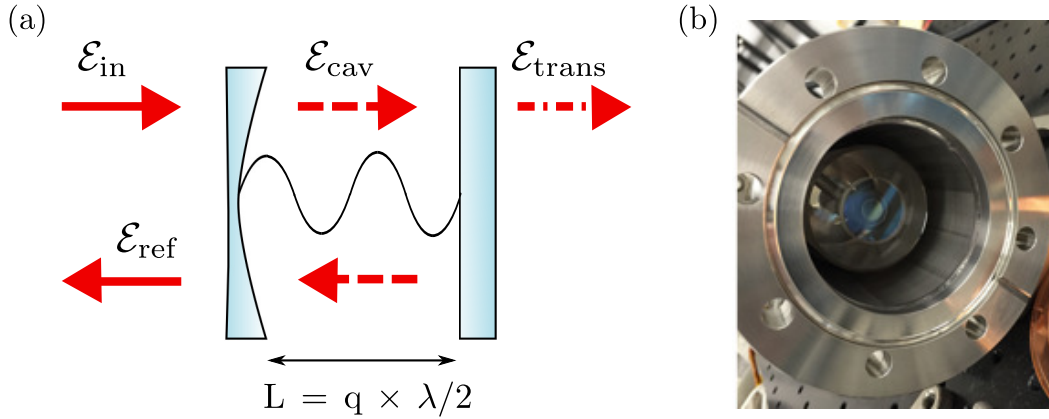


Figure 4.4: (a) Fabry-Perot cavity principle. Constructive interferences lead to a relation between the length of the cavity  $L$  and the wavelength  $\lambda$  such that  $L = q \times \lambda/2$ , where  $q$  is an integer number. (b) Photograph of the high-finesse ULE cavity within the stainless steel vacuum can before sealing.

The total intra-cavity field amplitude  $\mathcal{E}_{\text{cav}}$  is the sum of the transmitted beam and all the beams reflecting back and forth between the mirrors, given by [1]

$$\begin{aligned}
 \mathcal{E}_{\text{cav}} &= t \mathcal{E}_{\text{in}} (1 + r^2 e^{i\Phi} + r^4 e^{2i\Phi} + \dots), \\
 &= t \mathcal{E}_{\text{in}} \sum_{n=1}^{\infty} (r^2 e^{i\Phi})^n, \\
 &= t \mathcal{E}_{\text{in}} \frac{1}{1 - r^2 e^{i\Phi}},
 \end{aligned} \tag{4.1}$$

where  $\Phi = 2kL$  represents the phase shift accumulated due to propagation of the light for each round-trip and  $k = \omega/c = 2\pi\nu/c$  is the wavevector.

The cavity acts as a passive filter where the condition for constructive interference is reached when the optical path length given by  $n \times 2L$  ( $n$  being the refractive index between the two mirrors) is an integer multiple of the wavelength  $\lambda$ . This leads to a cavity transmission coefficient

$$T \equiv \frac{I_t}{I_{\text{in}}} = \frac{1}{1 + F \sin^2(\Phi/2)}, \tag{4.2}$$

where  $F = 4R/(1 - R)^2$  is the coefficient of finesse [1].

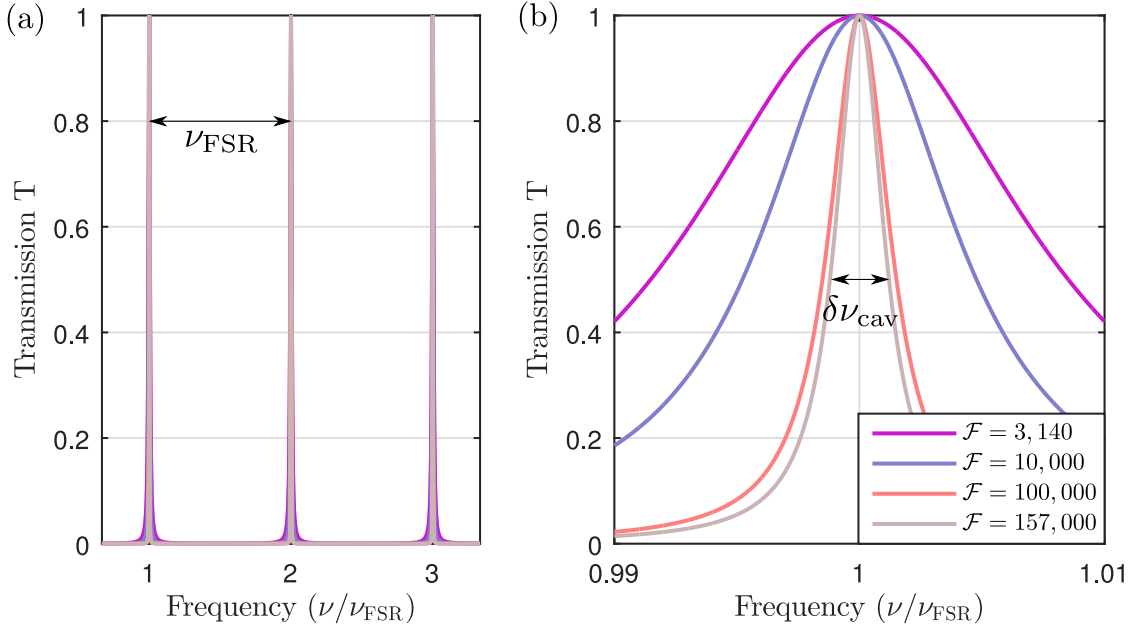


Figure 4.5: (a) Cavity transmission as a function of the incident laser frequency showing equidistant peaks separated by the free spectral range  $\nu_{\text{FSR}}$ . (b) Zoom of the cavity transmission peaks around a resonance for increasing value of the finesse  $\mathcal{F}$ . The higher the finesse, the narrower the cavity linewidth  $\delta\nu_{\text{cav}}$ .

Two important features of the cavity emerge :

1) The transmission coefficient corresponds to a periodic succession of peaks as shown in Fig. 4.5 (a), separated by a frequency interval called the free spectral range

$$\nu_{\text{FSR}} = \frac{c}{2L}, \quad (4.3)$$

where  $c$  is the speed of light. The free spectral range  $\nu_{\text{FSR}}$  is simply determined by the round-trip cavity length, meaning that when the ultra-stable cavity is used as a frequency reference, the distance between the two mirrors  $L$  has to be fixed with high accuracy. In order to give an estimation of the acceptable jitter we can tolerate on the distance  $L$ , one can differentiate Eq. 4.3 resulting in

$$\frac{\delta\nu}{\nu} = -\frac{\delta L}{L}. \quad (4.4)$$

For a cavity length  $L = 10$  cm and a frequency stability of  $\sim 1$  kHz, one needs to stabilise the cavity length to  $\delta L \sim 1$  pm, which is 2 orders of magnitude lower than

the diameter of a typical atom.

2) One can introduce a second figure of merit called the cavity finesse  $\mathcal{F}$ , defined as

$$\mathcal{F} = \frac{\pi\sqrt{F}}{2} \approx \frac{\pi\sqrt{R}}{1-R}, \quad (4.5)$$

for a large finesse ( $\mathcal{F} \gg 1$ ). This allows us to determine the full-width at half-maximum (FWHM) of the transmission peaks, namely the cavity linewidth  $\delta\nu_{\text{cav}}$  such that

$$\delta\nu_{\text{cav}} = \frac{\nu_{\text{FSR}}}{\mathcal{F}}. \quad (4.6)$$

As shown in Fig. 4.5 (b), narrower cavity linewidth  $\delta\nu_{\text{cav}}$  requires an increase of the finesse  $\mathcal{F}$ , hence of the cavity reflection coefficient  $R$ . Assuming that our locking scheme (see Sec. 4.4) can easily stabilise the lasers to 1–5% of the cavity linewidth  $\delta\nu_{\text{cav}}$ , allows us to give an estimate finesse needed for the experiment. The higher Rydberg lifetime used in this thesis will be on the order of  $\sim 200 \mu\text{s}$ , which gives us an upper bound laser linewidth  $\delta\nu_{\text{laser}}$  of 5 kHz. Given that the cavity is 10 cm long and the free spectral range  $\nu_{\text{FSR}} = 1.5 \text{ GHz}$ , our minimum cavity finesse requirement would be  $\mathcal{F} = 15,000$ . This is much bigger than typical cavity finesse of  $\mathcal{F} \approx 10-1000$  that we use for frequency doubling.

Looking at these two main requirements, it is essential to protect the cavity from environmental perturbations in order to reduce the laser linewidth. The first requirement on cavity length stability is related to temperature stabilisation. Our high-finesse cavity is made of Ultra-Low-Expansion (ULE) glass. We will see in Sec. 4.5.1 that we can minimise the effect of cavity length fluctuations by determining the critical temperature that leads to the vanishing of the first order coefficient of thermal expansion (CTE).

In addition to variations in temperature, atmospheric changes in pressure, humidity or acoustic noise can cause fluctuations in the refractive index of air, resulting in additional frequency shifts. Considering that air has a refractive index  $n - 1 \sim 3 \times 10^{-4}$  [206], we can relate the round-trip phase to the refractive index so that

$$\Phi = 2kL \frac{P}{P_{\text{atm}}} (n - 1), \quad (4.7)$$

where  $P$  is the pressure inside the cavity and  $P_{\text{atm}}$  is the atmospheric pressure.

Using the fact that a  $2\pi$  phase shift corresponds to one free spectral range  $\nu_{\text{FSR}}$ , we can determine the frequency shift attributed to a pressure variation  $\delta P$  by

$$\delta\nu = \frac{\delta P}{P_{\text{atm}}} (n - 1) \nu, \quad (4.8)$$

resulting in a shift of  $\sim 100$  Hz for a pressure change of  $10^{-7}$  mbar.

For this reason, the optical reference cavity is housed in a temperature stabilised evacuated vacuum chamber, as shown in Fig. 4.4 (b) and Fig. 4.6, to minimise fluctuations in cavity frequency due to changes in the refractive index.

### 4.3 Horizontal reference cavity experiment

In order to realise lasers with narrow linewidth and long-term stability, an ultra-stable cavity is required for generating a stable, long-term reference for Qubit A and both Rydberg A & B laser systems. When it comes to choosing the cavity parameters, one could use a long cavity length to increase the relative frequency stability. This has been adopted by Jiang *et al.* [207] with a 29 cm cavity length and later Häfner *et al.* [208] with a short term fractional laser frequency stability of  $8 \times 10^{-17}$  using a ULE cavity of 48 cm, at the cost of higher vibration sensitivity, but we do not require that level of accuracy.

Our 5 cm diameter and 10 cm long cylindrical reference cavity is provided by Advanced Thin Films in a plano-concave configuration with a radius of curvature  $R_2 = -50$  cm, as depicted in Fig. 4.6. We have chosen a plano-concave configuration in order to distinguish between transversal modes, contrary to the mode degeneracy that could be encountered in a confocal resonator [1]. Moreover, this configuration is less sensitive to beam misalignment or tilt with respect to the cavity axis. The assembly includes a pair of optically contacted 1 inch diameter mirrors and a spacer made of Ultra-Low-Expansion (ULE) glass. The cylindrical spacer is

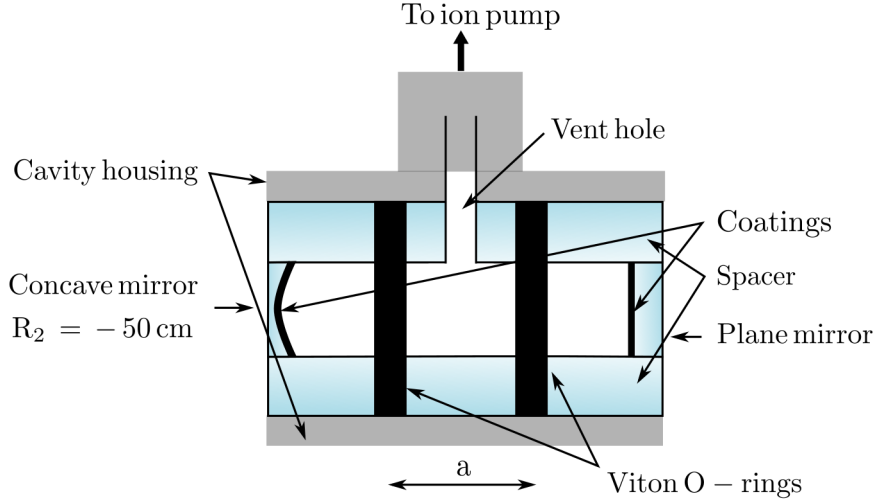


Figure 4.6: Side view schematic of our cylindrical high-finesse cavity in a plano-concave configuration, with a radius of curvature  $R_2 = -50$  cm. The assembly includes a pair of optically contacted 1 inch diameter mirrors and a spacer made of Ultra-Low-Expansion (ULE) glass. The cylindrical spacer is composed of 1 vent hole of 4 mm diameter which allows the internal space between the mirrors to be evacuated. The cavity is supported by two viton O-rings at the Airy points, such that their relative distance  $a = 0.5774L$ , with  $L$  the distance between the mirrors. This allows the mirrors to stay maximally parallel to each other and reduce sensitivity to vibration. The mirror substrates have a dual-wavelength coating to provide high finesse at both 852 nm for Qubit A laser and 1018 nm for Rydberg A & B lasers, simultaneously. Both the mirrors and the spacer are made of ULE glass. This material makes it possible to minimise thermal expansion of the cavity due to a zero-crossing of the linear CTE, which typically occurs at temperatures between 5 °C and 40 °C [189], providing long-term frequency stability. The external face of the mirrors are AR coated and make an angle with the optical axis to avoid etalon effect that would lead to residual amplitude modulation (RAM).

composed of 1 vent hole of 4 mm diameter and 2 through holes of 10 mm diameter, which allows the internal space between the mirrors to be evacuated. The mirror substrates have a dual-wavelength coating to provide high finesse at both 852 nm for Qubit A laser and 1018 nm for Rydberg A & B lasers, simultaneously. From the data sheet, the estimated finessees are  $\mathcal{F}_{852} > 680,000$  at 852 nm and  $\mathcal{F}_{1018} > 310,000$  at 1018 nm with a measured transmission of  $T_{852} = 0.00046186\%$  (4.6 ppm) and  $T_{1018} = 0.0010131\%$  (10.1 ppm) respectively. Both the mirrors and the spacer are made of ULE glass. This material makes it possible to minimise thermal expansion of the cavity due to a zero-crossing of the linear CTE, which typically occurs at temperatures between 5 °C and 40 °C [189], providing long-term frequency stability. The external face of the mirrors are AR coated and make an angle with the optical axis to avoid etalon effect that would lead to residual amplitude modulation (RAM).

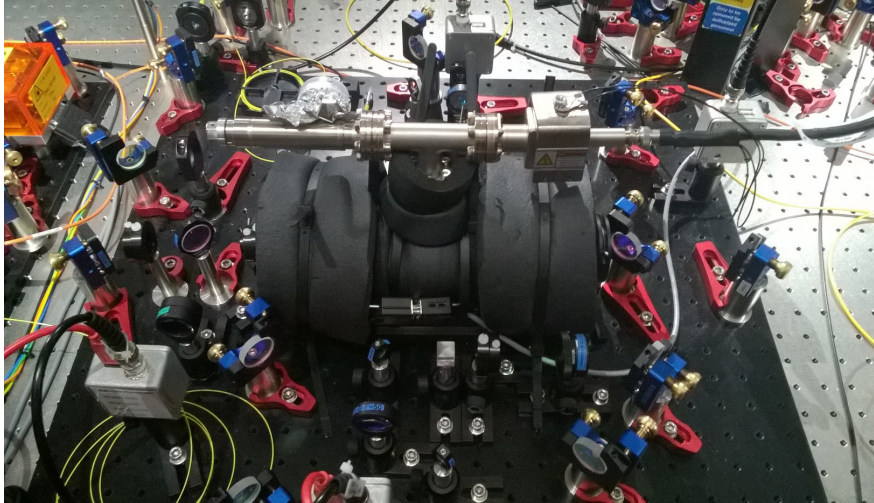


Figure 4.7: Photograph of the cavity locking setup used to lock two Rydberg lasers A and B (1018nm) and Qubit A laser (852 nm). The cavity housing is in middle while Rydberg A (B) beams are coming from bottom left (right) respectively and Qubit A laser beam is coming from the top left via fiber EOMs.

First, all the stainless steel components of the vacuum chamber have been washed in acetone using an ultrasound bath to avoid outgassing. Before inserting the cavity, the chamber is pre-baked at 200 °C for a week, after which the cavity is inserted in order to avoid damaging the coatings on the cavity mirrors and the system rebaked at 50 °C for 48 hours before sealing. A turbomolecular pump is used to reach a rough vacuum pressure of  $10^{-7}$  mbar before turning on the ion pump. Using a 3-l/s ion pump from GammaVacuum, we maintain a low pressure of  $3 \times 10^{-7}$  mbar.

The cavity is mounted horizontally, as shown in Fig. 4.4 (b) and Fig. 4.6, on a pair of Viton O-rings placed at the Airy points [209] where both mirrors can be maximally parallel to each other and reduce sensitivity to vibration. The vacuum chamber is externally temperature-stabilised using a PI temperature controller that drives a current through heater tapes connected in parallel and wound around the cavity vacuum can, itself surrounded by 1 cm thick foam insulation. For passive vibration isolation, the cavity is mounted on a 60 x 60 cm<sup>2</sup> breadboard that rests on a layer of Sorbothane on a floating optical table. The entire vacuum system is supported by two aluminium clamps bolted to the vibration isolation platform. Further improvements could be achieved using a radiation shield around the cavity in vacuum or enclosing the cavity setup within a second stage of temperature control. The full setup is shown in Fig. 4.7.

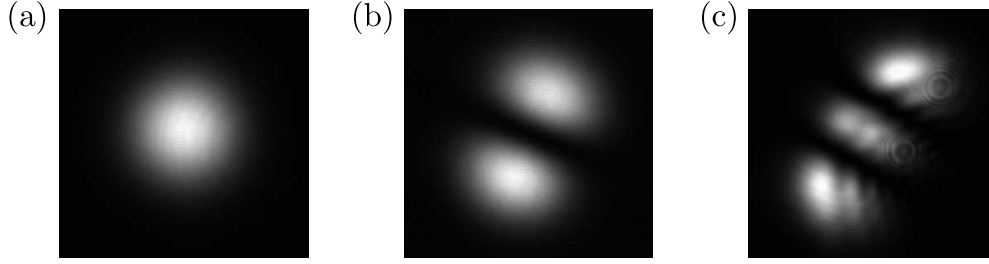


Figure 4.8: Intensity cavity transmission recorded with a camera and showing the three Hermite-Gauss cavity modes (a)TEM<sub>00</sub>, (b)TEM<sub>01</sub> and (c)TEM<sub>02</sub>.

### Cavity mode-matching

Light fields inside the resonator must fulfill boundary conditions imposed by the cavity mirrors. Efficient coupling of the laser beam with the cavity requires matching both the wavefront and radius of curvature of the incident laser beams to the mode of the optical cavity.

For a two-mirror cavity, the eigenmode can be determined using ABCD matrices [1] to obtain the TEM<sub>00</sub> cavity waist  $\omega_0$  and the distance  $d$  from the center of the cavity, using equations

$$\omega_0^2 = \frac{\lambda L}{\pi} \frac{\sqrt{g_1 g_2 (1 - g_1 g_2)}}{g_1 + g_2 - 2g_1 g_2}, \quad (4.9)$$

and

$$d = \frac{L(R_2 - R_1)}{2(2L - R_1 - R_2)}, \quad (4.10)$$

where  $g_i = \left(1 - \frac{L}{R_i}\right)$  is the stability parameter depending on the radius of curvature  $R_i$  of each mirrors. In our plano-concave configuration  $R_{1,2} = \infty, -50$  cm, resulting in  $d \approx -L/2$  such that the waist is located on the plane mirror. For the design wavelengths, the waists are respectively  $\omega_0^{852} = 233 \mu\text{m}$  and  $\omega_0^{1018} = 254 \mu\text{m}$ .

Coupling to the Gaussian mode TEM<sub>00</sub> requires input light to be mode-matched into the cavity to minimise excitation of higher order Hermite-Gauss beam modes. To achieve this, we have used a pair of lenses. One on either side of the cavity, with a focal length of 500 mm for  $f_1$  and 400 mm for  $f_2$ , at 852 nm and 1018 nm

respectively, as shown in Fig. 4.13. During the initial alignment procedure, the cavity transmission is monitored on a CCD camera and allows useful observation of Hermite-Gauss modes in the plane orthogonal to the optical axis, as shown on Fig. 4.8. We note that they are Hermite-Gauss modes and not Laguerre-Gauss modes due to broken symmetry when assembling the cavity.

Finally, one can find the eigenfrequencies of the Hermite-Gauss modes within the cavity [1] given by

$$\nu_{(q,m,n)} = \nu_{\text{FSR}} \left[ q + \frac{m+n+1}{\pi} \cos^{-1} \sqrt{g_1 g_2} \right], \quad (4.11)$$

where  $q$  is the longitudinal mode number, and the couple  $\{m, n\}$  define the transverse mode number. This leads to a theoretical cavity mode spacing of 221.4(1) MHz between each transverse mode.

## 4.4 Laser stabilisation

Due to external and internal perturbations, the laser frequency needs to be actively stabilised to counteract any disturbances. To achieve this, one needs to be able to measure the instantaneous laser frequency  $\nu$  and compare it to a frequency reference to create an error signal that will be fed back on the input laser parameters such as current and grating position.

This is often implemented using an atomic reference, but due to our excitation scheme, where we need control of the detuning of the lasers with respect to atomic transitions while keeping a very stable phase relationship between lasers, the idea is to compare the lasers to an ultra-stable cavity.

The first implementation would be to stabilise the laser's frequency to one of the cavity transmissions peaks [210], as shown in Fig. 4.5. Indeed, due to the precise control of the cavity length  $L$ , the frequency of the transmission peak maximum would be stable enough to sufficiently stabilise the laser frequency. However, the transmittance  $T$  is an even function of the frequency and doesn't enable us to discriminate if  $\nu$  is above or below the frequency corresponding to the maximum transmittance

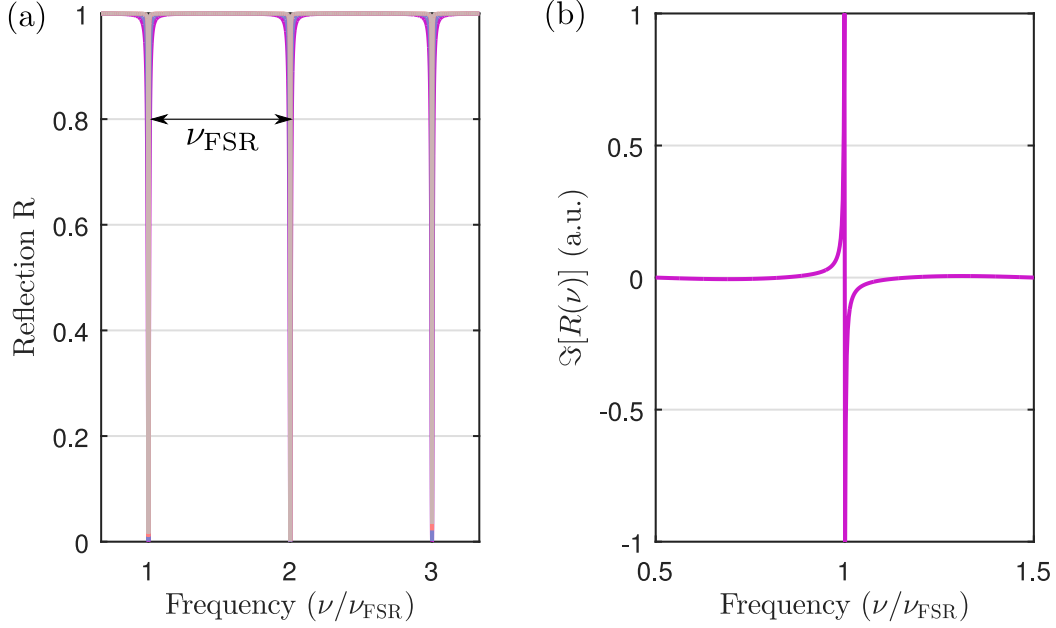


Figure 4.9: (a) Cavity reflection peaks as a function of the incident laser frequency showing equidistant separation by a free spectral range  $\nu_{\text{FSR}}$ . (b) Imaginary part of the reflection coefficient  $R(\nu)$  as a function of the incident laser frequency and a perfect dispersive shape for PDH laser locking.

$\nu_{\text{cav}}$ . One needs to create an odd error signal that crosses zero on the cavity resonance. We can fix this by locking on side of fringe [210], by using the derivative of it, with positive derivative if the frequency is too high and negative derivative for a too low frequency. However, this feedback scheme is not able to distinguish between intensity fluctuations and frequency fluctuations.

An alternative approach is to measure the light reflected from the cavity [210]. The reflected field amplitude  $\mathcal{E}_{\text{ref}}$  from the cavity is the sum of the directly reflected beam which acquires a  $\pi$  phase shift and the light leaking out of the cavity after multiple reflections, which leads to

$$\begin{aligned}\mathcal{E}_{\text{ref}} &= \mathcal{E}_{\text{in}}(-r + t^2 r e^{i\Phi} + t^2 r^3 e^{2i\Phi} + \dots), \\ &= \mathcal{E}_{\text{in}} r \frac{e^{i\Phi} - 1}{1 - r^2 e^{i\Phi}}.\end{aligned}\quad (4.12)$$

One can then show that the intensity reflection coefficient of the cavity [1] is

$$R \equiv \frac{I_{\text{ref}}}{I_{\text{in}}} = \frac{|\mathcal{E}_{\text{ref}}|^2}{|\mathcal{E}_{\text{in}}|^2} = \frac{F \sin^2(\Phi/2)}{1 + F \sin^2(\Phi/2)}.\quad (4.13)$$

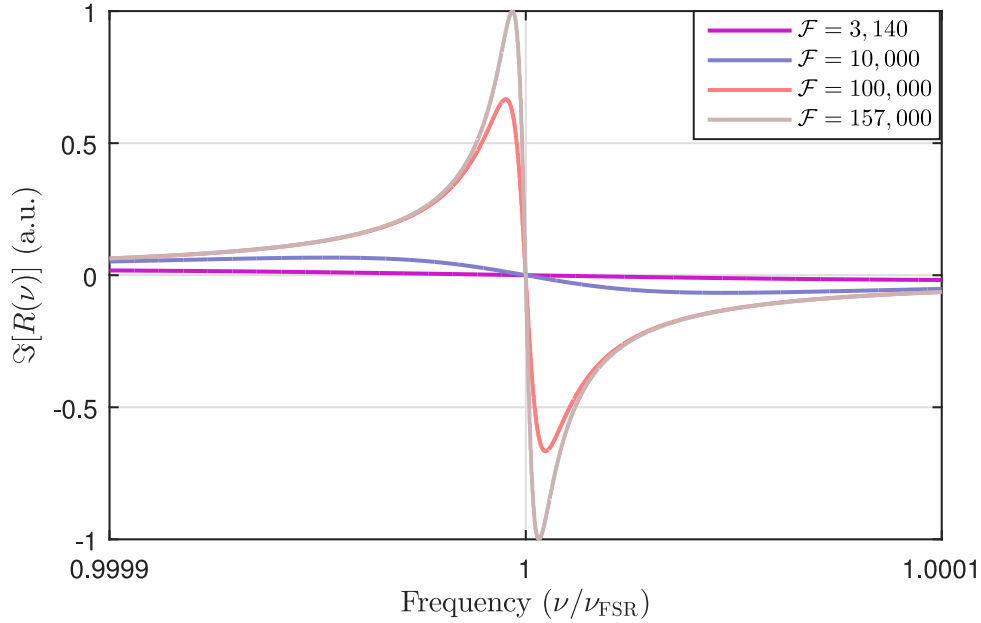


Figure 4.10: Zoom of the dispersive features from the imaginary part of the reflection coefficient  $R(\nu)$  around a resonance with increasing value of the finesse  $\mathcal{F}$ . For increasing finesse, the slope becomes steeper, leading to higher frequency discrimination for the PDH error signal.

Figure 4.9 (a) shows a plot of the intensity reflection coefficient  $R$  as a function of the incident laser frequency with an approximate parabolic shape around a minimum corresponding to the cavity's resonance frequency  $\nu_{\text{cav}}$ , equivalent to a  $2\pi$  phase shift. Although  $R$  is an even function, creating an error signal from here would enable decoupling the intensity fluctuations from the frequency's fluctuations.

#### 4.4.1 Pound-Drever-Hall locking

In fact, a brilliant idea came from Robert V. Pound, Ronald Drever and John L. Hall [210, 211] in 1983 at the University of Glasgow and the US National Bureau of Standards. An error signal could be derived from the imaginary part of the reflection coefficient, plotted in Fig. 4.9 (b), which shows a perfect dispersive behavior around the cavity resonance frequency  $\nu_{\text{cav}}$ . For increasing finesse, the slope becomes steeper, leading to higher frequency discrimination from the Pound-Drever-Hall (PDH) error signal as can be seen on Fig. 4.10.

An advantage of the PDH technique is that the bandwidth of the feedback loop is not limited by the response time of the reference cavity. Indeed, the field transmitted

through the output mirror of the cavity results from the interference of a large number of internal cavity reflections. The higher the finesse  $\mathcal{F}$ , the bigger the number of round-trips before light leaking out. Meaning that any drift in frequency of the incident cavity beam would need a delay dependent on the quality of the mirror, hence the reflection coefficient of the mirror  $R$ , before being transmitted. This delay is called the cavity decay time  $\tau_c$  and is related to the cavity linewidth  $\delta\nu_{\text{cav}}$  by the formula

$$\tau_{\text{cav}} = \frac{1}{2\pi \delta\nu_{\text{cav}}}. \quad (4.14)$$

In order to realise narrow linewidth lasers, we aim to achieve low cavity linewidth, creating large cavity decay time  $\tau_{\text{cav}}$ . However, the light reflected from the cavity results from the interference of the directly reflected light, transporting instantaneous information, and the backward leakage light coming from the cavity after many round-trips. The backward light is acting as a reference beam and the total reflected light reacts immediately to any frequency drift, dramatically increasing the achievable feedback loop bandwidth [211].

The first step of the PDH locking technique involves creating a phase-modulated monochromatic laser beam using an electro-optical-modulator (EOM) driven at a frequency  $\Omega$  with a modulation depth  $\beta$ , which can be described by

$$\mathcal{E}_{\text{in}} = \mathcal{E}_0 e^{i(\omega t + \beta \sin \Omega t)}. \quad (4.15)$$

In the limit of low modulation depth ( $\beta \ll 1$ ), this equation can be approximated using a Taylor expansion

$$\mathcal{E}_{\text{in}} \approx \mathcal{E}_0 (J_0(\beta) e^{i\omega t} + J_1(\beta) e^{i(\omega+\Omega)t} - J_1(\beta) e^{i(\omega-\Omega)t}), \quad (4.16)$$

where  $J_n$  is the first kind Bessel function of order  $n$ . Neglecting the power in higher orders, the field can be considered as the sum of one carrier at the frequency  $\omega$  and two sidebands at  $\omega \pm \Omega$  with opposite phase and a relative weighting controlled via the modulation depth.

After phase modulation, the beam is sent to the cavity where it will be partially reflected and partially transmitted depending on its frequency. Extracting the reflection coefficient  $\mathcal{R}(\omega)$  for the electric field from Eq. 4.12,

$$\mathcal{R}(\omega) = \frac{\mathcal{E}_{\text{ref}}}{\mathcal{E}_{\text{in}}} = r \frac{e^{i\Phi(\omega)} - 1}{1 - r^2 e^{i\Phi(\omega)}}, \quad (4.17)$$

allows us to derive an expression for the reflected phase modulated beam [212] as

$$\mathcal{E}_{\text{ref}} = \mathcal{E}_{\text{in}} \{ \mathcal{R}(\omega) J_0(\beta) e^{i\omega t} + \mathcal{R}(\omega + \Omega) J_1(\beta) e^{i(\omega+\Omega)t} - \mathcal{R}(\omega - \Omega) J_1(\beta) e^{i(\omega-\Omega)t} \}. \quad (4.18)$$

A photodiode will monitor the reflected cavity power  $\mathcal{P}_{\text{ref}} = |\mathcal{E}_{\text{ref}}|^2$  such as

$$\begin{aligned} \mathcal{P}_{\text{ref}} &= \mathcal{P}_c |\mathcal{R}(\omega)|^2 + \mathcal{P}_s |\mathcal{R}(\omega + \Omega)|^2 + \mathcal{P}_s |\mathcal{R}(\omega - \Omega)|^2 \\ &\quad + 2 \sqrt{\mathcal{P}_c \mathcal{P}_s} \{ \Re \left[ \mathcal{R}(\omega) \mathcal{R}^*(\omega + \Omega) - \mathcal{R}^*(\omega) \mathcal{R}(\omega - \Omega) \right] \cos \Omega t \\ &\quad + \Im \left[ \mathcal{R}(\omega) \mathcal{R}^*(\omega + \Omega) - \mathcal{R}^*(\omega) \mathcal{R}(\omega - \Omega) \right] \sin \Omega t \} \\ &\quad + O(2\Omega), \end{aligned} \quad (4.19)$$

where  $\mathcal{P}_c = J_0^2(\beta) \mathcal{P}_{\text{in}}$  and  $\mathcal{P}_s = J_1^2(\beta) \mathcal{P}_{\text{in}}$  are the power in the carrier and the sidebands respectively with  $\mathcal{P}_{\text{in}} = |\mathcal{E}_{\text{in}}|^2$ . We can identify three frequency components in Eq. 4.19. The three DC values corresponds to the reflected power for the carrier and the two sidebands respectively. The interference between the reflected sidebands and reflected carrier leads to the component at the frequency  $\Omega$  while a frequency component at  $2\Omega$  arises from the interference between the reflected sidebands.

## Demodulation

We are only interested in the frequency component at  $\Omega$  because the crucial phase information is contained in the term  $\mathcal{R}(\omega) \mathcal{R}^*(\omega + \Omega) - \mathcal{R}^*(\omega) \mathcal{R}(\omega - \Omega)$ , as plotted in Fig. 4.11. It can be extracted by demodulating the reflected signal with the local oscillator signal using a RF-mixer, whose output corresponds to the multiplication

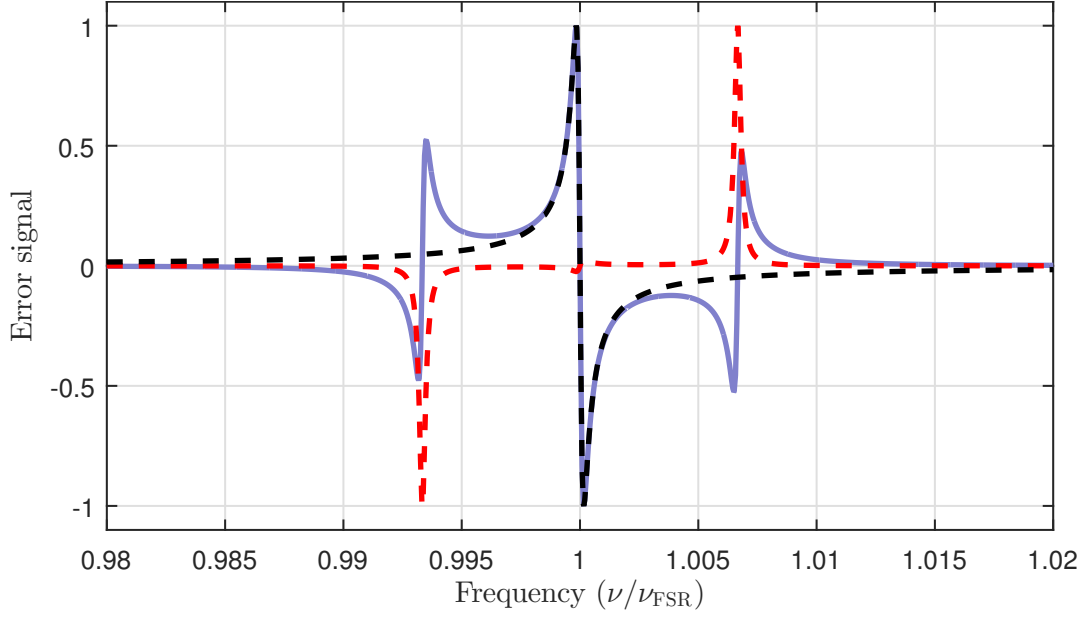


Figure 4.11: Imaginary part (PDH signal) in purple and real part in red of the demodulated reflected power from the cavity for a low finesse  $\mathcal{F} = 3140$  corresponding to a reflection coefficient of  $R = 0.999$ . The modulation is taken to  $\nu_{\text{PDH}} = 10$  MHz with  $\nu_{\text{FSR}} = 1.5$  GHz with approximated PDH signal of Eq. 4.22 reported in black dashed line.

of the two inputs. More precisely, the imaginary part is obtained by adjusting the phase of the local oscillator to  $\pi/2$  with respect to the reflected signal before going to the mixer. Using a low-pass filter with frequency cut-off  $\Omega$  allows us to obtain the time-independent PDH error-signal  $\epsilon(\omega)$

$$\epsilon(\omega) = 2\sqrt{\mathcal{P}_c\mathcal{P}_s} \Im\left[\mathcal{R}(\omega)\mathcal{R}^*(\omega + \Omega) - \mathcal{R}^*(\omega)\mathcal{R}(\omega - \Omega)\right]. \quad (4.20)$$

Using a modulation frequency  $\Omega$  high compared to the cavity linewidth  $\delta\nu_{\text{cav}}$ , one can consider that the sidebands are totally reflected, hence  $\mathcal{R}(\omega \pm \Omega) = -1$ , which allows to simplify the expression for  $\epsilon(\omega)$  [210] to

$$\epsilon(\omega) = -4\sqrt{\mathcal{P}_c\mathcal{P}_s} \Im\{\mathcal{R}(\omega)\}, \quad (4.21)$$

and the PDH error-signal of the main peak can be approximated by [210]

$$\epsilon(\omega) \approx -8\frac{\sqrt{\mathcal{P}_c\mathcal{P}_s}}{\delta\nu_{\text{cav}}} \delta\nu. \quad (4.22)$$

Figure 4.11 shows the resulting PDH error signal in purple, with the approxima-

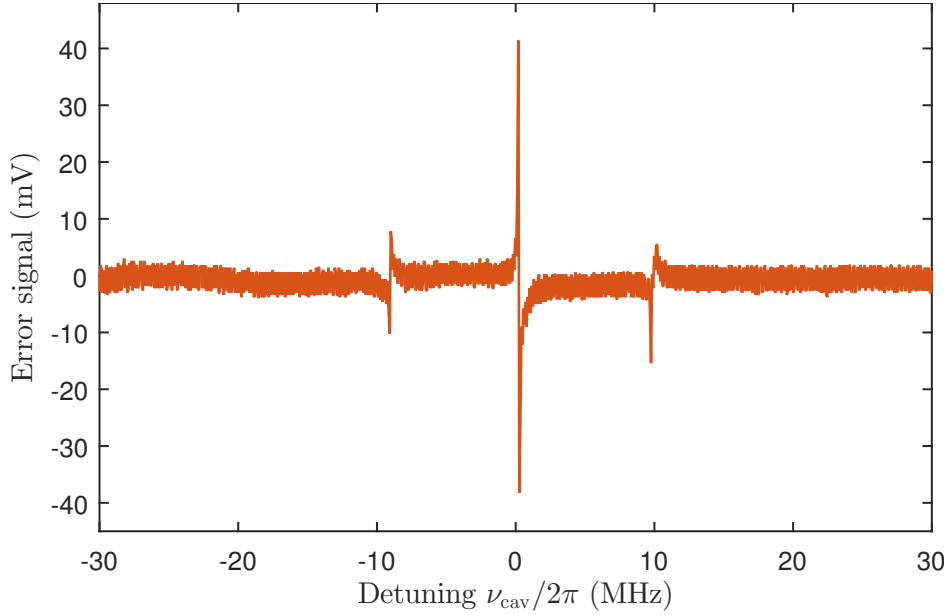


Figure 4.12: PDH signal showing a carrier slope optimised using a phase-delay of the local oscillator by varying a coaxial cable length before the local oscillator port of the RF-mixer, with sidebands at  $\pm 10$  MHz returning opposite slopes.

tion given by Eq. 4.22 shown by the black dashed line. The real part of the term  $\mathcal{R}(\omega)\mathcal{R}^*(\omega + \Omega) - \mathcal{R}^*(\omega)\mathcal{R}(\omega - \Omega)$  is shown in red dashed line. Higher cavity finesse corresponds to lower cavity linewidth  $\delta\nu_{\text{cav}}$  and hence steeper error-signal slope according to Eq. 4.22, allowing higher frequency discrimination. Figure 4.12 shows the experimental realization of the PDH error signal on the Qubit A laser. The slope of the error signal has been optimised by adjusting the coaxial cable length before the local oscillator port of the RF-mixer on Fig. 4.14. The function is asymmetric with respect to the laser frequency and allows the system to discriminate between positive and negative detuning for correct feedback. The cavity sidepeaks at the modulation frequency  $\Omega$  return the opposite slope on the error-signal that allows us to be sure we can only lock to the carrier when implementing it experimentally.

#### 4.4.2 Experimental implementation and frequency offset locking

As shown in Fig. 4.14, we pick off  $\sim 1$  mW of light from each ECDL and couple the light into fiber-coupled electro-optic phase modulators (EOM) (Jenoptik models PM-830 and PM-1064) for generating sidebands on the light. The fiber EOMs

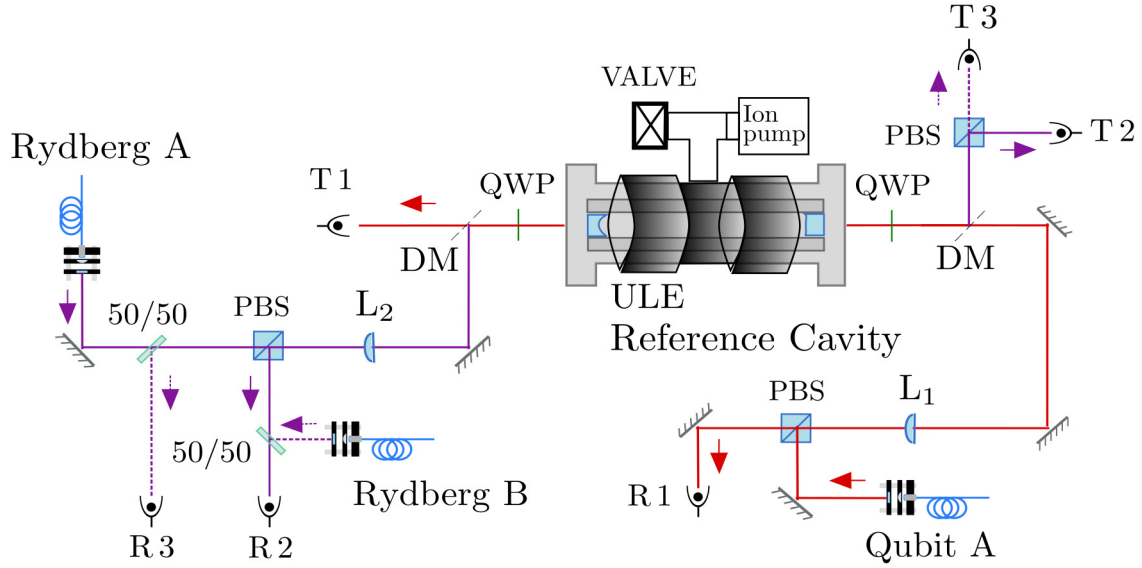


Figure 4.13: Schematic of the cavity locking setup for PDH locking. Key : L = cavity mode-matching lens, DM = Dichroic mirror, PBS = polarising beam splitter, QWP = quarter-wave plate, R : high-bandwidth photodiode, T = high-gain photodiode.

provide broadband phase modulation (up to 5 GHz) whilst minimizing residual amplitude modulation (RAM) and cleaning the mode shape and the polarisation incident on the cavity. Due to the high insertion loss of the modulators (4 - 4.6 dB for PM-830 and 5.5 dB for PM-1064), this leaves around 200  $\mu$ W available for laser stabilisation which is mode-matched into the cavity using lenses  $f_{1,2}$  to maximize coupling to the TEM<sub>00</sub> cavity mode.

The optical setup for laser locking is shown in Fig. 4.7 and its corresponding schematic in Fig. 4.13. Light from the two Rydberg master lasers (A & B) is combined on a polarising beam splitter (PBS) with orthogonal polarisation and coupled into the cavity using a dichroic mirror (DM) to separate the incident 1018 nm light from the transmitted 852 nm light (Qubit A) from the cavity. To isolate the reflected signal for cavity locking, 50:50 beam splitters are placed in each beam path prior to the PBS allowing independent detection photodiodes to be used. Similarly, after the cavity, a second DM and PBS are used to separate the transmission signals of the two Rydberg lasers.

### High-bandwidth and high-gain photodiodes

According to Sec. 4.4.1, the reflected cavity signal at the modulation frequency  $\Omega \sim 10$  MHz contains all the information about the PDH error signal. Therefore, the beatnote carrier-sidebands has to be detected fast enough that it doesn't add any distortion. Additionally, power level of  $\sim 20 \mu\text{W}$  (on resonance) must be detected with the minimum of noise.

However, high-bandwidth photodiodes combined with high-gain are difficult to find commercially and rather expensive. Thus, our high-bandwidth photodetectors are homebuilt with a circuit based on a fast photodiode (Hamamatsu S5971) combined with a transimpedance amplifier (see App. B), which allows to provide a bandwidth of 25 MHz and a gain of  $5 \times 10^4$  V/A.

Moreover, we also need a photodetector to monitor the transmission of the cavity. This requires a high-gain and low-noise photodetector due to the low level of light hitting it after the cavity ( $\sim \mu\text{W}$ ). Our high-gain homebuilt photodiode (see App. B) have been optimised for ring-down measurements on the ULE cavity (see Sec 4.5.3), with a total gain of  $2.5 \times 10^6$  V/A and a measured roll-off frequency of  $f_{-3\text{dB}} = 890$  kHz.

### Feedback electronics

Electronics for the PDH lock are shown schematically in Fig. 4.14. Each EOM is driven by a low frequency signal ( $\nu_{\text{PDH}}$ ) at +10 dBm to generate 1<sup>st</sup>-order sidebands with 10 % amplitude (phase modulation depth  $\beta = 0.7$  rad) with a frequency generator (Rigol DG1022A). To minimise cross-talk between lasers, frequencies of  $\nu_{\text{PDH}} = 8.4, 10.3, 11.7$  MHz are chosen, ensuring any interference effects occur at beat frequencies above the servo-bandwidth. The cavity reflected signal is measured using the home-made high-bandwidth photodiode, covered with a bandpass filter (Thorlabs FL05850-10) when selecting Qubit A beam. The DC-component is filtered out of the photodiode output signal using a DC-Block (Minicircuits BLK-89-S+), then amplified using a low-noise amplifier (Minicircuits ZFL-HLN500+ for Qubit A and ZFL-500+ for Rydberg A & B). The amplified signal is sent to a Cou-

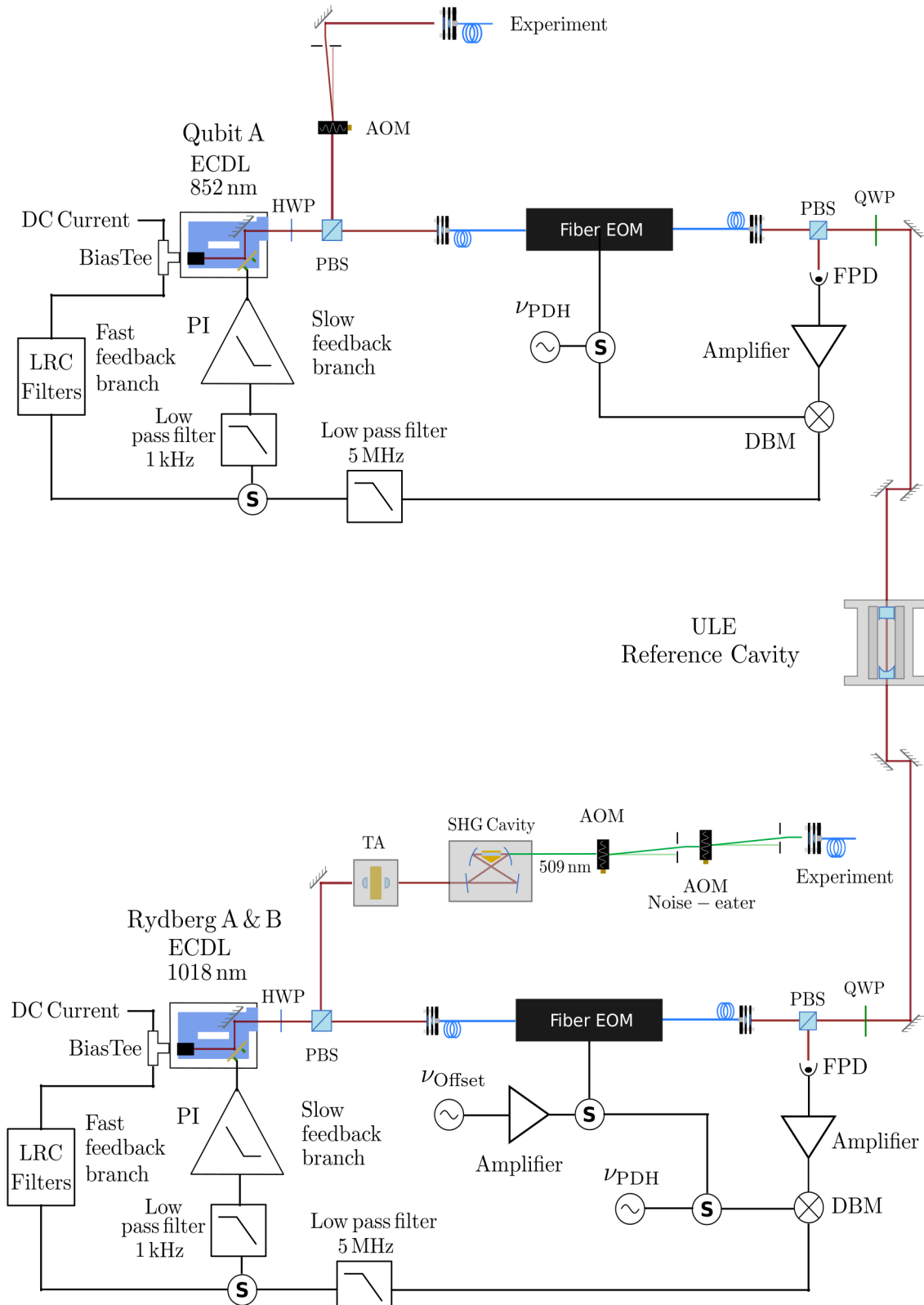


Figure 4.14: Laser setup for Qubit A at 852 nm driving transition from  $6S_{1/2} \rightarrow 6P_{3/2}$  and locking electronics for frequency doubled Rydberg lasers A & B driving the second stage transition at 509 nm. Key : PBS = Polarising beam splitter, HWP = Half wave plate, QWP = Quarter wave plate, FPD = Fast photodiode, DBM = Double balanced mixer, S = Splitter, PI = Proportional Integral, TA = Tapered amplifier, AOM = Acousto-optic modulator, EOM = Electro-optic modulator.



Figure 4.15: Photograph of the box containing electronics for PDH feedback.

pler (Minicircuits ZDC-20-3) which splits the signal into two paths. The first path goes to the RF spectrum analyser for recording the in-loop photodiode signal whilst the second path is used for generating the PDH error signal. This is generated from it by demodulation with the local oscillator at  $\nu_{\text{PDH}}$  on a RF - mixer (Minicircuits ZFM-4+), followed by a low-pass filter at 5 MHz (Minicircuits BLP-5+). After the filter, the error signal is split into two simultaneous feedback branches to the laser using a splitter (Minicircuits ZFSC-42-S+).

The first feedback branch is a low frequency PI servo loop (DC-300 Hz) which provides feedback to the piezo that controls the laser's grating position. This ensures the laser remains locked to the cavity peak and uses a RC filter with 1 kHz cut-off frequency. Figure 4.15 shows the box where the electronics are enclosed in order to avoid any interference effects. A second path provides fast feedback directly to the diode laser current. This path uses a resistor for direct feedback in parallel with

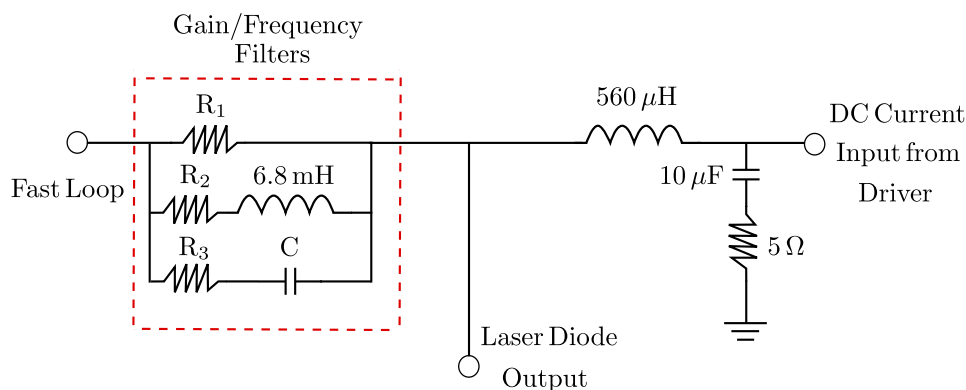


Figure 4.16: Schematic of the LRC filter that is combined with the laser drive current to provide fast-feedback to the laser.

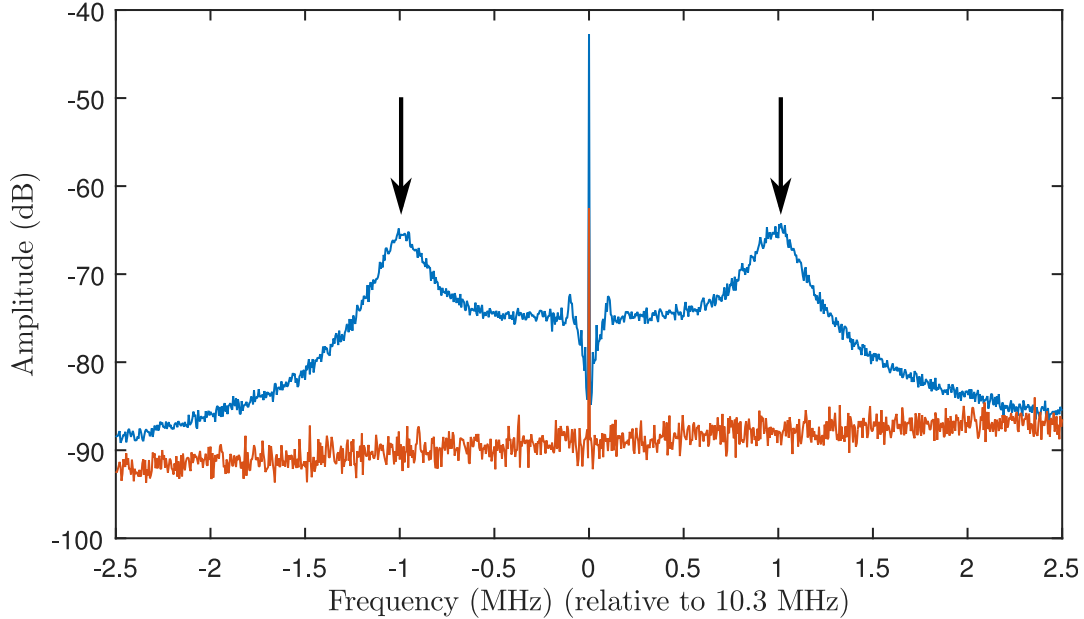


Figure 4.17: In-loop error signal of Qubit A when the laser is locked (blue) or unlocked (orange). The servo-bumps (black arrows) amplitude is 20 dB lower than the central peak, with a maximum achievable servo bandwidth of 1.1 MHz.

passive LRC phase advance and phase-delay filters as detailed in Ref. [212]. This LRC filter is combined with the laser drive current using a bias-tee as shown in Fig. 4.16.

Once the laser is locked, we optimise the laser lock parameters by recording the in-loop error signal on a RF spectrum analyser. As illustrated in Fig. 4.17, we observe servo-bumps either side of the PDH modulation frequency  $\nu_{\text{PDH}}$ . They correspond to the poles of the system transfer function and lead to positive feedback, meaning that there will be noise amplification at these specific frequencies. Thus, the position of the servo-bumps determines the maximal achievable bandwidth and need to be moved as far as possible from  $\nu_{\text{PDH}}$ .

Recording the in-loop error signal and varying the 3 resistors  $R_1, R_2, R_3$  and the capacitor  $C$  from the fast feedback loop, as shown in Fig. 4.16, allows us to maximise the servo bandwidth for each of the three locked lasers. The maximum servo bandwidth achieved for Qubit A is 1.1 MHz as well as for Rydberg A & B (see Sec. 4.6.1). The servo-bumps amplitude is 20 dB lower than the central peak and the noise is reduced at low frequencies.

Finally, another crucial point was to control the amount of feedback in the fast feedback branch. Indeed, too much feedback made it impossible to lock the lasers,

Laser	Attenuator	R <sub>1</sub>	R <sub>2</sub>	R <sub>3</sub>	C
Qubit A	23 dB	1 kΩ	200 Ω	4.7 Ω	561 pF
Rydberg A	19 dB	1 kΩ	200 Ω	4.7 Ω	1 nF
Rydberg B	18 dB	1 kΩ	200 Ω	4.7 Ω	1 nF

Table 4.2: Optimised parameters of the fast-feedback LRC filter.

and also increased the noise in the servo-bumps, hence decreasing the coherence time when driving coherent Rydberg Rabi oscillations as in Sec. 7.2.6. The feedback was controlled via an attenuator placed between the splitter and the Fast Output port of the LRC filter. The optimised parameters are recorded in Tab. 4.2.

### Frequency offset locking technique

As the cavity resonances are not necessarily commensurate with frequencies required for Rydberg excitation, we employ the "electronic sideband" [213, 214] technique to provide a continuously tunable offset from the cavity modes of the two Rydberg lasers A & B. A second frequency,  $\nu_{\text{Offset}}$ , is amplified to +25 dBm (Minicircuits ZFL-1000VH2+) and combined on a splitter (Minicircuits ZFSC-2-2S+) with the low frequency PDH signal,  $\nu_{\text{PDH}}$ , to drive the EOM with dual frequencies resulting in large first order sidebands at  $\pm\nu_{\text{Offset}}$ , each of which has secondary PDH sidebands to enable locking, as shown in Fig. 4.18. Through choice of phase in the PDH error signal, the laser can be locked to either the +1 or -1 sideband to achieve a frequency shift of  $\mp\nu_{\text{Offset}}$  on the master laser with respect to the cavity. The offset frequency is derived from a Digital Device Synthesizer (DDS AD9910) operating from 0.1 Hz to 460 MHz, which gives a tuning range of  $\pm 920$  MHz after doubling, representing more than a free spectral range. In practice, we have observed that we can keep lasers locked when the frequency sweeping of  $\nu_{\text{Offset}}$  is lower than the open-loop bandwidth.

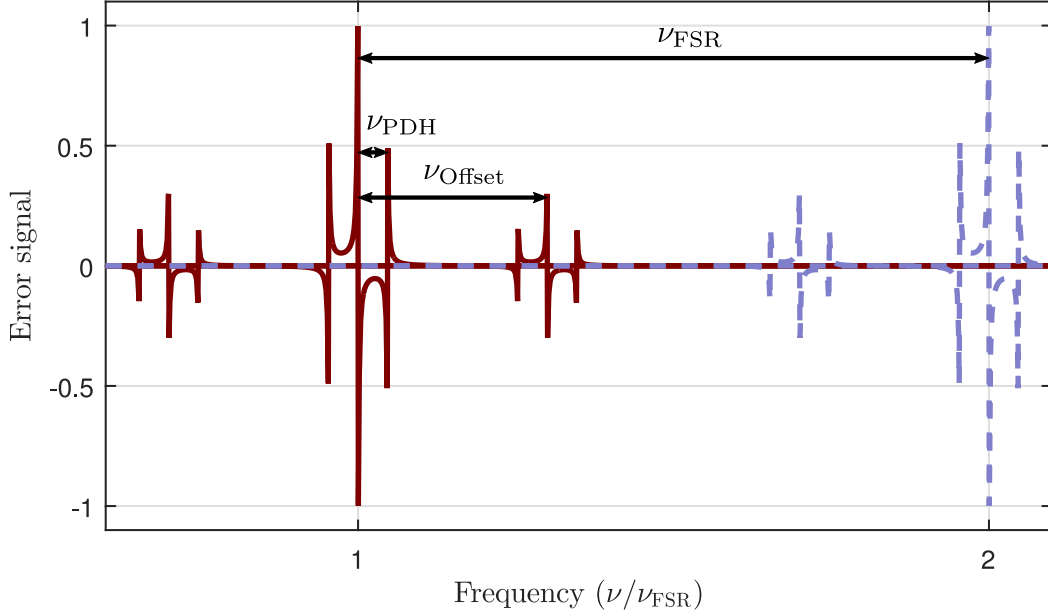


Figure 4.18: Sideband locking illustrated technique to provide a continuously tunable offset from the cavity modes of the two Rydberg lasers A & B at  $\pm\nu_{\text{Offset}}$ .

## 4.5 Cavity characterisation

### 4.5.1 Determination of the zero-CTE temperature

To evaluate the performance of the laser stabilisation system, we first characterise the ULE cavity using an optical beatnote between the 852 nm Qubit A laser locked onto a  $\text{TEM}_{00}$  mode of the cavity and a second independent laser (probe laser) stabilised to the  $|6s \ ^2S_{1/2}, F = 4\rangle \rightarrow |6p \ ^2P_{3/2}, F' = 5\rangle$  cooling transition using polarisation spectroscopy (see Sec. 5.2.2) with a frequency precision of the MHz.

Choosing ULE glass allows us to vanish the first-order coefficient of thermal expansion (CTE), which has the formula [189]

$$\alpha(T) = k_0 + 2.21 \times T + 0.0122 \times T^2 + 1.88 \cdot 10^{-5} \times T^3 (\times 10^{-9}/^\circ\text{C}). \quad (4.23)$$

For the critical temperature  $T_c$ , where the CTE  $\alpha$  vanishes, the cavity length is least sensitive to temperature variations, thereby increasing the instantaneous laser linewidth stability.

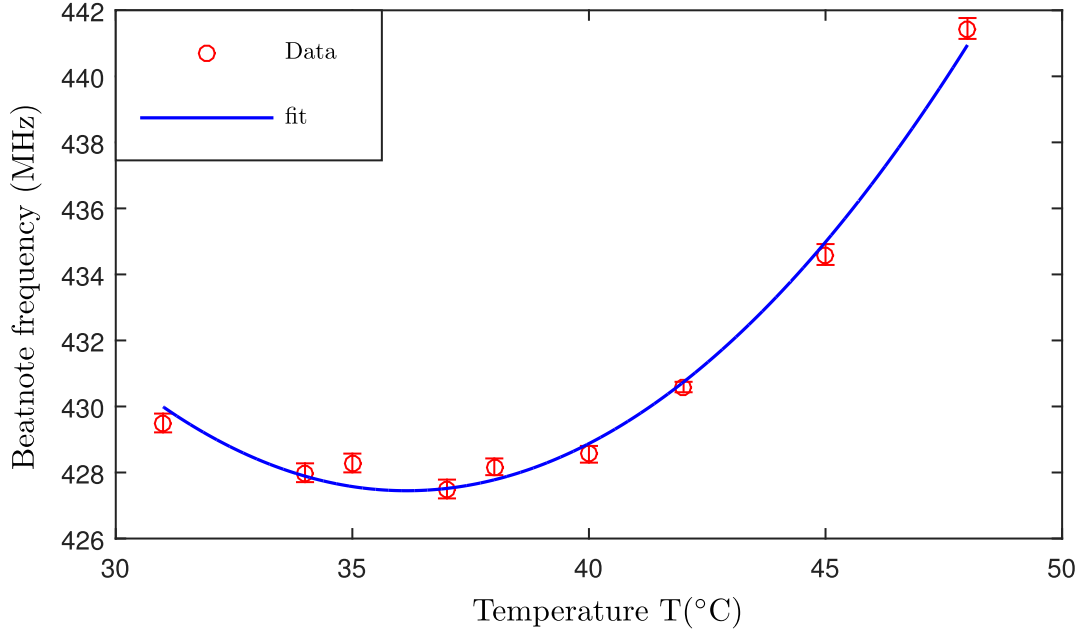


Figure 4.19: Optical beatnote between the 852 nm Qubit A laser locked onto a  $\text{TEM}_{00}$  mode of the cavity and a second independent laser (probe laser) stabilised to the  $|6s\ ^2S_{1/2}, F = 4\rangle \rightarrow |6p\ ^2P_{3/2}, F' = 5\rangle$  cooling transition using polarisation spectroscopy. Recording the beatnote frequency as a function of cavity temperature for varying temperature from  $32^\circ\text{C}$  to  $40^\circ\text{C}$ , results in a quadratic dependence due to the vanishing first-order coefficient of thermal expansion of the ULE cavity spacer. Due to the large thermalisation time-constant of the cavity (measured to be approximately 12 hours), each data point has been taken after a minimum period of 18 hours following a change in temperature and up to 48 hours later. The data are fitted with a quadratic dependence of the form  $A \times \nu_0 \times (T - T_c)^2 + \nu_{\text{Offset}}$ . The errors are given by one-standard deviation and are approximately  $0.1^\circ\text{C}$ . The fit returns an extracted temperature of the zero-CTE crossing as  $T_c = 36.1 \pm 0.1^\circ\text{C}$ .

An optical beatnote is realised by overlapping Qubit A laser and the probe laser through a 50:50 beamsplitter with the same polarisation. The beatnote signal is registered using a High Speed InGaAs photodetector from Newport (model 818-BB-51f) with 12.5 GHz bandwidth. We are using a wavemeter (Bristol model 721) to record the right mode of Qubit A when locked to the ULE cavity with a precision of  $\pm 20$  MHz. The signal is analysed by a spectrum analyser (N9010A EXA Signal Analyser) and subsequently fitted to give the beatnote frequency with a precision of 0.01 MHz.

In order to evaluate which temperature span we have to use for getting the zero-CTE critical temperature  $T_c$ , we first set the probe laser at the optimum MOT detuning of  $\Delta_p = -2.9 \Gamma$  using an AOM, as explained in Sec. 5.2. This results in a beatnote of 430 MHz with a starting temperature of  $30^\circ\text{C}$  (usually between  $20^\circ\text{C}$

and 40°C). Now, one needs to determine if the critical temperature is hotter or colder with respect to the starting temperature. Taking into account that the free spectral range is  $\nu_{\text{FSR}} = c/2L$ , we can evaluate the change in temperature needed for a cavity mode frequency change of  $\nu_{\text{FSR}}$ , such that

$$\frac{d\nu_{\text{cav}}}{dT} = \frac{d\nu_{\text{cav}}}{dL} \times \frac{dL}{dT} = -\frac{c}{2L^2} \times \frac{dL}{dT} = -\frac{\nu_{\text{cav}}}{L} \times \frac{dL}{dT}. \quad (4.24)$$

Using the definition of the coefficient of thermal expansion  $\alpha$  such that

$$\frac{dL}{L} = \alpha \times dT \iff \alpha = \frac{1}{L} \times \frac{dL}{dT}. \quad (4.25)$$

This allows us to connect the frequency variation of the cavity mode  $\nu_{\text{cav}}$  with temperature to the CTE  $\alpha$  by the relation

$$\frac{d\nu_{\text{cav}}}{dT} = -\alpha \times \nu_{\text{cav}}. \quad (4.26)$$

The beatnote is at the frequency

$$\nu_{\text{beat}} = |\nu_0 - \nu_{\text{cav}}|, \quad (4.27)$$

so that it is important to know which one is at higher frequency. As the probe AOM voltage increases (moving probe beam to positive detuning  $\Delta_p$ ), the beatnote frequency  $\nu_{\text{beat}}$  increases, confirming that  $\nu_0 > \nu_{\text{cav}}$ . Finally, one can differentiate Eq. 4.27 to obtain the frequency variation of the beatnote  $\nu_{\text{beat}}$  with temperature and relate it to the CTE  $\alpha$  :

$$\frac{d\nu_{\text{beat}}}{dT} = -\frac{d\nu_{\text{cav}}}{dT} = \alpha \times \nu_{\text{cav}}. \quad (4.28)$$

Moreover, considering a negligible  $T^2$  dependence in Eq. 4.23, one can approximate a linear dependence of  $\alpha$  with  $T$ . Combined to Eq. 4.25, we can deduce its gradient by

$$\frac{\Delta\alpha}{\Delta T} \approx \frac{1}{(\Delta T)^2} \cdot \frac{\Delta L}{L} \approx 2.21 \times 10^{-9} / ^\circ C^2. \quad (4.29)$$

Doing a measurement at 32°C ( $dT > 0$ ), the beatnote reduces to 428 MHz and thus the gradient  $d\nu_{\text{beat}}/dT$  is negative, requiring that  $\alpha < 0$  using Eq. 4.27. Thus, according to Eq. 4.29, the zero-CTE temperature  $T_c$  is hotter than 32°C. Recording the beatnote frequency as a function of cavity temperature for varying temperature from 32°C to 40°C, as shown in Fig. 4.19, results in a quadratic dependence due to the vanishing first-order coefficient of thermal expansion of the ULE cavity spacer [193]

$$\frac{\Delta L}{L} = -\frac{\Delta\nu}{\nu} \approx 2.21 \times 10^{-9} (T - T_c)^2. \quad (4.30)$$

Due to the large thermalisation time-constant of the cavity (measured to be approximately 12 hours), each data point has been taken after a minimum period of 18 hours following a change in temperature and up to 48 hours later. The data shown in Fig. 4.19 are fitted with a quadratic dependence of the form  $A \times \nu_0 \times (T - T_c)^2 + \nu_{\text{Offset}}$ . The errors are given by one-standard deviation and are approximately 0.1°C. The fit returns an extracted temperature of the zero-CTE crossing as  $T_c = 36.1 \pm 0.1^\circ C$ .

### 4.5.2 Determination of the FSR of the cavity

Following temperature stabilisation of the cavity length at  $T_c$ , the free-spectral range is measured by locking Qubit A laser to adjacent longitudinal cavity modes, as shown in Fig. 4.20. Since the beatnote frequency is a positive scalar, as the Qubit A laser scans from positive to negative frequencies with respect to the probe beam, the beatnote frequency is folded. The data are fitted with a function of the form  $|\nu_{\text{FSR}} \times i + \nu_{\text{Offset}}|$ , where  $i$  represents the mode number. This gives  $\nu_{\text{FSR}} = 1.49637(2)$  GHz, corresponding to a cavity length of  $L = 10.0173(1)$  cm which is compatible with the specified cavity length of 100 mm given by the manufacturer.

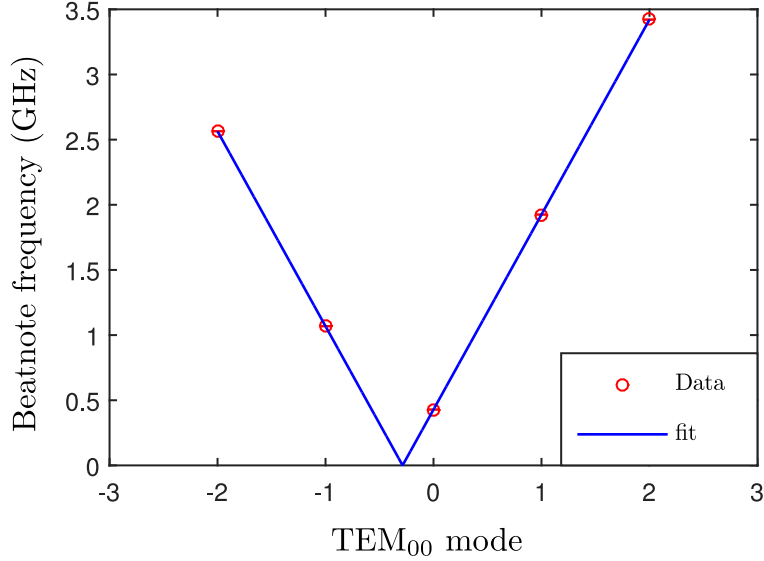


Figure 4.20: Free spectral range determination via the beat note between Qubit A laser and the cooling master laser locked to the  $|6s\ ^2S_{1/2}, F = 4\rangle \rightarrow |6p\ ^2P_{3/2}, F' = 5\rangle$  transition. The data are fitted of the form  $|\nu_{\text{FSR}} \times i + \nu_{\text{Offset}}|$  where  $i$  represents the mode number of Qubit A and returns  $\nu_{\text{FSR}} = 1.49637(2)$  GHz.

### 4.5.3 Ringdown-measurements and cavity parameters

One way to measure the finesse of the cavity  $\mathcal{F}$  is to scan the laser frequency through cavity transmission resonances (as shown in Fig. 4.5) and determined the ratio  $\nu_{\text{FSR}}/\delta\nu_{\text{cav}}$ . However, when it comes to a high-finesse cavity, the cavity linewidth  $\delta\nu_{\text{cav}}$  becomes orders of magnitude lower than that of the laser. This prevents us from using this method of determining the finesse as the laser linewidth would broaden the transmission resonances.

A general argument is to approximate the system consisting of the cavity and the light inside the cavity as an effective oscillatory system [215] whose energy loss will be related to the photon loss per round-trip, which itself depends on the mirror reflectivity  $R$ .

Indeed, after a time  $t = L/c$ , the energy loss is  $(1-R)$ . This implies that the intensity will decrease with a rate given by  $1/\tau_{\text{cav}} = (1 - R)c/L$ , where  $\tau_{\text{cav}}$  is the cavity decay time defined in Eq. 4.14, such that

$$\frac{dI_{\text{cav}}}{dt} = -\frac{(1 - R)}{L} c I_{\text{cav}}. \quad (4.31)$$

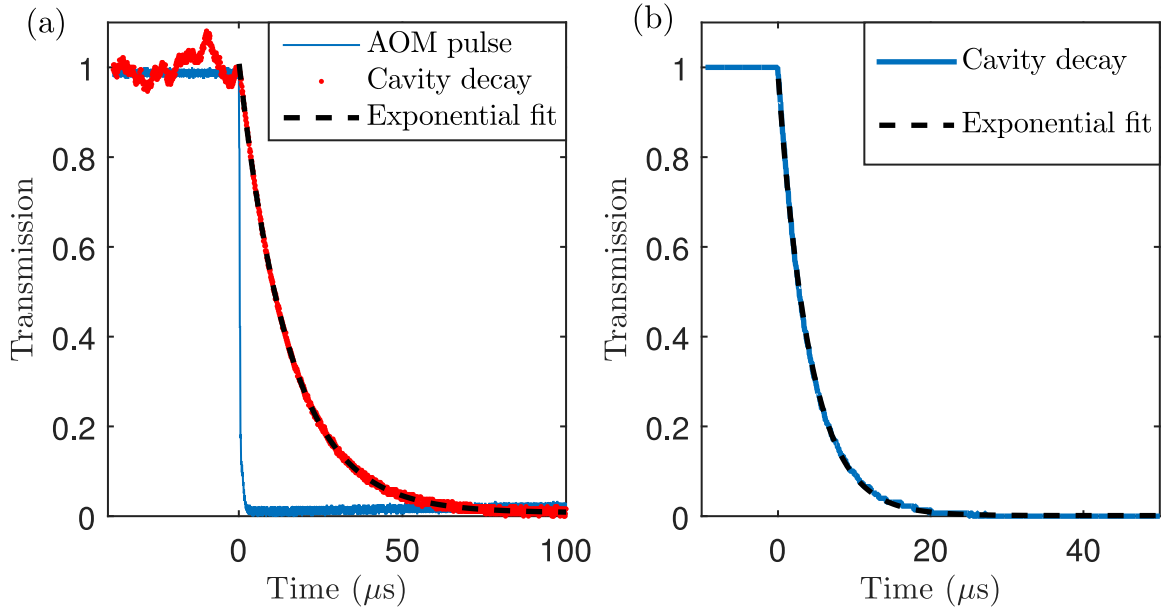


Figure 4.21: Ringdown measurements of the  $\text{TEM}_{00}$  cavity mode for (a) Qubit A laser at 852 nm giving a cavity build-up time of  $\tau_{\text{cav}} = 15.1(9) \mu\text{s}$  and (b) Rydberg A at 1018nm with a reduced cavity build up time of  $4.1(4) \mu\text{s}$ .

For a high-finesse cavity, one can approximate  $R \approx 1$  and according to Eq. 4.5 we can approximate  $\mathcal{F} \approx \pi/1 - R$ . Using Eq. 4.3, we can extract the ringdown decay time constant of the cavity

$$\tau_{\text{cav}} = \frac{\mathcal{F}}{\nu_{\text{FSR}}} = \frac{1}{2\pi\delta\nu_{\text{cav}}}. \quad (4.32)$$

The intra-cavity power will decrease exponentially such that  $P_{\text{cav}} = P_0 e^{-t/\tau_{\text{cav}}}$  with a characteristic time  $\tau_{\text{cav}}$  if we very quickly switch-off the incident light. This gives us a way to determine the cavity finesse  $\mathcal{F}$  given that we have a well known cavity length  $L$ .

We implement this measurement by using an incident power of  $200 \mu\text{W}$  in order to avoid damaging mirror coatings due high intra-cavity power that can potentially be of the order of a few Watts. Once Qubit A has been locked and a steady state field is achieved inside the cavity, an AOM is used to rapidly extinguish light incident on the cavity.

The transmitted light is recorded using our homebuilt photodiode (see Sec. 4.4.2) connected to an oscilloscope as shown in Fig. 4.21 (a). The first signal in blue

Parameters	Qubit A (852 nm)	Rydberg A & B (1018 nm)
Free spectral range $\nu_{\text{FSR}}$	1.49637(2) GHz	
Cavity length L	10.0173(1) cm	
Waist (plane mirror)	233 $\mu\text{m}$	254 $\mu\text{m}$
Cavity decay time $\tau_{\text{cav}}$	15.1(9) $\mu\text{s}$	4.1(4) $\mu\text{s}$
Finesse $\mathcal{F}$	$1.42(8) \times 10^5$	$3.9(4) \times 10^4$
Cavity linewidth $\delta\nu_{\text{cav}}$	10.5(4) kHz	38.5(2) kHz
Ideal transmitted power	4.36 %	1.55 %
Experimental transmitted power	1.64 %	0.21 %

Table 4.3: Cavity parameters summary.

shows the AOM pulse extinction, allowing us to be sure that we are not limited by the response time of the AOM  $< 1 \mu\text{s}$ . The second signal in red represents the mean trace over 5 measurements and is called the cavity “ringdown”. This corresponds to an exponential decay of the transmitted light with a  $1/e$  cavity decay time of  $\tau_{\text{cav}} = 15.1(9) \mu\text{s}$  at 852 nm, resulting in a finesse  $\mathcal{F} = 1.42(8) \times 10^5$  and a cavity linewidth  $\delta\nu_{\text{cav}} = 10.5 \text{ kHz}$ . For purely reflective losses, the theoretical transmission [216] should be 4.36 %. The measured transmission of 1.64 % is lower due to imperfect mode-matching and absorption of the cavity spacer.

Due to technical reasons, we can’t switch off the Rydberg A laser with an AOM as we have done with Qubit A. The idea was first to lock one sideband at  $\nu_{\text{Offset}} = 300\text{MHz}$  with respect to a cavity mode of Rydberg A using the cavity offset-lock technique (see Sec. 4.4.2). Once locked to the cavity, we can extinguish the sideband with the frequency generator driving  $\nu_{\text{Offset}}$ , similarly to the role played by the AOM with Qubit A. By triggering the oscilloscope on the extinction of the sideband, we have recorded the transmitted cavity decay of the light. As expected from the coating specification, at 1018 nm a reduced time constant of  $4.1(4) \mu\text{s}$  is measured as illustrated Fig. 4.21 (b), corresponding to  $\mathcal{F} = 3.9(4) \times 10^4$  and  $\delta\nu_{\text{cav}} = 38.5 \text{ kHz}$ . Moreover, the measured cavity transmission of 0.21 % compared to the theoretical transmission of 1.55 % shows the increased losses for the 1018 nm light. All the cavity parameters are summarised in Tab 4.3.

## 4.6 Laser characterisation

The fundamental result from this part of the thesis is the measurement of the linewidth of the lasers using an heterodyne optical beatnote recorded using an RF spectrum analyser. The second one concerns the bandwidth of the cavity locking electronics achieved for the servo-loop feedback.

### 4.6.1 Beatnote measurement at 509 nm

To evaluate the performance of the lock electronics, we measure the in-loop photodiode signal using a RF-spectrum analyser (N9010A EXA Signal Analyser), as shown in Fig. 4.22 (a) for Rydberg A. Either side of the central feature, we observe a pair of high-frequency servo-bumps at 1.1 MHz, corresponding to the bandwidth of the fast current feedback. Meanwhile, if we want to measure the achieved laser's linewidth, one would register the signal recorded with a photodiode connected to a spectrum analyser. However, optical frequency are of the order of hundreds of Terahertz and the electronic components have a maximum achievable bandwidth of the order of a few tens of Gigahertz. Therefore direct measurement of laser linewidth for sub-kHz lasers is challenging and requires either multiple stable lasers, a narrow atomic reference, or sufficiently long optical fiber to perform self-heterodyne interferometry [217]. At 852 nm, we are unable to perform either comparison; however, using the two Rydberg lasers A and B the linewidth can be measured from an optical beat note at 509 nm.

Rydberg A is locked to the  $TEM_{00}$  mode of the ULE cavity while Rydberg B is locked to the  $TEM_{01}$ , with a frequency spacing of 221.4 MHz in the infrared. Indeed, due to imperfect mode-matching between the incident beam and the cavity (see Sec. 4.5.3), we are able visualise and discriminate between the mode  $TEM_{00}$  and  $TEM_{01}$  on the transmission photodiodes (see Fig. 4.13). This allows us to ensure that we are locking each lasers on the right mode.

Figures 4.22 (b) and (c) show the optical beat note recorded on a RF spectrum analyser with each trace the RMS average of 100 shots recorded with a 190 ms sweep time. Figure 4.22 (b) reveals secondary peaks at harmonics of 1.1 MHz

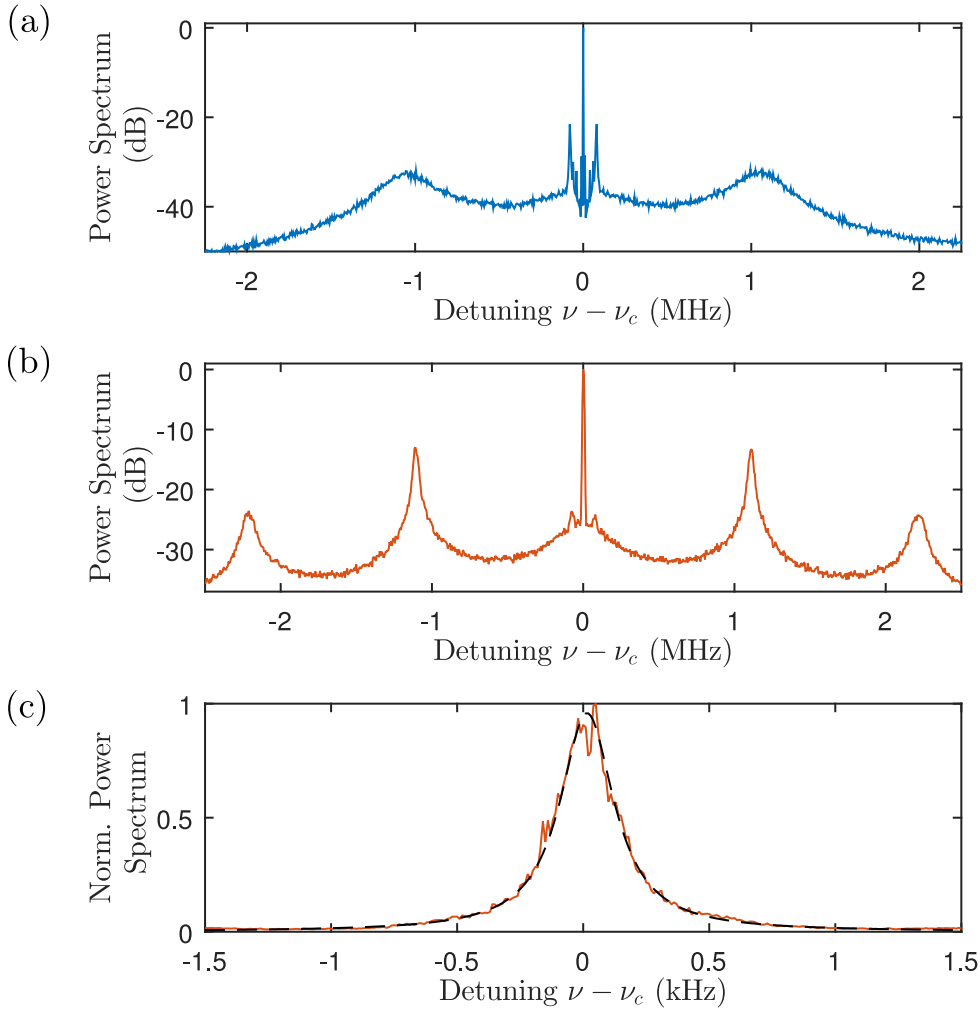


Figure 4.22: (a) In-loop error signal for Rydberg B plotted relative to the PDH frequency with 5 kHz resolution bandwidth (RBW) showing servo bandwidth at 1.1 MHz. (b) Optical beat note relative to  $\nu_c = 440$  MHz recorded at 509 nm between Rydberg A and B locked to consecutive  $\text{TEM}_{00}$  and  $\text{TEM}_{01}$  modes with 10 kHz RBW. (c) Linearized power spectrum recorded with 10 Hz RBW showing Lorentzian linewidth  $\text{FWHM} = 260(5)$  Hz. Data represent 100 rms averages using 190 ms sweep time.

corresponding to the fast-feedback servo-bumps for each laser. Fitting the central peak to a Lorentzian in Fig. 4.22 (c) returns a linewidth of 260(5) Hz relative to the cavity, from which we can estimate a linewidth of  $\sim 130$  Hz for each laser due to the fact that both lasers are locked using identical components. While this measurement may underestimate the linewidth due to common mode noise rejection from locking to a single cavity, this results in a 1018 nm linewidth  $< 100$  Hz with better performance expected at 852 nm due to the increase in cavity finesse by a factor four at this wavelength.

Our measurement has the drawback of being related to the cavity itself and doesn't correspond to an absolute measurement. Moreover, besides the instantaneous linewidth, there is a limit due to the long-term drift of the cavity arising from cavity aging. In Chap. 6, we evaluate this long-term drift using Rydberg EIT and take into account for future Rydberg state detection.

### 4.6.2 Analysis of the lasers performances

The use of a modulation frequency in the MHz range ( $\sim 10$  MHz) for realising the PDH error signal, provides a good immunity to low-frequency laser noise and low-frequency photodetector technical noise, while offering at the same time a high bandwidth feedback capability.

Most of the noise (to first order) like fluctuations of the input cavity power is falling as frequency increases [210], excepting the photon shot-noise which results from the discrete nature of light. It sets a limit on the laser frequency noise spectrum which is achievable using PDH locking. Because we are working on resonance, the photon shot-noise is related to the reflected sidebands. Considering that the average power falling on the high-bandwidth photodiode is  $2\mathcal{P}_s$ , the shot noise in the error signal has a flat spectrum (white noise) with a power spectral density given by [210]

$$S_\epsilon = 2h\nu(2\mathcal{P}_s) [\text{W}^2/\text{Hz}], \quad (4.33)$$

where  $\nu$  is the laser frequency. This can be converted, using the expression of the error signal in Eq. 4.22, in terms of frequency spectral density according to

$$S_f = \sqrt{\frac{h\nu}{16\mathcal{P}_c} \delta\nu_{\text{cav}}^2} [\text{Hz}/\sqrt{\text{Hz}}]. \quad (4.34)$$

For Qubit A laser at 852 nm, with our experimental parameters of  $\delta\nu_{\text{cav}} = 10.5$  kHz,  $\nu \approx 351.7$  THz and  $\mathcal{P}_c = 200 \mu\text{W}$ , we are shot noise limited to

$$S_f = 8.9 \times 10^{-5} [\text{Hz}/\sqrt{\text{Hz}}]. \quad (4.35)$$

It is impossible to get a better frequency resolution by using feedback control on the laser. A full description of other possible noise contributions, like the thermal noise arising from the Brownian motion on the spacer and the mirrors or the noise contribution from pressure and temperature fluctuations, can be found in [219]. However, given that we have relative lasers linewidth of  $\sim 100$  Hz and the limitations explained in Sec. 4.6.1, we didn't go into such a detailed description.

Converting the observed laser linewidth to gate fidelity is complex due to the error in a two-photon Raman transition being related to the relative phase noise between the two lasers [218], which due to their different wavelengths cannot be measured without performing gate operations on a single qubit. As the lasers are locked to a common cavity the correlations are also correlated, meaning the linewidths are not additive. However, using the available laser power, an effective two-photon Rabi frequency of  $\Omega_R/2\pi \sim 1$  MHz can be achieved with a few gigahertz intermediate detuning [107, 109, 117, 123, 125]. For a relative laser linewidth of 100 Hz, this results in an averaged gate error  $\epsilon = 10^{-5}$  when modelling the linewidth as a dephasing term following [89, 181]. Thus, the laser system is suitable for high-fidelity gates, with the laser-limited coherence time of 10's of ms, greatly exceeding the gate duration of the order of  $\sim \mu\text{s}$  timescale.

Nevertheless, the typical coherence time during Rydberg excitations is  $\sim 15 \mu\text{s}$  [123] and the dominant source of dephasing in our experiment is related to the high frequency noise coming from the servo-bumps [124, 125], as seen in-loop error signal of Fig. 4.22 (a). Around this broad peaks, the phase noise can even be amplified at high locking gain, which is highly detrimental for the Rydberg excitation coherence time. One approach to eliminate this phase noise, that has been followed by the Lukin's group, would be to optically filter those servo-sidebands from the laser spectrum [125, 220]. The cavity itself acting as a narrow bandpass optical filter, such that the transmitted light through the cavity gets a high spectral purity and suppresses the high-frequency noise by a factor  $\sim 4$  [125].

## 4.7 Summary

We have demonstrated sub-kHz linewidth lasers for Rydberg excitation with three lasers locked simultaneously to the same high-finesse ULE reference cavity. The lock configuration allows continuous tuning of the laser offset using the "electronic sideband" technique. After frequency doubling, we measure laser linewidth of  $\sim 130$  Hz at 509 nm, resulting in a 1018 nm linewidth  $< 100$  Hz with better performance expected at 852 nm due to the increase in cavity finesse. This results are suitable for performing coherent Rydberg excitation of single atom (see Chap. 7) and for future demonstration of high fidelity quantum gates (see Chap. 8).

# Chapter 5

## Cold Atom Experiment Setup

The ultimate goal of our project is to develop an hybrid quantum interface capable of performing generation, storage, and entanglement of optical photons using Rydberg atomic ensembles trapped above a superconducting coplanar microwave resonator. Key steps towards this goal include creating a cloud of cold atoms as well as performing single atom trapping and initialisation for applying quantum gates operations. In the first two sections of this chapter, the vacuum system as well as the main parts of our cold atoms experiment are presented. A more detailed description can be found in my colleague's thesis [221]. Thereafter, Sec. 5.3 reviews the two kind of imaging system implemented in the experiment. Section 5.4 describes the way to determine the atom number and the temperature of the MOT. Sections 5.5 and 5.6 explain single atom trapping and its characterisation in the microscopic optical dipole trap. Finally, the last section covers the atomic internal state preparation for implementation of either single or two-qubit gates.

### 5.1 Vacuum system

In contrast to pioneering work on cavity Quantum Electrodynamics (cQED), where the electromagnetic radiation is confined in a three dimensional resonator [185], we plan to bridge the world of neutral atoms with advanced superconducting circuits using coplanar waveguides (CPW). However, coplanar resonators are made of super-

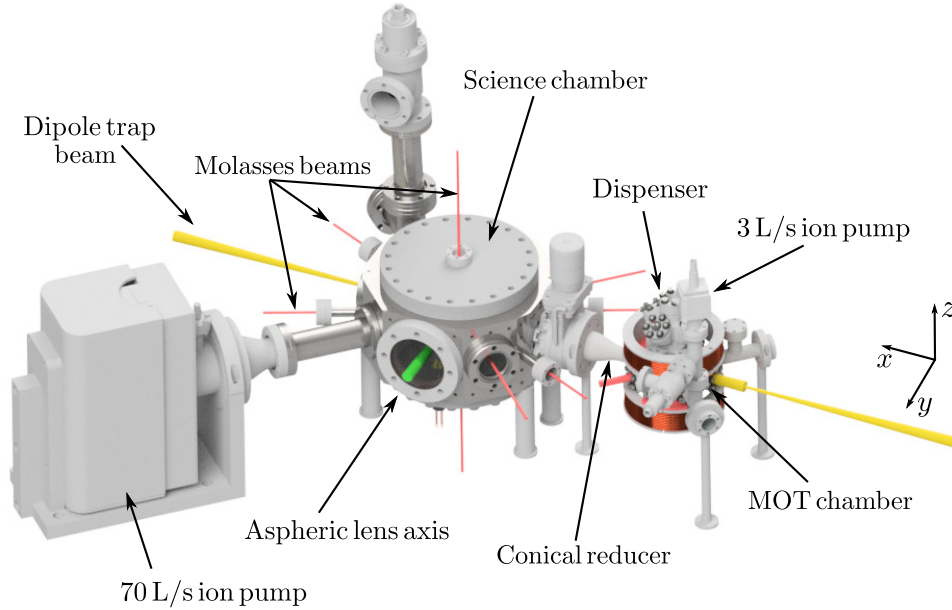


Figure 5.1: Overview of the vacuum system designed in a dual chamber configuration.  $^{133}\text{Cs}$  are loaded into the MOT from background vapour and transported over  $\sim 30$  cm to the science chamber using a 1064 nm dipole trap (yellow). Atoms are then transferred to  $1.8\ \mu\text{m}$  microscopic dipole traps using high-NA aspheric lenses while being cooled and imaged using three optical molasses beams (red). Two CF63 viewports are headed in the  $y$ -direction, creating large optical access for excitation beams (green)

conducting niobium that requires operation at cryogenic temperatures [222]. This breeds the necessity to create an experimental setup that allows compatibility between a cryostat and an ultra-high vacuum environment for cold atoms. For this reason, the vacuum system has been designed in a dual chamber system. Indeed, cold  $^{133}\text{Cs}$  atoms would stick to the wall of the chamber if they were directly loaded into a cryogenic environment as well as creating parasitic charges. The complete vacuum system is illustrated in the CAD drawing on Fig. 5.1.

A cold atoms experiment requires to work under *Ultra-high vacuum* (UHV) conditions to minimise collisions with background gas that would prevent single atom trapping or remove it from the trap. Our experimental setup consists of two distinct regions connected by a differential pumping tube (4 mm diameter and 10 mm length) creating a pressure ratio of  $\sim 10$ . The *high-vacuum* (HV) part called “MOT chamber”, which contains the source of  $^{133}\text{Cs}$  atoms, has a pressure of  $9.3 \times 10^{-9}$  mbar using a 3 L/s ion pump. The UHV part called “science chamber” is maintained at a

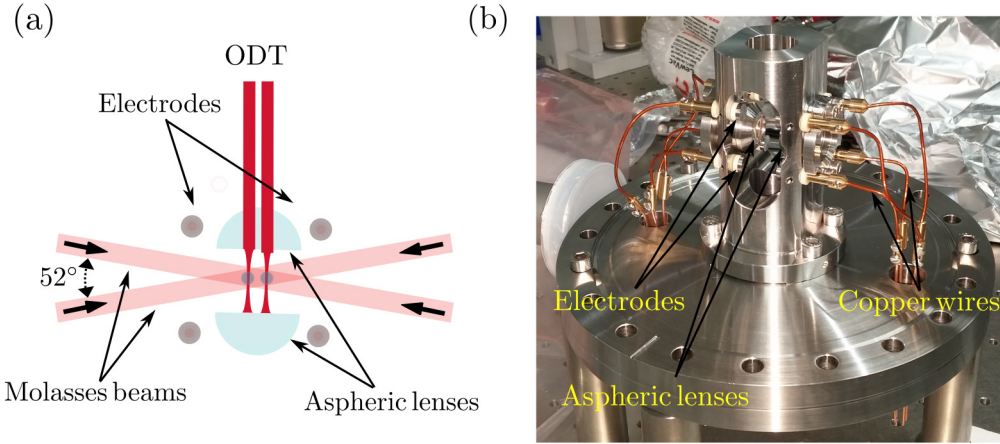


Figure 5.2: (a) Top view of the science chamber. Single atoms are trapped using two ODT beams focused down to  $1.8 \mu\text{m}$  using high-NA aspheric lenses (blue). Molasses beams (red) in the horizontal plane are doing a respective angle of  $52^\circ$  due to restricted access. (b) Electrode structure surrounding the high-NA lenses for active electric field compensation using a set of eight electrodes.

pressure of  $1.7 \times 10^{-10}$  mbar using a 70 L/s ion pump from Gamma Vacuum. The two chambers are sealed with an all-metal gate valve that allows isolation from each other and would preserve the vacuum in the MOT chamber when the cryostat will be added.

The science chamber is a large customized octagon chamber from the company Pink GmbH made of stainless steel 316LN with low magnetic permeability, to minimise material induced magnetic field, due to strong variations of the magnetic field. As shown in Fig. 5.1, the MOT chamber is connected to a CF40 to CF16 conical reducer that contains the differential pumping tube, itself connected to the gate valve leading to the science chamber. Combined to the opposite CF40 viewport of the science chamber, it allows for optical access of the dipole trap beam in the  $x$ -direction.

Due to the restricted optical access between the lenses contained in the science chamber, as shown in Fig. 5.1 and Fig. 5.2 (a), two molasses beams (see Sec. 5.2.1) are sent in the horizontal plane with a respective angle of  $52^\circ$ . This is combined with a third one that is using two CF16 viewports in the vertical  $z$ -direction. These three molasses beams allow for cooling and fluorescence imaging of single atoms. Finally, two CF63 viewports are headed in the  $y$ -direction, creating large optical access for

excitation beams. All the windows are anti-reflection (AR) coated on both sides at the principal wavelengths of our experiment (509 nm, 852 nm and 1064 nm).

### 5.1.1 Aspheric lenses

The single atom loading regime is conditioned by high two-body loss rates in the trapping volume of the science chamber [104]. This requires tight focusing ( $\sim \mu\text{m}^3$ ) of the optical dipole trap (ODT) beam at 1064 nm, only achieved with diffraction limited performances using numerical aperture (NA) of  $\sim 0.5$ . Furthermore, detecting the presence of the trapped atom as fast as possible is crucial for performing quantum information processing protocols, requiring to perform real time imaging. This stringent condition is realised with a high NA imaging system at 852 nm for collecting a large number of scattered photons from fluorescence imaging, increasing signal to noise ratio, hence detection efficiency. One solution would consist of using a long working distance microscope objective, as was done for sub- $\mu\text{m}$  addressing of single atom in optical lattices [223, 224]. However, this technique suffers from the fact that atoms have to be close to the vacuum window, which can be detrimental for Rydberg atoms that interacts with the surface [225, 226]. On the other hand, long working distance objective lenses allows to circumvent the close proximity of Rydberg atoms with the vacuum window [227] at the price of medium NA. Instead, we have implemented a solution based on high NA aspheric lenses located inside the science chamber, that have been designed in the group of Antoine Broweys [66, 67, 78, 167, 228, 229] at the Institut d'Optique, for simultaneously focusing the dipole trap beam as well as collecting single atom fluorescence. The two high NA aspheric lenses (Geltech 355561) have an effective focal length  $f = 10.1$  mm and a working distance of 7.0 mm. The clear aperture of 12 mm leads to a NA of  $\sim 0.5$  at 852 nm. As shown in Fig. 5.2 (b), the lenses are held inside a stainless steel custom designed mount and maintained with a PEEK <sup>1</sup> washer associated to a stainless steel ring [221, 230].

---

<sup>1</sup> Polyether ether ketone

### 5.1.2 Passive and active control of the electric field

Rydberg atoms exhibit huge polarisabilities (see Sec. 2.1) that makes them extremely sensitive to stray electric field. As will be shown in Sec 7.2.5, the electric field control over the atom's environment in the science chamber is essential and will be performed in two ways. First, patch charges resulting from atoms accumulating on the dielectric surfaces of lenses [225, 226, 230] are responsible for stray electric fields that can fluctuate over time. This can be overcome by covering the lenses using an indium tin oxide (ITO) conductive layer of 200 nm, with coated surfaces grounded. However, the ITO coating is not index matched with the aspheric lenses, resulting in transmission of 87%, 72%, 79% at 852 nm, 509 nm and 1064 nm respectively. Moreover, as illustrated in Fig 5.2 (b), an electrode structure is surrounding the high NA lenses inside the science chamber for active electric field compensation. It is implemented using a set of eight individually controllable electrodes arranged in two rings quarter-split and placed symmetrically around the science chamber centre.

## 5.2 Laser cooling

Reaching the regime of single atom manipulation using optical tweezers breaks down to three parts. The first part is based on laser cooling and trapping of atoms using light-matter interactions and more precisely, the force acting on the atoms when illuminated by a laser radiation. This force is the sum of two components [231]. The first component, called the radiation pressure force, is due to scattering of light as well as an asymmetry between absorption of the laser field and random spontaneous emission. The second component is the dipole force, a conservative force that can be derived from a potential and is proportional to the field gradient. Using the dissipative radiation pressure force will allow us to tackle the first challenge which consists in getting a cold atomic sample using a Magneto-Optical Trap (MOT) [21].

### 5.2.1 Working principle of the magneto-optical trap (MOT)

The scattering rate resulting from the interaction of an atom with a laser beam characterised by its wavevector  $\mathbf{k}_L$  is given by  $R_{\text{sca}} = \rho_{ee}^{ss} \Gamma_e$  with  $\rho_{ee}^{ss}$  the steady state solution of the OBE for the two-level atom given by Eq. 3.16a and  $\Gamma_e$  the natural linewidth. After substitution, one obtains [11, 21]

$$R_{\text{sca}} = \frac{\Gamma_e}{2} \frac{s_0}{1 + s_0 + 4\left(\frac{\Delta - \mathbf{k}_L \cdot \mathbf{v}}{\Gamma}\right)^2}, \quad (5.1)$$

where  $\mathbf{v}$  is the atomic velocity,  $\Delta$  is the detuning from resonance such that  $\Delta = \omega - \omega_0$  with  $\omega_0$  the atomic resonant frequency,  $\Omega$  is the Rabi frequency on the cycling transition and  $s_0 \equiv I/I_{\text{sat}} = \frac{2\Omega^2}{\Gamma_e^2}$  is the on-resonance saturation parameter defined by the ratio of the laser intensity to the saturation intensity with

$$I_{\text{sat}} = \frac{\hbar \omega_0^3}{12\pi c^2} \Gamma_e. \quad (5.2)$$

From Eq. 5.1 and considering the laser light is red-detuned from the atomic transition such that  $\Delta < 0$ , one observes that atoms will preferentially diffuse photons counter-propagating with the direction of motion. By scattering a photon from the laser, the atom experiences a force  $\mathbf{F} = R_{\text{sca}} \hbar \mathbf{k}_L$ , leading to a momentum kick imposed to the atom in the direction of the laser light. Linearising the force of two counterpropagating lasers around  $v = 0$  leads to a friction force  $\mathbf{F} = -\beta \mathbf{v}$  [232] where  $\beta$  is a positive constant when  $\Delta < 0$ . Thus, the motion of the atom can be damped towards  $v = 0$  for negative detuning. Subsequently, the atomic deexcitation is achieved via random spontaneous emission, leading to a second momentum transfer of the atom averaging to zero. Hence, an optical molasses made of three orthogonal pairs of counter-propagating laser beams slightly red detuned with respect to an atomic transition allows damping of the atomic motion, cooling the atoms in three dimensions. However, in order to trap the atoms, one needs to add a position-dependent restoring force. This can be realised using a quadrupole magnetic field, creating a confinement of the atoms towards the region of zero magnetic field. The minimum cooling limit arises from a stochastic mechanism between laser cooling



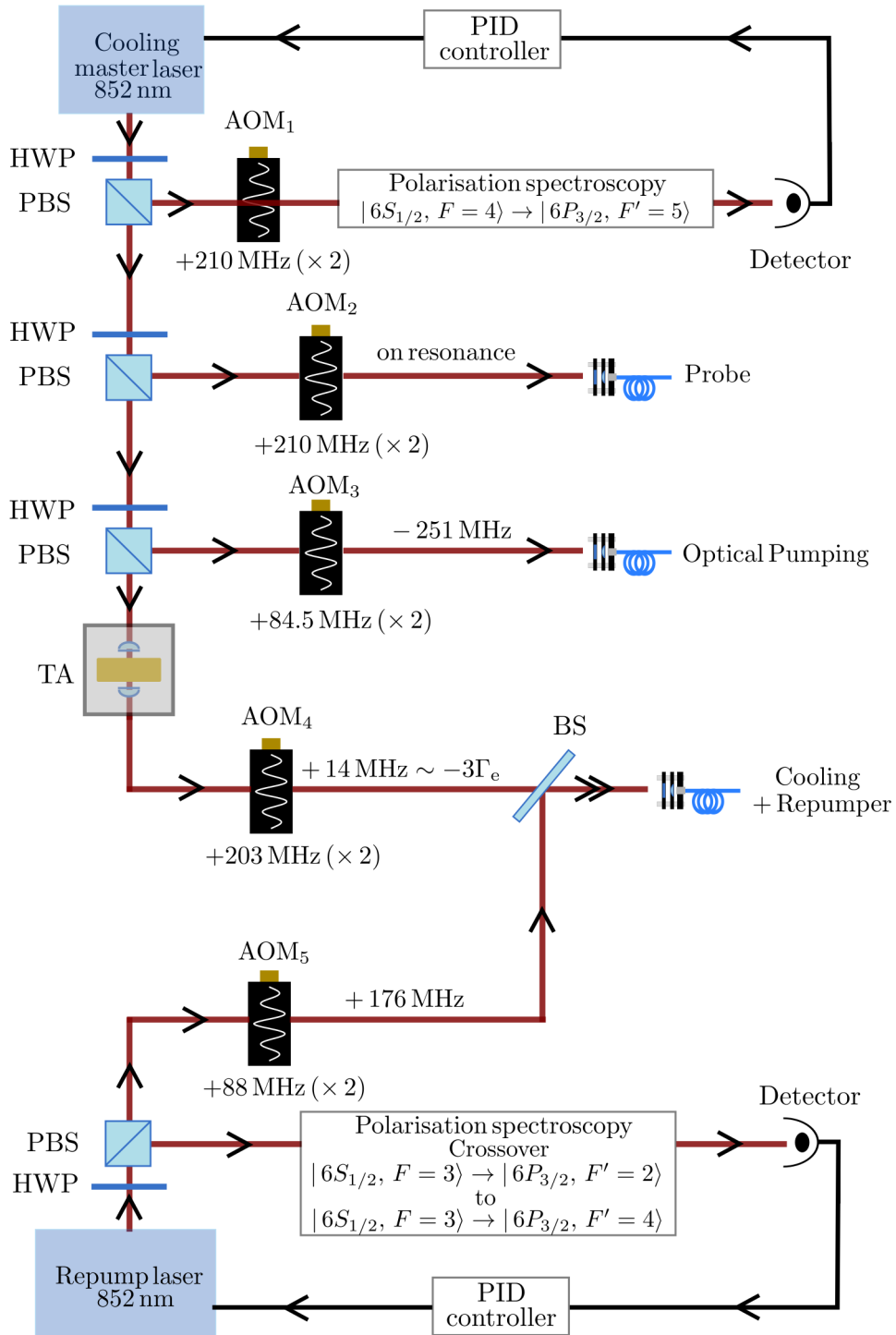


Figure 5.4: Overview of the cooling laser system. A master laser (ECDL) is locked via polarisation spectroscopy and amplified using tapered amplifier (TA). The beam is split in three arms for probe, optical pumping, and cooling light. Each arm uses an AOM in double-pass configuration in order to control laser frequency and beam intensity before being sent to the experimental table via polarisation maintaining (PM) fiber. A second ECDL provides repump light, which is combined with the cooling beam on a 50:50 non-polarising beamsplitter with the same polarisation before being delivered to the science and MOT chambers. Key : PBS = Polarising beam splitter, HWP = Half wave plate, BS = Beam splitter, TA = Tapered amplifier, AOM = Acousto-optic modulator.

time of 30.47 ns, giving a maximum scattering rate of  $\Gamma_e/2 = 2\pi \times 2.61$  MHz. The saturation intensity  $I_{\text{sat}}$  is 1.1 mW/cm<sup>2</sup> when driving  $|F = 4, m_F = \pm 4\rangle \rightarrow |F = 5, m_F = \pm 5\rangle$  closed transitions with  $\sigma^\pm$  circularly polarised light [160] but, taking into account of all the different  $m_F$  states and polarisations [235], leads to an averaged value of 2.7 mW/cm<sup>2</sup> [160].

### Cooling laser system

Our cooling master laser is an home-made ECDL (Thorlabs L852P150) locked via polarisation spectroscopy on the  $|6s\ ^2S_{1/2}, F = 4\rangle \rightarrow |6p\ ^2P_{3/2}, F' = 5\rangle$  transition, as explained in the next section, and red-detuned by 420 MHz via an acousto-optical modulator (AOM<sub>1</sub>) in double-pass configuration using the +1 diffraction order and a centre frequency of 210 MHz. Using a combination of polarising beam splitters (PBS) and half-waveplates (HWP), the beam is splitted into three independent arms as shown in Fig. 5.4. Each arm uses an AOM in double-pass configuration in order to control laser frequency and beam intensity, whilst preserving the direction of the outgoing laser beam when the driving frequency is changed. We have also added mechanical shutters on each laser beam paths in order to avoid stray beams when AOMs keep being turn on.

The first path is dedicated to the creation of the probe beam for fluorescence imaging (see Sec. 5.3) and EIT measurements (see Chap. 6). This requires shifting the beam back to resonance with the cycling transition using the +1 diffraction order of AOM<sub>2</sub> and a centre frequency of 210 MHz. AOM<sub>3</sub> generates light in resonance with  $|6s\ ^2S_{1/2}, F = 4\rangle \rightarrow |6p\ ^2P_{3/2}, F' = 4\rangle$  for optical pumping using the +1 diffraction order with a centre frequency of 84.5 MHz, resulting in an effective red-detuning of - 251 MHz with the cycling transition. For EIT experiments on the cloud of cold atoms (see Sec. 6.2), probe and optical pumping beams can be coupled to two independent single mode polarisation maintaining (PM) fiber for being routed to the experimental table. However, in the case of single atom experiments, both beams are combined on a 50:50 beam splitter before being coupled to a common PM fiber. The third beam is used to seed a tapered tamplifier (TA) with 29 mW, generating an output power of 375 mW. Following power amplification, this beam picks up

a shift of 406 MHz using the +1 diffraction order of AOM<sub>4</sub> driven at a centre frequency of 203 MHz, giving an effective detuning of  $\sim -3 \Gamma_e$  with respect to  $|6s \ ^2S_{1/2}, F = 4\rangle \rightarrow |6p \ ^2P_{3/2}, F' = 5\rangle$  and creating the cooling beam for both science and MOT chambers.

Moreover, due to a small but non-zero probability for off-resonant excitation to  $|6p \ ^2P_{3/2}, F' = 4\rangle$  by the cooling laser, atoms can depump in the  $|6s \ ^2S_{1/2}, F = 3\rangle$  dark state via spontaneous emission and will neither be cooled nor trapped. Hence, we need to apply a second laser called “repump laser” locked on the  $|6s \ ^2S_{1/2}, F = 3\rangle \rightarrow |6p \ ^2P_{3/2}, F' = 4\rangle$  transition to bring the atoms back to the cycling transition. The repumper is a second home-built ECDL (Thorlabs L852P150) locked using polarisation spectroscopy on the crossover between  $|6s \ ^2S_{1/2}, F = 3\rangle \rightarrow |6p \ ^2P_{3/2}, F' = 2\rangle$  and  $|6s \ ^2S_{1/2}, F = 3\rangle \rightarrow |6p \ ^2P_{3/2}, F' = 4\rangle$  transitions, due to a better signal-to-noise ratio of this transition. The repump beam is passing through AOM<sub>5</sub> in double-pass configuration with a centre frequency of 88 MHz using +1 diffraction order, picking up a shift of 176 MHz. With this configuration the repump is shifted back to resonance with  $|6s \ ^2S_{1/2}, F = 3\rangle \rightarrow |6p \ ^2P_{3/2}, F' = 4\rangle$  and is combined with the cooling beam on a 50:50 non-polarising beamsplitter with the same polarisation before being delivered to the science and MOT chambers through a single mode PM fiber as detailed in Fig. 5.4.

### Polarisation spectroscopy

Polarisation spectroscopy is a sub-Doppler spectroscopic technique [236] in which birefringence is induced in an atomic medium by a circularly polarised pump beam, and interrogated with a counterpropagating weak probe beam. As illustrated in Fig. 5.5 (a), a thick glass window (GW) picks off a fraction of the laser beam to split the beam into two counterpropagating beams called the probe and pump beams. The beams overlap inside a 71.5 mm Cs reference vapour cell. The polarisation angle of the probe beam is rotated of  $45^\circ$  with respect to the PBS using a half-waveplate ( $\lambda/2$ ), such that in absence of the pump beam, the two arms will have equal intensities and the differential photodiode will have a nulled signal. A quarter-waveplate ( $\lambda/4$ ) converts the pump beam light to circular polarisation. The two

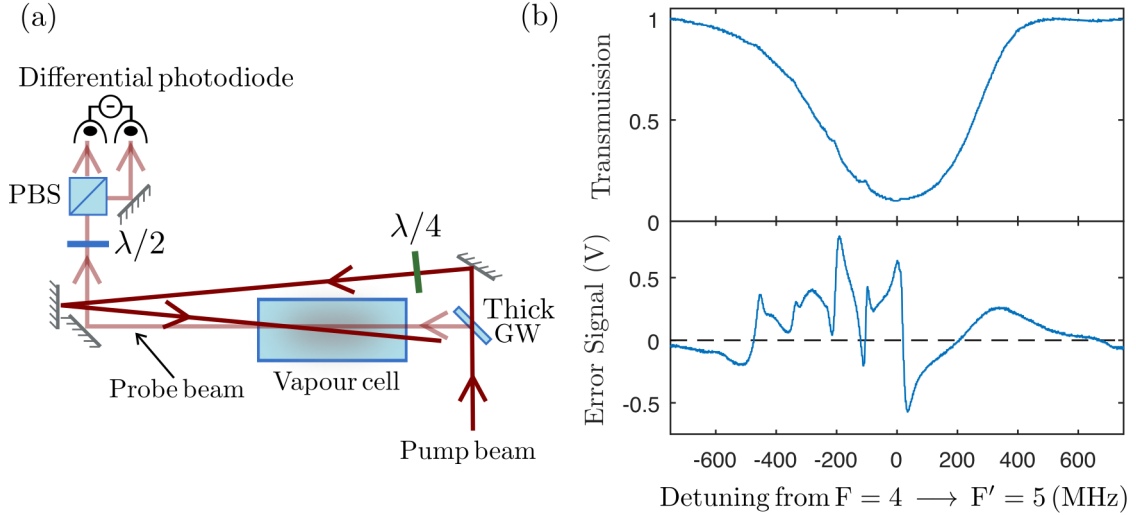


Figure 5.5: (a) Experimental layout for polarisation spectroscopy. A thick glass window (GW) picks off a fraction of the laser beam to split the beam into two counterpropagating beams called the probe and pump beams. The beams overlap inside a 71.5 mm Cs reference vapour cell. The polarisation angle of the probe beam is rotated of  $45^\circ$  with respect to the PBS using a half-waveplate ( $\lambda/2$ ) and a quarter-waveplate ( $\lambda/4$ ) converts the pump beam light to circular polarisation. (b) At the top, we observe an absorption spectrum on the  $|6s\ ^2S_{1/2}, F = 4\rangle \rightarrow |6p\ ^2P_{3/2}, F' = 3, 4, 5\rangle$  for the probe laser alone. At the bottom, one can see the error signal obtained by the differential photodiode in the presence of the pump beam.

output beams from the PBS are subtracted with the differential photodiode to obtain a polarisation spectrum. Figure 5.5 (b) shows at the top an absorption spectrum on the  $|6s\ ^2S_{1/2}, F = 4\rangle \rightarrow |6p\ ^2P_{3/2}, F' = 3, 4, 5\rangle$  for the probe laser alone and at the bottom, the error signal obtained by the differential photodiode in the presence of the pump beam.

### MOT setup

A caesium dispenser from SAES mounted on an electrical feedthrough, located on top of the MOT chamber, provides a background gas for loading of the MOT. The typical current used for heating the dispenser is 3.1 A. The cooling lasers emerge out of the collimator on the optical table. Two independent beams are created using a PBS and a HWP for controlling the power balance between the science chamber and the MOT chamber. The MOT beam is magnified using a 1:5 telescope to a  $1/e^2$  radius of 4.7 mm, in order to trap the maximum of atoms. One third of the power is sent vertically to the MOT chamber using HWP and PBS. The remaining power

is split equally into two perpendicular paths with another combination of HWP and PBS. Each of the three beams are retroreflected and include two quarter-waveplates (QWP) fixed at the correct polarisation for creating the MOT.

The confining quadrupole magnetic field is created by two circular coils in an anti-Helmholtz configuration in the MOT chamber, producing a vertical magnetic field gradient of 1.11 G/cm/A. In addition, cancellation of stray magnetic field is achieved by three pairs of rectangular compensation coils arranged in Helmholtz configuration, surrounding both chambers and providing 1 G/A.

### 5.3 Imaging system performance

Experiment diagnostics are based on absorption or fluorescence imaging. These two imaging procedures either require a resonant probe beam locked on the closed transition or the molasses beams respectively.

#### 5.3.1 MOT chamber imaging

We use absorption imaging [237] to diagnose the atoms number and go back to the temperature of the atomic cloud in the MOT. This technique is based on the resonant absorption of light at low intensity by atoms. Shining a probe laser tuned to resonance with the cycling transition leads to absorption from the atomic cloud, resulting in a shadow in the beam. By imaging the probe beam on a charge-coupled device (CCD) camera and measuring its loss of intensity, one can retrieve the number of atoms in the cloud. According to the Beer-Lambert law, the light intensity profile reaching the camera, situated in the the  $x - z$  plane, is given by

$$I(x, z) = I_0(x, z) \exp\left(- \int n(\mathbf{r}) \sigma(\Delta) dy\right), \quad (5.3)$$

where  $I(x, z)$  is the intensity in the  $x - z$  plane,  $I_0(x, z)$  is the intensity in the  $x - z$  plane without the atomic cloud,  $\Delta$  is the detuning with respect to the closed transition,  $n(\mathbf{r})$  is the atomic cloud density and  $\sigma(\Delta)$  is the scattering cross section.

Experimentally, the probe pulse duration is 100  $\mu$ s with a power of 2  $\mu$ W. The

probe  $1/e^2$ -radius of 5 mm is much larger than typical radial width of  $\sigma_r \sim 200 \mu\text{m}$  of the cloud at our range of temperature, ensuring the condition  $I \ll I_{\text{sat}}$ . Three consecutive images are necessary. The first one is taken with atoms, giving  $I(x, z)$ , while the second one is done without atoms and corresponds to  $I_0(x, z)$ . Finally, a third image without atoms or the probe laser beam is taken, allowing subtraction of the background noise  $I_{\text{bg}}(x, z)$ .

In the limit of low saturation ( $I \ll I_{\text{sat}}$ ) and at resonance ( $\Delta = 0$ ), one can make the assumption that  $\sigma(\Delta) = \sigma_0$ , where  $\sigma_0 \equiv 3\lambda^2/2\pi$  corresponds to the on-resonance scattering cross section.

By integrating along the  $y$ -axis, the density becomes the column density defined by

$$\int n(\mathbf{r}) dy = -\frac{1}{\sigma_0} \ln \left( \frac{I(x, z) - I_{\text{bg}}(x, z)}{I_0(x, z) - I_{\text{bg}}(x, z)} \right) = \frac{N(x, z)}{A(x, z)}, \quad (5.4)$$

where  $N(x, z)$  is the number of atoms in a column of the cloud and  $A(x, z)$  is the corresponding area of this column. One can rearrange the above expression to give the number of atoms

$$N(x, z) = \frac{A(x, z)}{\sigma_0} \ln \left( \frac{I_0(x, z) - I_{\text{bg}}(x, z)}{I(x, z) - I_{\text{bg}}(x, z)} \right). \quad (5.5)$$

The camera used for absorption imaging of the MOT is a charge-coupled device (CCD) camera (DMK 33G445 GigE) from Imaging Source. This camera offers a resolution of  $1280 \times 960$  with a pixel size of  $3.75 \times 3.75 \mu\text{m}$  and it is operating with a  $\times 5$  magnification to give an effective field of view of  $4.8 \times 3.6 \text{ mm}$ , allowing to image an atomic cloud expansion (see Sec. 5.4.2) up to 10 ms. The calibration of the camera, which has been realised using an attenuated laser beam at 852 nm and an AOM for fast switching ( $< 1 \mu\text{s}$ ), is shown in Fig 5.6. It allows us to verify the linearity of the total counts as a function of the number of photons for different gain settings and to deduce the calibration factor of the camera

$$\kappa = \frac{14.3}{10^{G/20}} \text{ photons/counts}, \quad (5.6)$$

where  $G$  represents the camera gain. All the subsequent experimental acquisitions

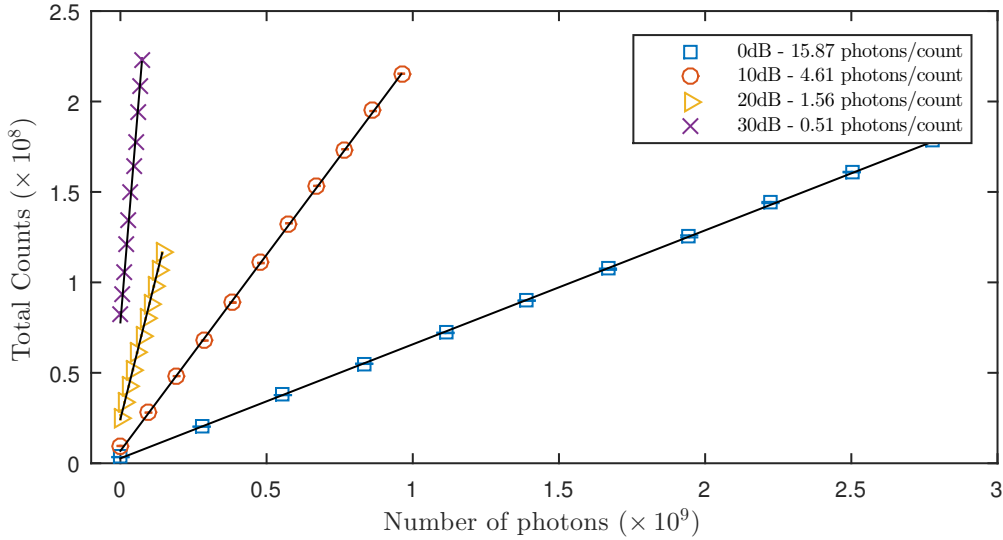


Figure 5.6: MOT chamber CCD camera calibration using an attenuated laser beam at 852 nm and an AOM for fast switching. We verify the the linearity of the total counts as a function of the number of photons and have decided to operate experimental acquisitions with a 10 dB gain, corresponding to 4.61 photons/count.

in this thesis have been operating with a 10 dB gain, corresponding to 4.61 photons/count. The trigger delay has been evaluated to  $5.1 \mu\text{s}$  whilst the minimum delay to separate two consecutive pulses is 76.2 ms.

### 5.3.2 Science chamber imaging

The camera used for real time imaging is a scientific complementary metal-oxide semiconductor (sCMOS) camera from Andor, model Zyla 5.5-USB. Single atom imaging requires both spatial and number resolution using fluorescence imaging, resulting from the collection of a finite number of scattered photons using high-NA aspheric lenses (see Sec. 5.1). Typical EMCCD Camera used to collect fluorescence in laboratories need for an amplification stage that increases clock induced noise charge [238] and can only perform global readout, limiting the imaging speed. We have decided to take advantage of an sCMOS camera with the possibility to read out independently each pixels for speeding up imaging as well as allowing superior signal-to-noise ratio (SNR) at intermediate incident photon rates  $\sim 10$  photons/ms/atom. The camera offers a large sensor size with a resolution of  $2560 \times 2160$  pixels and

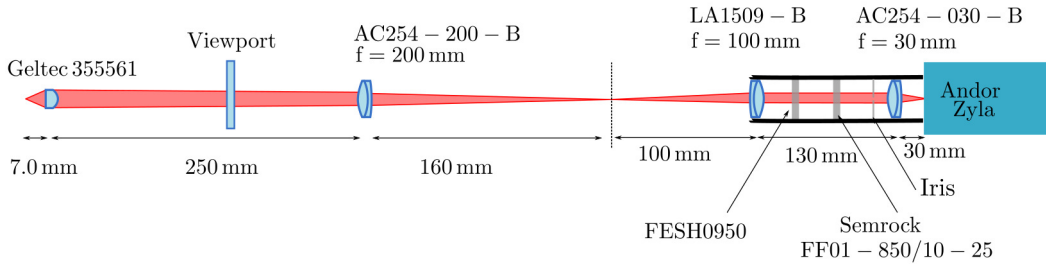


Figure 5.7: Science chamber optics to image atoms trapped in microscopic ODT. The atoms sit at the focal plane of the high NA-lenses ( $f = 7.0$  mm) where the collected fluorescence is focused outside of the chamber using an achromatic doublet with focal length of 200 mm. The intermediate image is transmitted through a relay telescope to decrease the magnification and enables filtering in the Fourier plane via an iris. A bandpass filter centred around 852 nm and a shortpass filter with a cut-off wavelength of 950 nm allow to filter out light at the 1064 nm. The imaging system gives sub- $\mu\text{m}$  spatial resolution in the atom plane and high sensitivity single atom detection.

a  $6.5 \times 6.5 \mu\text{m}$  pixel size. The imaging system is located in the  $x - z$  plane. The camera allows to work using either 12 bits or 16 bits and gives the choice to have a readout speed of 200 MHz or 560 MHz. We have used the Global shutter mode with 200 MHz readout speed and 12 bit low noise with a median noise of  $2.2 e^-$  RMS. At our imaging wavelength of 852 nm, the quantum detection efficiency is 22 % with imaging performance comparable to EMCCD camera for medium photon rates of  $\sim 100$  photons/pixel. The camera calibration returns  $\sim 2$  counts/photons in the 200 MHz - 12 bit low noise setting.

Figure 5.7 gives an overview of the imaging system used to collect fluorescence from single atom onto the sCMOS camera sensor. The working distance from the atoms to the high NA aspheric lenses (Geltec 355561) is 7.0 mm and the lens radius is 6.0 mm. The collection efficiency of the imaging lens is  $\Omega/4\pi \sim 5.4\%$ . After passing through the CF40 vacuum viewport and a dichroic mirror to decouple it from the dipole trap light, the fluorescence light at 852 nm is focused using a 200 mm focal length achromatic doublet (Thorlabs AC254-200-B) situated 250 mm away from the aspheric lens, giving a paraxial magnification of  $-20.5$  according to Zemax calculations. The intermediate image is transferred through an image relay to decrease the magnification. The relay telescope has been calibrated precisely using a negative USAF 1951 resolution test chart. It consists in a N-BK7 plano-convex lens

(Thorlabs LA1509-B) with focal length 100 mm and a 30 mm focal length achromatic doublet (Thorlabs AC254-200-B) both mounted into a tube screwed onto the C-mount port of the Zyla camera. The lens separation has been set to 130 mm in order to realise a confocal 2f-2f telescope. This configuration enables filtering in the Fourier plane via a calibrated iris mounted within the lens tube in front of the final doublet. The relay telescope gives a magnification of - 0.3, yielding a net magnification of  $M = + 6.2$  between the object plane in the chamber and the image plane on the Zyla camera sensor chip, corresponding to  $\sim 1 \mu\text{m}/\text{pixel}$  and a total field of view of  $\sim 100 \mu\text{m}$ . Furthermore, a pair of filters have been added in the tube, a band pass interference filter centred at 850 nm with a bandwidth of 10 nm (Semrock FF01-850/10-25) to allow only 852 nm light coming onto the camera and a shortpass filter with a cut-off wavelength of 950 nm (Thorlabs FESH0950) to filter out light at the 1064 nm trapping wavelength, leading to a total imaging system detection efficiency of 3.5 %. Finally, the characterisation of the blurring of our camera has been evaluated through measurement of its point spread function (PSF). We have found a sub-pixel size for the PSF of only  $4.6 \pm 0.5 \mu\text{m}$ , corresponding to a sub- $\mu\text{m}$  spatial resolution in the atom plane and allowing high sensitivity single atom detection.

## 5.4 Characterisation of the MOT

Using the absorption imaging setup, one can determine various parameters of the atomic cloud in the MOT chamber such as the loading rate, the number of atoms, the temperature as well as the size of the atomic cloud.

### 5.4.1 MOT loading rate

The rate at which the number of atoms  $N$  changes in the MOT is connected to the loading rate ( $R$ ), the loss rate ( $N/\tau$ ) due to collision with background gas and the term describing two-body collisions between trapped atoms ( $\beta \int n^2(\mathbf{r}) d^3\mathbf{r}$ ), according to the differential equation [239]

$$\frac{dN}{dt} = R - \frac{N}{\tau} - \beta \int n^2(\mathbf{r}) d^3\mathbf{r}, \quad (5.7)$$

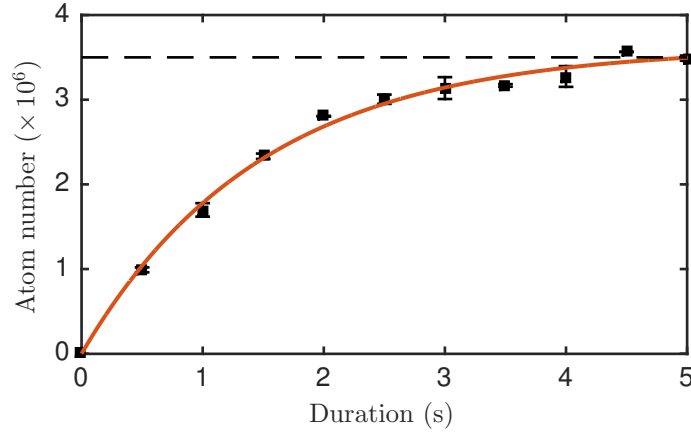


Figure 5.8: MOT loading curve giving a characteristic loading time  $\tau = 1.5$  s and a steady-state atom number of  $3.5 \times 10^6$ .

where  $N$  describes the number of atoms in the MOT and  $\tau$  is the characteristic loading time. One can neglect the two-body decay rate  $\beta$  compared to the single-body decay rate  $1/\tau$ , due to low atomic density of the MOT region and the fact that predominant loss appears through collisions with background gas due to a pressure of  $\sim 10^{-9}$  mbar. This leads to an exponential growth of the MOT atom number given by

$$N(t) = N_s (1 - e^{-\frac{t}{\tau}}), \quad (5.8)$$

where  $N_s$  describes the steady-state atom number. Various parameters had to be optimised for maximising the MOT atom number and a detailed analysis can be found in [221]. A total cooling power of 65 mW and repump power of 6.5 mW are split equally between the three arms of the MOT. A detuning of  $\Delta \sim -3 \Gamma_e$  combined with a magnetic field gradient of 13 G/cm have been identified as the optimal parameters for the MOT atom number.

Figure 5.8 shows a loading curve corresponding to the number of atoms in the MOT as a function of time. Equation 5.8 has been fitted to the data, providing a value of  $\tau = 1.5$  s and a steady-state atom number of  $3.5 \times 10^6$ . It takes approximately 4 s to saturate the MOT atom number. However, all subsequent experiments have been done for a load time of 1 s. This speeds up the experimental duty cycle because we are only interested in single atom loading in the UHV science chamber.

### 5.4.2 MOT temperature

Following the loading of the MOT for 1 s, an additional phase of “optical molasses” is applied to further reduced the temperature using sub-Doppler polarisation gradient cooling (PGC) [231]. The quadrupole coils are switched-off, the cooling beam intensity is reduced to  $I = 0.1 I_{\text{sat}}$  per beam, the repump is turned-off and the detuning is increased to  $\Delta = -15 \Gamma_e$  for a period of 10 ms.

The standard method for measuring the temperature of cold neutral atoms is to measure the expansion rate of the cloud of atoms released from the trap in free fall by taking an image for different ballistic expansion time  $\Delta t$ , called time of flight (TOF) imaging technique [240]. Assuming that the spatial distribution of the atoms is a Gaussian at any time, the rms size of the cloud after expansion follows the equation

$$\sigma_i^2 = \sigma_{0,i}^2 + \frac{k_B T}{m} \Delta t^2, \quad (5.9)$$

where  $i = x, y, z$  corresponds to indices in each directions,  $\sigma_{0,i}$  are the initial rms widths,  $T$  is the temperature of the cloud and  $m$  is the atomic mass of caesium.

By varying the expansion time  $\Delta t$ , we extract a temperature of  $T = 3.0 \pm 0.2 \mu\text{K}$  from a linear fit of  $\sigma_i^2$  as a function of  $\Delta t^2$ , resulting in an atom cloud with a Gaussian rms width of  $\sigma_r \sim 170 \mu\text{m}$ .

## 5.5 Optical transport

Once atoms are cooled and trapped, they must be transported from the MOT chamber to the science chamber over a distance of 30 cm in order to reach the single atom regime. This is achieved using an optical dipole trap (ODT), implemented for the first time by Chu *et al.* [241] on sodium atoms, allowing us to transfer atoms through the differential pumping tube thanks to the tight confinement of the atomic cloud offered along the transverse direction.

### Dipole force

Previously, the radiation pressure force relying on scattering of photons has been introduced but another component arises from the interaction between an induced electric dipole and the laser beam. The in-phase component of the atomic dipole leads to a radiation force called “dipole force”, coming from the AC Stark shift of an atom driven by a far-detuned laser field. The light shift acts as a potential  $U_{\text{dip}} \propto I/\Delta$ , creating a conservative force proportional to the intensity gradient of the applied field according to  $\mathbf{F}_{\text{dip}} = -\nabla U_{\text{dip}}$ . For a red detuned laser, the atom is trapped at the point of highest intensity. To obtain the requisite field gradient, a Gaussian laser beam is strongly focused with a waist  $\omega_0$ , achieving an optical dipole trap. However, the out of phase component of the atomic dipole leads to the scattering force  $\propto I/\Delta^2$ . Thus, one needs to work with large detuning to reduce the scattering rate responsible for heating, while increasing the intensity for maintaining the requisite trap depth.

The trap potential is given by [177]

$$U_{\text{dip}}(r, x) = -\frac{U_0 \exp[-2r^2 / \omega(x)^2]}{1 + (x/x_R)^2} \quad (5.10)$$

where  $\omega(x) = \omega_0 \sqrt{1 + (x/x_R)^2}$  is the  $1/e^2$  intensity radius along the propagation axis  $x$ ,  $x_R = \pi\omega_0^2/\lambda$  denotes the Rayleigh length and  $U_0 = U(r=0, x=0)$  is the trap depth.

Around its minimum  $U_0$ , the trap potential has radially a Gaussian behavior with a radius  $\omega_0$  compare to the Lorentzian behavior in the longitudinal  $x$ -direction with a radius  $x_R$ . For atoms with energy low enough compared to  $U_0$ , one can approximate the potential by a 3D harmonic potential and make a Taylor expansion of Eq. 5.10 around  $r = x = 0$ , so that

$$U_{\text{dip}}(r, x) \approx -U_0 \left[ 1 - 2\left(\frac{r}{\omega_0}\right)^2 - \left(\frac{x}{x_R}\right)^2 \right], \quad (5.11)$$

leading to radial and longitudinal trap oscillation frequencies given by

$$\omega_r = \sqrt{\frac{4U_0}{m\omega_0^2}} \text{ and } \omega_x = \sqrt{\frac{2U_0}{mx_R^2}}. \quad (5.12)$$

For typical waist size of tens of microns, radial trap frequencies are two order of magnitude higher than the axial ones, resulting in an elongated shape of the cloud along the transport axis.

### Transport setup

Dipole trap can be easily realised at 1064 nm due to high power lasers available. This light is strongly detuned from  $D_1$  and  $D_2$ -transitions of caesium and thus the scattering of this light is strongly suppressed. The ODT light is provided by a Nd:YAG laser operating at 10 W. After being sent through an 80 MHz AOM for fast switching control, the ODT beam is expanded to 1.9 mm before being focused to a waist of  $\omega_0 = 42.3 \mu\text{m}$  using a lens with focal length  $f = 200 \text{ mm}$ . The beam focus can be moved from the MOT chamber to the science chamber over 30 cm using a set of 2 mirrors on a translation stage coupled to a relay telescope, keeping the waist constant during the optical transport [221].

To load the dipole trap, the MOT has to be overlapped with the focus of the trapping beam. The experimental sequence consists in loading the MOT for 1s, followed by an overlap time of 50 ms between the MOT and the ODT beam, resulting in  $10^5$  trapped atoms with an efficiency of  $\sim 10\%$ . We then apply a molasses phase of 20 ms by turning the magnetic field off to cool atoms at  $10 \mu\text{K}$  and let atoms that are not trapped falling away of the dipole trap. Finally, the atoms are adiabatically transported towards the science chamber in 800 ms.

The lifetime of the atoms in the ODT of 4.9 s [221] has been determined by varying the time atoms are held in the trap, which is found to be predominantly dominated by collision with background collisions gas. The axial frequency has been evaluated by applying a kick with the trap laser light along the  $x$ -optical axis using the translation stage. As a result, the atoms oscillate around the bottom of the potential in the same direction with an axial frequency  $\omega_x/2\pi \sim 8 \text{ Hz}$  for 6.8 W of trapping laser power, corresponding to a large spatial extension of  $2 \sigma_x \sim 4.4 \text{ mm}$ . The

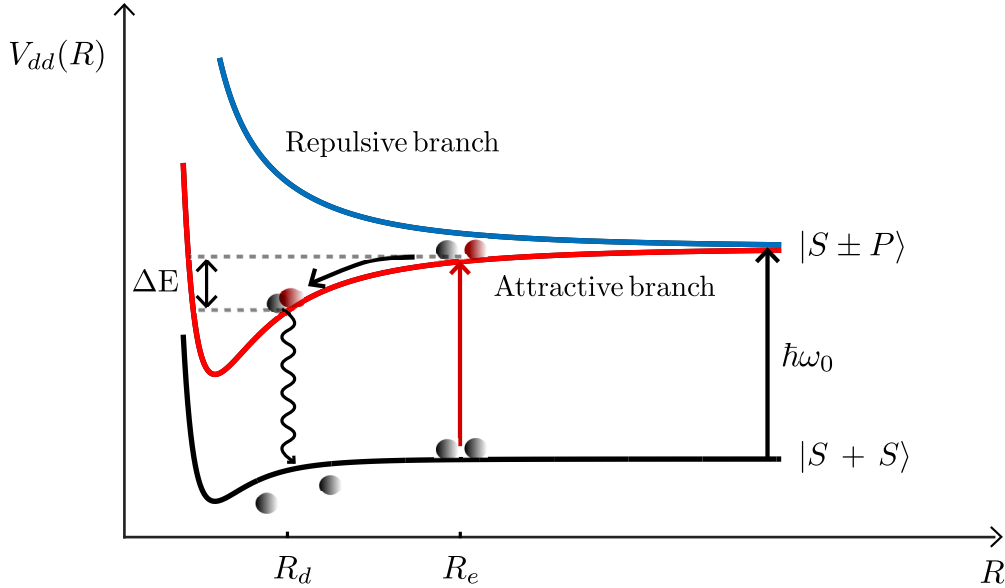


Figure 5.9: Schematic of light assisted collisions in a microscopic dipole trap. At intermediate inter-atomic distance  $R_e$ , the two-atom ground state  $|S + S\rangle$  is excited to the state  $|S \pm P\rangle$  through absorption of one photon, experiencing an attractive potential for red-detuned light. Atoms accelerate towards each other and if the kinetic energy  $\Delta E$  gained before the excited state radiates back to the ground state is such that  $\Delta E/\hbar \gg U_0$ , both atoms are ejected together from the trap.

radial frequency is obtained via parametric heating [242] where the trap amplitude is modulated and results in atom loss at twice the trap frequency. The deduced radial frequency is  $\omega_r/2\pi \sim 1.1$  kHz at 4 W, leading to tight radial confinement of the atomic cloud over  $2\sigma_r \sim 14$   $\mu\text{m}$ .

## 5.6 Single atom trapping

The last challenge to enter into the single atom regime consists in loading microscopic optical dipole traps from the ODT. Single atom trapping uses a technique developed by Schlosser *et al.* [71, 104] called "collisional blockade", which exploits the regime where the trapping volume is in the order of few  $\mu\text{m}^3$  and the two-body light-assisted collisions rate  $\beta$  (inversely proportional to the trapping volume) becomes the predominant term during the loading of the trap, ensuring only 0 or 1 atom in the trap.

### 5.6.1 Light assisted collisions

The mechanism by which one can trap single atom in microscopic ODT requires to introduce energy dissipation through light-assisted collisions (LAC) [71, 104]. This interaction involves a change of internal structure of the atoms via inelastic collisions and can be understood as follows.

We consider two identical atoms separated by a distance  $R$ , with a ground state  $|S\rangle$  and the first excited state  $|P\rangle$ . For large inter-atomic distance, the two-atoms ground state denoted by  $|S + S\rangle$  weakly interacts via vdW interactions of the form  $V(R) = C_6/R^6$ . Moreover, it can reach the first excited state  $|S \pm P\rangle$  through absorption of one photon of energy  $\hbar\omega_0$ , as illustrated in Fig. 5.9. At intermediate inter-atomic distance, while the ground state interaction potential can still be neglected, the first excited state interacts through resonant dipole-dipole interaction. This induces a splitting of the potential between a repulsive and an attractive branch, as represented in Fig. 5.9. The asymptote take the form  $\hbar\omega_0 \pm C_3/R^3$  corresponding to negative or positive detuning respectively. In our experiment, we will deal with negative detuning, thus we will focus on the attractive interaction between the excited atom-pair. In this case, atoms accelerate towards each other until desexcitation can occur via spontaneous emission. If the kinetic energy  $\Delta E$  gained before the first excited state radiates back to the ground state is such that  $\Delta E/\hbar \gg U_0$ , both atoms are ejected together from the trap. This regime of “collisional blockade” [71] ensures that 50 % of the time the trap is empty and the remaining 50 % only one atom is loaded. This processus is stochastic but can reach  $\sim 90\%$  single atom loading efficiency via blue detuned light on the  $D_1$ -transition that introduces a coupling on the repulsive branch of the two-atom resonant dipole-dipole interaction [238].

### 5.6.2 Single atom loading

After the optical transport, single atom trapping occurs in two steps. First, atoms are overlapped with a pair of tightly focused optical traps during 60 ms using molasses beams at an intensity  $I = I_{\text{sat}}$  per beam and a detuning of  $\Delta = -6\Gamma_e$  [221], for loading multiple atoms into each of the microscopic dipole traps. In order to

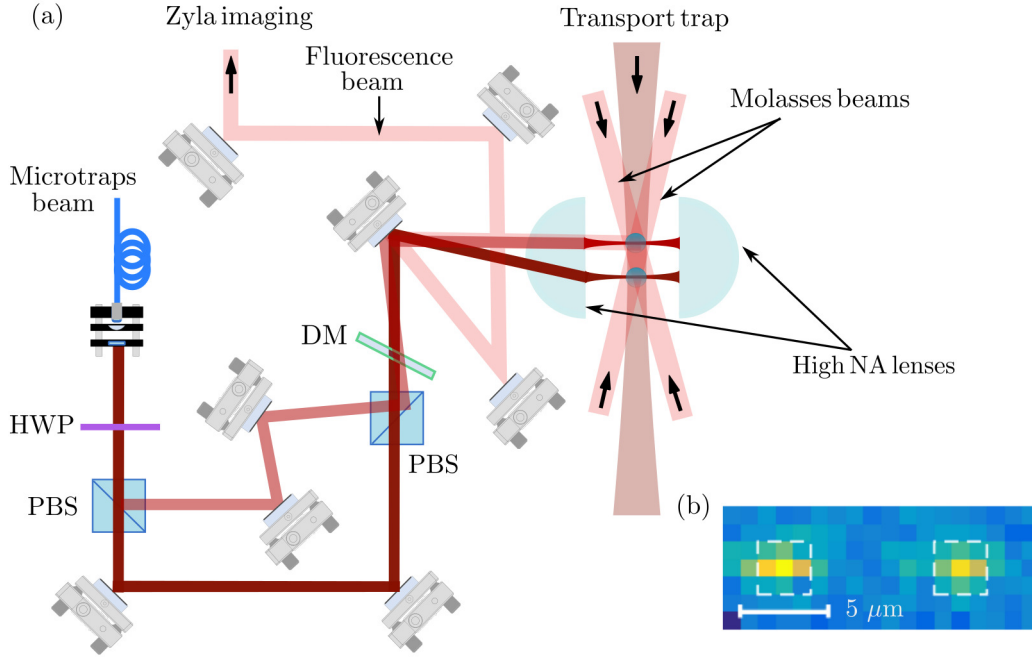


Figure 5.10: Optical layout for the creation of two microscopic ODT and fluorescence imaging. Two dipole trap beam paths are created using one half-waveplate (HWP) and a polarising beamsplitter (PBS). The beams are recombined using another PBS and strongly focused ( $1/e^2$  radius of  $1.85\ \mu\text{m}$ ) by the high-NA aspheric lens for trapping single atoms. The same aspheric lens collects the fluorescence at  $852\ \text{nm}$  from the trapped atoms and a dichroic mirror (DM) allows to separate it from the  $1064\ \text{nm}$  trapping light. Finally, the fluorescence is sent towards the imaging system for real-time imaging. (b) Single shot imaging of two single atoms separated by  $10\ \mu\text{m}$ .

avoid AC stark shift induced by the ODT beams, the cooling light is modulated out of phase with the ODT at a rate of  $1\ \text{MHz}$  with  $35\ \%$  duty cycle. Finally, a single atom loading phase is performed using cooling beams at an intensity  $I = 0.5 I_{\text{sat}}$  per beam and a detuning of  $\Delta = -8\Gamma_e$  [243], allowing to take advantage of LAC to ensure that only 0 or 1 atom is present in the traps.

Each trap is formed by focusing a dipole trap beam ( $\lambda = 1064\ \text{nm}$ ) through the high NA lenses inside the vacuum chamber to a waist of  $1.85\ \mu\text{m}$ . The trapping light is delivered from a commercial narrow-linewidth and low-noise laser from the company Coherent (Mephisto). In order to control the intensity of the beam as well as switching time, the beam is passing through an AOM before being coupled to a single mode PM fiber. The output beam of the fiber is split in two paths using a combination of HWP and PBS, as shown in Fig. 5.10 (a), before being recombined to create two microscopic dipole traps with control over their mutual distance.

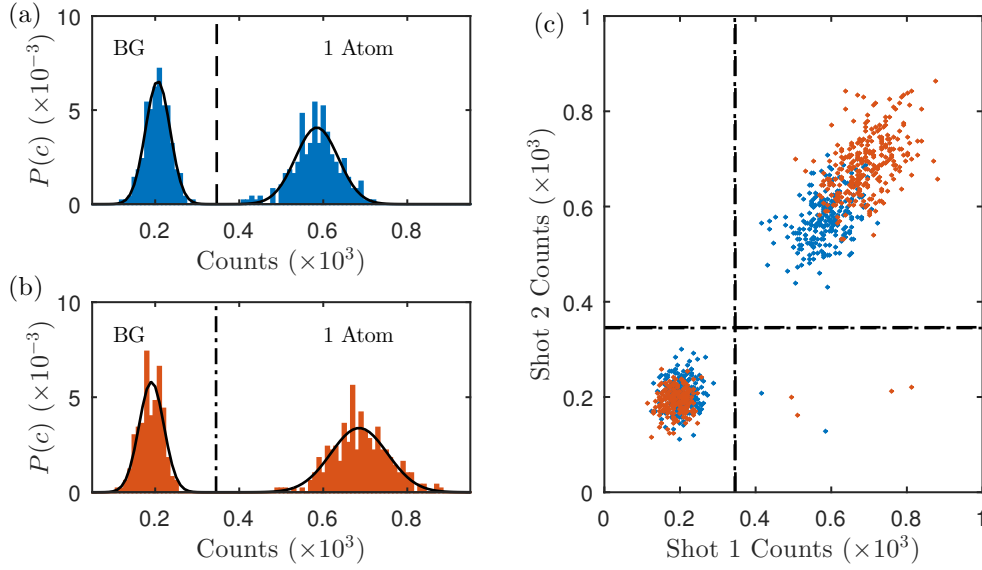


Figure 5.11: Probability distribution of counts obtained from 500 repeated measurements for (a) trap1 and (b) trap2 for an imaging time of 40 ms, showing two Poisson distributions for each traps corresponding to either 0 or 1 atom. (c) Correlations between two fluorescence readouts separated by 50 ms. The fluorescence of the second readout is plotted as a function of the fluorescence in the first readout showing distinct clusters which confirms single atom loading.

### 5.6.3 Single atom readout

Imaging single atom with accuracy requires high collection efficiency of the scattered photons coming from the cooling beams. The solution implemented in our experiment consists in using the same aspheric lenses under vacuum for focusing the ODT beam and collecting single atom fluorescence [104, 230], with an additional dichroic mirror (Thorlabs DMLP950) to separate both wavelengths, as shown in Fig. 5.10 (a).

In order to distinguish between background light and single atom fluorescence, one has to maximise the photon scattering rate  $R_{sc}$  (see Sec. 5.1) from the trapped atom. Although working on resonance would clearly achieved the best signal, we worked at a detuning  $\Delta = -3\Gamma_e$  with an intensity of  $I = 0.5I_{sat}$  [243] per beam to reduce heating associated with spontaneous emission, resulting in a scattering rate of  $\sim 440$  photons/ms and corresponding to a flux of  $\sim 14$  photons/ms at the camera detector. Figure 5.10 (b) shows fluorescence imaging of two resolved trapped atoms separated by  $10\ \mu\text{m}$  using a detection time of 40 ms and defining two regions of

interest (ROIs).

Figures 5.11 (a) and (b) shows the probability distribution of the counts obtained from 500 repeated measurements using the imaging parameters described above for each ROIs. One can identify a bimodal distribution of photon counts corresponding to the presence or absence of an atom in the traps. The two distributions are described by a Poisson distribution centred at two different mean count rates corresponding to either 0 or 1 atom loaded in the trap.

For most measurement cycles, an image is taken to confirm the presence or absence of an atom, followed by an experiment and a final image taken to measure the presence or absence of the atom. Figure 5.11 (c) shows correlations in the same ROI between counts in shot 1 and counts in a second shot taken 50 ms later. In both camera shots, we are detecting discrete fluorescence clusters corresponding to either 0 or 1 atom present in the traps. The top right quadrant corresponds to an atom present in both shots while the lower right quadrant corresponds to an atom initially loaded in shot 1 but having been lost by shot 2, allowing us to observe  $> 98\%$  retention probability [243].

However, during the experimental cycle, we are only interested in the results of the second image if an atom was present in the first. This requires us to post-select the data to only include measurements associated with successful loading. In depth explanations about this post-selection process and single atom readout performances are covered in [243] or my colleague's thesis [221].

#### 5.6.4 Characterisation of the single atoms in the ODT

Lifetime of the atoms in the microscopic optical dipole trap has been found of 8.7 s [221] at a trap depth of  $U_0 = 1$  mK, mainly limited by background collisions gases and atom's heating, thus well suited for performing future implementation of quantum gates protocols. Nevertheless, a complete characterisation of the single atoms requires to determine their temperature as well as their trapping frequencies.

### Single atom temperature

High temperature leads to dephasing from the atom exploring differential AC Stark shift of the trap [244], therefore it has to be minimised to maintain long coherence of single atomic qubits. While temperature determination using TOF technique works well on a sample with high number of atoms, where one can easily measure the velocity distribution of the cloud from an image, this technique becomes impractical to determine single atom distribution with enough signal to noise. Instead, the usual way to determine single atom temperature is to use a release and recapture technique [233, 245]. The trap is quickly turned off for a period of time  $t_{\text{drop}}$ , and the fraction of atoms that are recaptured is measured as the time  $t_{\text{drop}}$  is varied. The probability of recapture is reconstructed by repeating the sequence 100 times and the data are fitted using a Monte-Carlo simulation [245] to estimate the temperature. Figure 5.12 shows an example with simulations done for 1,3,5,7 and 10  $\mu\text{K}$ , from which we can estimate a single atom temperature of 5  $\mu\text{K}$ , allowing to reduce the effect of Doppler dephasing.

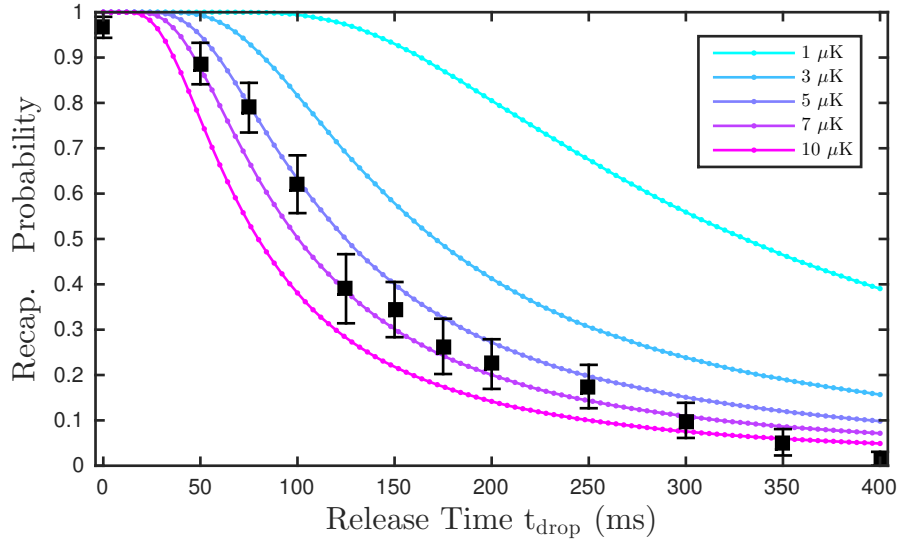


Figure 5.12: Single atom temperature determination using a release and recapture technique. Data are fitted using Monte-Carlo simulations and lead to a temperature of 5  $\mu\text{K}$ . Each point is an average over 100 sequences.

### Trap frequencies

Due to the tight focusing of the ODT beams for the single atom regime, we have used a new method initiated by [246] to measure more precisely the radial frequencies of the atoms in the microscopic dipole traps. After detection of the single atoms, the traps are switched off twice for a fixed period of time  $t_1 = t_2 = 20 \mu s$  separated by a variable delay  $\tau$  where the trap is kept on. The recapture probability of the atoms is measured as a function the variable delay  $\tau$ , which exhibits oscillations at twice the radial frequency. The experiment [221] is repeated over 100 trials and this results in a radial single atoms frequency of  $\omega_r/2\pi \sim 23 \text{ kHz}$  at a trapping power of 6.5 mW, yielding to a radial extent of  $\sigma_r \sim 0.3 \mu m$ . This allows us to deduce the trap waist using Eq. 5.12 to  $\omega_0 = 1.85 \mu m$  for both traps. The axial frequency is evaluated using the fact that

$$\omega_x = \frac{\lambda}{\sqrt{2} \pi \omega_0} \omega_r, \quad (5.13)$$

resulting in  $\omega_x/2\pi \sim 2.9 \text{ kHz}$  with a corresponding variance of the atom's position of  $\sigma_x \sim 2 \mu m$ . The tiny spatial extent explored by the trapped atom decreases beam pointing inhomogeneities that would result in Rabi frequency variations while applying the quantum gate pulse sequence [89].

## 5.7 Qubit state preparation

Atoms are distributed over all possible hyperfine states after the phase of optical molasses. However, EIT experiments on the MOT (see Chap. 6) and coherent control of a single atom (see Chap. 7) requires to prepare the ground state in a specific internal state. Therefore, one needs to apply standard methods of optical pumping which involves producing a magnetic field to define a quantisation axis and driving the atoms with polarised light.

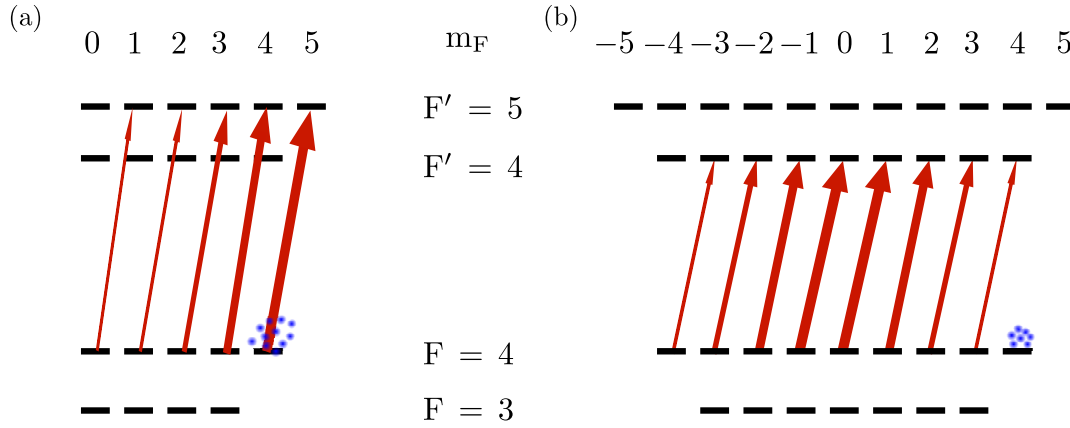


Figure 5.13: Optical pumping schemes for  $^{133}\text{Cs}$  to prepare atoms in the  $|F = 4, m_F = 4\rangle$  stretched state either using (a) bright state leading to heating or (b) dark state optical pumping with the transition-strengths represented by the arrow thickness.

### 5.7.1 Stretched state pumping

In the MOT chamber, the quantisation axis is defined by producing a magnetic field from the rectangular compensation coils arranged in Helmholtz configuration, surrounding both chambers and providing 1 G/A. However, for coherent control of single atoms, an extra pair of circular coils producing 1.3 G/A is added in the  $y$ -direction of the science chamber. It increases the magnetic field used for Zeeman shifting of the hyperfine states, allowing better energy state separations either for Raman transitions or Rydberg excitations.

In order to make a two-photon transition from the ground state to a Rydberg state, we would often need to take advantage of the maximum transition strength associated to the transition  $|6s\ ^2S_{1/2}, F = 4\rangle \rightarrow |6p\ ^2P_{3/2}, F' = 5\rangle$ , driven with  $\sigma^+$ -polarised light, requiring to pump atoms in the stretched state  $|F = 4, m_F = 4\rangle$ .

The first possibility would be to apply a “bright-state” optical pumping scheme, as shown in Fig. 5.13 (a). This would only require a pump beam derived from the cooling master laser driving  $|6s\ ^2S_{1/2}, F = 4\rangle \rightarrow |6p\ ^2P_{3/2}, F' = 5\rangle$  transition with  $\sigma^+$ -polarised light. However, it suffers from the fact that atoms pumped into the state  $|F = 4, m_F = 4\rangle$  would be continuously heated by scattering due to the pump beam itself.

In contrast, we have chosen a “dark-state” optical scheme that is set by the  $\sigma^+$ -polarisation of the driving field on the  $|6s\ ^2S_{1/2}, F = 4\rangle \rightarrow |6p\ ^2P_{3/2}, F' = 4\rangle$  transi-

tion, depicted on Fig. 5.13 (b). Indeed, this scheme imposes restriction on the fact that atoms falls into the  $|F = 4, m_F = 4\rangle$  stretched state with the additional gain of being no longer sensitive to the driving field. However, atoms can decay from the  $F' = 4$  state to the lower hyperfine ground state  $F = 3$ , which requires the repump beam for driving  $|6s\ ^2S_{1/2}, F = 3\rangle \rightarrow |6p\ ^2P_{3/2}, F' = 4\rangle$  transition.

### 5.7.2 Clock state pumping

In the case of single atom coherent excitation, atoms initialisation in the clock state  $|F = 4, m_F = 0\rangle$  will be a great advantage due to magnetic field fluctuations insensitivity of the transition between the clock states  $|F = 3, m_F = 0\rangle$  and  $|F = 4, m_F = 0\rangle$  at first-order.

This requires to drive the transition  $|6s\ ^2S_{1/2}, F = 4\rangle \rightarrow |6p\ ^2P_{3/2}, F' = 4\rangle$  with  $\pi$ -polarised light. Indeed, the transition  $|F = 4, m_F = 0\rangle \rightarrow |F' = 4, m_F = 0\rangle$  is dipole forbidden due to momentum selection rules but spontaneous emission happens randomly on different  $m_F$  states according to  $\Delta m_F = \{-1, 0, +1\}$ , thus accumulating atoms in the dark state  $|F = 4, m_F = 0\rangle$ .

## 5.8 Summary

Combining laser cooling and trapping techniques, we have created a cloud of cold atoms in a MOT that can be transported towards a science chamber, allowing to implement single atom trapping with high NA aspheric lenses and offering careful control of the surrounding electric field. Real-time single atom imaging with diffraction limited performances has been implemented using an sCMOS camera. Finally, using appropriate light polarisation, atoms can be initialised in a well defined internal state in both MOT and science chambers.

## Chapter 6

# Absolute Frequency Calibration of ULE Cavity

In Chap. 4, we described stabilisation of lasers to a high-finesse reference cavity. This transfers the stability of the cavity onto the lasers, however in order to quantify the absolute long-term stability of the laser frequencies we must perform an absolute measurement relative to a more stable reference.

Using the ULE cavity stabilised at the zero-CTE temperature  $T_c$  allows us to counteract thermal drifts and obtain narrow linewidth lasers at short timescales. However, the ULE cavity length drifts due to material aging which typically is on the order of the MHz per day [247]. Moreover, cavity resonant frequencies are not necessarily commensurate with the one required for Rydberg excitation. Thus, if we want to perform two-photon Rydberg excitation, one needs to quantify the ULE cavity mode frequencies drift over long timescales and calibrate it with respect to Rydberg transitions.

One way to measure the absolute cavity drift would be to operate a beatnote with an optical frequency comb [216], however we do not have this option. Another method is to measure the offset between the atomic and cavity resonant frequencies using electromagnetically induced transparency (EIT) (see Sec. 3.2.1). EIT is a suitable approach for detecting atomic Rydberg states, providing non-destructive optical detection [248], unlike micro-channel plate (MCP) which requires ionisation of the Rydberg atoms [249]. This gives us a stable atomic reference as well as calibrat-

ing the frequencies needed for off-resonant coherent Rydberg excitation. Moreover, measuring the drift of the resonant frequency condition for EIT will allow us to quantify the ULE aging drift.

## 6.1 Vapour cell EIT

To find the EIT resonances, we initially use a vapour cell and coarse frequency tuning over a wide range of coupling beam detuning  $\Delta_c$ .

### 6.1.1 Qubit A detuning with respect to the probe laser using $67D_{5/2}$ Rydberg state

Rydberg excitation via the caesium D<sub>2</sub>-line uses lasers at 852 nm (probe laser) and 509 nm (coupling laser), as described in Sec. 3.2.1. Relevant wavelengths can be calculated for transitions from the  $|6p^2P_{3/2}, F = 5\rangle$  state using energy levels [160] and Rydberg energies derived from Sec. 2.1. Due to the limitation of the TEC in the SHG cavity for Rydberg A, we cannot reach crystal temperatures for efficient doubling of wavelengths above 1018.5 nm, limiting operation to addressing Rydberg states with principal quantum number  $n \geq 60$ . The second SHG system for Rydberg B has been designed to give better heating range allowing access to Rydberg states with  $n \geq 49$ . However, the wavelengths calculated from the D<sub>2</sub>-line are valid for the case that the probe laser is resonant with the transition from

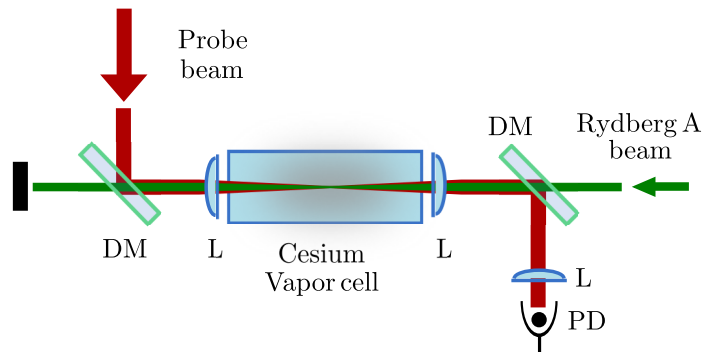


Figure 6.1: Schematic of EIT in vapour cell using counter-propagating Rydberg A (green) and probe (red) beams through a 71.5 mm Cs reference vapour cell. Key : L = Lens, DM = Dichroic mirror, PBS = polarising beam splitter, PD = Photodiode.

$$|6s \ ^2S_{1/2}, F = 4\rangle \rightarrow |6p \ ^2P_{3/2}, F' = 5\rangle.$$

For cold atoms, the two-photon resonance condition is achieved for  $\Delta_c = -\Delta_p$  [181, 184], as described in Sec. 3.2.1. Nevertheless, at a room temperature of 19°C, Cs atoms in a vapour cell have a most probable velocity of 191 m.s<sup>-1</sup>. This means that the Doppler effect becomes important due to the fact that atoms moving at different velocities experience different detuning [248]. The expression of the Doppler shift is  $\Delta_{\text{Doppler}} = -\mathbf{k} \cdot \mathbf{v}$ , where  $\mathbf{k}$  is the wavevector of the incoming beam, and occurs for components of the velocity along the beam axis. To account for the Doppler effects we must modify the susceptibility derived for atoms at rest in Eq. 3.27.

Considering that the number of atoms per unit of volume with velocity  $v$  is  $N(v)dv$ , their contribution to the total susceptibility is [181]

$$\chi(v)dv = \frac{i\mu_{eg}^2/\epsilon_0\hbar}{\gamma_{ge} - i\Delta_p - i\frac{\omega_p}{v}c + \frac{\Omega_c^2/4}{\gamma_{gr} - i(\Delta_p + \Delta_c) - i(\omega_p - \omega_c)v/c}} N(v)dv. \quad (6.1)$$

Given that atoms are at thermal equilibrium, the velocity can be described by a Maxwellian distribution and the atomic density for a given velocity class  $N(v)$  is given by

$$N(v) = \frac{N_0}{u\sqrt{\pi}} e^{-v^2/u^2}, \quad (6.2)$$

with the most probable velocity  $u = \sqrt{2k_B T/m}$ , where T represents the vapour temperature and m is the atomic mass.

To calculate the total susceptibility, we must integrate the optical response over all velocity classes [250] weighted by the Maxwell-Boltzmann distribution. This leads to inhomogeneous linewidth of the absorption line, with a Doppler width of  $\omega_{\text{Doppler}}/2\pi \sim 224$  MHz at room temperature on the Cs D<sub>2</sub>-line using  $\lambda = 852$  nm.

To reduce sensitivity to the Doppler-mismatch from the residual k-vector of the two-photon excitation, we use a counter-propagating configuration for probe and coupling beams, as shown in Fig. 6.1. Hence, an atom moving at velocity  $v$  towards the probe beam sees its frequency shifted by an amount  $\omega_p v/c$  and  $-\omega_c v/c$  with respect to the coupling beam, which leads to the relationship  $\Delta_c = -(\lambda_{852}/\lambda_{509})\Delta_p$

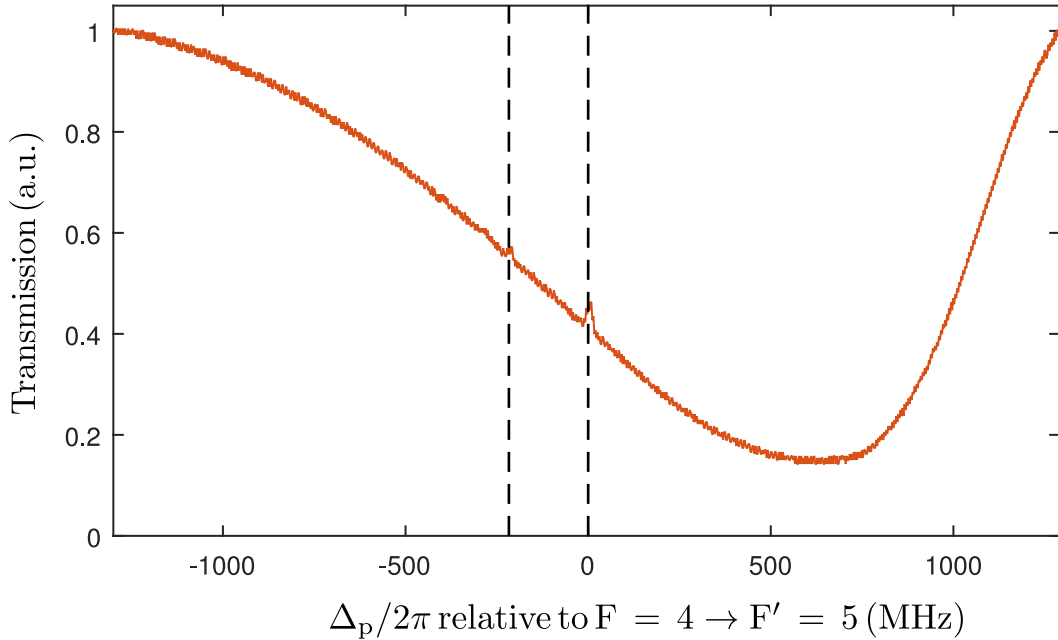


Figure 6.2: vapour cell EIT showing probe beam sweeping across the  $|6s\ ^2S_{1/2}, F = 4\rangle \rightarrow |6p\ ^2P_{3/2}\rangle$  and the appearance of  $67D_{3/2}$  and  $67D_{5/2}$  peaks separated by 225 MHz.

[181, 248]. Thus for a non-resonant probe laser, the vapour cell EIT occurs at a shifted frequency to that expected in cold atoms.

Initially, we perform EIT spectroscopy in a 71.5 mm Cs reference vapour cell at room temperature based on the  $|6s\ ^2S_{1/2}, F = 4\rangle \rightarrow |6p\ ^2P_{3/2}, F' = 5\rangle \rightarrow |67D_{5/2}\rangle$  transition. A schematic of the spectroscopy setup is drawn in Fig. 6.1. The probe laser is resonant with the transition from  $|6s\ ^2S_{1/2}, F = 4\rangle$  to  $|6p\ ^2P_{3/2}, F' = 5\rangle$ . As shown in Fig. 5.4, it is derived from the cooling master and can be set to  $\Delta_p = 0$  with a power of  $4\ \mu\text{W}$ . The coupling laser, Rydberg A, has a power of 220 mW. It can be scanned through the resonance using the electronic sideband technique (see Sec. 4.4.2), allowing for continuous frequency tuning of  $\Delta_c$  by locking to  $\nu_{\text{Offset}}$ .

In order to reduce Doppler broadening, the weak probe beam and counter-propagating coupling beam are carefully aligned using two irises. The higher the Rabi frequency  $\Omega_c$  of the coupling beam the larger will be the EIT amplitude [149, 184]. Thus, the probe and coupling beams are focused using two lenses of 150 mm focal length either side of the cell, giving a  $1/e^2$  radius of  $630\ \mu\text{m}$  and  $200\ \mu\text{m}$  respectively. The probe and the coupling beams are decoupled from each side of the cell using dichroic mirrors. The probe beam transmission is recorded with a photodiode allowing variable gain (Thorlabs PDA-36EC). As seen in Fig. 6.2, the

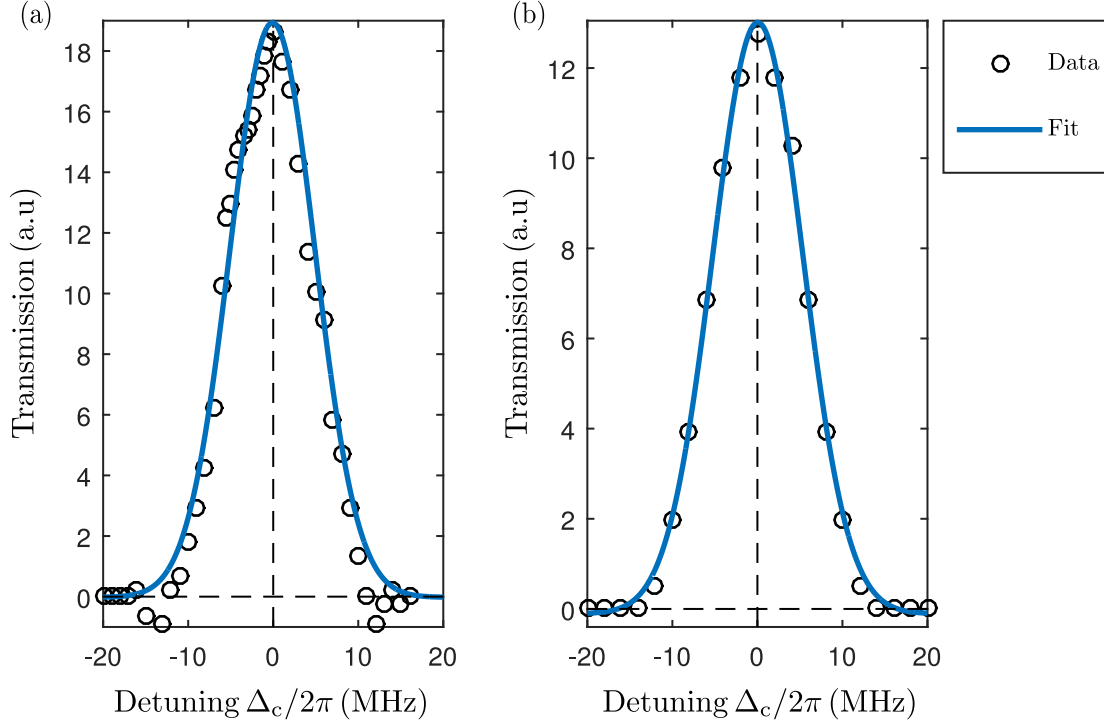


Figure 6.3: (a) EIT spectroscopy on  $67D_{5/2}$  Rydberg state with probe beam resonant on the transition  $|6s\ ^2S_{1/2}, F=4\rangle \rightarrow |6p\ ^2P_{3/2}, F'=5\rangle$  registering the EIT resonance at  $\nu_{\text{Offset } 1} = -430$  MHz. (b) EIT spectroscopy on  $67D_{5/2}$  Rydberg state with Qubit A registering the EIT resonance at  $\nu_{\text{Offset } 2} = -200$  MHz.

transmission lineshape shows two EIT peaks corresponding to the  $67D_{3/2}$  and  $67D_{5/2}$  Rydberg states.

We then record the EIT transmission for the Rydberg state  $67D_{5/2}$  by locking the probe laser and varying the coupling beam detuning  $\Delta_c$  with 0.5 MHz steps, which results in Fig. 6.3 (a). The EIT maximum corresponds to a coupling detuning  $\Delta_{C1} = 0$ . This is obtained for  $\nu_{\text{Offset } 1} = -430$  MHz while the wavemeter indicates an average frequency of  $\nu_{\text{Rydberg A}} = (294\,513\,580 \pm 30)$  MHz for the  $\text{TEM}_{00}$  mode of the coupling beam. The result is compatible with the theoretical frequency of  $\nu_{00\text{theo}}^{1018} = 294\,513\,141$  MHz.

The relatively large EIT linewidth of 12.5 MHz can be explained by power broadening, the fact that we are working in a magnetically unshielded environment and transit time broadening due to the finite time of interaction between the atoms with the laser beams. However, we are only interested in determining the EIT central frequency peak. Thus, we have preferred to increase the EIT amplitude than narrowing the EIT feature, as a first calibration test before cold Rydberg excitation.

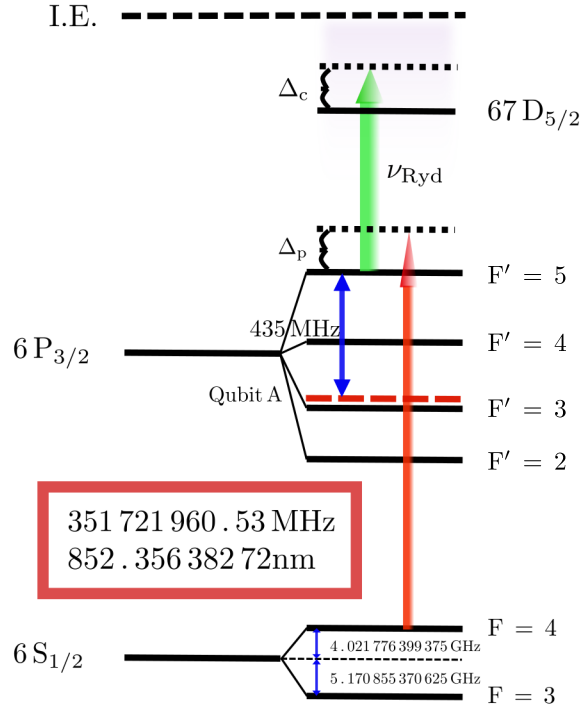


Figure 6.4: Detunings and fundamental cavity mode for Qubit A laser at  $\Delta_{00}/2\pi = -435\text{ MHz}$ .

The second spectroscopy is realised using Qubit A laser stabilised to the  $\text{TEM}_{00}$  mode of our high finesse ULE cavity. This laser is locked and shifted by 160 MHz using an AOM in double-pass configuration before being sent through the vapour cell. The EIT maximum is registered for  $\nu_{\text{Offset } 2} = -200\text{ MHz}$  as shown in Fig. 6.3 (b).

We deduce from this measurement that the Rydberg A detuning  $\Delta_c$  relative to Qubit A, such that

$$\frac{\Delta_c}{2\pi} = 2 \times (\nu_{\text{Offset } 2} - \nu_{\text{Offset } 1}) = 460\text{ MHz}. \quad (6.3)$$

This results in a value of

$$\Delta_p = -\frac{\lambda_{509}}{\lambda_{852}} \times \Delta_c = -2\pi \times 275\text{ MHz}. \quad (6.4)$$

This leads to a fundamental cavity mode for Qubit A laser at  $\Delta_{00}/2\pi = -435\text{ MHz}$ , as illustrated in Fig. 6.4. Thus for cold atoms experiment we require  $\Delta_c/2\pi = 275\text{ MHz}$ , whilst in a Doppler-broadened vapour cell we require  $\Delta_c/2\pi = 460\text{ MHz}$ .

### 6.1.2 Determination of accessible Rydberg states

Using the fact we have determined the free spectral range  $\nu_{\text{FSR}} = 1.49637(2)$  GHz of the ULE cavity in Sec. 4.5.2, we are now able to determine which Rydberg states we can reach. Indeed, Rydberg A laser frequency can be tuned in the range

$$\nu_{509} = 2\nu_{1018} = 2(m \times \nu_{\text{FSR}} \pm \nu_{\text{Offset}}), \quad (6.5)$$

using the sideband offset locking technique derived in Sec. 4.4.2 at  $\pm \nu_{\text{Offset}}$ , where  $m$  is the mode index of the cavity and  $\nu_{509}$  is the doubled IR Rydberg laser frequency. Whilst the sideband locking technique provides agility, the limited frequency range of  $\pm 450$  MHz due to low pass filtering of the DDS evaluation board means that between mode  $m$  and  $m + 1$  of the cavity, it is only possible lock in 60% of the available free-spectral range. Thus, with the present locking scheme, some Rydberg states cannot be utilised as they require a sideband frequency in the range 450 - 1050 MHz. The laser detuning is equal to

$$\frac{\Delta_c}{2\pi} = \nu_{509} - \nu_{\text{Ryd}} = 2(m \times \nu_{\text{FSR}} \pm \nu_{\text{Offset}}) - \nu_{\text{Ryd}}, \quad (6.6)$$

which can be rearranged to obtain

$$\nu_{\text{Offset}} = \left( \frac{\Delta_c}{2\pi} + \nu_{\text{Ryd}} \right) / 2 - m \times \nu_{\text{FSR}}, \quad (6.7)$$

where index  $m$  is chosen to minimise the magnitude of the sideband frequency. To improve the accuracy of this technique, the precision measurement of the  $67D_{5/2}$  state has been used to obtain an absolute measurement of the fundamental cavity mode as

$$\begin{aligned} \nu_{00} &= (\nu_{00\text{theo.}}^{509} + 2 \times \nu_{\text{Offset}1}) / 2 \\ &= 294.513571 \text{ THz}. \end{aligned} \quad (6.8)$$

All subsequent sideband frequencies are then calculated with respect to this value, in integer steps of the free spectral range. Rydberg states outside of the range of the AD9910 DDS evaluation board have been ignored.

The sideband frequencies required for locking to the relevant states have been decomposed in three cases according to

- i)  $\Delta_c/2\pi = 460$  MHz as for two-photon excitation using Qubit A laser in a vapour cell,
- ii)  $\Delta_c = \Delta_p = 0$  as for EIT in cold atoms configurations,
- iii)  $\Delta_c/2\pi = 275$  MHz as for two-photon excitation using Qubit A laser on cold atoms.

### 6.1.3 Experimental verification of Rydberg state frequencies

In order to verify if the theoretical frequencies derived from Sec. 6.1.2 match the experiment, we have made measurements on the Rydberg state  $68S_{1/2}$ . The expected Rydberg A sideband frequency for EIT conditions with the probe laser is  $\nu_{\text{Offset, probe theo.}} = -183.7$  MHz. However, the resonant frequency is found at  $\nu_{\text{Offset, probe exp.}} = -177$  MHz, giving a discrepancy of  $\delta\nu_{\text{Offset, probe}} = 6.7$  MHz. This can be related to the probe frequency variations derived from the MOT beam, that is locked using polarisation spectroscopy. When it comes to use Qubit A, we expect a theoretical sideband frequency of  $\nu_{\text{Offset, Qubit A theo.}} = 46.5$  MHz, which matches with the experimental one  $\nu_{\text{Offset, Qubit A exp.}}$ . This results mean that we can predict the expected Rydberg excitation frequencies quite accurately.

Finally, we have decided to move from nS state to nD state. Indeed, the coupling strength from  $6P_{3/2}$  to either  $nS_{1/2}$  or  $nD_{5/2}$  can be expressed in terms of the Rabi frequency  $\Omega = -\boldsymbol{\mu} \cdot \mathbf{E}/\hbar$ , which scales linearly with the dipole matrix element. For experiments where the coupling Rabi frequency is to be kept constant over a range of  $n$ , it is necessary to calculate the dipole matrix elements for the transition. Using the core potential and the energy of the  $6P_{3/2}$  state<sup>1</sup>, an approximate  $6P_{3/2}$  wave-

<sup>1</sup> Below  $n \sim 20$  the quantum defects give poor agreement as the electron has a strong interaction with the core.

function can be calculated to find the radial dipole matrix elements  $\langle 6P_{3/2}|er|n\ell j\rangle$  for the allowed transitions using the Numerov algorithm [251, 252]. The results show a stronger coupling to the  $nD_{5/2}$  state. The matrix elements are fitted using the scaling  $C_\ell n^{*-3/2}$  to obtain the coefficients  $C_{S_{1/2}} = 5.021 ea_0$  and  $C_{D_{5/2}} = 11.348 ea_0$ . This will allow us to obtain larger EIT signals when we will use cold atoms instead of a vapour cell in Sec. 6.2.

The expected sideband frequency required for EIT conditions on the Rydberg state  $68D_{5/2}$ , using the probe laser, is  $\nu_{\text{Offset, probe theo.}} = -438.8 \text{ MHz}$ . The experimental sideband is found at  $\nu_{\text{Offset, probe exp.}} = -431 \text{ MHz}$ , which is compatible with the shift  $\delta\nu_{\text{Offset, probe}} = 6.7 \text{ MHz}$  obtained previously on  $68S_{1/2}$ .

## 6.2 EIT experiments in cold atoms

Increasing Rydberg EIT signal precision requires cancellation of Doppler effects and controlling surrounding magnetic field. Using cold atoms enables to operate high-resolution EIT spectroscopy, allowing further detection of Rydberg states in the single atom case (see Sec. 7.2).

### 6.2.1 Optical pumping optimisation

Atoms in the MOT are loaded as detailed in Sec. 5.4 using a load time of 1 s, giving  $1.7 \times 10^6$  atoms at  $3 \mu\text{K}$ . Following cooling, atoms are distributed over all possible ground hyperfine states. However, as explained in Sec. 5.7.1, the EIT experiment requires us to prepare the ground state  $|g\rangle$  into the stretched state  $|6s \ ^2S_{1/2}, F = 4, m_F = 4\rangle$  to take advantage of the maximum transition strength. Optical pumping efficiency is evaluated via state-selective magnetic imaging [149]. This technique consists in applying a strong magnetic gradient as well as a bias field in the vertical  $z$ -direction for creating a magnetic trap. The bias magnetic field comes from shim coils that are placed outside the quadrupole coils, itself creating the magnetic field gradient in the  $z$ -direction. The principle of magnetic trapping is the interaction of the atomic magnetic dipole moment  $\boldsymbol{\mu}$  and an inhomogeneous magnetic field  $\mathbf{B}(\mathbf{r})$  given by the formula [21]

$$U = -\boldsymbol{\mu} \cdot \mathbf{B}(\mathbf{r}). \quad (6.9)$$

This interaction removes the energy degeneracy for a certain state  $|I, J, F, m_F\rangle$  due to linear Zeeman effect

$$\Delta E(m_F) = m_F g_F \mu_B B_z, \quad (6.10)$$

where  $m_F$  is the Zeeman sublevel of the hyperfine state  $F$ ,  $\mu_B$  is the Bohr magneton with  $\mu_B/h \sim 1.4$  MHz/G,  $g_F$  the Landé factor [253] and  $B_z$  is the component of  $\mathbf{B}(\mathbf{r})$  along the  $z$ -direction of the magnetic field.

The resultant force along the axis  $z$  is given by [21]

$$F = -m_F g_F \mu_B \frac{dB_z}{dz}. \quad (6.11)$$

This can be used for trapping neutral atoms and was first demonstrated in 1985 for a cooled Na beam by Migdall *et al.* [254]. Because of the fact that local maxima of magnetic fields are forbidden in free space [255], we need to use a magnetic field minimum to trap atoms magnetically. The corresponding atoms are known as “weak field seekers” and require  $m_F g_F > 0$ . They become trappable when the magnetic force becomes larger than gravity.

For  $^{133}\text{Cs}$  ground state, the stretched state  $|F = 4, m_F = 4\rangle$  is trappable because  $m_F g_F = 1$  and only requires a magnetic field gradient of 24 G/cm. However, the other weak field seeking states  $|F = 4, m_F = 3\rangle$  and  $|F = 3, m_F = -3\rangle$  both give a product  $m_F g_F = 3/4$  corresponding to a magnetic field gradient of 31 G/cm. In order to be sure that we are only trapping  $|F = 4, m_F = 4\rangle$ , we set the magnetic field gradient to 24 G/cm, corresponding to 8.5 V for the current supplier.

The optical pumping beam is coming from a PM fibre and collimated using a lens

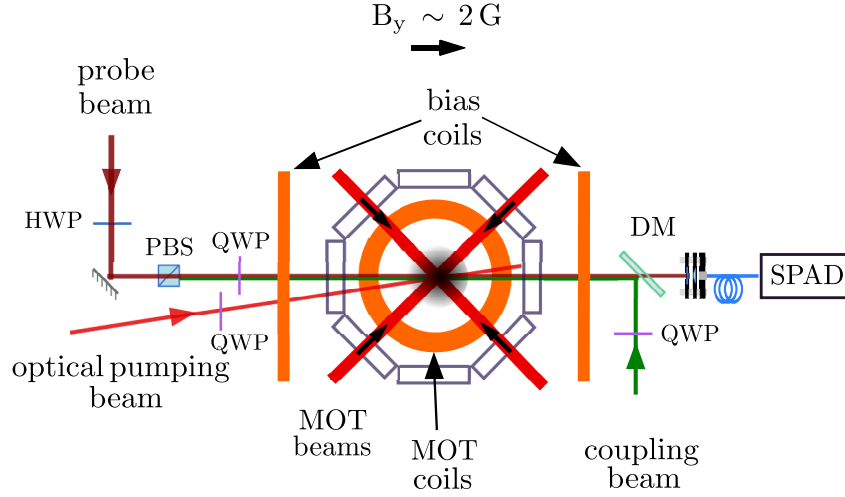


Figure 6.5: Schematic of the experimental setup for Rydberg EIT in cold atoms. A strong coupling beam (green) counter-propagates with a weak probe beam (red) through a cold atom cloud of Cs atoms optically pumped in the  $|F = 4, m_F = 4\rangle$  stretched state using a bias field of 2 G with a single-photon counter (SPAD) for probe detection due to tight focusing of the probe beam to a  $1/e^2$  radius of  $13 \mu\text{m}$ .

with focal length of  $f = 6.24 \text{ mm}$  giving a  $1/e^2$  waist radius of  $550 \mu\text{m}$ , as shown in Fig. 6.5. Repump light has been combined with the MOT beam path, as explained in Sec. 5.2.2. The optical pumping beam is aligned on the MOT by using light on resonance with the  $|6s \ ^2S_{1/2}, F = 4\rangle \rightarrow |6p \ ^2P_{3/2}, F' = 5\rangle$  transition. Maximising the loss of atoms in the MOT following a resonant pulse applied after the molasses stage, while gradually decreasing its power, allows us to coincide the beam with the MOT center.

Once the beams are aligned on the MOT, we need to find a good time scale for optical pumping. Following the molasses phase, the cooling light is turned off while the repump light is kept on for 0.25 ms, which pumps atoms in the  $F = 4$  ground state. A bias field is applied in the  $y$ -direction for 0.5 ms to define the quantisation axis, after which time the optical pumping pulse is applied. The magnetic quadrupole field is then turned on at  $24 \text{ G/cm}$  for 100 ms with a bias field of  $B_y \sim 2 \text{ G}$ . Atoms in the state  $|F = 4, m_F = 4\rangle$  are trapped whilst unpumped atoms fall away, and the atom number is imaged. The bias field along the quantisation axis, pumping duration and beam powers are optimised by maximising the number of pumped atoms after the 100 ms trap time.

Figure 6.6 shows the atom number as a function of the pumping duration with  $370 \mu\text{W}$  of optical pumping light,  $100 \mu\text{W}$  for the repump transition and a bias field

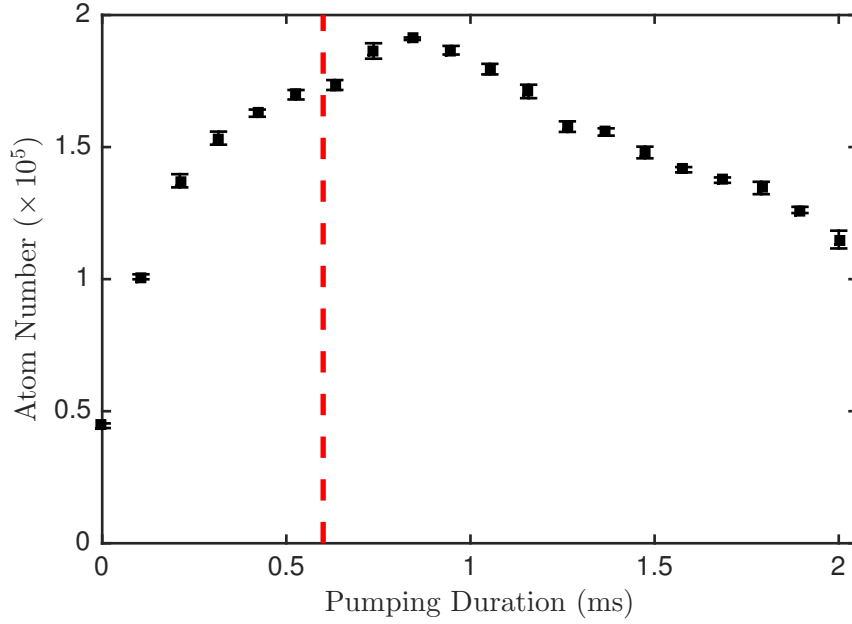


Figure 6.6: Optical pumping optimisation into the  $|F = 4, m_F = 4\rangle$  stretched state evaluated using state-selective magnetic imaging, This gives the atom number in the optical dipole trap versus optical pumping duration. The red dashed vertical line corresponds to the optical pumping duration chosen for EIT experiment close to the maximum.

of 2 G. At short pumping times, the number of atoms is enhanced approximately five times after 0.8 ms compared to the unpumped case. For longer pumping time, the number of atoms decreases because atoms from the dark state gradually decay into untrapped states. Additional parameters optimised to improve the atom number include the wave-plate angle and compensating the residual shallow angle between probe and optical pumping beams using a bias-field along the  $x$ -axis of 0.1 G. Finally, we ended up putting a mechanical shutter in the optical beam path in order to get rid of the TA leakage light from the cooling master laser that causes depumping into untrapped states.

## 6.2.2 EIT alignment procedure

Performing EIT spectroscopy on cold atoms requires two counter-propagating probe and coupling beams well aligned with the quantisation axis  $y$ , as shown in Fig. 6.5. The EIT visibility is enhanced with increasing Rabi frequency of the coupling beam  $\Omega_c$  [184], which has been implemented by reducing the coupling beam to a  $1/e^2$  waist radius of  $84 \mu\text{m}$  at the MOT chamber center. Additionally, we have strongly focused the probe beam using a lens of 200 mm focal length before the MOT chamber with

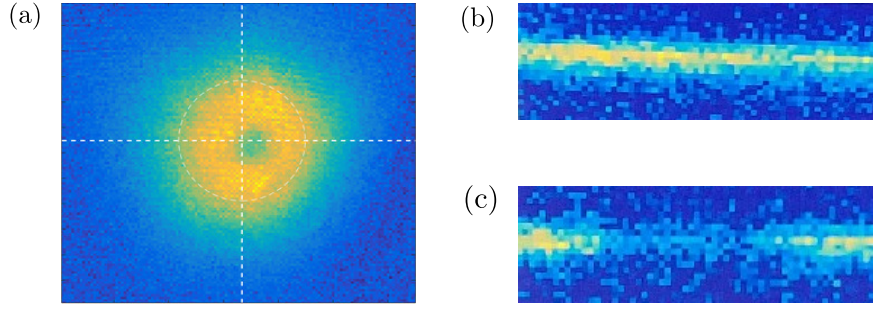


Figure 6.7: Photograph of the steps corresponding to the alignment procedure. (a) Rough alignment of the coupling beam on the MOT center. (b) Region of interest (ROI) where the probe laser and the ODT are aligned. (c) Optimisation of the coupling beam alignment using the ROI.

a  $1/e^2$  waist radius of  $13\ \mu\text{m}$ , ensuring the coupling Rabi frequency  $\Omega_c$  is uniform across the probe beam. The small beams size and restricted chamber access have drastically increased the difficulty to superimposed both beams. To circumvent day to day misalignment due its the extreme sensitivity, we had to develop a procedure to get EIT signal reliably.

We start with a rough alignment of the coupling beam on the MOT center by looking at minimising the number of atoms, when imaging the MOT using live fluorescence with the DMK camera until seeing a hole in the center of the MOT due to the creation of Rydberg atoms, as shown in Fig. 6.7 (a). The alignment optimisation begins with the loading of the MOT for 1 s before being compressed for a 20 ms duration with a magnetic field gradient of 28 G/cm using quadrupole coils, allowing the loading of the optical dipole trap with a maximum of atoms for 20 ms. We then align the probe beam onto the ODT by superimposing the probe laser image to the fluorescence imaging of the ODT, defining a pixel's region of interest (ROI), as shown in Fig. 6.7 (b).

Finally, using this ROI on the experimental control program, we can optimise the coupling beam alignment. After ODT loading, we apply both probe and coupling beams for a varying amount of time from 0 to 0.5 ms, followed by a TOF of 0.1 ms before recording the atom number in the ROI. Sitting at the time corresponding to half the initial number of atoms being blown away, we vary the Rydberg sideband to miminise it, as shown in Fig. 6.7 (c). Iteratively reducing the probe beam power from  $80\ \mu\text{W}$  to  $10\ \mu\text{W}$  allows us to improve the coupling beam alignment onto the probe beam as well as determining the sideband frequency needed for Rydberg excitation.

### 6.2.3 EIT experiment

Once the cold atomic ensemble is optically pumped in the  $|F = 4, m_F = 4\rangle$  stretched state, the atomic cloud expands freely for a duration of 1.5 ms, allowing the optical pumping and repump beam's mechanical shutters to close. Subsequently, the probe and coupling laser AOMs are turned on and EIT spectroscopy is performed using a two-photon scheme. The probe laser is driving the  $|6s\ ^2S_{1/2}, F = 4\rangle \rightarrow |6p\ ^2P_{3/2}, F' = 5\rangle$  closed transition using  $\sigma^+$  polarised light while the coupling beam is either  $\sigma^-/\sigma^+$  polarised to address  $nS_{1/2}$  or  $nD_{5/2}$  states respectively. Moreover, good polarisation purity for the probe beam is ensured via a polarising beam splitter (PBS) placed before the quarter-waveplate, as shown in Fig. 6.5. The EIT spectra are obtained by scanning the probe frequency twice from  $\Delta_p/2\pi = -12 \rightarrow +12$  MHz across the resonance in 1 ms. The frequency ramps are controlled via a 9910 DDS evaluation board to vary the probe AOM frequency smoothly across the transition whilst the coupling beam is locked to the ULE reference cavity.

Precision Rydberg EIT spectroscopy requires  $\Omega_c \gg \Omega_p$  to prevent creating Rydberg population, hence must be performed with low probe power to avoid suppression due to cooperative effect arising from dipole-dipole interactions [166]. However, using a tight probe laser with a  $1/e^2$  radius of  $13\ \mu\text{m}$  enhanced drastically the probe Rabi frequency, so that saturation intensity  $I_{\text{sat}} = 1.1\ \text{mW}/\text{cm}^2$  is already reached for a probe power of 3 nW. At such weak powers, it is no longer possible to use conventional photodetectors. Instead, we have used a single-photon avalanche photodiode (SPAD) Perkin-Elmer SPCM-AQRH-14-FC with very low dark-count rate of 50 Hz and a dead time of 28 ns. The typical background count-rate was around 2 kHz during the experimental sequence, due to leakage light mostly coming from the dipole trap and coupling beams. The SPAD output is not proportional to the probe intensity, instead a 15 ns TTL pulse is emitted each time that one or more photons are detected. The output TTL signal from the SPAD is recorded with the SensL HRMTime time correlated counting card, recording the arrival time of this TTLs with 27 ps resolution. In order to prevent damaged of the SPAD due to possible large photon flux, the SPAD can be gated with an external TTL using a homebuilt circuit following [149]. The maximum count rate is limited by the counting card to

4.5 MHz while the single-photon counter can detect counts with a rate of 25 MHz. The SPAD quantum efficiency is  $\eta \sim 50\%$  and  $95\%$  for the fiber at 852 nm, which gives a total quantum efficiency for the SPAD of  $47.5\%$ . After passing through the vacuum chamber, the diverging probe beam is re-collimated with a 200 mm lens, cleaned with a narrow-band filter (Semrock FF01-850/10-25) and focused down to a fiber connected to the SPAD using a lens with 40 mm focal length. In order to avoid saturation of the counter, the probe beam is attenuated to give a counting rate of 1 MHz after the chamber, giving on average 1 count/ $\mu\text{s}$  corresponding to  $2.1 \times 10^6$  photons/s. This corresponds to a probe beam power of 0.5 pW after the chamber and an input power of 1.25 pW before the chamber, realising the condition  $I/I_{\text{sat}} \sim 5 \times 10^{-4} \ll 1$ . Each spectrum is recorded by taking 100 shots to build up a histogram of arrivals, using a 1  $\mu\text{s}$  bin width.

### 6.3 Data analysis and extracted lasers parameters

We present measurements of the offset between the atomic and cavity resonant frequencies using EIT for high-resolution spectroscopy on a cold atom cloud. Each datasets requires 3 different stages in a single experimental run. Once atoms are loaded, the first stage requires a probe-only absorption spectrum. During the second stage, an EIT measurement is taken with the probe and coupling lasers both turned on. Finally, the last stage consists of recording a probe-only transmission spectrum without atoms to get a background counts, compensating the spatial deviation of the probe beam when AOM frequency is scanned across the resonance [166] during the measurements.

#### 6.3.1 EIT experiment on $68D_{5/2}$ and $69S_{1/2}$

Figure 6.8 shows a full dataset for  $68D_{5/2}$  state with a probe power of 0.3 pW and 98 mW of coupling power derived from Rydberg A running at a TA current of 2.9 A. The principal quantum number  $n = 68$  has been chosen because it only requires a TEC laser temperature of  $21.7^\circ\text{C}$  while the  $D_{5/2}$  state's radial dipole matrix element  $\langle 6P_{3/2} | er | nlj \rangle$  is two times higher than corresponding  $S_{1/2}$  state

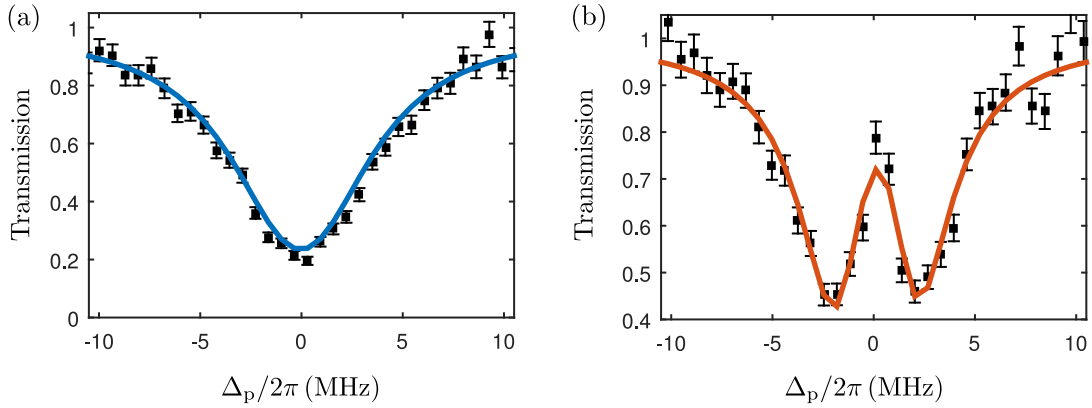


Figure 6.8: EIT data on  $68D_{5/2}$  Rydberg state in cold atoms. (a) Fit to probe-only absorption data using Eq. 6.12. (b) EIT transmission data fitted using Eq. 6.13.

according to Sec. 6.1.3, thus increasing the EIT peak signal for its first observation with SPAD. The blue data on Fig. 6.8 (a) shows a probe-only absorption spectrum as a function of the probe detuning  $\Delta_p$ . Error bars represent one standard deviation. Following work of [149], the absorption spectrum is fitted with a theoretical two-level transmission profile obtained by combining equations 3.26, 3.25 and 3.16b to give

$$T = \exp\left(-\frac{k_p OD \mu_{eg}^2}{\epsilon_0 \hbar} \frac{\gamma_{ge}}{\Omega_p^2/2 + \gamma_{ge}^2 + \Delta_p^2}\right), \quad (6.12)$$

where  $OD \equiv \rho_0 \ell$  is the optical depth,  $\rho_0$  the density,  $\ell$  the optical path length through the cloud,  $\gamma_{ge}$  and  $\Delta_p$  are fit parameters while the dipole matrix element  $\mu_{eg}$  for the closed transition can be calculated using A.7 combined to the radial matrix element  $\langle 6S_{1/2}|er|6P_{3/2}\rangle = 4.4786 ea_0$  [160] to give  $\mu_{eg} = \sqrt{1/3} \times 4.4786 ea_0$  and a probe Rabi frequency of  $\Omega_p/2\pi = 0.03$  MHz. The absorption fit shows good agreement with a reduced chi-squared value of  $\chi_\nu^2 = 1.2$  and structureless residuals.

A similar procedure is applied to the EIT spectrum in Fig. 6.8 (b) and data are fitted with the weak-EIT transmission using the susceptibility from Eq. 3.27

$$T = \exp\left(-\frac{k_p OD \mu_{eg}^2}{\epsilon_0 \hbar} \text{Im}\left\{\frac{i}{\gamma_{ge} - i \Delta_p + \frac{\Omega_c^2/4}{\gamma_{gr} - i(\Delta_p + \Delta_c)}}\right\}\right), \quad (6.13)$$

to obtain the parameters  $\gamma_{gr}$ ,  $\Omega_c$  and  $\Delta_c$  where  $OD$ ,  $\Delta_p$  and  $\gamma_{eg}$  are constrained from

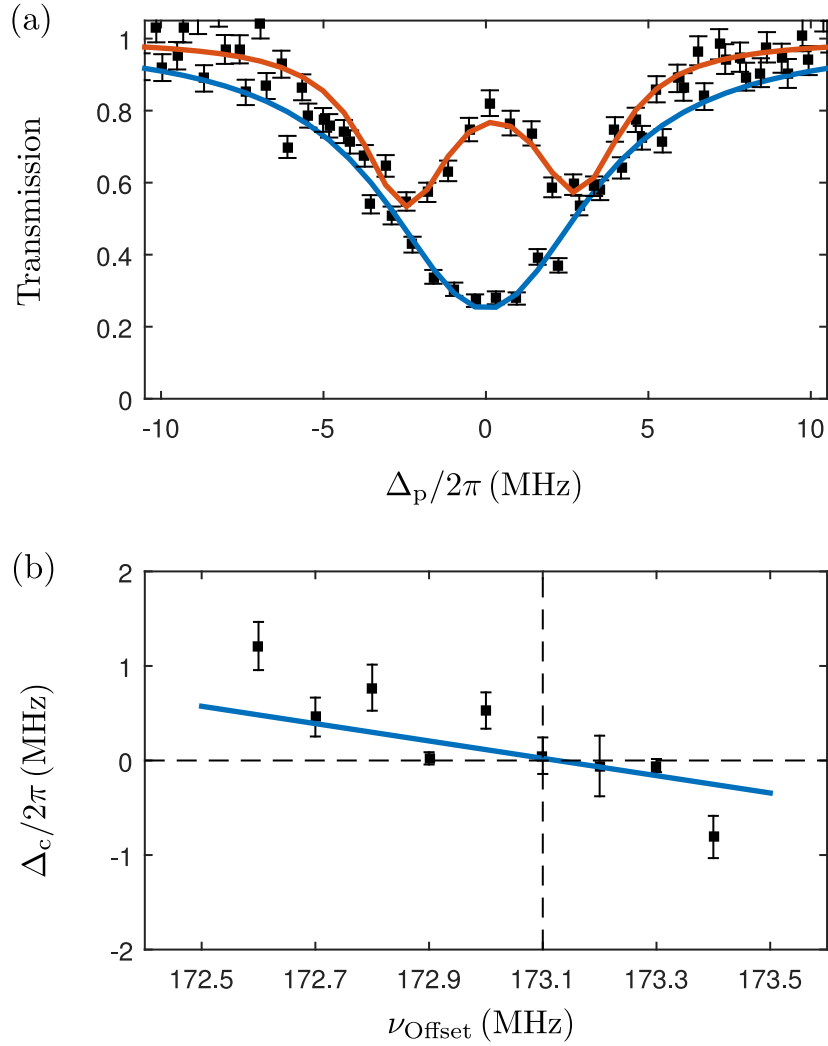


Figure 6.9: EIT spectroscopy on  $69S_{1/2}$  Rydberg state in cold atoms. (a) Probe-only absorption (blue) and EIT transmission (red) data. (b) Determination of the resonant sideband frequency of  $\nu_0 = +173.1$  MHz.

the absorption fit. The fit shows good agreement with the data, giving  $\chi_\nu^2 = 1.2$  and structureless residuals even around the EIT resonance. The position corresponding to the two-photon resonance where  $\Delta_p = -\Delta_c = 0$  is obtained with a resolution of 0.5 MHz for the negative sideband frequency  $\nu_{\text{Offset}} = -401$  MHz with respect to the  $\text{TEM}_{00}$  cavity mode frequency  $\nu_{\text{IR}} = 294\,525\,200$  MHz. EIT therefore provides a non-destructive probe of Rydberg state energies without transferring population to Rydberg states. However, one can observe progressive loss of atoms in the reverse direction across the resonance. This can be explained by the creation of Rydberg atoms resulting in a reduced absorption in the wings of the EIT resonance [166].

One way to improve the EIT signal was to take advantage of  $S_{1/2}$  states compared

to  $D_{5/2}$  states. Indeed, atoms in  $S_{1/2}$  states experience isotropic, repulsive dipole-dipole interactions (see Sec. 2.2), which significantly reduce the ionisation rate compare to D-states. Figure 6.9 (a) shows EIT spectroscopy for  $69S_{1/2}$  state with a probe power of 0.3 pW and 100 mW of coupling power derived from Rydberg A running at a TA current of 2.9 A. Increasing the coupling power above 100 mW coupling power led to suppression of the EIT peak due to interactions. From the complete set of spectra, the coupling laser detuning  $\Delta_c$  as a function of sideband frequency is plotted in Fig. 6.9 (b) and fitted using the formula  $\Delta_c = \alpha(\nu_{\text{Offset}} - \nu_0)$ , enabling the determination of the resonant sideband frequency  $\nu_0 = +173.1$  MHz with a resolution of 0.1 MHz corresponding to the  $\text{TEM}_{00}$  cavity mode frequency  $\nu_{\text{IR}} = 294\,518\,300$  MHz.

Finally, the last way to improve the EIT peak signal and resonant frequency determination, before moving to more challenging single atom EIT spectroscopy, is by changing the principal quantum number  $n$ . Indeed, the strength of long range van der Waals interactions is characterised by the  $C_6$  parameter which scales proportionally to  $n^{*11}$  while the polarisability  $\alpha$  scales proportionally to  $n^{*7}$ , as seen in Sec. 2.1. Due to the temperature tuning limitations of the TEC in the SHG cavity of Rydberg A, we moved to Rydberg B laser for  $50S_{1/2}$  state spectroscopy. This is chosen as one of the lowest  $n$  levels accessible with the current setup. Performing measurement using  $50S_{1/2}$  instead of  $69S_{1/2}$  Rydberg state will reduce sensitivity to stray electric field by a factor  $\sim 10$  while minimising interaction strength by a factor  $\sim 35$ , which must drastically increase EIT signal.

### 6.3.2 $50S_{1/2}$ : EIT and ULE cavity drift calibration

After optimising the absorption as shown in Fig. 6.10 (a), we have performed EIT spectroscopy on  $50S_{1/2}$  Rydberg state using a probe power of 0.3 pW and 56 mW of coupling power. Figure 6.10 (b) shows the EIT spectrum for a sideband frequency  $\nu_{\text{Offset}} = 120.8$  MHz which results in a coupling Rabi frequency of  $\Omega_c/2\pi = 5.1(2)$  MHz. The normalised residuals on the lower panel show excellent agreement between theory and experiment with  $\chi^2_\nu = 1.0$ . Using the complete set of spectra whose examples are shown in Fig. 6.11 and as we previously did with  $69S_{1/2}$

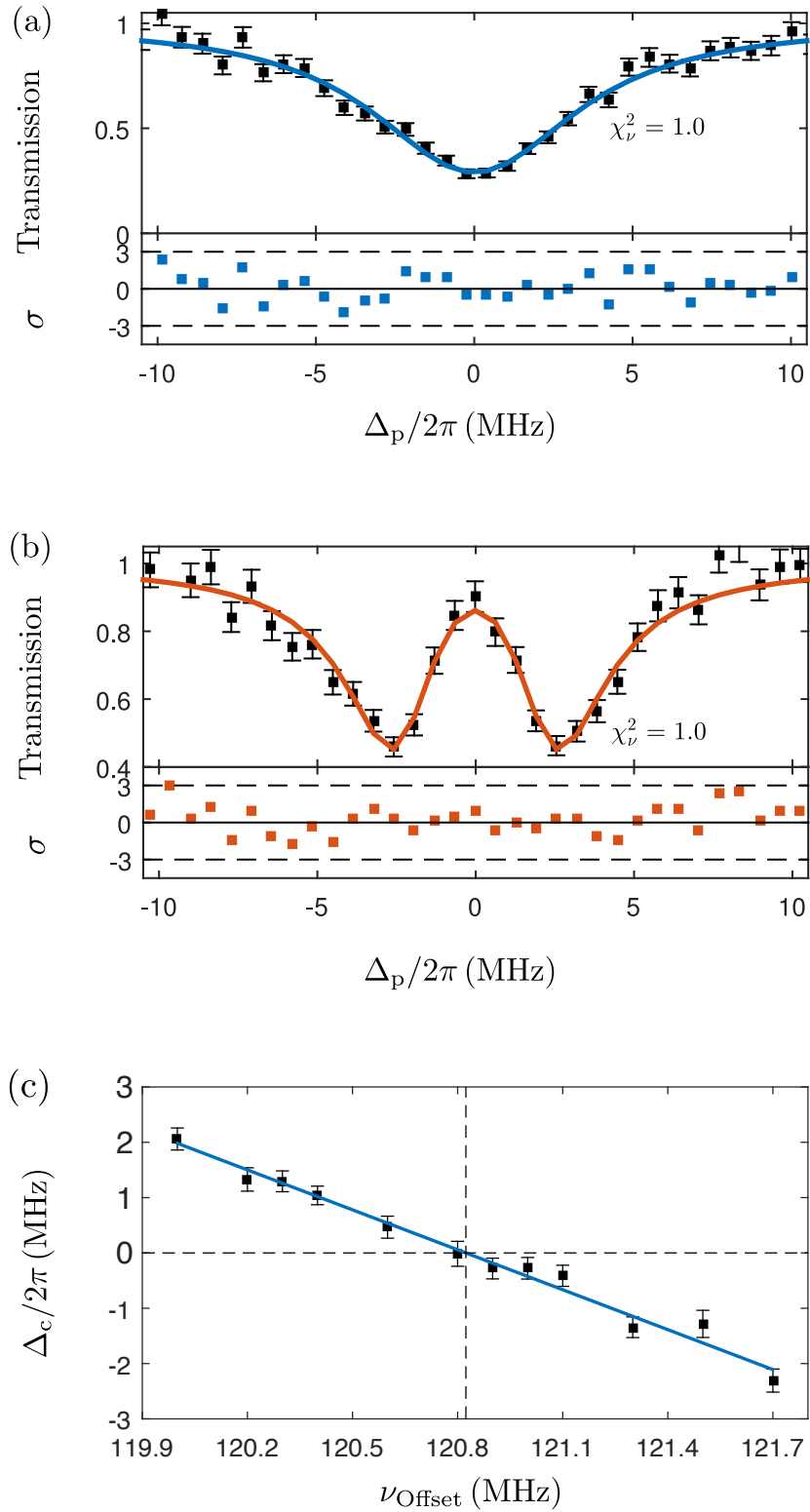


Figure 6.10: EIT on  $50S_{1/2}$  Rydberg state in cold atoms with (a) probe-only absorption and (b) EIT transmission. (c) Determination of the resonant sideband frequency of  $\nu_0 = +120.82(4)$  MHz.

Rydberg state, Fig. 6.10 (c) allows us to determine a resonant sideband frequency of  $\nu_0 = +120.82(4)$  MHz with a resolution of less than 0.1 MHz.

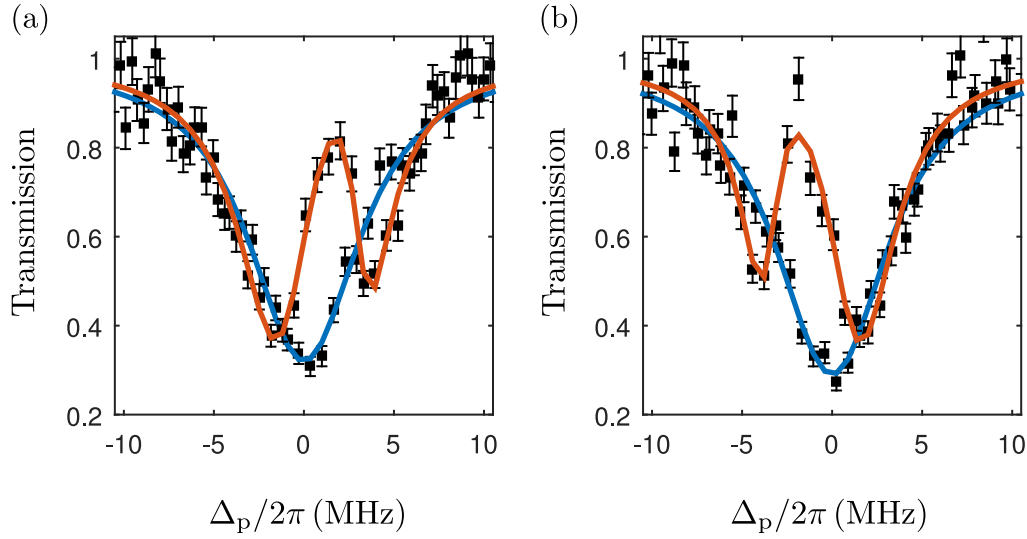


Figure 6.11: Spectroscopy of the  $50S_{1/2}$  Rydberg state showing two off-resonant spectra at (a)  $\nu_{\text{Offset}} = 120\text{MHz}$  and (b)  $\nu_{\text{Offset}} = 121.7\text{MHz}$  sideband frequencies.

Due to unavoidable inherent ULE material aging, the resonant frequency was changing every day. Using this high-resolution method to extract the resonant transition frequency, we repeat the EIT spectroscopy over a period of 20 days to determine the long-term frequency drift of the cavity with respect to atomic transition as shown in Fig. 6.12. The results show an average linear frequency drift of 1 Hz/s, confirming the ULE cavity is optimised close to the zero-CTE temperature but still limited by creep of the spacer or outgassing in the ULE cavity vacuum.

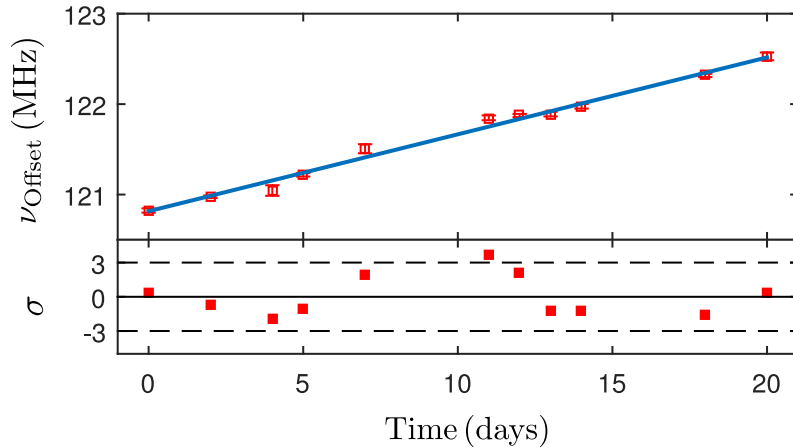


Figure 6.12: EIT resonance's frequency of  $50S_{1/2}$  recorded for a period of 20 days. Using a linear fit, the constant cavity's drift is evaluated at 1 Hz/s. Inset shows normalized residuals and error bars reflect standard errors.

## 6.4 Summary

Using high-resolution spectroscopy on a cold atom cloud, we have calibrated the cavity frequencies with respect to the Rydberg transitions with a precision of  $< 0.1$  MHz. We have demonstrated long-term stability with a linear drift of  $\sim 1$  Hz/s relative to an atomic reference. These measurements are competitive against doubly stabilised optical clocks [195, 256] and offer an order of magnitude compared to similar cavity-stabilised Rydberg laser systems [247, 257]. As will be seen in the next chapter, our frequencies calibration will allow us to perform single atom spectroscopy that are significantly more challenging due to low broadening of the two-photon excitation, with typical Rabi frequency of  $\Omega_R/2\pi \sim 1$  MHz.

## Part III

# Manipulation of Single and Two Qubits

# Chapter 7

## Coherent Control of Atoms

This chapter demonstrates in a first part that we are able to perform coherent control measurements of single atoms via single qubit rotations or coherent Rydberg excitations, essential for quantum information processing [91, 158, 258]. However, the possibility to operate with more than one atom in the Rydberg state would provide us the opportunity to take advantage of the dipole-dipole interactions to perform multi-qubit operations. The last part of the chapter will show its first consequence through the emergence of the Rydberg atom dipole blockade between two trapped atoms and subsequent the creation of a maximally entangled Bell state [123] .

In the first three sections, we will show that we can coherently manipulate single caesium atoms between the internal clock states  $|F = 3, m_F = 0\rangle = |0\rangle$  and  $|F = 4, m_F = 0\rangle = |1\rangle$  using Raman lasers. The other sections are focused on coherent control of Rydberg excitations. First, we will present spectroscopy and coherent Rydberg excitations from the clock state  $|F = 4, m_F = 0\rangle$  to  $50S_{1/2}$  using a coupling beam coming from the side of our high-NA lenses setup. Due to high sensitivity of Rydberg states to electric field, we show our ability to implement DC-electric field environment control on the order of  $\sim 1\text{mV/cm}$  in the science chamber as well as laser intensity stabilisation with less than 1% amplitude variation via AOM based noise-eater, obtaining precise and repeatable pulse area during excitations. Then, relying on both probe and coupling beams counter-propagating through the high-NA lenses, we will show an increase in speed of the Rabi oscillations using Rydberg excitation from the stretched state  $|F = 4, m_F = 4\rangle$  to  $50S_{1/2}$ .

This will be followed by coherent control towards  $69S_{1/2}$  and  $81D_{5/2}$  Rydberg states in the same configuration. Finally, we will report on the demonstration of Rydberg blockade between two atoms separated by  $6\ \mu\text{m}$  and the creation of a maximally entangled Bell state with high-fidelity [123].

## 7.1 Ground state manipulation

The ability to perform fast ground state rotations is a key requirement for implementing quantum information processing, as they provide a platform for single qubit gate operations. The usual way to perform ground state rotations is by exploiting dipolar magnetic transitions with microwave radiations but there are several advantages to use stimulated Raman transitions instead. First, using microwave radiations with a wavelength  $\lambda \sim \text{cm}$  doesn't allow single atom addressability while the shorter wavelength  $\lambda < \mu\text{m}$  of optical frequencies allow for fine spatial resolution with strongly focused beam. Moreover, the higher value of electric dipole matrix element combined with high beam intensities achievable at the atom allows for fast rotations with MHz rate [105] compared to typical Rabi frequencies values  $\Omega/2\pi \leq 100\ \text{kHz}$  [259] using microwave radiations emitted via antenna.

### 7.1.1 Hyperfine state detection

Each experimental cycle begins by preparing single atoms in microscopic dipole traps, as described in Sec. 5.6. Before realising ground state rotations, a first readout verifies the presence of a single atom using 40 ms of fluorescence imaging with molasses beams, as shown in the experimental timing protocol Fig. 7.1. Atoms are then cooled down with a PGC phase of 10 ms to increase the retention before initialisation in the states  $|F = 4, m_F = 4\rangle$  or  $|F = 4, m_F = 0\rangle$  via appropriate optical pumping, as explained in Sec. 5.7. The readout and optical pumping stages are done out of phase with the dipole trap to avoid unwanted AC Stark shifts.

After ground state rotations, we need precise determination of the atom's hyperfine state from the final readout. Hyperfine state detection is realised via a "blow away" (BA) protocol [105] where atoms in the hyperfine state  $|6s\ ^2S_{1/2}, F = 4\rangle$  are pushed

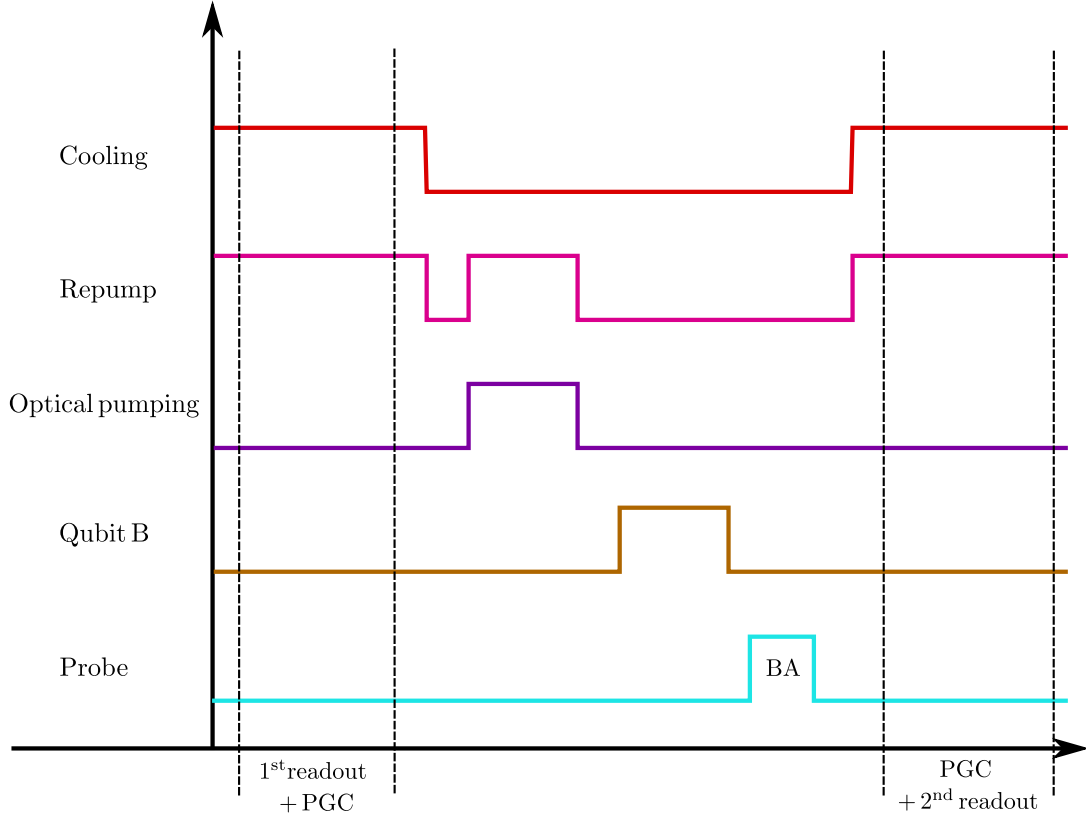


Figure 7.1: Timing sequence for single atom ground state rotations between the hyperfine sublevels  $|F = 3, m_F = 0\rangle = |0\rangle$  and  $|F = 4, m_F = 0\rangle = |1\rangle$ . After ground state rotation with Qubit B laser, the determination of the atom's hyperfine state from the final readout is done using a blow-away (BA) beam.

out using the probe beam locked on the cycling transition  $|6s\ ^2S_{1/2}, F = 4\rangle \rightarrow |6p\ ^2P_{3/2}, F' = 5\rangle$ . This beam will eject atoms in the hyperfine state  $F = 4$ . This ensures that only atoms in the  $F = 3$  hyperfine state are detected when fluorescence imaging is applied, to verify if the atom is still present at the end of the experimental cycle. The power of the probe beam is only  $20\ \mu\text{W}$  to avoid possible off-resonance excitation to  $F' = 4$  that could depump atoms into  $F = 3$ . On the optical table, the probe and optical pumping beams have been combined into the same single mode PM fibre. The output fibre beams with a waist radius of  $\omega_0 = 500\ \mu\text{m}$  pass through a Glan-Taylor polariser to clean up the horizontal polarisation before using a quarter waveplate, if needed, for creating circular polarisation. The beams are overlapped with single atoms along the  $x$ -direction, as illustrated in Fig. 7.2 (a).

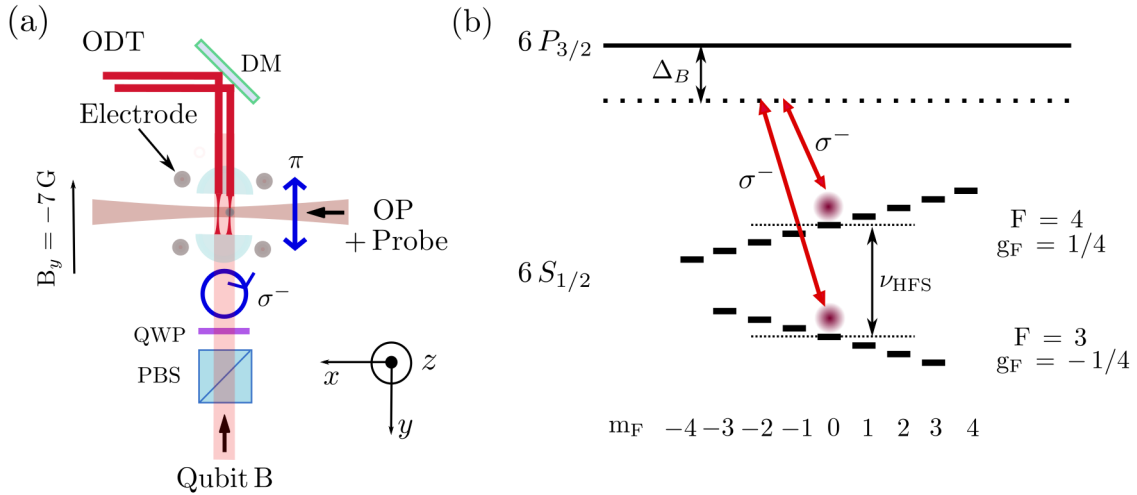


Figure 7.2: (a) Schematic of the ground state rotations experimental setup with optical pumping (OP) and probe beams coming from the same fibre with a  $1/e^2$  radius of  $\omega_0 = 500 \mu\text{m}$ ,  $\pi$ -polarised in the  $x$ -direction, while Qubit B is aligned on the lenses axis with a  $1/e^2$  radius of  $\omega_B = 4.5 \mu\text{m}$  and a quantisation axis defined by applying a magnetic field  $B_y = -7 \text{ G}$ , along  $y$ . (b) Schematic of the magnetic sublevels used to drive ground state rotations with a detuning  $\Delta_B/2\pi = -45 \text{ GHz}$  and the laser beam configuration implemented in a  $\sigma^-/\sigma^-$  configuration whose AC Stark shift contributes to increase magnetic sublevels separation.

### 7.1.2 Two-Photon Raman spectroscopy

We have decided to work in the clock states basis

$$\{ |F = 3, m_F = 0\rangle = |0\rangle, |F = 4, m_F = 0\rangle = |1\rangle \},$$

to perform ground state initialisation and rotations because of its first order robustness to magnetic field [105]. The ground state rotations experimental sequence is illustrated in Fig. 7.1. Once single atoms have been optically pumped using  $\pi$ -polarised light along the  $y$ -direction in the  $|F = 4, m_F = 0\rangle = |1\rangle$  state, Qubit B laser is used to perform ground state rotations between states  $|1\rangle$  and  $|0\rangle$ .

Qubit B laser is built in the same ECDL configuration than Qubit A laser (see Sec. 4.1), with a Fabry-Perot laser diode (Thorlabs L852P150). After the isolator, light is coupled into a fibre-coupled EOM (Jenoptik model PM-830) to generate strong sidebands at half the hyperfine ground state splitting  $\pm\omega_{\text{HFS}}/2$ , with  $\omega_{\text{HFS}}/2\pi = 9.192\,631\,770 \text{ GHz}$ . The separation of the frequency modulation sidebands from the carrier is done using a Haubrich-Dornseifer-Wynands (HDW) in-

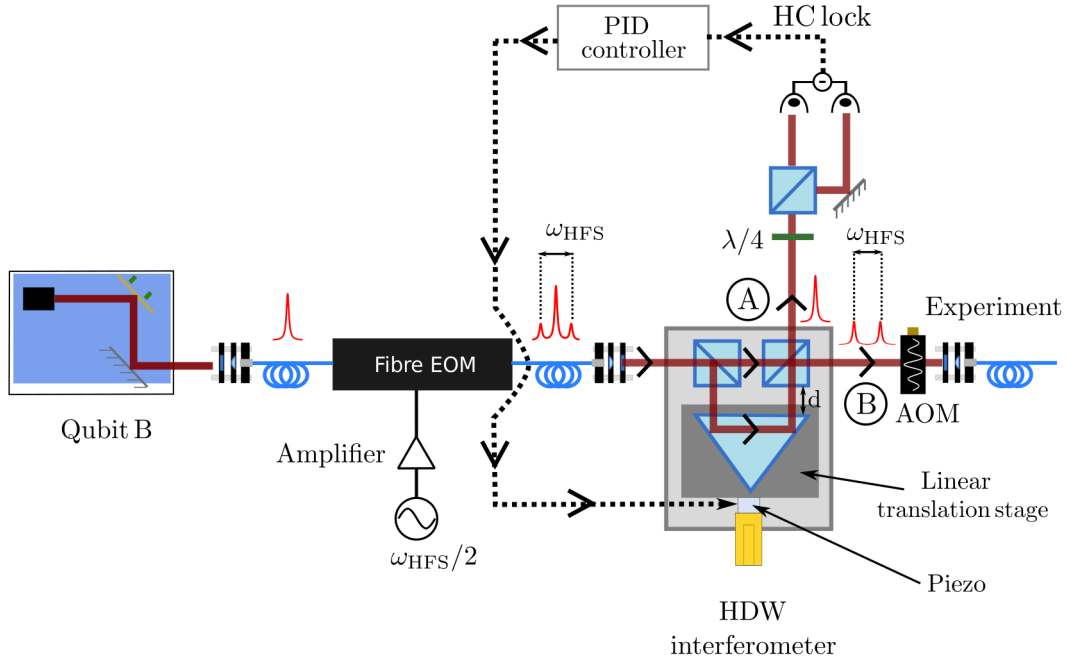


Figure 7.3: Setup of Qubit B laser. The laser is frequency modulated using an EOM before the beam was splitted into two paths. The control over the distance  $d$  between the prism and the non-polarising beam splitters allow to take advantage of beams interference to separate the carrier frequency in port A from the sidebands in port B. The carrier signal from the output port A is used for creating an error signal using the Hänsch-Couillaud technique [202], which is fed back to the piezo actuator controlling the distance  $d$  of the HDW interferometer. In the port B, the light which is filtered from the carrier frequency, passes through an 80 MHz AOM for control of frequency and intensity before being delivered to the experiment via a single mode PM fibre.

terferometer [260], as shown in Fig. 7.3. The interferometer uses two non-polarising beamsplitter cubes (Edmund Optics) and a N-BK7 right-angle prism (Thorlabs PS908H-B), whose relative distance  $d$  (see Fig. 7.3) is controlled via a piezoelectric actuator (Thorlabs PA4GKW) acting on a linear translation stage. By adjusting this distance, the optical path length between the two paths can either constructively or destructively interfere depending on the frequency. This allows to separate the sidebands in port B from the carrier in port A with 90% contrast.

The carrier signal from the output port A is used for creating an error signal using the Hänsch-Couillaud technique [202] (see Sec 4.1.2), which is fed back to the piezo actuator controlling the distance  $d$  of the HDW interferometer. In the port B, the light which is filtered from the carrier frequency, passes through an 80 MHz AOM for control of frequency and intensity before being delivered to the experiment via a single mode PM fibre.

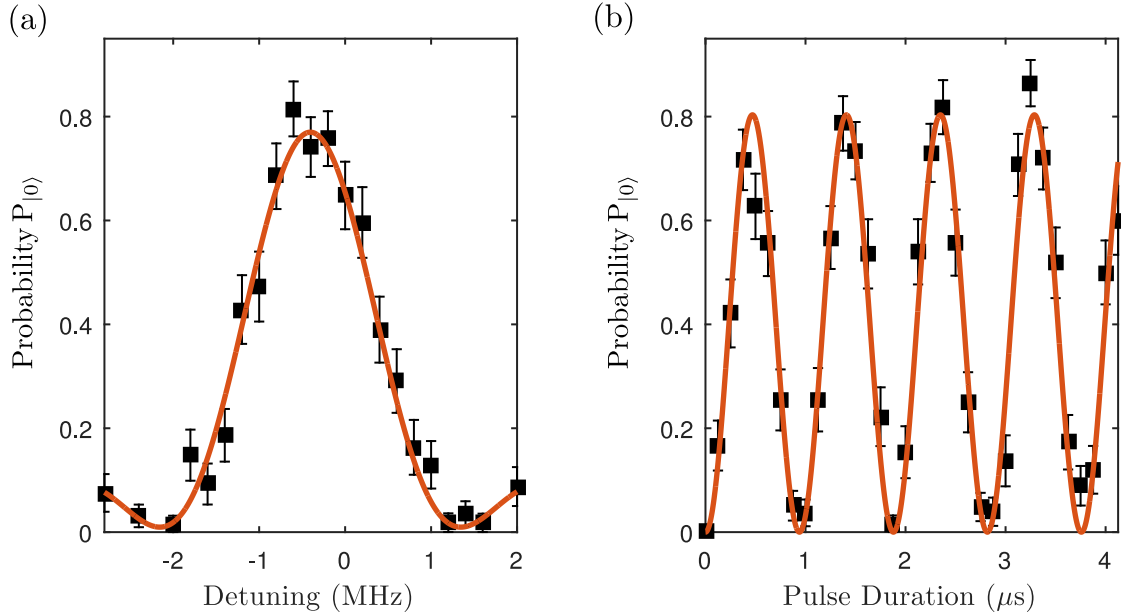


Figure 7.4: (a) Two-photon spectroscopy of the clock states transition for a  $\pi$ -pulse at  $t_\pi = 500$  ns, yielding to a peak transfer at the two-photon resonance  $\delta/2\pi = -410$  kHz. (b) Coherent Rabi oscillations between the clock states at a fixed detuning of  $\delta/2\pi = -410$  kHz, leading to a Rabi frequency of  $\Omega_{43} = 2\pi \times 1.06$  MHz.

As shown in Fig. 7.2, Qubit B is aligned onto the single atom in the  $y$ -direction with a waist radius  $\omega_B = 4.5 \mu\text{m}$  [221] and a large detuning  $\Delta_B/2\pi = -45$  GHz from the  $D_2$ -transition. The beam is passed through a PBS to clean the polarisation, followed by a quarter-waveplate (QWP) to fix the polarisation. In order to be sure that we have the right polarisation, we have used the QWP previously characterised in the EIT experiment. The quantisation axis is defined by applying a magnetic field  $B_y = -7$  G along the lens axis to separate hyperfine sublevels as much as possible. The non-separability of the two driving fields imposes the selection rule  $\Delta m_F = 0$  for stimulated Raman transitions between the clock states  $|F = 4, m_F = 0\rangle = |1\rangle$  and  $|F = 3, m_F = 0\rangle = |0\rangle$ . Hence, transitions can be driven either using  $\sigma^+/\sigma^+$  or  $\sigma^-/\sigma^-$  configurations. The laser beam configuration has been implemented in a  $\sigma^-/\sigma^-$  configuration, whose AC Stark shift contributes to increase magnetic sublevels separation. Once the state rotation sequence is completed, the blow away beam is turned on. Finally, this is followed by a PGC phase for cooling atoms prior to applying the final read out.

We have experimentally performed two-photon spectroscopy by applying a  $\pi$ -pulse with a Qubit B power of  $45 \mu\text{W}$  and scanned the microwave frequency of the side-

bands until we observe complete transfer, corresponding to the two-photon resonance (see Chap. 3). Figure 7.4 (a) shows the two-photon spectroscopy for a pulse length of  $t_\pi = 500$  ns. The data are fitted using a modeled function of Eq. 3.6 given by

$$P_{|0\rangle}(t) = A + \frac{\Omega_{43}^2}{\Omega_{43}^2 + (\delta - \delta_{AC})^2} \sin^2 \left( \sqrt{\Omega_{43}^2 + (\delta - \delta_{AC})^2} \cdot \frac{t_\pi}{2} \right), \quad (7.1)$$

with a background offset  $A$ , leading to a peak transfer at the two-photon resonance  $\delta_{AC}/2\pi = -410$  kHz, attributed to the differential AC Stark shift and in agreement with a Qubit B waist of  $\omega_B = 4.5 \mu\text{m}$  while the Rabi frequency is found to be  $\Omega_{43}/2\pi = 0.97$  MHz.

Following the spectroscopy, we have performed Rabi oscillations between  $|1\rangle$  and  $|0\rangle$ , as shown in Fig. 7.4 (b), by fixing the microwave source at  $-410$  kHz and varying the pulse length  $t$ . The Rabi flopping is fitted using Eq. 3.15 and returns a Rabi frequency of  $\Omega_{43}/2\pi = 1.06$  MHz, which exhibits only a small mismatch with the previous result  $\Omega_{43}/2\pi = 0.97$  MHz found in the spectroscopy. It can principally be interpreted by Doppler broadening of the transition arising from finite temperature of the atoms ( $\sim 70 \mu\text{K}$ ) that was not optimised and small variations from batch to batch of the AC Stark shift seen by the atoms, due to the Gaussian profile of the laser. Moreover, the maximum population transfer of 80%, due to limited optical pumping efficiency, has been later optimised to 96% [123].

### 7.1.3 Ground state coherence

According to Chap. 1, phase precession of a single qubit in the Bloch sphere is the complete analog to qubit operations. The control of the relative phase between  $|1\rangle$  and  $|0\rangle$  under time evolution is a crucial challenge for the realisation of quantum information protocols. Thus, a first characterisation consists in determining the phase accumulation acquired when the qubit is not addressed, with the Ramsey method of separated oscillatory fields, as described in Sec. 3.1.3.

After initialisation with optical pumping in the state  $|1\rangle$ , an initial  $\pi/2$ -pulse is applied to create a superposition state, followed by a fixed evolution time  $T$  where the qubit state can precess freely in the Bloch sphere for varying two-photon detun-

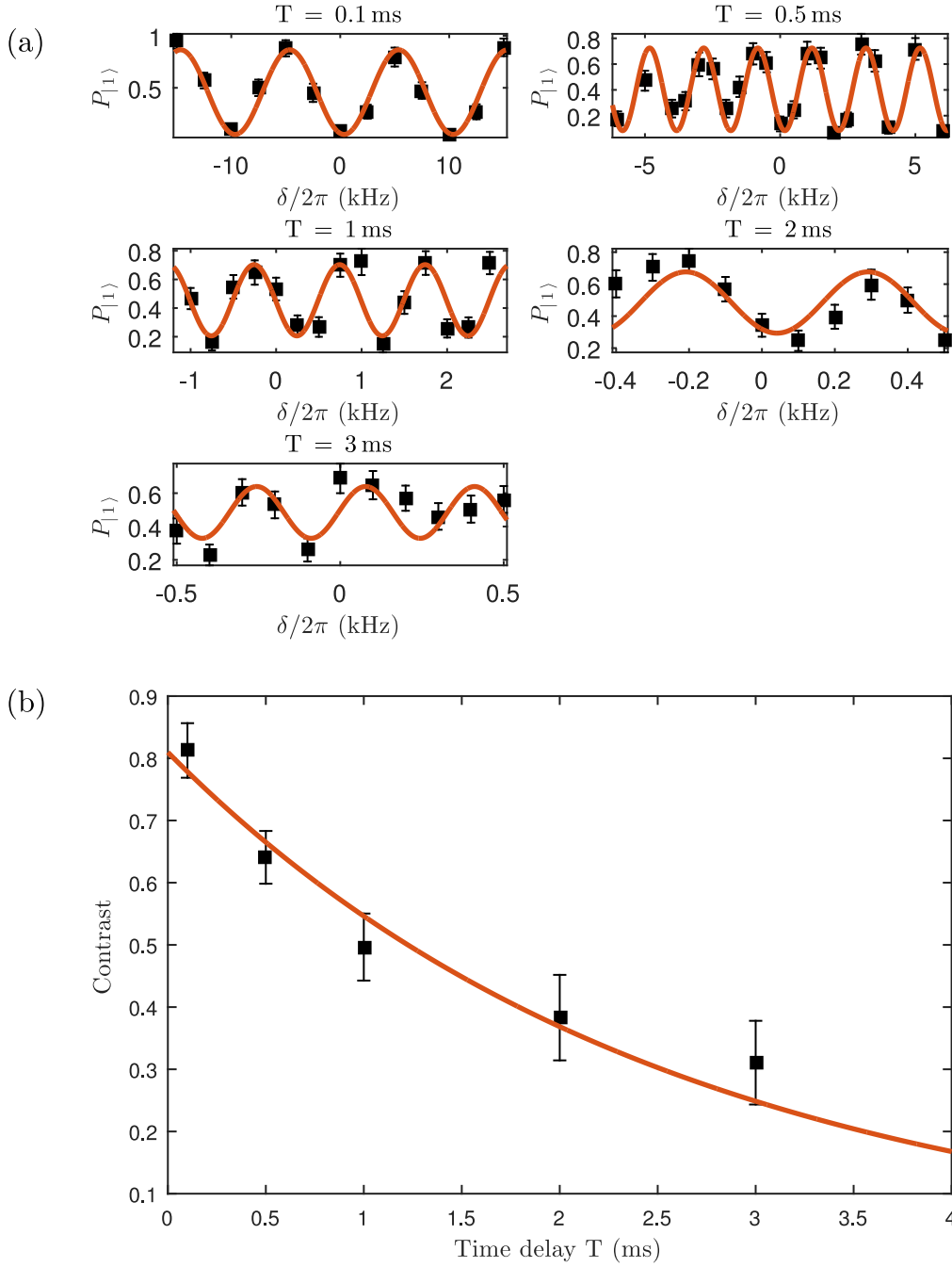


Figure 7.5: (a) Ground States Ramsey experiment performed for different fixed delay times  $T$ , where the two-photon detuning  $\delta$  is scanned across the resonance. (b) Plot of the fringe's contrast as a function of the delay times  $T$ , giving a dephasing time of  $T_2^* = 2.5 \pm 0.4$  ms.

ing  $\delta$  and a second  $\pi/2$ -pulse detects the final state. The probability of transferring the population in state  $|0\rangle$  exhibits an oscillatory pattern given by Eq. 3.17. In Fig. 7.5 (a), we plot the probability  $P_{|1\rangle}$  for different time delays  $T$  between the excitation pulses, in order to determine the decoherence time of our single qubit.

Figure 7.5 (b) shows a plot of the oscillations amplitude as a function of the time delay  $T$ . The data are fitted with an exponential decay of the form  $A_0 \cdot e^{-T/T_2^*}$ , where

$A_0$  is the amplitude coefficient at  $T = 0$  and  $T_2^*$  is related to the rate of inhomogeneous dephasing of the trapped atoms. The fit gives a value of  $T_2^* = 2.5 \pm 0.4$  ms,  $\approx 5000 \times$  larger than the time needed to execute a  $\pi$ -pulse. This allows us to circumvent decoherence and creates a good basis for performing quantum information processing. Further upgrades on the experiment have managed to increase the value of  $T_2^*$  to 10 ms, only limited by Doppler effect, and an homogeneous dephasing time of 150 ms using spin-echo technique [123].

## 7.2 Rydberg state manipulation

Our ultimate goal is to perform quantum gate operations with Rydberg atoms, this implies to use Rydberg states with the highest principal quantum number  $n$  to reduce gate errors [89, 157]. In order to take advantage of the long radiative lifetime  $\propto (n^*)^3$  and the large interaction strength  $\propto (n^*)^{11}$ , our principal quantum number values range from 50 to 81.

### 7.2.1 Rydberg state detection

The negative polarisability of Rydberg atoms leads to a blue light-shift of the Rydberg levels under exposure to the dipole trap beam, which causes atoms in the Rydberg state to photo-ionise. Rydberg atoms are expelled from the trap before decaying back to the ground state due their long lifetime ( $\tau \geq 60 \mu\text{s}$  for  $n \geq 50$ ). Thus, Rydberg state detection is implemented via photo-ionisation using the dipole trap beam in our experiment.

During coherent Rydberg excitation, the dipole trap beam is turned off to avoid unwanted AC Stark shift or photo-ionisation. The retention is observed to be better than 98 % for typical duration of less than  $10 \mu\text{s}$ . The dipole trap beam is restored at the end of the excitation to distinguish between ground and Rydberg states population. Every measurement is repeated 100 times to perform statistical analysis, from which we can determine the ground state population  $P_g$  and the corresponding Rydberg population  $P_r = 1 - P_g$ .

Nevertheless, the measurement of the ground state population  $P_g$  would never be perfect due to inherent state preparation and measurement (SPAM) errors. They can be decomposed in three components [124] : detection errors, imperfect optical pumping, false positive errors (e.g. inferring atom loss from the trap due Rydberg excitation while it is due to background gas collisions) and false negative errors (e.g. recapturing a Rydberg atom that has rapidly decay back to the ground state). A full description can be found in [124] and has been estimated for our experiment in the thesis of my colleague [221], giving an estimated achievable Rydberg detection efficiency of 90 %.

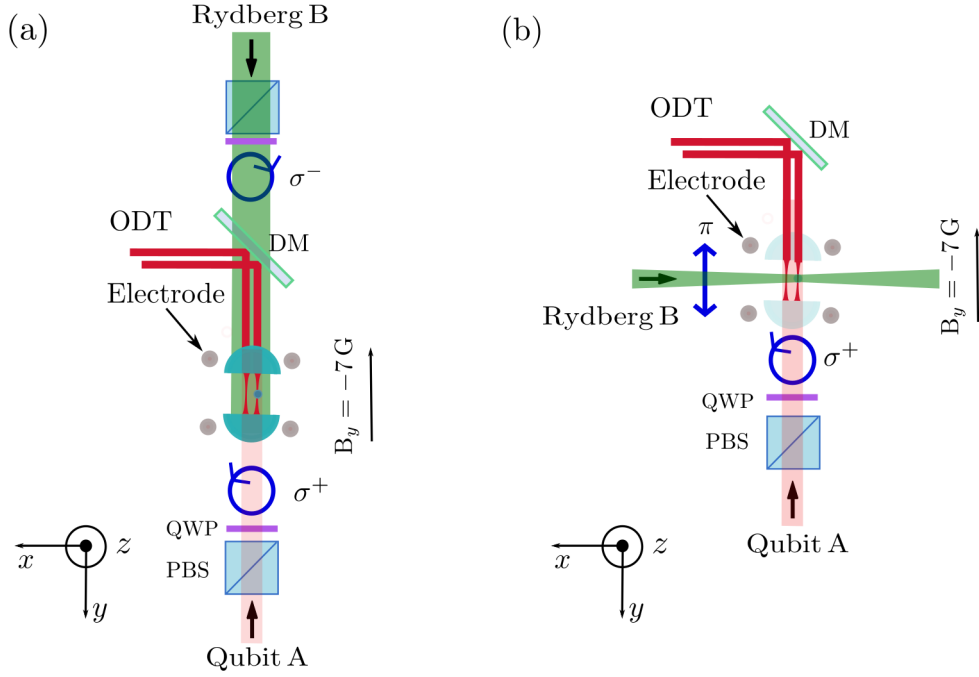


Figure 7.6: Setup for excitation to  $50S_{1/2}$  Rydberg state with laser beams configuration. (a) Two-photon excitation setup with Qubit A polarised  $\sigma^+$  and Rydberg B polarised  $\sigma^-$ , in a counterpropagating configuration to minimise Doppler broadening. (b) Two-photon excitation setup with Rydberg B coming from the side of the lenses  $\pi$ -polarised, orthogonally to Qubit A polarised  $\sigma^+$ .

### 7.2.2 Rydberg excitation setup

Following the EIT experiments in Chap. 6, we have been able to determine which Rydberg states are accessible using Qubit A and Rydberg A/B lasers, in order to perform off-resonant Rydberg excitation. However, going from EIT in cold atoms to single atom two-photon excitation can be extremely challenging, either due to the difficulty in addressing the narrow linewidth of the transition, a frequency mismatch with the theoretical prediction or beams alignment. Thus, we have decided to use the most accurately studied Rydberg state  $50S_{1/2}$  for observing the first off-resonant two-photon excitation.

During Rydberg state spectroscopy and excitation, we load only a single atom to avoid any energy shift that could arise from interactions between trapped atoms. The first attempt for off-resonant excitation has been achieved using Qubit A and Rydberg B lasers, both counter-propagating through the high-NA lenses in order to minimise Doppler effect, as shown in Fig. 7.6 (a). Qubit A laser is using the same path as Qubit B for driving ground-state rotations with a polarisation fixed

to  $\sigma^+$ . The Qubit A beam waist radius is  $14.6 \mu\text{m}$  to ensure the same intensity for each atom when we will drive double atoms experiment later. From the other side of the science chamber, the final dichroic mirror is a Nd:YAG mirror that reflects the 1064 nm ODT beam and transmits Rydberg B beam at 509 nm. Rydberg B beam is combined with the ODT beam on this mirror and addresses the trapping sites through the same final lens as the dipole trap. Rydberg B beam output of the fibre has a waist radius of  $1.7 \mu\text{m}$  which is collimated using a 4 mm lens, giving a measured waist radius of  $380 \mu\text{m}$  and allowing to obtain a final waist radius of  $4 \mu\text{m}$  at the atom. However, our high-NA lenses show a strong chromatic dependence for the working distance and diffraction limited performances, with optimisation made at 852 nm. Using Zemax software, we have determined that Rydberg B beam is focused  $400 \mu\text{m}$  before the lenses, meaning an expected waist radius of  $18 \mu\text{m}$  by the time it reaches the atom, in agreement with observed data.

### 7.2.3 Rydberg excitation beams parameters

In the same way as Sec. 6.2.2, the first attempt to find evidence of single atom Rydberg excitation to  $50S_{1/2}$  in the science chamber has been done on-resonance with the molasses beams, to take advantage of the larger excitation linewidth. The spectroscopy was achieved by applying the molasses and Rydberg B beams out-of-phase with the dipole trap, while scanning an 80 MHz AOM in double pass configuration in the Rydberg laser path, to find the Rydberg resonance. The Rydberg resonance is detected by a significant loss of atoms from the dipole trap. However, we found rapid depumping on a timescale of  $\sim 10 \mu\text{s}$  at a detuning of  $-24 \text{ MHz}$  with respect to the predicted EIT resonant frequency on  $50 S_{1/2}$  state. This detrimental depumping was related to the Qubit A frequency, given by  $\nu_{\text{Qubit A}} = 351\,721.76 \text{ GHz}$ , used in Chap. 6 for EIT on cold atoms. Indeed, this frequency was  $24 \text{ MHz}$  red-detuned from the transition  $|F = 4\rangle \rightarrow |F' = 4\rangle$  using the +1 diffraction order of the AOM in double-pass configuration and a central frequency of  $80 \text{ MHz}$ .

To avoid this problem and ensure that we can adiabatically eliminate the state  $|e\rangle$  for off-resonant excitation, Qubit A is blue-detuned from the  $6P_{3/2}$  intermediate state using the next cavity mode at the frequency  $\nu_{\text{Qubit A}} = 351\,723.25 \text{ GHz}$ .

The detuning of Qubit A with respect to the transition  $|F = 4\rangle \rightarrow |F' = 5\rangle$  is  $\Delta/2\pi = +1.03$  GHz, far greater than both Rabi frequencies  $\Omega_p$  and  $\Omega_c$ , resulting in  $\Delta/2\pi = +870$  MHz using the -1 diffraction order of Qubit A AOM in double-pass configuration with a central frequency of 80 MHz. The -1 order has been favored with respect to the +1 order although it results in smaller detuning. Indeed, the DDS board acts as a sharp frequency filter giving rapid roll off for sideband frequencies over 460 MHz. In order to match EIT conditions, Rydberg B frequency must satisfy  $\nu_{\text{RydB}} = 294\,128.52$  GHz and while the -1 order needs a Rydberg B sideband frequency of  $\nu_{\text{Offset}} = +263.5$  MHz that can easily be cavity locked with an RF power of  $-16$  dB, the +1 order would require a Rydberg B sideband frequency of  $\nu_{\text{Offset}} = -480$  MHz that can only be locked with a minimum of 0 dB.

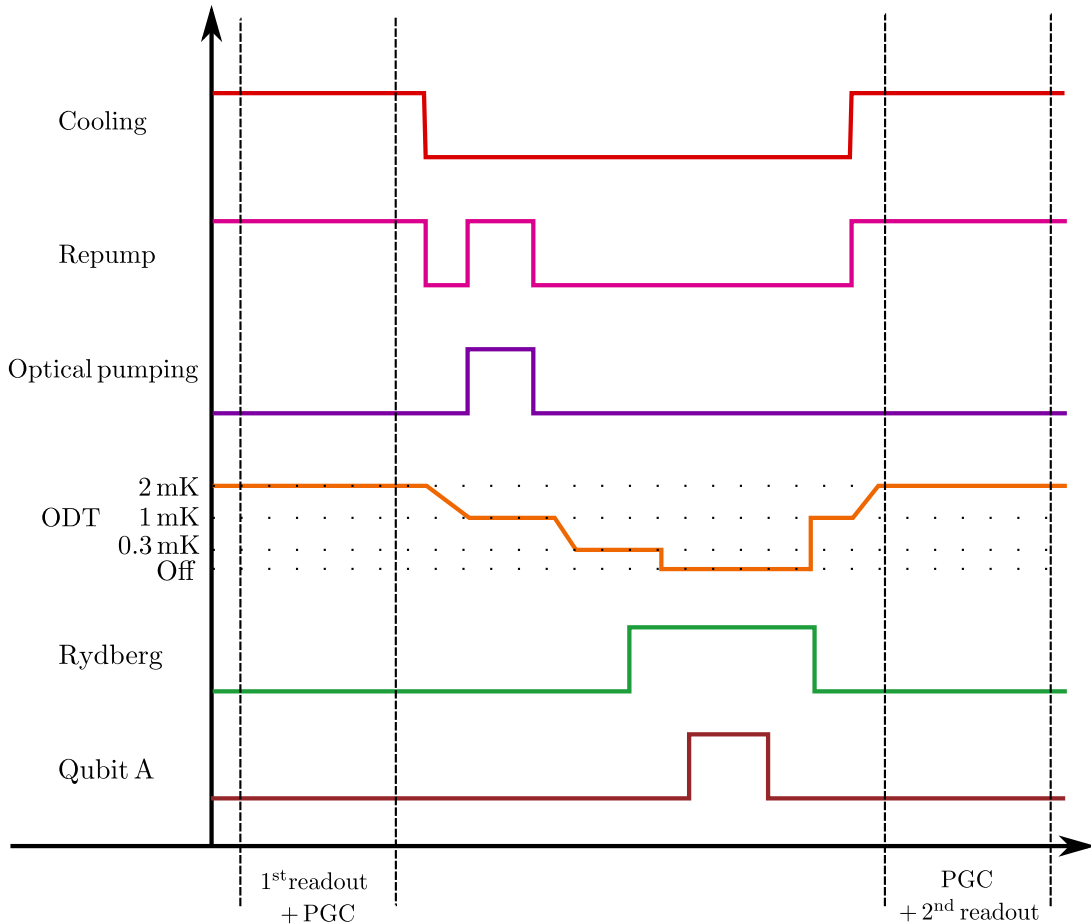


Figure 7.7: Rydberg excitation timing sequence.

### 7.2.4 Rydberg excitation sequence

The single atom spectroscopy of the EIT resonance for  $50 S_{1/2}$  shows agreement with the predicted Rydberg B sideband frequency of  $\nu_{\text{Offset}} = + 263.5$  MHz and has been used to optimise Rydberg B alignment by maximising single atom loss.

Rydberg atom spectroscopy is done similarly to the optimised sequence used for ground-state rotations [123] and a time diagram of the experimental cycle can be found in Fig. 7.7. After verification of single atom loading in the microscopic dipole trap and a 10 ms PGC stage, the dipole trap is adiabatically ramped down to  $U_0 = 1$  mK. The quantisation bias field of  $B_y = -7$  G is turned on, allowing the preparation of atoms in a define state using optical pumping. The dipole trap is adiabatically ramped down until  $U_0 = 0.3$  mK for further cooling of the atom before being turned off for Rydberg excitation. The Qubit A beam is turned on for a period of time  $\tau$  at the middle of Rydberg B pulse to reduce error that could arise on the pulse area associated with Qubit A. Finally, the dipole trap is turned back on with a trap depth of 1 mK to increase the detection efficiency before the atom is illuminated by molasses beams to verify its presence or not. Qubit A is  $\sigma^+$ -polarised whilst Rydberg B is transmitted though a PBS and polarised  $\sigma^-$  with the quarter-waveplate used for cold atoms EIT experiments.

Unfortunately, it turns out that switching to off-resonant excitation with Qubit A didn't show any sign of Rydberg excitation. In order to decouple too many problems among misalignment, transition energy shift due to stray electric field or a wrong polarisation for Rydberg B, we used an alternative beam configuration. Introducing Rydberg B from the side of the lens, orthogonally to Qubit A as shown in Fig. 7.6 (b), allows us to drive the transition from  $|F = 4, m_F = 0\rangle = |1\rangle$  to  $50 S_{1/2}$ .

In this configuration, Rydberg B beam is first collimated using a -50 mm lens in combination with a 100 mm lens, before being focused into the science chamber using a 500 mm lens. Theoretically, we expect a collimated beam waist radius of  $\sim 4$  mm, and a focused waist radius of  $28 \mu\text{m}$  at the atom. The Rayleigh length is around 4.8 mm, meaning that using a micrometer plate to align Rydberg B onto the atoms should be quite forgiving axially.

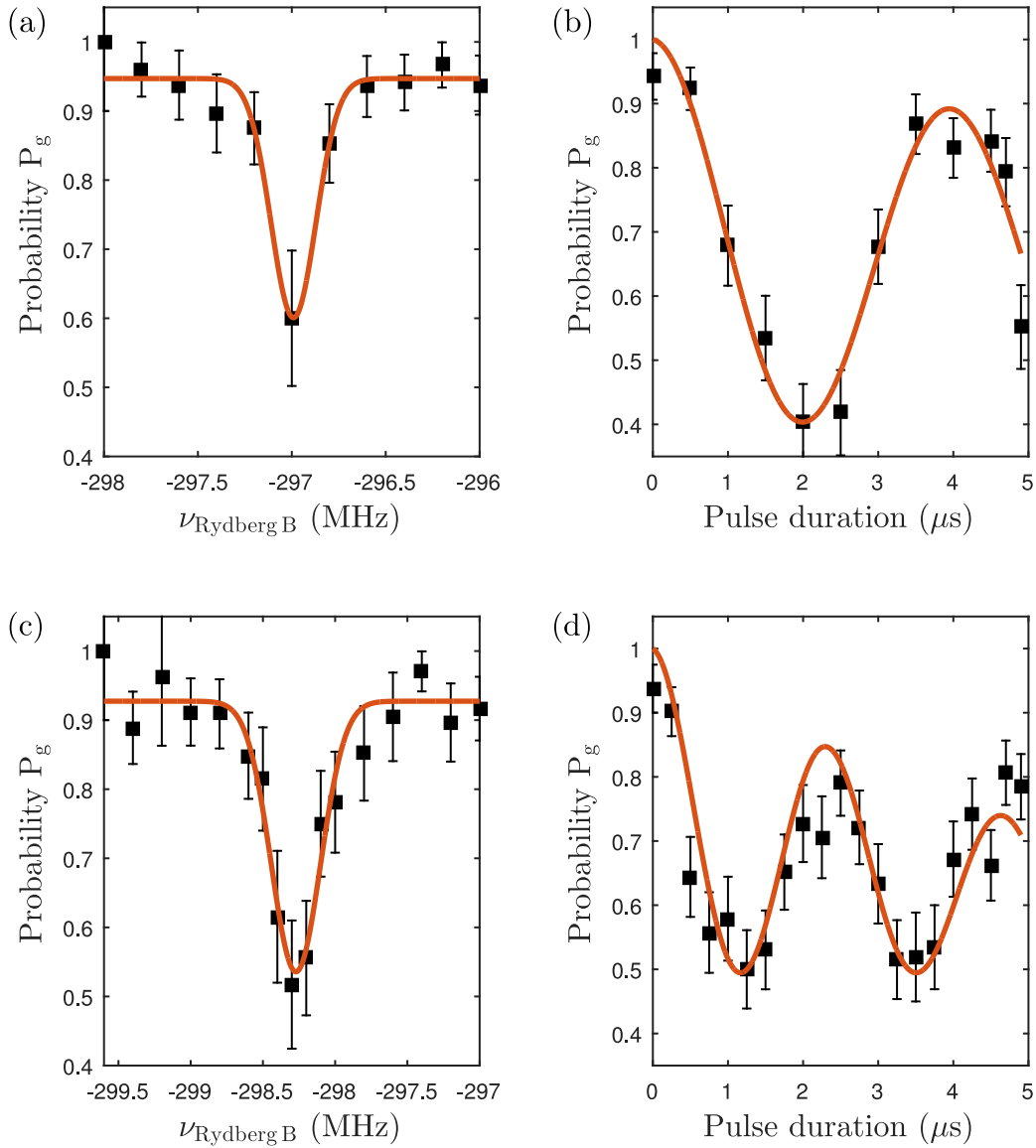


Figure 7.8: (a) Single atom two-photon spectroscopy on the  $|4, 0\rangle$  to  $50S_{1/2}$  transition using a Qubit A laser power of  $P_{\text{Qubit A}} = 200 \text{ nW}$  and a Rydberg B laser power of  $P_{\text{Ryd B}} = 44 \text{ mW}$  for a spectroscopy time of  $\tau = 2 \mu\text{s}$ . (b) Subsequent Rabi Flopping with a fitted two-photon Rabi frequency of  $\Omega_{\text{fit}}/2\pi = 0.25 \text{ MHz}$ , sitting at the resonance frequency at  $\nu_{\text{Ryd B}} = -297 \text{ MHz}$ . (c) Spectroscopy and (d) Rabi oscillations from  $|4, 0\rangle$  to  $50S_{1/2}$  showing agreement with theoretical modelling for AC Stark shift and Rabi oscillations frequency using Qubit A beam power increased by a factor of 3.

Luckily, the  $50S_{1/2}$  state is the lowest Rydberg state accessible, hence the least sensitive to electric field, giving us a chance to observe its spectroscopy in an uncompensated electric field environment. We have performed single atom two-photon spectroscopy on the  $|4, 0\rangle$  to  $50S_{1/2}$  transition using a Qubit A laser power of  $P_{\text{Qubit A}} = 200 \text{ nW}$  with a waist radius  $\omega_{\text{Qubit A}} = 4.6 \mu\text{m}$  and a Rydberg B laser power of  $P_{\text{Ryd B}} = 44 \text{ mW}$  with an estimated waist radius of  $\omega_{\text{Ryd B}} = 28 \mu\text{m}$ .

Using our theoretical model, we are expecting a two-photon Rabi frequency of  $\Omega_{\text{exp}}/2\pi = 0.25$  MHz and a resonance frequency at  $\nu_{\text{RydB}} = -297$  MHz, so that we have used a spectroscopy time of  $\tau = 2 \mu\text{s}$  for Qubit A. The spectroscopy on Fig. 7.8 (a) has been fitted with a Gaussian of the form  $A + B e^{-(\nu_{\text{RydB}} - \nu_0)^2 / 2\sigma^2}$  where A represents the background offset, B is the amplitude,  $\nu_{\text{RydB}}$  is the Rydberg B sideband frequency,  $\nu_0$  is the resonance frequency and  $\sigma$  is the standard deviation. As shown in Fig. 7.8 (a), we observe a perfect matching between the experimental and the predicted resonance frequency  $\nu_{\text{RydB}} = -297$  MHz.

Then, it becomes possible to coherently drive Rabi oscillations between  $|4, 0\rangle$  and  $50 S_{1/2}$ . We use the same protocol as that used for spectroscopy but sitting at  $\nu_{\text{RydB}} = -297$  MHz, we vary the Rydberg B pulse duration. Rabi oscillations on Fig. 7.8 (b) are fitted with an exponentially decaying sinusoidal function  $P_g(t) = 1 - [A - A e^{-t/\tau} \sin(2\pi \nu_{\text{RydB}} t)]$ . This exponential decay takes into account the decoherence. The Rabi frequency of  $\Omega_{\text{fit}}/2\pi = 0.25$  MHz is found to be in total agreement with the predicted one and the decay constant  $\tau = 9.9 \mu\text{s}$  gives a lower bound for  $T_2^*$ . The low amplitude value of  $A < 0.25$  can be attributed to the finite temperature of the atoms, as well as intensity variations of Rydberg B and Qubit A leading to time dependent Rabi frequencies seen by the atom.

In order to further test our calculations, we have done the spectroscopy with a higher beam power. The power of Qubit A beam is roughly increased by a factor of 3 to  $P_{\text{Qubit A}} = 583$  nW with an identical Rydberg B beam power of  $P_{\text{RydB}} = 44$  mW. We expect a differential AC-Stark shift of - 1.4 MHz and an increased two-photon Rabi frequency of  $\Omega_{\text{exp}}/2\pi = 0.42$  MHz. As shown in Fig. 7.8 (c) and (d), the two-photon resonance is shifted from  $\nu_{\text{RydB}} = -297$  MHz to -298.4 MHz and the fitted two-photon Rabi frequency is  $\Omega_{\text{fit}}/2\pi = 0.42$  MHz, in good agreement with the calculated value. However, the decoherence time has decreased to  $\tau = 6.5 \mu\text{s}$ , showing the trade-off between high speed Rabi oscillations and coherence time.

### 7.2.5 Control of the electric field

The high polarisability  $\alpha$  of Rydberg atoms generates their extreme sensitivity to stray electric fields. Indeed, the interaction of a static electric field  $\mathbf{E}$  with the atom leads to a Stark shift of the bare atom energy levels, which exhibits a quadratic dependence at low electric field for low orbital momentum ( $l \leq 3$ ) according to [21]

$$\Delta E = -\frac{1}{2} \alpha \mathbf{E}^2. \quad (7.2)$$

Due to low hyperfine splitting of energy levels under the application of a magnetic field, we are working in the fine state basis  $|n, l, j\rangle$  where the static polarisability  $\alpha$  is evaluated according to [21]

$$\alpha = \sum_{n', l', j', m'_j \neq n, l, j, m_j} \frac{|\langle n', l', j', m'_j | \hat{\mathbf{d}} \cdot \mathbf{E} | n, l, j, m_j \rangle|^2}{E_{n', l', j'} - E_{n, l, j}}, \quad (7.3)$$

where  $\hat{\mathbf{d}}$  is the electric dipole moment of the atom. We have seen in Sec. 2.1 that the radial matrix element  $\langle n', l', j' | \hat{\mathbf{r}} | n, l, j \rangle$  is proportional to  $(n^*)^2$  and the energy difference between two neighboring Rydberg states scales as  $(n^*)^{-3}$ , giving rise to a  $(n^*)^7$  dependence of the static polarisability. For the state  $50 S_{1/2}$ , we have calculated a polarisability of  $\alpha(50 S_{1/2}) = 53.45 \text{ MHz}/(\text{V}/\text{cm})^2$  by taking into account the first 20 pair states. Going towards higher value of  $n$ , as we will require later in this chapter, increases the polarisability dramatically to  $\alpha(69 S_{1/2}) = 534.52 \text{ MHz}/(\text{V}/\text{cm})^2$  and  $\alpha(81 D_{5/2}) = 1667.37 \text{ MHz}/(\text{V}/\text{cm})^2$ . A typical residual electric field of  $450 \text{ mV}/\text{cm}$  at the atoms [230], resulting from patch charges on the dielectric surface of the lenses, would give rise to a shift of  $\sim 5.4 \text{ MHz}$  for  $50 S_{1/2}$  and  $\sim 168.8 \text{ MHz}$  for  $81 D_{5/2}$ . Therefore, any inhomogeneous or stray electric field in the science chamber would lead to a position dependent Stark shift. One understands the necessity to control the DC-electric field environment seen by the atoms as much as possible to avoid possible Rydberg state mixing and decoherence of Rydberg oscillations. As explained in Sec. 5.1.2, we have taken advantage of the work carried out in Antoine Browey's group [230] to minimise the residual electric field at the atoms. First, we took care to passively cancel the amplitude of possible permanent electric fields

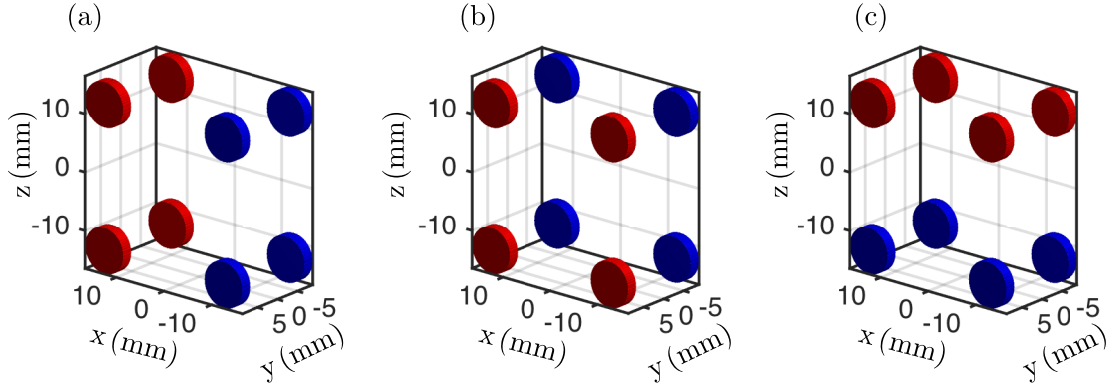


Figure 7.9: Active electric field compensation using 8 electrodes in an octopole configuration. (a) The same potential is applied to four electrodes  $V_x^+$  (red) from the same plane and connecting the other four electrodes from the opposite side to the potential  $V_x^- = 0$  (blue), creating an electric field  $E_x$  in the  $x$ -direction. (b) Creation of an electric field  $E_y$  in the  $y$ -direction. (c) Creation of an electric field  $E_z$  in the  $z$ -direction.

surrounding the atoms by grounding most of the materials around it and covering the lenses using an ITO conductive layer, also grounded to prevent the formation of patch charges.

Active electric field compensation is implemented using 8 electrodes in an octopole configuration [230]. We create an electric field in one direction, for example  $x$ , by applying the same potential  $V_x^+$  over four electrodes from the same plane and connecting the other four electrodes from the opposite side to the potential  $V_x^-$  as shown in Fig. 7.9 (a), creating a difference of potential  $\Delta V_x = V_x^+ - V_x^-$ , hence an electrical field  $E_x$  directly orthogonal to both planes. Applying this rule for  $y$  and  $z$  directions, allows us to create any electric field of the form

$$\mathbf{E} = E_x \mathbf{u}_x + E_y \mathbf{u}_y + E_z \mathbf{u}_z, \quad (7.4)$$

and gives control over amplitude and direction of the applied electric field. In practice, we are varying  $V_i^+$  with  $i = x, y, z$  and grounding the opposite side such that  $V_i^- = 0$  and  $\Delta V_i = V_i^+$ . In order to evaluate the minimum residual electric field we can reach after compensation, we have performed a Stark map by registering the resonance frequency shift of the Rydberg state  $50S_{1/2}$  as a function of the applied voltage across the electrodes for each direction  $x, y$  and  $z$ . Each point of the Stark maps corresponds to the resonance frequency for a given potential  $V_i^+$ .

Direction	$\kappa$ (mV/cm)/V	Monitor (mV)	Residual Electric field (mV/cm)
$x$	$125.29 \pm 0.45$	$1.5 \pm 0.4$	$0.00 \pm 1.45$
$y$	$14.96 \pm 0.03$	$-86.5 \pm 3.4$	$0.00 \pm 1.31$
$z$	$117.12 \pm 0.21$	$4.2 \pm 0.3$	$0.00 \pm 0.98$

Table 7.1: Table resulting from Stark spectroscopy of the Rydberg state  $50S_{1/2}$  with  $\kappa$  the conversion factor from high voltage to electric field. Monitor represents the voltage applied to the home-made high-voltage low-noise amplifier for minimising the residual electric field at the atom. Finally, the last column gives the residual electric field for each components.

Resonance frequencies have been evaluated by applying a frequency scan of  $\pm 1$  MHz around the resonance with a step size of 0.1 MHz and where each data point is the average result over 100 realisations.

Figure 7.10 (a) represents the Stark Map for varying  $\Delta V_x$  with  $\Delta V_y = \Delta V_z = 0$ . It has been fitted using the formula  $C_1 - 1/2 \times C_2 \times (V_x - C_3)^2$  with  $C_1$ ,  $C_2$  and  $C_3$  three constants, which is compared to the theoretical formula

$$\Delta E = E_0 - \frac{1}{2} \alpha (50S_{1/2}) \kappa_x^2 (V_x - V_{0,x})^2, \quad (7.5)$$

where  $E_0$  is the resonant energy transition,  $\kappa$  is the conversion factor from high voltage to electric field and  $V_{0,x}$  represents the high voltage applied to minimise the residual electric field at the atom. The Stark maps have also been realised for the  $y$  and  $z$ -axes, as shown in Fig. 7.10 (b) and (c) respectively, with the experimental results combined in table 7.1. Numerical simulations have been achieved using finite element analysis to compare with the experimental results.

Spectra corresponding to the transverse directions with respect to the quantisation axis, along the  $x$  and  $z$ -axes, show a nice agreement with theoretical calculations for the considered energy shift range below 30 MHz. Due to their symmetric behavior with respect to the quantisation axis, we expect an equality between the conversion factors along  $x$  and  $z$  directions such that  $\kappa_x = \kappa_z$ . This has been validated with theoretical calculations, giving  $\kappa_{x,\text{theo}} = \kappa_{z,\text{theo}} = 124.46$  (mV/cm)/V. The experimental measurements fit the theory with an error better than 1% for the  $x$ -axis and 7% for the  $z$ -axis. However, the Stark map along the quantisation axis  $y$  shows an extreme unconformity between experimental and theoretical results, most likely due

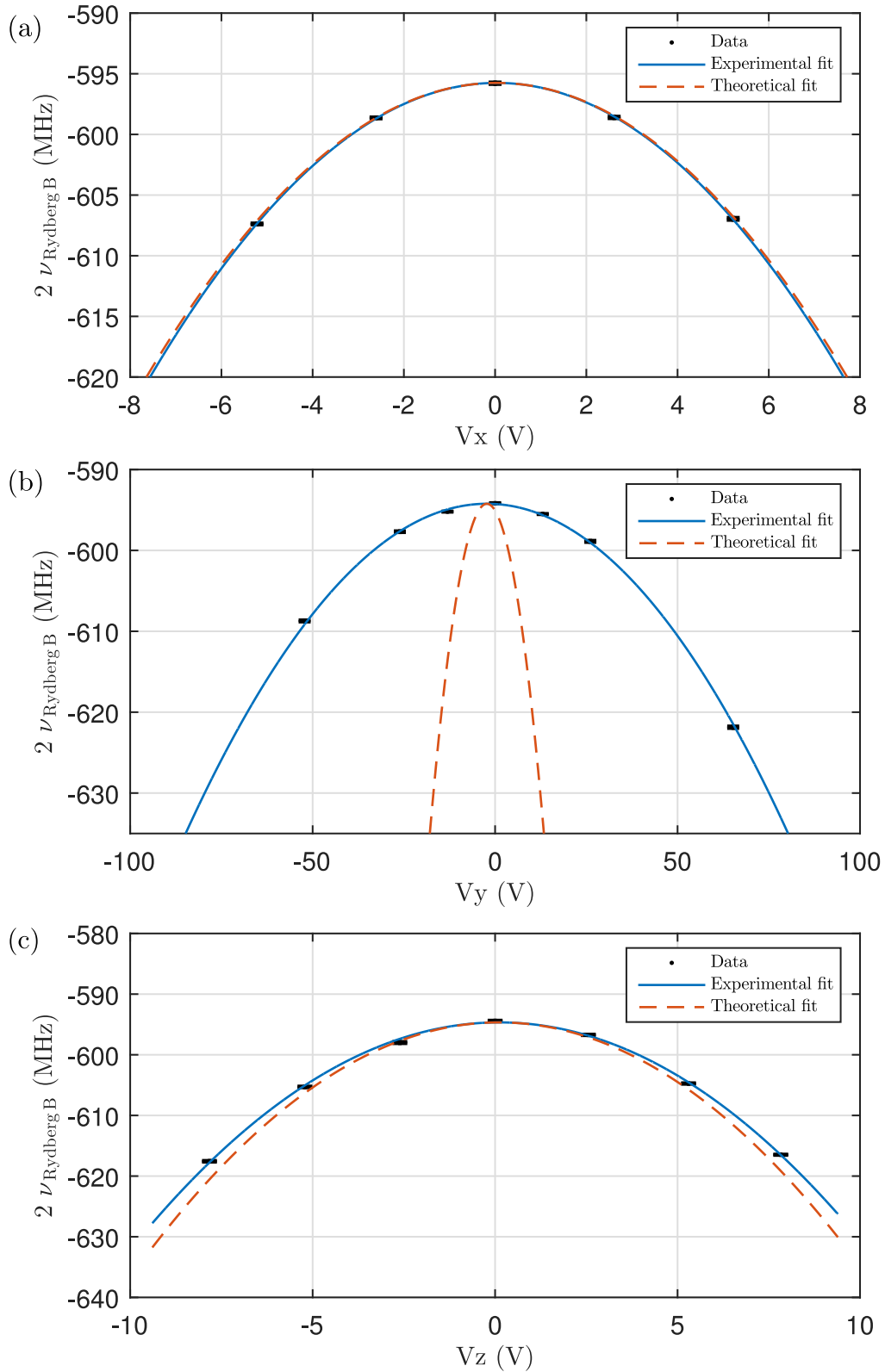


Figure 7.10: Stark spectroscopy of the Rydberg state  $50S_{1/2}$  representing the transition frequency as a function of the potential (a)  $V_x$ , (b)  $V_y$  and (c)  $V_z$ . Resonance frequencies have been evaluated by applying a frequency scan of  $\pm 1$  MHz around the resonance with a step size of 0.1 MHz, where each data points where the average result over 100 realisations.

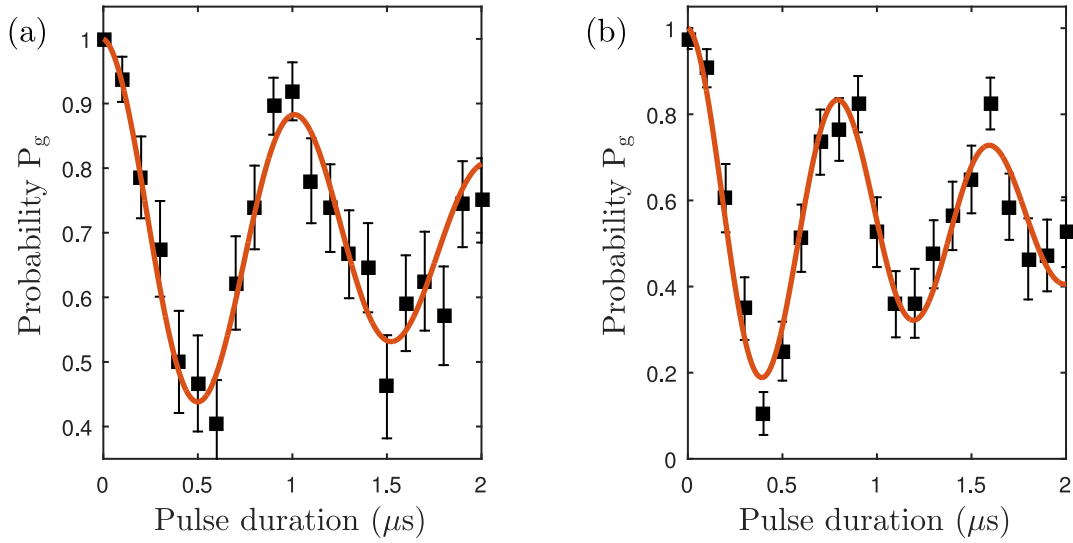


Figure 7.11: Improvement of the Rabi oscillations for  $50S_{1/2}$  Rydberg excitation from (a)  $|4,0\rangle$  with a Rabi frequency of  $\Omega_{\text{fit}} = 2\pi \times 0.98$  MHz or (b)  $|4,4\rangle$  with a Rabi frequency of  $\Omega_{\text{fit}} = 2\pi \times 1.24$  MHz.

to the effect of the ITO lens grounding.

Table 7.1 shows the voltage needed to be applied on the power supply (PSU) monitor to cancel electric fields. This PSU voltage is amplified using a home-made high-voltage low-noise amplifier that can supply up to 1 kV at the electrodes, with an amplification factor of 26.1. In the end, we can compensate for stray electric field with a precision of the order of  $\sim 1\text{mV/cm}$  for single atom experiments, corresponding to induced energy shifts  $\leq 50$  Hz for the  $50S_{1/2}$  Rydberg state.

After this characterisation, we came back to the original configuration for realising coherent Rydberg excitation from ground state to  $50 S_{1/2}$  using both beams counterpropagating through the high-NA lenses, as shown Fig. 7.6 (a). Rydberg B power is 31mW and Qubit A power is 580 nW. Moreover, Rydberg B is focused 50 mm before the aspheric lenses, which corresponds to an expected Rydberg B beam waist radius of  $18 \mu\text{m}$ .

The spectroscopy for off-resonant excitation with Qubit A returns a dip at  $\nu_{\text{RydB}} = -293.8$  MHz. The subsequent Rabi flop is shown in Fig. 7.11 (a) with a fitted Rabi frequency of  $\Omega_{\text{fit}} = 2\pi \times 0.98$  MHz and a decoherence time  $\tau = 4.6 \mu\text{s}$ . The theoretical calculations for the Rabi frequency match with the expected Rydberg waist of  $\omega_{\text{RydB}} = 18 \mu\text{m}$ .

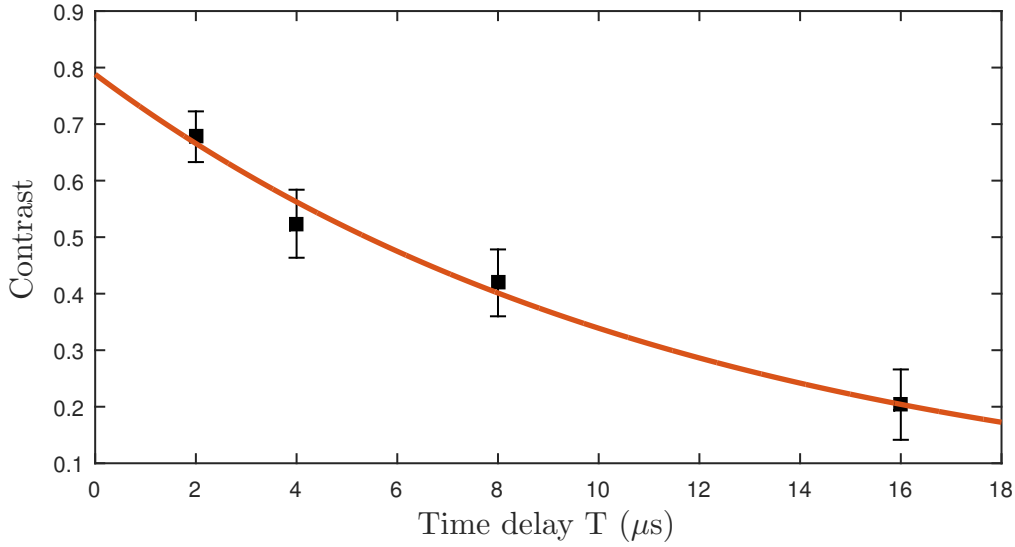


Figure 7.12: Ramsey spectroscopy for the  $|4, 4\rangle \rightarrow 50S_{1/2}$  Rydberg excitation, giving a coherence time  $T_2^* = 11.9 \mu\text{s}$ .

In addition, we have shown that we can increase the speed of Rabi flopping using stretched states optical pumping to  $|F = 4, m_F = 4\rangle = |4, 4\rangle$ , due to higher dipole matrix element for the  $|4, 4\rangle \rightarrow 50S_{1/2}$  transition. Indeed, we observe in Fig. 7.11 (b), a faster Rabi frequency of  $\Omega_{\text{fit}} = 2\pi \times 1.24 \text{ MHz}$  as well as a better contrast  $> 90\%$ . Finally, we have repeated the Ramsey method to obtain informations about the coherence time of the  $|4, 4\rangle \rightarrow 50S_{1/2}$  Rydberg excitation, as shown in Fig 7.12. Applying Ramsey pulse sequence allows us to extract a coherence time  $T_2^* = 11.9 \mu\text{s}$ . This coherence time can be considered as a good starting point to perform quantum logical gate by noticing that applying  $\pi$  – pulse requires only 806 ns,  $\sim 15$  times smaller than  $T_2^*$ .

### 7.2.6 Coherent excitation to Rydberg states $69S_{1/2}$ and $81D_{5/2}$

Now that we have observed well defined Rabi flopping through high-NA lenses, we can move forward by using a Rydberg state with higher principal quantum number for the implementation of Rydberg blockade, as shown in the next section. However, coherent Rydberg excitation is dependent upon stabilised Rabi pulse area. Thus, we have implemented active intensity stabilisation using homebuilt AOM-based noise

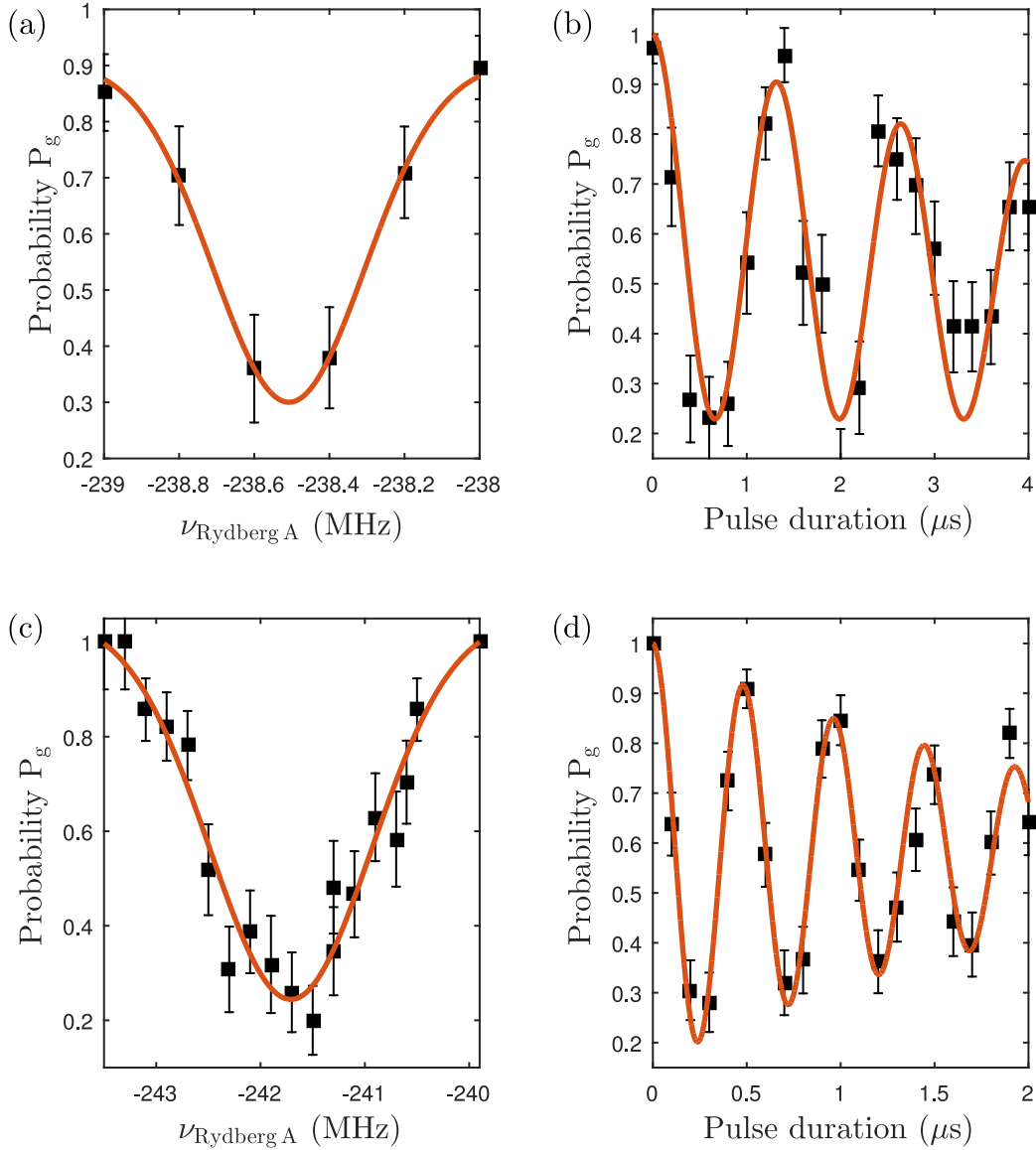


Figure 7.13: (a) Spectroscopy of the  $|4, 4\rangle \rightarrow 69S_{1/2}$  transition with a spectroscopy time of  $\tau_{\text{spec}} = 1\mu\text{s}$  and  $\nu_{\text{Rydberg A}} = -238.5\text{ MHz}$ , (b) Rabi Flopping with  $\Omega_{\text{fit}}/2\pi = 0.76\text{ MHz}$  and  $\tau = 7.4\mu\text{s}$ , (c) Spectroscopy of  $69S_{1/2}$  with a spectroscopy time of  $\tau_{\text{spec}} = 250\text{ ns}$  and  $\nu_{\text{Rydberg A}} = -241.71\text{ MHz}$  and (d) Rabi Flopping with  $\Omega_{\text{fit}}/2\pi = 2.07\text{ MHz}$  and  $\tau = 2.2\mu\text{s}$ .

eater on Rydberg A & B lasers. This allows us to stabilise the amplitude of the Rydberg A & B beams to better than 1 % for optimising the coherence time of the Rabi oscillations, knowing that Qubit A has less than 2 % amplitude fluctuations over a day.

The EIT experiment on cold atoms has already been achieved on the  $69S_{1/2}$  Rydberg state in Sec. 6.3.1 and seems a good state to begin with. The first spectroscopy on the  $|4, 4\rangle \rightarrow 69S_{1/2}$  transition is performed with a Qubit A power  $P_{\text{Qubit A}} = 670\text{ nW}$

and a Rydberg A power  $P_{\text{Rydberg A}} = 92.5 \text{ mW}$ . Figure 7.13 (a) shows a resonance at  $\nu_{\text{Rydberg A}} = -238.5 \text{ MHz}$  for a spectroscopy time of  $\tau_{\text{spec}} = 1 \mu\text{s}$ . Subsequent Rabi flopping has been achieved in Fig. 7.13 (b) with a two-photon Rabi frequency of  $\Omega_{\text{fit}}/2\pi = 0.76 \text{ MHz}$  and a decoherence time  $\tau = 7.4 \mu\text{s}$ .

Changing the value of the attenuator in the fast-feedback branch of Rydberg A, as explained in Sec. 4.4.2, allows us to reduce the amplitude of the servo-bumps at  $\pm 1.1 \text{ MHz}$  before trying to drive faster oscillations with  $P_{\text{Qubit A}} = 5.2 \mu\text{W}$  and  $P_{\text{Rydberg A}} = 89.5 \text{ mW}$ . Figure 7.13 (c) illustrates the spectroscopy with a dip at

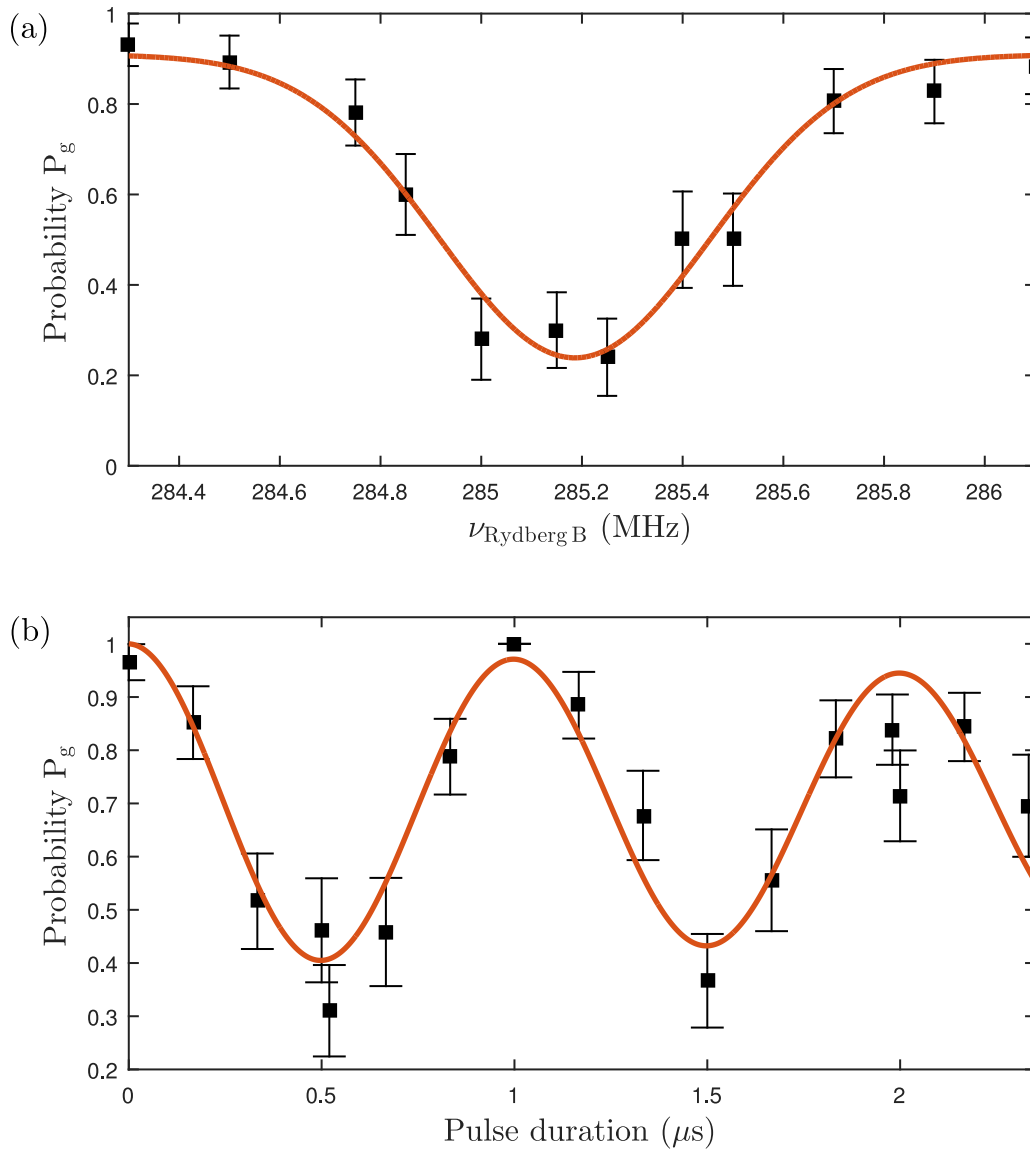


Figure 7.14: (a) Spectroscopy of  $|4,4\rangle \rightarrow 81D_{5/2}$  transition with a spectroscopy time of  $\tau_{\text{spec}} = 500 \text{ ns}$  and  $\nu_{\text{Rydberg B}} = -285.04 \text{ MHz}$  and (b) Rabi Flopping with  $\Omega_{\text{fit}}/2\pi = 1.05 \text{ MHz}$  and  $\tau = 10 \mu\text{s}$ .

$\nu_{\text{Rydberg A}} = -241.7$  MHz for a spectroscopy time of  $\tau_{\text{spec}} = 0.25 \mu\text{s}$  and Fig. 7.13 (d) shows Rabi flopping with a substantially increased two-photon Rabi frequency of  $\Omega_{\text{fit}}/2\pi = 2.07$  MHz and a decoherence time  $\tau = 2.2 \mu\text{s}$ .

Following coherent Rydberg excitation on the  $|4, 4\rangle \rightarrow 69S_{1/2}$ , C. J. Picken [123] has extended the results and shown that we can perform Rydberg state excitation from the  $|F = 4, m_F = 0\rangle = |1\rangle$  to the Rydberg state  $69S_{1/2}$ . A Ramsey sequence has been realised to characterise the coherence time associated with the  $|4, 0\rangle \rightarrow 69S_{1/2}$  transition. The experiment demonstrates ground-Rydberg coherence time, with an inhomogeneous dephasing time of  $T_2^* = 15 \pm 4 \mu\text{s}$  [123] that appears to be mainly Doppler limited.

In order to perform the EIT mesoscopic quantum gate, the simulations proved (see Chap. 8) that using the  $81D_{5/2}$  Rydberg state would be an ideal candidate to operate with, which is accessible via a two-photon excitation via Qubit A and Rydberg B lasers. Spectroscopy on the  $81D_{5/2}$  Rydberg state is depicted on Fig. 7.14 (a) with  $P_{\text{Qubit A}} = 453$  nW and  $P_{\text{Rydberg B}} = 74$  mW, showing a resonance at  $\nu_{\text{Rydberg B}} = 285.04$  MHz for a spectroscopy time of  $\tau_{\text{spec}} = 500$  ns. The Rabi oscillations on Fig. 7.14 (a) exhibit a higher coupling to the  $D$  state with a two-photon Rabi frequency of  $\Omega_{\text{fit}}/2\pi = 1.05$  MHz and a decoherence time  $\tau = 10 \mu\text{s}$ , a very promising result to begin with for the mesoscopic EIT gate implementation.

### 7.2.7 Rydberg excitation limitations

The damping of the Rabi oscillations can be attributed to several causes, the first one is due to finite lifetime of the Rydberg state. However, due to the high values of the principal quantum number  $n$  taken in our experiment, it's definitely not the limiting factor considering lifetimes of  $134 \mu\text{s}$  and  $163 \mu\text{s}$  for  $69S_{1/2}$  and  $81D_{5/2}$  Rydberg states respectively.

Another contribution is due to finite temperature of the atoms in the traps with  $T \sim 10 \mu\text{K}$ , leading to Doppler broadening. The two-photon detuning becomes a random variable [165, 230, 261, 262] defined by a Gaussian probability distribution whose standard deviation is given by  $\sigma = |\mathbf{k}_R + \mathbf{k}_G| \times v_{th} \sim 2\pi \times 20$  kHz where  $v_{th} = \sqrt{k_B T/m} \sim 0.025$  m/s is the thermal velocity of the atom and  $\mathbf{k}_R, \mathbf{k}_G$  are

the wavevectors associated with the red and green beams. Its contribution has been minimised by using a counterpropagating configuration during Rydberg excitation.

The third contribution corresponds to the spontaneous emission from the intermediate state  $6P_{3/2}$ , which has been ruled out through the observation of the symmetric damping of the oscillations and has been further verified in my colleague's PhD thesis [221] by varying Qubit A power. One can also think about the spatially dependent AC-Stark shift arising from the finite width of the Gaussian pulse. This may vary the Rabi frequency seen by the atom from shot to shot. However, due to the small displacement of the atom during the excitation ( $< 1 \mu\text{m}$ ), it can't be a significant part responsible for the damping.

The main contribution to the damping of the oscillations can be attributed to the laser phase noise [124] due to the limited servo bandwidth of the loop that controls the lasers, as explained in Sec. 4.6.2. Indeed, the PDH servo-loop reduces low frequency noise below the servo bandwidth but is not able to suppress high-frequency noise, which even increases at the servo-bumps frequencies of  $\pm 1.1 \text{ MHz}$ . However, our typical Rydberg Rabi frequencies are  $\sim 2\pi \times 1 \text{ MHz}$ , which are unfortunately situated at the servo bumps position and are responsible for the main dephasing mechanism of the Rabi oscillations.

This limitation has been overcome by the Harvard group, leading to a major increase of the coherence time up to  $27 \mu\text{s}$  [125] using passive filtering of the servo-bumps from the cavity itself, in order to inject a new slave diode used for Rydberg excitation. Our group is going to upgrade the home-made Rydberg laser with a Ti:Sapph laser for additional noise-suppression.

### 7.3 Observation of Rydberg blockade between two single atoms

As explained in Sec. 2.3, the Rydberg blockade regime [91] appears when the energy of the doubly excited state  $|rr\rangle$  is larger than the excitation bandwidth, such that the excitation of one atom in the Rydberg state prevents the excitation of a nearby second atom within a certain sphere defined by the blockade radius  $R_b = \left(\frac{C_6}{\Omega}\right)^{1/6}$  in

the case of the van der Waals interactions. The experimental timing protocol is the same as previously used in Sec. 7.2.6 for driving Rydberg excitations and only differs by the fact that we must simultaneously excite two atoms instead of one. However, the traps are loaded stochastically and only  $\sim$  a quarter of the trials contain two atoms simultaneously present, which explains the need for post-selecting after the first readout stage. The datasets are separated between the events where only one trap is loaded, used for single atom excitation datasets, to the one where both atoms are present for observation of the dipole blockade regime, requiring to repeat the experiment 200 times for statistical analysis.

From the expression of the van der Waals interaction  $\Delta E = -C_6/R^6$  (see Sec. 2.2.1), it appears that one way to increase the interaction strength is to reduce the distance  $R$  between both atoms. Experimentally, we can't reduce the separation distance lower than  $6 \mu\text{m}$  if we want to discriminate between each sites due to possible hopping of atoms between traps. To calculate the magnitude of the interaction, we have evaluated the coefficient  $C_6$  as explained in Sec. 2.2.2.

We first drove single atom Rydberg excitation from the ground state  $|g\rangle = |F = 4, m_F = 4\rangle$  to the Rydberg state  $|r\rangle = 69 S_{1/2}$  for each atoms 1 and 2 alone using a Qubit A laser power of  $P_{\text{Qubit A}} = 574 \text{ nW}$  and a Rydberg A laser power of  $P_{\text{Rydberg A}} = 90 \text{ mW}$ , as shown in Fig. 7.15 (a). It results in Rabi oscillations with an identical single atom Rabi frequency of  $\Omega_1/2\pi \sim \Omega_2/2\pi = 0.69 \pm 0.01 \text{ MHz}$  for atoms 1 and 2, assuring us that both atoms are seeing the same laser intensities. For the  $|69 S_{1/2}, 69 S_{1/2}\rangle$  pair state, we obtain the coefficient  $C_6 = -575 \text{ GHz}\cdot\mu\text{m}^6$ , corresponding to a Rydberg blockade radius of  $R_b \sim 9.7 \mu\text{m}$  for a Rabi frequency of  $\Omega/2\pi = 0.69 \text{ MHz}$ . The theoretical energy shift expected for both atoms placed at a distance of  $6 \mu\text{m}$  is  $\Delta E/\hbar \sim 2\pi \times 12.3 \text{ MHz}$ , which is an order of magnitude higher than the typical Rabi frequency of  $\Omega/2\pi \sim 1 \text{ MHz}$ , verifying the dipole blockade condition  $\Delta E/\hbar \gg \Omega$ .

The evidence of Rydberg blockade is observed on the transition between the double-atom ground state  $|gg\rangle$  with  $|g\rangle = |F = 4, m_F = 4\rangle$  to the Rydberg state  $|rr\rangle$  where  $|r\rangle = |69 S_{1/2}\rangle$  when atoms 1 and 2 are simultaneously loaded.

Four different probabilities are related to the double-atom excitation :

- $P_{gg}$  represents the probability that both atoms remain in the ground state.
- $P_{rg}$  and  $P_{gr}$  represent the probability for one atom to be promoted to the Rydberg state while the other one stays in ground state.
- $P_{rr}$  represents the probability that both atoms are excited in the Rydberg state.

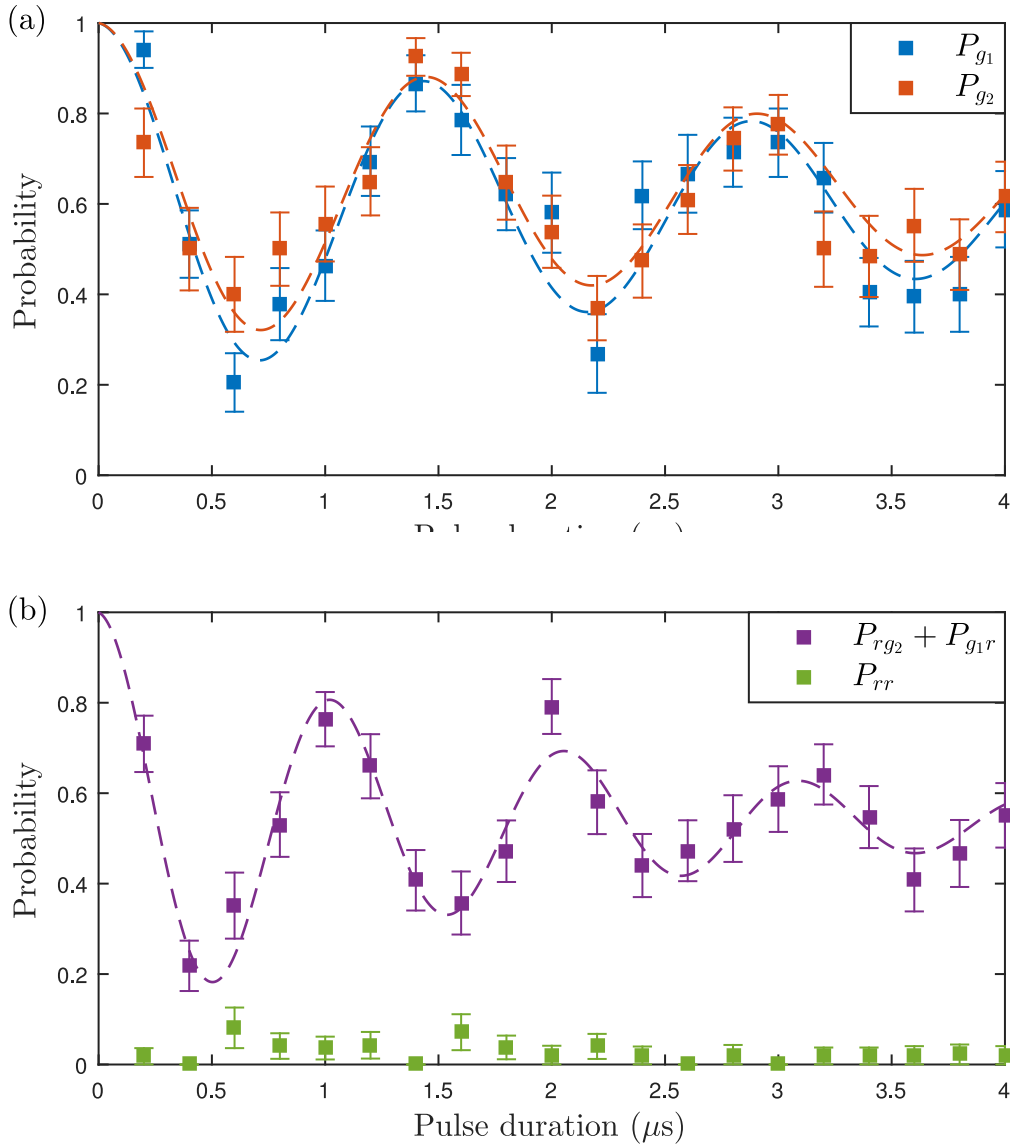


Figure 7.15: (a) Single atom Rabi flopping from the ground state  $|g\rangle = |F = 4, m_F = 4\rangle$  to the Rydberg state  $|r\rangle = 69S_{1/2}$  for each atoms 1(blue) and 2(red) alone, resulting in identical Rabi frequency  $\Omega_1/2\pi \sim \Omega_2/2\pi = 0.69 \pm 0.01$  MHz. (b) Probability  $P_{rg_2} + P_{g_1r}$  (purple) of exciting only one of the two atoms in the Rydberg state with an enhanced Rabi frequency  $\Omega' \sim \sqrt{2}\Omega_1$  showing collective excitation to the entangled state  $|\mathcal{W}\rangle$  and suppression of the doubly excited state probability with  $P_{rr} \ll 5\%$  (green).

Figure 7.15 (b) shows the probability  $P_{rg_2} + P_{g_1r}$  of exciting only one of the two atoms in the Rydberg state. This probability oscillates at a Rabi frequency  $\Omega' / 2\pi = 0.97 \pm 0.01$  MHz, much faster than the corresponding single atom excitation probability. The ratio of  $\Omega' / \Omega_1 = 1.41 \pm 0.02$  confirms the creation of a collective excitation towards the entangled state  $|\mathcal{W}\rangle$  (see Sec. 2.3), leading to an enhanced Rabi frequency  $\Omega' \sim \sqrt{2} \Omega_1$ .

However, guided by our goal to perform the mesoscopic EIT gate based on Rydberg-Rydberg interaction, we have demonstrated in Sec. 7.2.6 coherent control of single atom in the Rydberg state  $81D_{5/2}$  due to the opportunity to achieve strong coupling Rabi frequency  $\Omega_c$  from higher dipole matrix element. Moreover, for a fixed interatomic distance, using the state  $81D_{5/2}$  allows us to take advantage of the scaling laws for  $C_6 \sim n^{*11}$ , in order to enhance the interaction strength and increase the blockade efficiency.

Single atom Rydberg excitation from the ground state  $|g\rangle = |F = 4, m_F = 4\rangle$  to the Rydberg state  $|r\rangle = |81 D_{5/2}\rangle$  results in Rabi oscillations with an identical single atom Rabi frequency of  $\Omega'_1 / 2\pi \sim \Omega'_2 / 2\pi = 0.72 \pm 0.02$  MHz, using a Qubit A laser power of  $P_{\text{Qubit A}} = 210$  nW and a Rydberg B laser power of  $P_{\text{Rydberg B}} = 74$  mW, as shown in Fig. 7.16 (a).

For  $|81 D_{5/2}, 81 D_{5/2}\rangle$  pair state, we find a coefficient  $C_6 = -1626$  GHz $\cdot\mu\text{m}^6$ , corresponding to an extended Rydberg blockade radius of  $R_b \sim 11.5 \mu\text{m}$  for a Rabi frequency of  $\Omega / 2\pi = 0.72$  MHz. The theoretical energy shift expected for the Rydberg state  $81 D_{5/2}$  with both atoms placed at a distance of  $6 \mu\text{m}$  is  $\sim 34.9$  MHz, three times higher than for the state  $69S_{1/2}$ . The probability  $P_{rg_2} + P_{g_1r}$  of exciting only one of the two atoms in the Rydberg state is shown Fig. 7.16 (b) and oscillates at a Rabi frequency  $\Omega'' / 2\pi = 1.05 \pm 0.03$  MHz. The ratio of  $\Omega'' / \Omega'_1 = 1.46 \pm 0.04$  MHz confirms again the creation of the collective excitation towards the entangled state  $|\mathcal{W}\rangle$  with an enhanced Rabi frequency  $\Omega'' \sim \sqrt{2} \Omega'_1$ .

In order to corroborate the realisation of an entangled state, one can observe in Fig. 7.15 (b) and Fig. 7.16 (b) that the probability of exciting the atoms at the same time is negligible, with  $P_{rr} \ll 5\%$  for both excitations. Finally, despite the anisotropy of the dipole-dipole interaction for  $D$  states compare to the isotropic

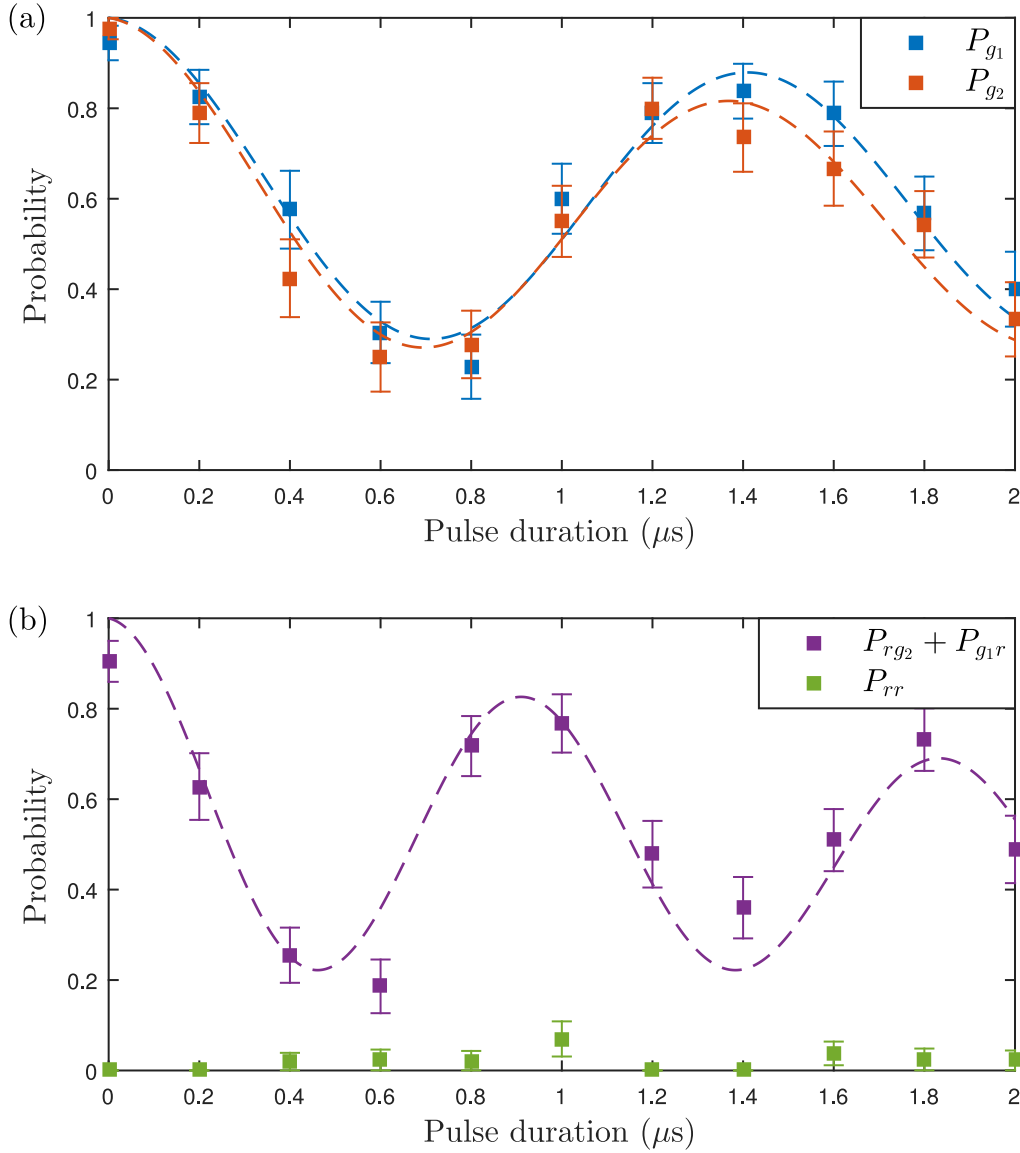


Figure 7.16: (a) Single atom Rabi flopping from the ground state  $|g\rangle = |F = 4, m_F = 4\rangle$  to the Rydberg state  $|r\rangle = 81 D_{5/2}$  for each atoms 1(blue) and 2(red) alone, resulting in identical Rabi frequency  $\Omega'_1/2\pi \sim \Omega'_2/2\pi = 0.72 \pm 0.02$  MHz, increased with respect to the previous excitation to  $69 S_{1/2}$ . (b) Probability  $P_{rg2} + P_{g1r}$  (purple) of exciting only one of the two atoms in the Rydberg state with an enhanced Rabi frequency  $\Omega'' \sim \sqrt{2}\Omega'_1$  showing collective excitation to the entangled state  $|\mathcal{W}\rangle$  and suppression of double excitation to the state  $|rr\rangle$  with  $P_{rr} \ll 5\%$  (green).

case of  $S$  states (see Sec. 2.2.2), we found a better coupling for  $81 D_{5/2}$  Rydberg state and strong Rydberg blockade, a promising result for the implementation of the mesoscopic EIT gate.

### 7.3.1 Entanglement between two atoms in their ground state

The entangled state  $|\mathcal{W}\rangle$  involves the Rydberg state  $|r\rangle$  which can't be trapped, limiting its lifetime and utility to perform quantum information. Therefore, the idea consists in transferring the Rydberg state to the hyperfine ground state [110] to create a long-lived entangled state.

Following coherent Rydberg excitation and demonstration of Rydberg blockade on the  $|4, 4\rangle \rightarrow 69S_{1/2}$  transition, C. J. Picken [123] has extended the results above and shown that we can perform Rydberg state excitation from the  $|F = 4, m_F = 0\rangle = |1\rangle$  to the Rydberg state  $69S_{1/2}$  as well as Rydberg blockade. This opens the possibility to work in the clock state basis  $\{|F = 3, m_F = 0\rangle = |0\rangle, |F = 4, m_F = 0\rangle = |1\rangle\}$  for creating a maximally entangled Bell state [123]

$$|\Psi^+\rangle = \frac{|01\rangle + |10\rangle}{\sqrt{2}}. \quad (7.6)$$

In order to create this Bell state, we need to combine Rydberg excitation with ground state rotations. The state preparation has been evaluated using the fidelity, which for the state  $|\Psi^+\rangle$  is defined as  $\mathcal{F} = \langle\Psi^+|\rho_{\text{exp}}|\Psi^+\rangle$ , quantifying the overlap between the experimental state described by the density matrix  $\rho_{\text{exp}}$  and the target Bell state  $|\Psi^+\rangle$ . The extracted fidelity of  $\mathcal{F} \sim 0.63(3)$  is far from the classical limit of  $\mathcal{F} = 0.5$  to go beyond for proof of entanglement, while the loss-corrected fidelity is found to be  $\mathcal{F}_{\text{pairs}} = \mathcal{F}/p_{\text{recap}} = 0.81(5)$  [123]. This work represents the highest post-selected ground-state entanglement using Rydberg blockade and comparable to that obtained via Rydberg dressing [122]. Laser phase-noise arising from the servo-feedback is the main limiting factor and its reduction could potentially lead to higher ground state entanglement fidelity. It has been possible to perform ground-rydberg operations with  $\mathcal{F} > 0.97$  fidelity [125] and more recently [117] high fidelity two-qubit and multi-qubit operations with  $\mathcal{F} > 0.95$ .

## 7.4 Summary

We have demonstrated fast ground state rotations, allowing us to perform single qubit gate on the Bloch sphere with long coherence time. We have equally shown our ability to perform high contrast Rabi oscillations on the Rydberg states  $50S_{1/2}$ ,  $69S_{1/2}$  and  $81D_{5/2}$  with fast transfer ( $\sim 2\pi \times 2$  MHz), using precise control of the electric field environment and laser beam intensity stabilisation. We have demonstrated dipole blockade between two single atoms separated by  $6\ \mu\text{m}$  for excitation to the Rydberg states  $69S_{1/2}$  and  $81D_{5/2}$ , with observation of the collective enhancement of the Rabi frequency arising from the preparation of the entangled state  $|\mathcal{W}\rangle$ . This is confirmed by an almost complete suppression of the doubly excited state probability of  $P_{rr} \ll 5\%$ . Due to the limited lifetime of the entangled state  $|\mathcal{W}\rangle$ , we have reported on the mapping to the hyperfine ground state to create a long-lived and maximally entangled Bell state  $|\Psi^+\rangle$  with a loss-corrected fidelity of  $\mathcal{F}_{pairs} = \mathcal{F}/p_{recap} = 0.81(5)$  [123]. This work represents the highest post-selected ground-state entanglement using Rydberg blockade and comparable to that obtained via Rydberg dressing [122]. This gives us a good starting point for further investigation of quantum information processing protocols such as the mesoscopic EIT gate.

# Chapter 8

## Mesoscopic Rydberg EIT Gate

Our ability to perform double-atom experiment offers the possibility to create a two-qubit quantum gate based on Rydberg blockade with high-fidelity [68, 91, 112, 114, 117, 258]. Scaling up from single atom to atomic ensembles, the blockade effect leads to a collective enhancement of the Rabi frequency for an effective two-level atom called a “super-atom” (see Sec. 2.3), which for  $N$  atoms is proportional to  $\sqrt{N}$  as we have shown in Sec. 7.3.

However, whilst this collective enhancement allows faster gate operations, it has the drawback of being sensitive to the number fluctuations expected for Poisson loading statistics  $\propto \sqrt{N}$  which limits the ability to perform high fidelity operations without dynamic control of amplitude, detuning and phase of the excitation lasers [263]. To circumvent this problem, an original gate scheme has been proposed by Müller *et al.* [158] to entangle a mesoscopic ensemble of atoms with a single atom in a single step using electromagnetically induced transparency (EIT).

As a proof of principle, we propose to demonstrate the possibility to create a mesoscopic controlled-NOT (cNOT) gate using our experiment, with a single control atom acting onto a single target atom.

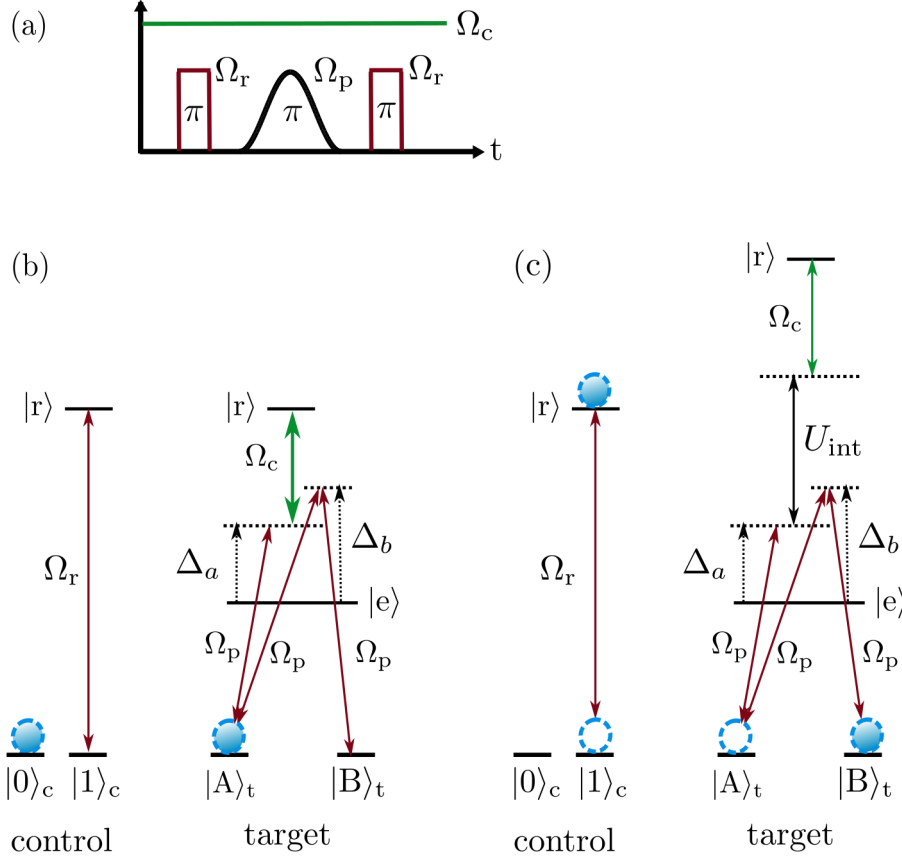


Figure 8.1: (a) Schematic of the laser pulse sequence for the EIT gate. (b) If the control atom is initially in state  $|0\rangle_c$ , the target atom adiabatically follows the dark state  $|D\rangle$  due to EIT conditions, leading to  $|A\rangle_t \rightarrow |A\rangle_t$ . (c) If the control atom is initially in state  $|1\rangle_c$ , the target atom is transferred from  $|A\rangle_t$  to  $|B\rangle_t$ .

## 8.1 Overview of the Rydberg EIT gate

As shown in Sec. 1.2, the two-qubit cNOT gate is given by the following truth table,

$$|0\rangle_c |A\rangle_t \rightarrow |0\rangle_c |A\rangle_t, \quad (8.1)$$

$$|0\rangle_c |B\rangle_t \rightarrow |0\rangle_c |B\rangle_t, \quad (8.2)$$

$$|1\rangle_c |A\rangle_t \rightarrow |1\rangle_c |B\rangle_t, \quad (8.3)$$

$$|1\rangle_c |B\rangle_t \rightarrow |1\rangle_c |A\rangle_t, \quad (8.4)$$

where the subscripts  $c$  and  $t$  are the notations for control and target atoms. The effect of the cNOT gate is to flip the state of the target qubit conditionally to the

control qubit being in the state  $|1\rangle_c$ .

The excitation scheme required for the quantum gate protocol is represented on Fig. 8.1 (b) & (c). The control qubit is encoded in the the long-lived and magnetically insensitive clock state basis  $|0\rangle_c = |F = 3, m_F = 0\rangle$  and  $|1\rangle_c = |F = 4, m_F = 0\rangle$ . It can be excited from  $|1\rangle_c$  to the Rydberg state  $|r\rangle$  using a two-photon excitation with a Rabi frequency  $\Omega_r$ , as performed in Sec. 7.2. The target atom involves the two states  $|A\rangle_t = |F = 4, m_F = 0\rangle$  and  $|B\rangle_t = |F = 3, m_F = 0\rangle$ . This states can be coherently coupled via Raman transitions using Qubit B laser, as illustrated in Sec. 7.1. Single qubit rotation can be done using a time-dependent Rabi frequency  $\Omega_p(t)$  and a detuning  $\Delta_b = \omega_{B_t} - \omega_e$  from the intermediate state  $|e\rangle = 6P_{3/2}$ .

Additionally, in order to be able to work in the Rydberg EIT regime, a two-photon transition can be driven using Qubit A laser for the transition  $|A\rangle_t \rightarrow |e\rangle$  with a time dependent Rabi frequency  $\Omega_p(t)$  and a detuning  $\Delta_a = \omega_{A_t} - \omega_e$ , combined to Rydberg B laser for the transition  $|e\rangle \rightarrow |r\rangle$  with a Rabi frequency  $\Omega_c$  ( $\Omega_c > \Omega_p^{\max}$ ) and a detuning  $\Delta_c = \omega_r - \omega_e$ .

The Hamiltonian for the target atom in the rotating wave approximation is given by  $\mathcal{H} = \mathcal{H}_0 + \mathcal{H}_{al}$  where

$$\mathcal{H}_0 = \hbar\omega_{A_t}|A\rangle_t\langle A| + \hbar\omega_{B_t}|B\rangle_t\langle B| + \hbar\omega_e|e\rangle\langle e| + \hbar\omega_r|r\rangle\langle r|, \quad (8.5)$$

and

$$\mathcal{H}_{al} = \hbar\frac{\Omega_p(t)}{2}(|e\rangle_t\langle A| + \text{h.c.}) + \hbar\frac{\Omega_p(t)}{2}(|e\rangle_t\langle B| + \text{h.c.}) + \hbar\frac{\Omega_c}{2}(|r\rangle\langle e| + \text{h.c.}). \quad (8.6)$$

In the basis ( $|A\rangle_t, |B\rangle_t, |e\rangle, |r\rangle$ ), this results in a Hamiltonian of the form

$$\mathcal{H} = \hbar \begin{pmatrix} 0 & 0 & \Omega_p(t)/2 & 0 \\ 0 & -(\Delta_a - \Delta_b) & \Omega_p(t)/2 & 0 \\ \Omega_p(t)/2 & \Omega_p(t)/2 & -(\frac{\Delta_a + \Delta_b}{2}) & \Omega_c/2 \\ 0 & 0 & \Omega_c/2 & -(\frac{\Delta_a + \Delta_b}{2} + \Delta_c) + U_{\text{int}} \end{pmatrix}, \quad (8.7)$$

where  $U_{\text{int}}$  represents the van der Waals (vdW) interaction.

For large detuning  $\Delta = \frac{\Delta_a + \Delta_b}{2}$ ,  $\Delta_a, \Delta_b \gg \Omega_c, \Omega_p^{\text{max}}$ , we can adiabatically eliminate the intermediate state  $|e\rangle$  as shown in Sec. 3.2.2.

Following the work of Müller *et al.* [158], we introduce the symmetrical and anti-symmetrical superposition of the two hyperfine ground states  $|\pm\rangle = \frac{|A\rangle_t \pm |B\rangle_t}{\sqrt{2}}$  as well as the rescaled Raman laser Rabi frequency  $x(t) = \sqrt{2}\Omega_p(t)/\Omega_c$ .

Under this condition, we obtain an effective Hamiltonian of the form

$$\mathcal{H}_{\text{eff}} = \frac{\hbar \Omega_c^2}{4\Delta} [x^2(t)|+\rangle\langle+| + (1 + U_{\text{int}})|r\rangle\langle r| + x(t)(|+\rangle\langle r| + \text{h.c.})]. \quad (8.8)$$

Looking at Fig. 8.1 (b), if the the control atom is in the state  $|0\rangle_c$ , it stays unaffected by the first  $\pi$ -pulse with Rabi frequency  $\Omega_R$ . Thus, the dipole-dipole interaction term vanishes and this effective Hamiltonian has two dark states

$$|d_1\rangle = |-\rangle, \quad (8.9)$$

$$|d_2\rangle = \frac{1}{\sqrt{1 + x^2(t)}} [|+\rangle - x(t)|r\rangle]. \quad (8.10)$$

If the coupling laser is resonant with the Rydberg level  $|r\rangle$  ( $\Delta_c = 0$ ), the target atom is reaching EIT conditions and becomes transparent for Qubit B Raman laser, leading to the transfer between  $|A\rangle_t$  and  $|B\rangle_t$  being blocked. Hence, the smooth  $\pi$ -pulse makes the target atom follow adiabatically the dark state given by  $|D\rangle = \frac{1}{\sqrt{2}}(|d_1\rangle + |d_2\rangle)$ , such that for  $x(t) \ll 1$ , the atom is beginning and ending in state  $|A\rangle_t$ . In the same way, if the target atoms is initially in the state  $|B\rangle_t$ , it will stay in the same state at the end of the sequence due to the prevented Raman tranfer.

Conversely, if the the control atom is in the state  $|1\rangle_c$ , then it can be coherently excited to the Rydberg state  $|r\rangle$  as shown in Fig. 8.1 (c). However, the strong dipole-dipole interaction  $U_{\text{int}}$  shifts the target atom Rydberg level  $|r\rangle$  out of resonance with excitation lasers.

Thus, the transformation associated with the smooth  $\pi$ -pulse allows for full Raman

transfer resulting in

$$|1\rangle_c |A\rangle_t \rightarrow |1\rangle_c |B\rangle_t, \quad (8.11)$$

$$|1\rangle_c |B\rangle_t \rightarrow |1\rangle_c |A\rangle_t. \quad (8.12)$$

## 8.2 Preliminary calculations and expected fidelities

The experimental sequence that needs to be implemented is illustrated in Fig. 8.1 (a). The sequence begins with a first short  $\pi$ -pulse on the control atom, followed by an adiabatic pulse on the target atom of the form

$$\Omega_p(t) = \Omega_p^{\max} \times \sin^2(\pi t/\tau), \quad (8.13)$$

where we have defined the pulse duration  $\tau$  such that  $\int_0^\tau \frac{(\Omega_p^{\max})^2}{2\Delta} \sin^4(\pi t/\tau) dt = \pi$ , giving  $\tau = \frac{16\pi}{3} \frac{\Delta}{(\Omega_p^{\max})^2}$ . Finally, a last  $\pi$ -pulse is applied on the control atom to end up the gate. The strong coupling Rabi frequency  $\Omega_c$  arising from Rydberg B laser is turned on for the whole sequence of pulses. In order to characterise the expected performances of our experiment and compare them with respect to the work of Müller *et al.* [158], we will use the fidelity defined as [12]

$$\mathcal{F} = \text{Tr}(\sqrt{\sqrt{\rho_i} \rho \sqrt{\rho_i}}), \quad (8.14)$$

where  $\rho_i$  represents the ideal density matrix for the desired output state.

### Case 1 : control atom in state $|0\rangle_c$

For the control atom in the state  $|0\rangle_c$ , as shown in Fig 8.1 (b), we require that the target atom follows the dark state  $|D\rangle$  during the smooth  $\pi$ -pulse, such that the Raman transfer between  $|A\rangle_t$  and  $|B\rangle_t$  is blocked.

Initially, the targeted state for implementing the gate protocol was the Rydberg state  $69S_{1/2}$ . Single atom Rabi flopping was obtained in Sec. 7.3 with a two-photon

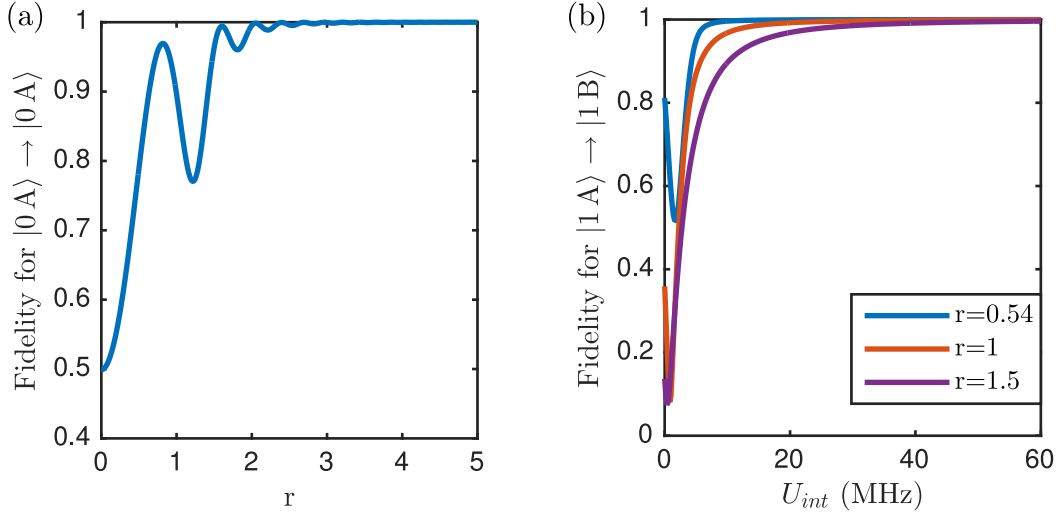


Figure 8.2: (a) Fidelity in the blockaded regime for  $|0 A\rangle \rightarrow |0 A\rangle$  as a function of the ratio  $r = \Omega_c / \Omega_p^{\max}$ . (b) Fidelity in the non-blockaded regime for  $|1 A\rangle \rightarrow |1 B\rangle$  as a function of the van der Waals (vdW) interaction energy  $U_{int}$  with three values of  $r$ , where  $r = 0.54$  corresponds to the Rydberg state  $69S_{1/2}$  and  $r = 1.5$  corresponds to the Rydberg state  $81D_{5/2}$ .

Rabi frequency of  $\Omega_r / 2\pi = 0.69$  MHz. The corresponding single-photon Rabi frequencies are  $\Omega_p^{\max} / 2\pi = 48.0$  MHz and  $\Omega_c / 2\pi = 25.9$  MHz, leading to a value of  $r = \Omega_c / \Omega_p^{\max} = 0.54$ . Using the experimental detunings  $\Delta_a / 2\pi = \Delta_b / 2\pi = 870$  MHz and  $\Delta_c = -\Delta_a$  for EIT resonance, results in a smooth  $\pi$ -pulse of duration  $\tau = 1$   $\mu$ s.

Figure 8.2 (a) shows the fidelity associated to the operation  $|0\rangle_c |A\rangle_t \rightarrow |0\rangle_c |A\rangle_t$  as a function of the ratio  $r = \Omega_c / \Omega_p^{\max}$ , for  $\Omega_p^{\max} / 2\pi = 48.0$  MHz. One can notice that for a critical value of  $r > 2$ , the fidelity reaches 99 % and the transfer becomes fully blocked after a value of 2.5. However, our experimental value of  $r = 0.54$  would limit the fidelity to  $\mathcal{F} = 0.79$ .

Giving that we can't reduce the waist size of the Rydberg beam to increase the coupling Rabi frequency  $\Omega_c$ , we have decided to take advantage of higher dipole matrix element offered by excitation towards a  $D$ -state, as explained in Sec. 6.1.3. From the ULE cavity modes calibration achieved in Chap. 6, the Rydberg state  $81D_{5/2}$  is found to be the state with the smallest principal quantum number we can lock to, along with the requirement of a vdW interaction  $U_{int} > 30$  MHz at an interatomic distance of  $6$   $\mu$ m. Single-photon Rabi frequencies (see Sec. 7.3) of  $\Omega_p^{\max} / 2\pi = 29.0$  MHz and  $\Omega_c / 2\pi = 43.7$  MHz, corresponding to the two-photon Rabi

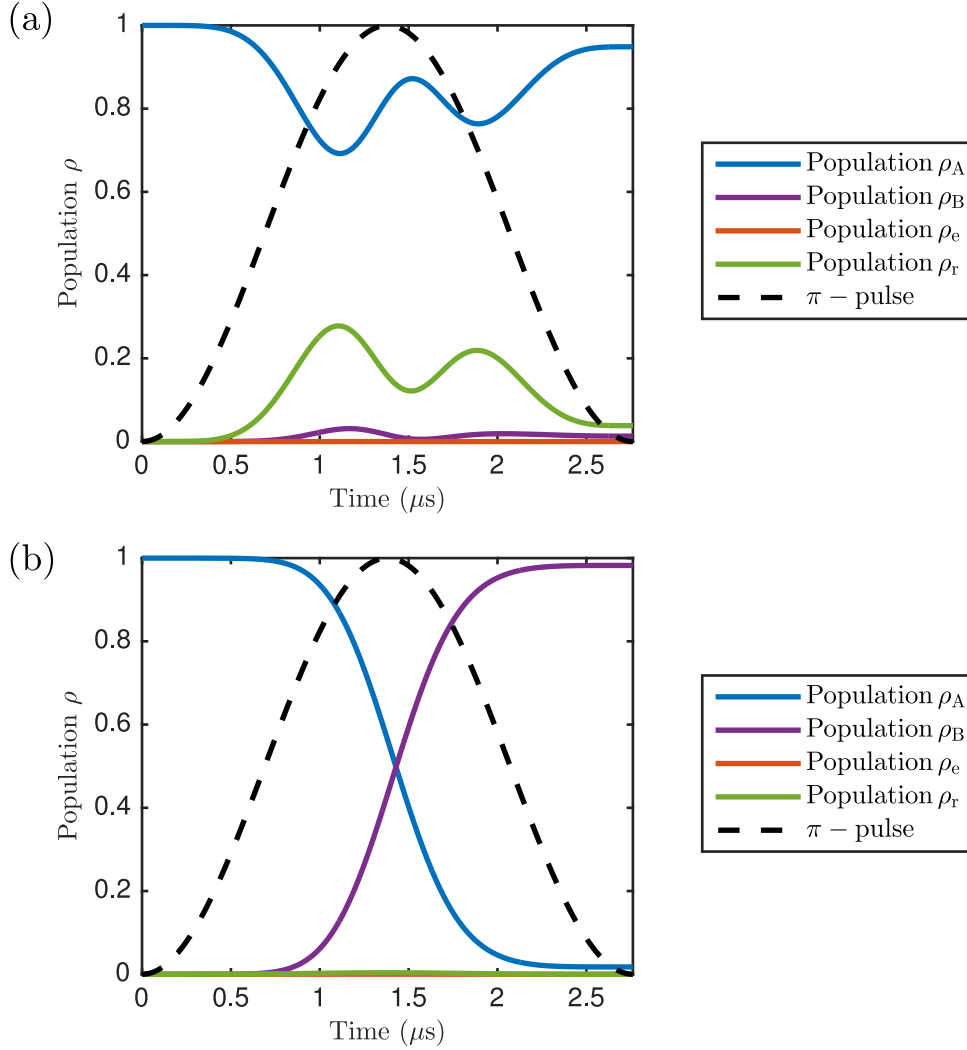


Figure 8.3: Evolution of the populations during the smooth  $\pi$ -pulse, relative to the Rydberg state  $81D_{5/2}$ , when (a) the control atom in state  $|0\rangle_c$  and (b) the control atom in state  $|1\rangle_c$ .

frequency of  $\Omega_r/2\pi = 0.72$  MHz, return a value of  $r = 1.5$  with a large increase of the fidelity to  $\mathcal{F} = 0.96$ .

The fidelity of the blocked transfer can be confirmed by looking at the evolution of the populations while applying the smooth  $\pi$ -pulse. Figure 8.3 (a) shows population's evolution as a function of the smooth  $\pi$ -pulse completion, when the control atom is in state  $|0\rangle_c$  and the Rydberg state is  $81D_{5/2}$ . The intermediate state  $6P_{3/2}$  and the state  $|B\rangle_t$  have almost negligible population due to Rydberg EIT conditions, whilst the population is transferred between the states  $|A\rangle_t$  and  $81D_{5/2}$  over the smooth  $\pi$ -pulse. The atom starting and ending in state  $|A\rangle_t$  with 96% efficiency, confirming its adiabatic evolution through the dark state  $|D\rangle$  under EIT conditions.

#### Case 2 : control atom in state $|1\rangle_c$

If the control atom is initially in the state  $|1\rangle_c$ , the two-photon resonance on the target atom must be lifted by the vdW interaction  $U_{int}$ , such that the Raman laser couples off-resonantly the states  $|A\rangle_t$  to  $|B\rangle_t$  via the intermediate state  $6P_{3/2}$ . The transfer fidelity associated to the flip of the target atom state  $|1\rangle_c|A\rangle_t \rightarrow |1\rangle_c|B\rangle_t$  is plotted in Figure 8.2 (b). The fidelity is represented with three different values of  $r$  as a function of the vdW interaction shift  $U_{int}$ .

Choosing the Rydberg state  $81D_{5/2}$ , given the values of  $r = 1.5$  and an interaction energy  $U_{int} = 34.9$  MHz (see Sec. 7.3), allows for a transfer fidelity  $\mathcal{F} = 0.99$  associated to a smooth  $\pi$ -pulse of duration  $\tau = 2.75$   $\mu$ s. However, it is interesting to notice that the fidelity is also of 99 % for the Rydberg state  $69S_{1/2}$ , corresponding to  $r = 0.54$  and an interaction energy  $U_{int} = 12.3$  MHz. Finally, Fig. 8.3 (b) depicts the evolution of the populations in the case of the control atom being in state  $|1\rangle_c$  and the Rydberg state  $81D_{5/2}$ , showing a transfer efficiency of 99% from the initial state  $|A\rangle_t$  to the final state  $|B\rangle_t$ .

## 8.3 Possible improvements

The analysis of the Rydberg EIT gate shows high fidelity possible using our existing parameters. However, further improvements should be addressed to reach higher fidelities  $\mathcal{F} > 0.999$ . Firstly, it would be necessary to change the excitation scheme from  $|4, 4\rangle \rightarrow 81D_{5/2}$  to  $|4, 0\rangle \rightarrow 81D_{5/2}$ , that would allow to phase lock Qubit A & B to get a common detuning from the excited state  $6P_{3/2}$ . Secondly, realising single site addressability with Qubit A & B would give us the opportunity for global and local rotations to realise states initialisation  $\{|00\rangle, |01\rangle, |10\rangle, |11\rangle\}$ . Lastly, upgrading the Rydberg laser system with a commercial one (SolsTiS from the company M Squared Lasers) would allow us to get higher coupling Rabi Frequency  $\Omega_c$  and better fidelities up to 0.999.

## 8.4 Summary

We have shown that we can implement the mesoscopic Rydberg EIT gate [172] between two atoms with high fidelity, through the choice of the Rydberg state  $81D_{5/2}$ . Although we plan to demonstrate the cNOT Rydberg EIT gate between two-qubits, this scheme provides a scalable approach to performing entanglement of large ensembles using a single control atom whilst circumventing challenges of the collective Rabi frequency. The resulting cNOT<sup>N</sup> is robust against atom number fluctuations and represents a large resource for quantum information processing such as demonstrating surface codes in atomic arrays [121] or high precision measurement beyond the standard quantum limit [264].

## Part IV

# Conclusion and Outlook

# Chapter 9

## Conclusion

This thesis describes the construction of the core system required for performing high fidelity quantum operations with Rydberg atoms, focusing on establishing laser technology and measurement protocols to ensure even in the absence of a cavity high fidelity operations are possible. In this work we have established coherent control of atomic qubits, including observation of long ground-Rydberg coherence times needed for two-qubit quantum gates and demonstrated blockade and entanglement between atoms.

We have built three lasers for Rydberg excitations, stabilised simultaneously to an ultra-high finesse ULE cavity, to provide narrow linewidth and long-term stability. The optical reference cavity has been stabilised to the zero-CTE temperature of  $T_c = 36.1 \pm 0.1^\circ\text{C}$ , reducing the CTE to tiny quadratic dependence with temperature around  $T_c$ . Ringdown-measurements give an estimate finesse of  $\mathcal{F} = 1.42(8) \times 10^5$  at 852 nm and  $\mathcal{F} = 3.9(4) \times 10^4$  at 1018 nm. The cavity performances are ideal for driving two-photon excitations, detuned from the intermediate state, towards  $\sim 2\pi \times 10$  kHz wide Rydberg states.

Frequency stabilisation has been implemented using the PDH technique, achieving high-bandwidth feedback of  $\sim$  MHz. The lock configuration allows continuous tuning of the laser frequency offset using the "electronic sideband" technique. An optical beatnote between two 509 nm lasers returns a laser linewidth  $\sim 130$  Hz at 509 nm, resulting in a 1018 nm linewidth  $< 100$  Hz, with better performance expected at 852 nm due to the increase in cavity finesse.

We have created an experimental setup capable of laser-cooling atoms in a magneto-optical trap (MOT) and trap single atoms in optical tweezers using high NA lenses. The setup allows for careful control of the electric field environment for Rydberg excitations. We have proved high fidelity readout using an sCMOS camera [243] in combination with a high resolution imaging system characterised by a sub- $\mu\text{m}$  point-spread function (PSF). Single atom temperature of  $\sim 5 \mu\text{K}$  and the possibility to prepare atoms in well defined atomic state using optical pumping, makes from the setup an ideal platform for single atom manipulations.

We have performed high-resolution spectroscopy on a cold atom cloud to determine the offset between the atomic and cavity resonant frequencies using the phenomenon of electromagnetically induced transparency (EIT). The long-term stability of the lasers has been determined from repeated spectra over a period of 20 days, yielding a linear frequency drift of 1 Hz/s [198], which is an order of magnitude improvement compared to similar cavity-stabilised Rydberg laser systems [247, 257].

We have shown coherent control of a single atom between hyperfine ground states and ground-Rydberg excitations. Fast ground state rotations have been achieved with  $\sim$  MHz rates and homogeneous dephasing time of a few ms whilst we have performed coherent Rydberg excitation to few Rydberg states  $50S_{1/2}$ ,  $69S_{1/2}$  and  $81D_{5/2}$ . The main limitation of Rydberg excitation coherence times being the laser phase noise from the servo-loop. However, this is not an issue regarding the large inhomogeneous dephasing time of 15  $\mu\text{s}$  [221] compared to  $\mu\text{s}$ -time scale for gate operations.

We have demonstrated Rydberg blockade between two atoms separated by 6  $\mu\text{m}$  and shown an almost complete suppression of the doubly excited state probability. The evidence of the creation of the entangled state  $|\mathcal{W}\rangle$  is deduced from the  $\sqrt{2}$  collective-enhancement of the Rabi oscillation with respect to the single atom case. The state is mapped to the hyperfine ground states to create a maximally entangled Bell state with long coherence time. The loss-corrected fidelity is found to be  $\mathcal{F}_{pairs} = 0.81(5)$  [123], which represents the highest corrected ground state neutral atom entanglement fidelity via Rydberg Blockade and is equal to that achieved via Rydberg dressing [122].

Finally, we have shown that our experimental setup could realise a proof of principle of the mesoscopic EIT gate [99] using the Rydberg state  $81D_{5/2}$ . In order to increase the fidelity of the gate up to 0.999, a couple of points should be addressed such as phase locking Qubit A & B to get a common detuning, realise single site addressability with Qubit A & B or upgrading the Rydberg laser system in order to get higher coupling Rabi Frequency  $\Omega_c$ .

## Outlook

Future directions for the project involve integration of a superconducting microwave resonator within the vacuum chamber. This will involve rebuilding the system to integrate a 4 K low-vibration closed-cycle cryostat, with high NA lenses mounted onto the 77 K shielding to suppress black body radiation on the low temperature region whilst maintaining good optical access. Whilst 4 K operation is too hot for integration of superconducting qubits, this system will enable initial demonstration of strong-coupling to a microwave cavity, requiring atom-cavity interaction to be stronger than the dissipation rates.

At 4 K, the quality factor of superconducting resonators is limited by quasi-particle excitations due to finite temperature effects [144]. Using optimised resonator geometries,  $Q \sim 10^5$  are achievable which at 15 GHz, chosen to suppress thermal loading of the resonator to  $n_{\text{th}} \sim 5$  photons, gives  $\kappa/2\pi \sim 0.3$  MHz and an RMS field of order 0.2 V/m. This frequency is resonant with the  $65S_{1/2} - 64P_{3/2}$  transition in Cs with matrix element of  $\sqrt{2/9} \times 4000 ea_0$ , leading to a vacuum Rabi frequency  $g = \boldsymbol{\mu} \cdot \mathbf{E}_0/\hbar$  of  $g/2\pi \sim 5$  MHz.

The resulting cooperativity is  $C = g^2/(\kappa\gamma) > 10^4$ , whilst the number of observable vacuum Rabi oscillations is  $n_{\text{Rabi}} = 2g/(\kappa + \gamma) = 38$ , before decay. As well as allowing demonstration of strong coupling, this hybrid quantum device would offer the potential to develop a large range of applications such as scalable long range interactions for mm-scale entanglement between atomic ensembles [141, 146], microwave-to-optical conversion [145] and cavity cooling [147], offering a new platform for scalable quantum information processing.

# Part V

## Appendices

# Appendix A

## Calculating Rabi frequencies on dipole transitions

The ability to perform accurate ground-state rotations and Rydberg excitation using two-photon excitation schemes is critical in developing quantum gates. This appendix deals with the calculation of single photon Rabi frequency for Raman ground state transitions and Rydberg excitation rates via the intermediate state  $|e\rangle = |6P_{3/2}\rangle$ .

The Rabi frequency for a dipole transition is given by  $\Omega_{i,j} = \boldsymbol{\mu}_{i,j} \cdot \mathbf{E}/\hbar$ , where  $\boldsymbol{\mu}_{i,j} = \langle i | e\mathbf{r} \cdot \boldsymbol{\epsilon} | j \rangle$  is the dipole matrix element between states  $|i\rangle$  and  $|j\rangle$ . Assuming that we are using a Gaussian beam, the electric field amplitude is simply fixed from its power  $\mathcal{P}$  and waist  $\omega_0$  such that  $\mathcal{E} = \sqrt{4\mathcal{P}/\pi c \epsilon_0 \omega_0^2}$  where  $c$  is the speed of light and  $\epsilon_0$  is the vacuum dielectric constant.

The dipole matrix element can be expressed according to angular momentum algebra. The Wigner-Eckart theorem shows that transition from the hyperfine state  $|f, m_f\rangle$  to  $|f', m'_f\rangle$  is given by the product of the Wigner-3j symbol with a reduced dipole matrix element [160, 265] such that

$$\Omega_{f,m_f \rightarrow f',m'_f} = \frac{\mathcal{E}}{\hbar} (-1)^{f-m_f} \begin{pmatrix} f & 1 & f' \\ -m_f & q & m'_f \end{pmatrix} \langle n'\ell'j'f' || e\hat{r} || n\ell j f \rangle, \quad (\text{A.1})$$

where  $q = -1, 0, 1$  denotes the electric field polarisation. The Wigner-3j symbol is

non-zero only if  $m'_f = m_f - q$ . This can be further reduced to the fine-structure basis via the introduction of the Wigner-6j symbol [160, 265]

$$\langle n'\ell'j'f' || e\hat{r} || n\ell j f \rangle = (-1)^{j+I+f'+1} \sqrt{(2f+1)(2f'+1)} \begin{Bmatrix} f & 1 & f' \\ j' & I & j \end{Bmatrix} \langle n'\ell'j' || e\hat{r} || n\ell j \rangle, \quad (\text{A.2})$$

where the curly bracket denotes the the Wigner-6j symbol. By gathering this expression in Eq. A.1, one obtains

$$\Omega_{f,m_f \rightarrow j',m'_j} = \frac{\mathcal{E}}{\hbar} (-1)^{f-m_f+j+I+f'+1} \sqrt{(2f+1)(2f'+1)} \times \begin{pmatrix} f & 1 & f' \\ -m_f & q & m_f - q \end{pmatrix} \begin{Bmatrix} f & 1 & f' \\ j' & I & j \end{Bmatrix} \langle n'\ell'j' || e\hat{r} || n\ell j \rangle. \quad (\text{A.3})$$

### Ground to excited states transition

The reduced matrix element  $\langle n'\ell'j' || e\hat{r} || n\ell j \rangle$  can be determined using the Einstein A coefficient for the transition via

$$A_{j' \rightarrow j} = \frac{\omega_0^3}{2\pi\epsilon_0\hbar c^3} \frac{|\langle n'\ell'j' || e\hat{r} || n\ell j \rangle|^2}{2j'+1}. \quad (\text{A.4})$$

If we want to estimate the Rabi frequency associated to the transition between ground to excited state, we just need to stay in the fine-structure basis. Indeed, in our experiment we are working on the  $6S_{1/2} \rightarrow 6P_{3/2}$  transition where the reduced matrix element can be evaluated using  $\langle J = 1/2 || e\mathbf{r} \cdot \boldsymbol{\epsilon} || J' = 3/2 \rangle = 4.4786 ea_0$  [160].

### Excited to Rydberg states transition

The expression of the dipole matrix element will be evaluated in a different way if it concerns the excitation from the intermediate state to the Rydberg state. For the excitation of Rydberg atoms with unresolved hyperfine structure from a state

with well defined hyperfine quantum numbers it is necessary to evaluate the dipole matrix element for coupling  $|f, m_f\rangle$  to  $|j', m'_j\rangle$ . This is achieved by decomposition of the state  $|j', m'_j\rangle$  into  $|f', m'_f\rangle$  using Clebsch-Gordan<sup>1</sup> algebra

$$|j'I; m'_j m_I\rangle = \sum_{f', m'_f} C_{j'm'_j I m_I}^{f' m'_f} |j'I; f', m'_f\rangle. \quad (\text{A.5})$$

Following angular momentum selection rules  $m'_f = m_f - q$  and  $m_I = m_f - q - m'_j$ . Thus for transitions from a single initial state  $|f, m_f\rangle$  this simply reduces to a summation over the excited state  $f'$ ,

$$\begin{aligned} \Omega_{f, m_f \rightarrow j', m'_j}^{E1} &= \frac{\mathcal{E}}{\hbar} \sum_{f'} C_{j'm'_j I(m_f - q - m'_j)}^{f'(m_f - q)} (-1)^{f - m_f + j + I + f' + 1} \sqrt{(2f + 1)(2f' + 1)} \\ &\times \begin{pmatrix} f & 1 & f' \\ -m_f & q & m_f - q \end{pmatrix} \begin{Bmatrix} f & 1 & f' \\ j' & I & j \end{Bmatrix} \langle n'\ell'j' || e\hat{r} || n\ell j \rangle. \end{aligned} \quad (\text{A.6})$$

This expression can be fully decomposed in terms of the uncoupled reduced matrix element, which can be evaluated from integration of the radial wavefunctions via

$$\langle n'\ell'j' || e\hat{r} || n\ell j \rangle = (-1)^{\ell + s + j' + 1} \sqrt{(2j + 1)(2j' + 1)} \begin{Bmatrix} j & 1 & j' \\ \ell' & s & \ell \end{Bmatrix} \langle n'\ell' || e\hat{r} || n\ell \rangle. \quad (\text{A.7})$$

The reduced dipole matrix element  $\langle n'\ell' || e\hat{r} || n\ell \rangle$  can be transformed using the Wigner-Eckart theorem as

$$\langle n'\ell' || e\hat{r} || n\ell \rangle = (-1)^\ell \sqrt{(2\ell + 1)(2\ell' + 1)} \begin{pmatrix} \ell & 1 & \ell' \\ 0 & 0 & 0 \end{pmatrix} \langle n\ell | er | n'\ell' \rangle. \quad (\text{A.8})$$

where the radial matrix element  $\langle n\ell | er | n'\ell' \rangle$  represents the overlap integral between

<sup>1</sup> Clebsch-Gordan coefficients defined as

$$\langle j_1, m_1; j_2 m_2 | j_1 j_2; JM \rangle \equiv C_{j_1 m_1 j_2 m_2}^{JM} \equiv (-1)^{j_1 - j_2 + M} \sqrt{2J + 1} \begin{pmatrix} j_1 & j_2 & J \\ m_1 & m_2 & -M \end{pmatrix}.$$

the radial wavefunctions and the dipole moment

$$\langle n\ell|er|n'\ell'\rangle = \int_{r_i}^{r_o} R_{n,\ell}(r)erR_{n',\ell'}(r)r^2 dr. \quad (\text{A.9})$$

The radial matrix elements have been evaluated using numerical integration over the wavefunctions [251, 252], allowing to find  $\mathcal{R}_{nS_{1/2}} = |\langle 6P_{3/2}||er||nS_{1/2}\rangle| = 5.021 ea_0 (n^*)^{-3/2}$  and  $\mathcal{R}_{nD_{5/2}} = |\langle 6P_{3/2}||er||nD_{5/2}\rangle| = 11.36 ea_0 (n^*)^{-3/2}$  [149].

# Appendix B

## Homebuilt photodiodes

This appendix details the design parameters of USB photodiode boards used for laser stabilisation to the high finesse ULE cavity (See Chap. 4). These boards have been designed to fit in a small diecast box with minimal mechanical modifications, as shown in Fig. B.1 (a) and Fig. B.1 (b). Moreover, the voltages are regulated using TO252 package surface mount regulators to provide  $-12\text{V}$  for biasing the photodiodes, and  $\pm 5\text{V}$  for powering the operational-amplifiers (OPA).

### B.1 High bandwidth photodiode

The design of our high-bandwidth photodiode was optimised for the ULE cavity locks requiring a bandwidth of up to 20 MHz for fast demodulation of the Pound-Drever-Hall signal. This circuit is based on using a fast Hamamatsu S5971 photodi-

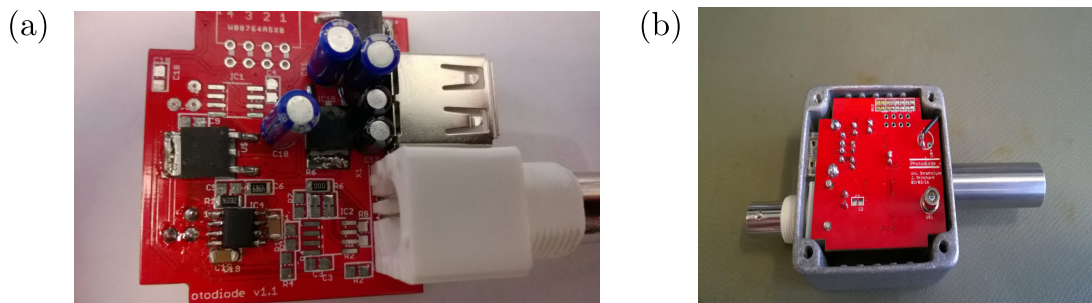


Figure B.1: (a) Photograph of the circuit board front facet with the USB power supply in the upper right, the SMD components soldered and the BNC adaptor in the lower right. (b) Photograph of the circuit board rear facet with the photodiode in the lower right and placed into the diecast box.

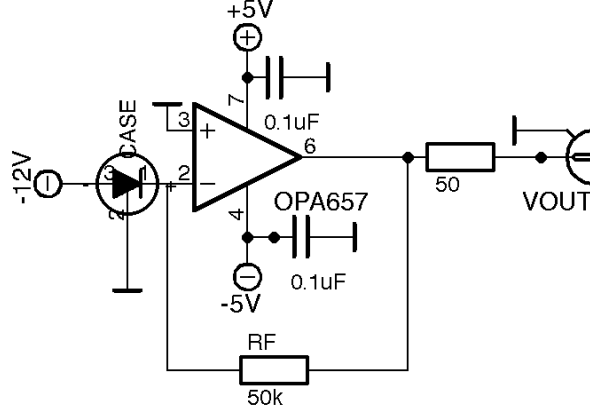


Figure B.2: Circuit of high bandwidth photodiode using a fast photodetector and transimpedance amplifier to obtain a high bandwidth of 25 MHz and a gain of  $5 \times 10^4$  V/A.

ode with small area (diameter  $\phi = 1.2$  mm) and low capacitance for high-bandwidth detection. Moreover, the ground plane under the chip is modified to minimize parasitic stray capacitance that will limit the device bandwidth.

As shown in Fig. B.2, the transimpedance amplifier [266] is using a high gain-bandwidth product (GBP) operational-amplifier (OPA657) of 1.6 GHz. At -12V, the photodiode has an intrinsic capacitance  $C_d = 3$  pF. Adding the capacitance of  $C_{in} = 4.5$  pF of the OPA, resulting in a 25 MHz bandwidth [266] for a feedback resistor of  $R_f = 50$  k $\Omega$  and a feedback capacitor of  $C_f = 0.2$  pF. The last value is comparable to the stray capacitance of an SMD resistor and has been omitted.

Finally, the output is 50  $\Omega$  terminated to ensure impedance matching with the BNC cables. This results in a total gain of  $5 \times 10^4$  V/A.

## B.2 High gain photodiode

The high gain photodiode design was optimised for ring-down measurements on the ULE cavity (see Sec. 4.5.3), requiring large input gain and a bandwidth of  $\sim 1$  MHz. For lower bandwidth, an AOP (AD8675) is chosen for reduced noise performance and a feedback capacitor of  $C_f = 3.3$  pF is added to maintain stability due to the lower 10 MHz GBP. A second stage line AOP (AD829) is used to provide an additional gain of 50 and to boost the output current to drive a 50  $\Omega$  line. The theoretical bandwidth for the device is 1.4 MHz, using an AOM to modulate the light before the photodiode, we measured a roll-off frequency of  $f_{-3dB} = 890$  kHz. The lower

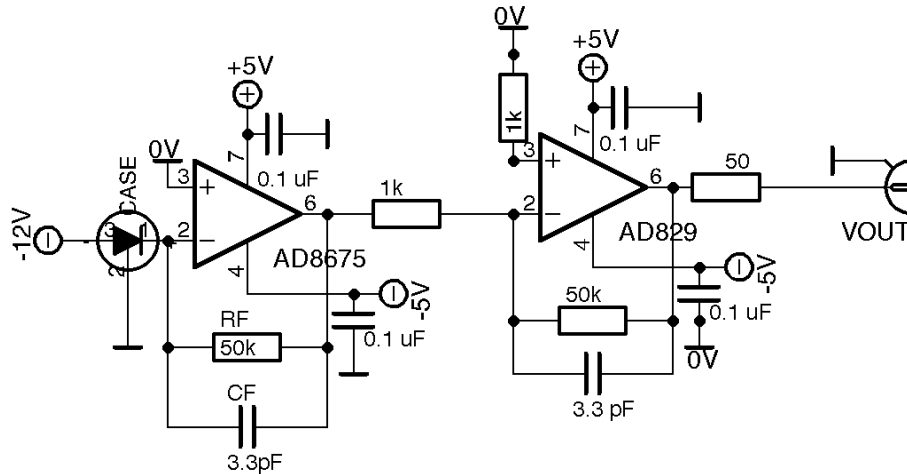


Figure B.3: Circuit of the high gain photodiode using a fast photodetector and a double stage transimpedance amplifier to obtain a gain of  $2.5 \times 10^6$  V/A and a roll-off frequency of  $f_{-3\text{dB}} = 890$  kHz.

bandwidth is due to requiring higher capacitance (3.3 pF) than calculated (2.2 pF) as this is the lowest available capacitor value. Without the capacitor, the output shows an unstable oscillation. The total gain is  $2.5 \times 10^6$  V/A and this design has been sufficient to provide clean ring-down measurements on the ULE cavity.

The figure below shows the results of calibration measurements taken to determine the photodiode performance. The blue trace is the modulation recorded on a com-

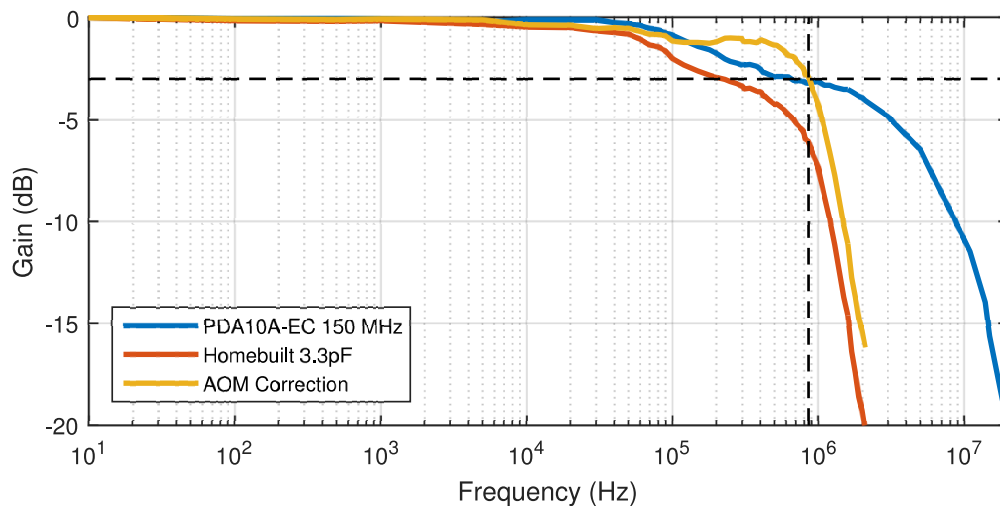


Figure B.4: Bode diagram of the high gain photodiode. The blue trace is the modulation recorded on a commercial high bandwidth (150 MHz) photodiode (Thorlabs PDA10A-EC), revealing the AOM transfer function. The red is the data recorded with the homebuilt high-gain photodiode, and the yellow has the AOM response subtracted to reveal the performance of the photodiode with a roll-off frequency of  $f_{-3\text{dB}} = 890$  kHz.

mercial high bandwidth (150 MHz) photodiode (Thorlabs PDA10A-EC), revealing the AOM transfer function. The red is the data recorded with the homebuilt high-gain photodiode, and the yellow has the AOM response subtracted to reveal the performance of the photodiode.

# Bibliography

- [1] A. Siegman, *Lasers*, University Science Books(1986)
- [2] M. Grundmann, *The Physics of Semiconductors* (Springer, 2016)
- [3] G. Moore, *Cramming more components onto integrated circuits*, *Electronics* **38**, 9 (1965)
- [4] R. Feynman, *Simulating physics with computers*, *International journal of theoretical physics* **21**, 467–488 (1982)
- [5] Y. I. Manin, *Computable and Uncomputable (in Russian)*, Sovetskoye Radio, 2(1980)
- [6] Y. I. Manin, *Classical computing, quantum computing, and Shor’s factoring algorithm*, arXiv:quant-ph/9903008, 2(1999)
- [7] P. Benioff, *The computer as a physical system : A microscopic quantum mechanical Hamiltonian model of computers as represented by Turing machines*, *J. Stat. Phys.* **22**, 563–591 (1980)
- [8] P. Benioff, *Quantum mechanical models of Turing machines that dissipate no energy*, *Phys. Rev. Lett.* **48**, 1581–1585 (1982)
- [9] D. Deutsch, *Quantum theory, the Church-Turing principle and the universal quantum computer*, *Proceedings of the royal society of London A* **400** (1985)
- [10] D. Deutsch, *Quantum computational networks*, *Proceedings of the royal society of London A* **425**, 13 (1989)
- [11] R. Loudon, *The Quantum Theory of Light*, 2nd ed. (OUP, UK, 1997)

- [12] M. A. Nielsen and I. L. Chuang, *Quantum Computation and Quantum Information* (CUP, Cambridge, 2005)
- [13] Robert Raussendorf and Hans J. Briegel, *A One-Way Quantum Computer*, [Phys. Rev. Lett.](#) **86**, 5188 (2001)
- [14] P. Walther *et al.*, *Experimental one-way quantum computing*, [Nature](#) **434**, 169–176 (2005)
- [15] E. Farhi, J. Goldstone, S. Gutmann, and M. Sipser, *Quantum computation by adiabatic evolution* (2000)
- [16] A. Yu. Kitaev, *Fault-tolerant quantum computation by anyons*, *Annals of Physics* **303**, 2–30 (2003)
- [17] D. Barenco *et al.*, *Elementary gates for quantum computation*, [Phys. Rev. A](#) **52**, 3457–3467 (1995)
- [18] D. P. DiVincenzo, *Two-bit gates are universal for quantum computation*, [Phys. Rev. A](#) **51**, 1015–1022 (1995)
- [19] P. O. Boykin *et al.*, *A new universal and fault-tolerant quantum basis*, [Inform. Process. Lett.](#) **75**, 101–107 (2000)
- [20] J. S. Bell, *On the Einstein Podolsky Rosen paradox*, *Physica* **1**, 195–200 (1964)
- [21] C. J. Foot, *Atomic Physics* (OUP, Oxford, 2005)
- [22] P. W. Shor, *Polynomial-Time Algorithms for Prime Factorization and Discrete Logarithms on a Quantum Computer*, [SIAM J. Comput.](#) **26**, 1484–150 (1997)
- [23] R. L. Rivest, A. Shamir, and L. Adleman, *A method for obtaining digital signatures and public-key cryptosystems*, *Communications of the ACM* **21**, 120–126 (1978)
- [24] A. K. Ekert, *Quantum cryptography based on bell's theorem*, [Phys. Rev. Lett.](#) **67**, 661–663 (1991)

- [25] C. H. Bennett and G. Brassard, *Quantum Cryptography: Public Key Distribution and Coin Tossing*, in *Proceedings of IEEE International Conference on Computers, System and Signal Processing* (IEEE, 1984) p. 175
- [26] N. Gisin, G. Ribordy, W. Tittel, and H. Zbinden, *Quantum cryptography*, [Rev. Mod. Phys.](#) **74**, 145–195 (2002)
- [27] L. K. Grover, *A fast quantum mechanical algorithm for database search*, *Proceedings, 28th annual ACM symposium on the theory of computing*, 212(1996)
- [28] X.-W. Yao *et al.*, *Quantum Image Processing and Its Application to Edge Detection: Theory and Experiment*, [Phys. Rev. X](#) **7**, 031041 (2017)
- [29] S. de Leseleuc *et al.*, *Accurate Mapping of Multilevel Rydberg Atoms on Interacting Spin-1/2 Particles for the Quantum Simulation of Ising Models*, [Phys. Rev. Lett.](#) **120**, 113602 (2017)
- [30] Vincent Lienhard *et al.*, *Observing the Space- and Time-Dependent Growth of Correlations in Dynamically Tuned Synthetic Ising Models with Antiferromagnetic Interactions*, [Phys. Rev. X](#) **8**, 021070 (2018)
- [31] S. Weber *et al.*, *Topologically protected edge states in small Rydberg systems*, [Quantum Sci. Technol.](#) **3**, 044001 (2018)
- [32] S. de Leseleuc *et al.*, *Observation of a symmetry-protected topological phase of interacting bosons with Rydberg atoms*, *Science*(2019)
- [33] M. Schuld, I. Sinayskiy, and F. Petruccione, *An introduction to quantum machine learning*, *Contemporary Physics* **56**, 172–185 (2015)
- [34] J. O’Gorman and E. T. Campbell, *Quantum computation with realistic magic-state factories*, [Phys. Rev. A](#) **95**, 032338 (2017)
- [35] A. M. Steane, *Overhead and noise threshold of fault-tolerant quantum error correction*, [Phys. Rev. A](#) **68**, 042322 (2003)
- [36] R. Blatt and D. Wineland, *Entangled states of trapped atomic ions*, [Nature](#) **453**, 1008 (2008)

- [37] J. I. Cirac and P. Zoller, *Quantum Computations with Cold Trapped Ions*, [Phys. Rev. Lett.](#) **74**, 4091–4094 (1995)
- [38] C. Monroe *et al.*, *Resolved-Sideband Raman Cooling of a Bound Atom to the 3D Zero-Point Energy*, [Phys. Rev. Lett.](#) **75**, 4011 (1995)
- [39] Myerson, A. H. and Szwer, D. J. and Webster, S. C. and Allcock, D. T. C. and Curtis, M. J. and Imreh, G. and Sherman, J. A. and Stacey, D. N. and Steane, A. M. and Lucas, D. M., *High-Fidelity Readout of Trapped-Ion Qubits*, [Phys. Rev. Lett.](#) **100**, 200502 (2008)
- [40] M. Riebe *et al.*, *Deterministic quantum teleportation with atoms*, [Nature](#) **429** (2004), doi:\bibinfo{doi}{10.1038/nature02570}
- [41] M. D. Barrett *et al.*, *Deterministic quantum teleportation of atomic qubits*, [Nature](#) **429** (2004), doi:\bibinfo{doi}{10.1038/nature02608}
- [42] Q. A. Turchette *et al.*, *Deterministic Entanglement of Two Trapped Ions*, [Phys. Rev. Lett.](#) **81**, 3631 (Oct 1998)
- [43] C. A. Sackett *et al.*, *Experimental entanglement of four particles*, [Nature](#) **404**, 256 (2000)
- [44] Thomas Monz *et al.*, *14-Qubit Entanglement: Creation and Coherence*, [Phys. Rev. Lett.](#) **106**, 130506 (2011)
- [45] J. P. Gaebler *et al.*, *High-Fidelity Universal Gate Set for  $^9\text{Be}^+$  Ion Qubits*, [Phys. Rev. Lett.](#) **117**, 060505 (2016)
- [46] C. J. Ballance *et al.*, *High-Fidelity Quantum Logic Gates Using Trapped-Ion Hyperfine Qubits*, [Phys. Rev. Lett.](#) **117**, 060504 (2016)
- [47] T. P. Harty *et al.*, *High-Fidelity Preparation, Gates, Memory, and Readout of a Trapped-Ion Quantum Bit*, [Phys. Rev. Lett.](#) **113**, 220501 (2014)
- [48] V. M. Schäfer *et al.*, *Fast quantum logic gates with trapped-ion qubits*, [Nature](#) **555**, 75–78 (2018)

- [49] Y. Wang *et al.*, *Single-qubit quantum memory exceeding ten-minute coherence time*, [Nature Photon.](#) **11**, 646–650 (2017)
- [50] Thomas Monz *et al.*, *Realization of a scalable Shor algorithm*, [Science](#) **351**, 1068 (2016)
- [51] C. Figgatt *et al.*, *Complete 3-Qubit Grover search on a programmable quantum computer*, [Nat. Comm.](#) **8**, 1918 (2017)
- [52] K. Wright *et al.*, *Benchmarking an 11-qubit quantum computer*, [Nature Comms.](#) **10** (2019), doi:\bibinfo{doi}{10.1038/s41467-019-13534-2}
- [53] D. Kielpinski, C. Monroe, and D. J. Wineland, *Architecture for a large-scale ion-trap quantum computer*, [Nature](#) **417**, 709–711 (2002)
- [54] C. Monroe and J. Kim, *Scaling the Ion Trap Quantum Processor*, [Science](#) **339**, 1164 (2011)
- [55] R. Barends *et al.*, *Coherent Josephson Qubit Suitable for Scalable Quantum Integrated Circuits*, [Phys. Rev. Lett.](#) **111**, 080502 (2013)
- [56] R. Barends *et al.*, *Superconducting quantum circuits at the surface code threshold for fault tolerance*, [Nature](#) **508**, 500 (2014)
- [57] C. Song *et al.*, *10-qubit entanglement and parallel logic operations with a superconducting circuit*, [Phys. Rev. Lett.](#) **119**, 180511 (2017)
- [58] C. Song *et al.*, *Generation of multicomponent atomic Schrödinger cat states of up to 20 qubits*, [Science](#) **365**, 547–577 (2019)
- [59] K. X. Ken Wei *et al.*, *Verifying Multipartite Entangled GHZ States via Multiple Quantum Coherences*, arXiv:1905.05720(2019)
- [60] Y. Dudin, R. Zhao, T. Kennedy, and A. Kuzmich, *Light storage in a magnetically dressed optical lattice*, [Phys. Rev. A](#) **81**, 041805 (2010)
- [61] Y. O. Dudin, L. Li, and A. Kuzmich, *Light storage on the time scale of a minute*, [Phys. Rev. A](#) **87**, 031801 (2013)

- [62] C. S. Adams, J. D. Pritchard, and J. P. Schaffer, *Rydberg atom quantum technologies*, arXiv:1907.09231(2019)
- [63] R. Grimm, M. Weidemüller, and Yu. B. Ovchinnikov, *Optical dipole trap for neutral atoms*, [Adv. At. Mol. Opt. Phys.](#) **42**, 95–170 (2000)
- [64] I. Bloch, *Ultracold atoms in optical lattices*, [Nature Phys.](#) **1**, 23–30 (2005)
- [65] M. J. Piotrowicz *et al.*, *Two-dimensional lattice of blue-detuned atom traps using a projected gaussian beam array*, [Phys. Rev. A](#) **88**, 013420 (2013)
- [66] F. Nogrette *et al.*, *Single-Atom Trapping in Holographic 2D Arrays of Microtraps with Arbitrary Geometries*, [Phys. Rev. X](#) **4**, 021034 (2014)
- [67] Henning Labuhn *et al.*, *Tunable two-dimensional arrays of single Rydberg atoms for realizing quantum Ising models*, [Nature](#) **534**, 667 (2016)
- [68] K. M. Maller *et al.*, *Rydberg-blockade controlled-not gate and entanglement in a two-dimensional array of neutral-atom qubits*, [Phys. Rev. A](#) **92**, 022336 (2015)
- [69] T. Xia *et al.*, *Randomized Benchmarking of Single-Qubit Gates in a 2D Array of Neutral-Atom Qubits*, [Phys. Rev. Lett.](#) **114**, 100503 (2015)
- [70] L. Graham *et al.*, *Rydberg mediated entanglement in a two-dimensional neutral atom qubit array*, arXiv:1908.06103(2019)
- [71] N. Schlosser, G. Reymond, I. Protsenko, and P. Grangier, *Sub-poissonian loading of single atoms in a microscopic dipole trap*, [Nature](#) **411**, 1024 (2001)
- [72] A. V. Carpentier *et al.*, *Preparation of a single atom in an optical microtrap*, [Laser Phys. Lett.](#) **10**, 125501 (2013)
- [73] Brian J. Lester *et al.*, *Rapid Production of Uniformly Filled Arrays of Neutral Atoms*, [Phys. Rev. Lett.](#) **115**, 073003 (2015)
- [74] M. O. Brown *et al.*, *Gray-Molasses Optical-Tweezer Loading: Controlling Collisions for Scaling Atom-Array Assembly*, [Phys. Rev. X](#) **9**, 011057 (2019)

- [75] M. Endres *et al.*, *Atom-by-atom assembly of defect-free one-dimensional cold atom arrays*, [Science](#) **354**, 1024 (2016)
- [76] H. Kim *et al.*, *In situ single-atom array synthesis using dynamic holographic optical tweezers*, *Nature Comms.* **7** (2016)
- [77] Daniel Barredo *et al.*, *An atom-by-atom assembler of defect-free arbitrary two-dimensional atomic arrays*, [Science](#) **354**, 1021 (2016)
- [78] Daniel Barredo *et al.*, *Synthetic three-dimensional atomic structures assembled atom by atom*, [Nature](#) **561**, 79 (2018)
- [79] Yang Wang *et al.*, *Coherent Addressing of Individual Neutral Atoms in a 3D Optical Lattice*, [Phys. Rev. Lett.](#) **115**, 043003 (2015)
- [80] M. A. Norcia, A. W. Young, and A. M. Kaufman, *Microscopic Control and Detection of Ultracold Strontium in Optical-Tweezer Arrays*, [Phys. Rev. X](#) **8**, 041054 (2018)
- [81] A. Cooper *et al.*, *Alkaline-Earth Atoms in Optical Tweezers*, [Phys. Rev. X](#) **8**, 041055 (2018)
- [82] S. Saskin, J. T. Wilson, B. Grinkemeyer, and J. D. Thompson, *Narrow-Line Cooling and Imaging of Ytterbium Atoms in an Optical Tweezer Array*, [Phys. Rev. Lett.](#) **122**, 143002 (2019)
- [83] N. C. Jackson, R. K. Hanley, C. S. Adams, and M. P. A. Jones, *Number-resolved imaging of  $88\text{Sr}$  atoms in a long working distance optical tweezer*, arXiv:1904.03233(2019)
- [84] L. Anderegg *et al.*, *An Optical Tweezer Array of Ultracold Molecules*, arXiv:1902.00497(2019)
- [85] O. Mandel *et al.*, *Controlled collisions for multi-particle entanglement of optically trapped atoms*, [Nature](#) **425**, 937–940 (2003)
- [86] M. Anderlini *et al.*, *Controlled exchange interaction between pairs of neutral atoms in an optical lattice*, [Nature](#) **448**, 452–456 (2007)

- [87] T. Fukuhara *et al.*, *Spatially Resolved Detection of a Spin-Entanglement Wave in a Bose-Hubbard Chain*, [Phys. Rev. Lett.](#) **115**, 035302 (2015)
- [88] A. M. Kaufman *et al.*, *Entangling two transportable neutral atoms via local spin exchange*, [Nature](#) **527**, 208 (2015)
- [89] M. Saffman, T. G. Walker, and K. Mølmer, *Quantum information with Rydberg atoms*, [Rev. Mod. Phys.](#) **82**, 2313 (2010)
- [90] D. Jaksch *et al.*, *Fast Quantum Gates for Neutral Atoms*, [Phys. Rev. Lett.](#) **85**, 2208 (2000)
- [91] M. D. Lukin *et al.*, *Dipole Blockade and Quantum Information Processing in Mesoscopic Atomic Ensembles*, [Phys. Rev. Lett.](#) **87**, 037901 (2001)
- [92] D. Tong *et al.*, *Local Blockade of Rydberg Excitation in an Ultracold Gas*, [Phys. Rev. Lett.](#) **93**, 063001 (2004)
- [93] K. Singer *et al.*, *Suppression of Excitation and Spectral Broadening Induced by Interactions in a Cold Gas of Rydberg Atoms*, [Phys. Rev. Lett.](#) **93**, 163001 (2004)
- [94] R. Heidemann *et al.*, *Evidence for Coherent Collective Rydberg Excitation in the Strong Blockade Regime*, [Phys. Rev. Lett.](#) **99**, 163601 (2007)
- [95] T. C. Liebisch, A. Reinhard, P. R. Berman, and G. Raithel, *Atom Counting Statistics in Ensembles of Interacting Rydberg Atoms*, [Phys. Rev. Lett.](#) **95**, 2530002 (2005)
- [96] M. Saffman and T. G. Walker, *Creating single-atom and single-photon sources from entangled atomic ensembles*, [Phys. Rev. A](#) **66**, 065403 (2002)
- [97] O. Firstenberg, C. S. Adams, and S. Hofferberth, *Nonlinear quantum optics mediated by Rydberg interactions*, [J. Phys. B](#) **49**, 152003 (2016)
- [98] R. G. Unanyan and M. Fleischhauer, *Efficient and robust entanglement generation in a many-particle system with resonant dipole-dipole interactions*, [Phys. Rev. A](#) **66**, 032109 (2002)

- [99] T Müller *et al.*, *Towards a guided atom interferometer based on a superconducting atom chip*, *N. J. Phys.* **10**, 073006 (2008)
- [100] M. Saffman and K. Mølmer, *Efficient Multiparticle Entanglement via Asymmetric Rydberg Blockade*, *Phys. Rev. Lett.* **102**, 240502 (2009)
- [101] A. Omran *et al.*, *Generation and manipulation of Schrödinger cat states in Rydberg atom arrays*, *Science* **365**, 570–574 (2019)
- [102] H. Weimer *et al.*, *A Rydberg quantum simulator*, *Nature Phys.* **6**, 382 (2010)
- [103] Peter Schauss, *Quantum simulation of transverse Ising models with Rydberg atoms*, *Quantum Sci. Technol.* **3**, 023001 (2018)
- [104] N. Schlosser, G. Reymond, and P. Grangier, *Collisional Blockade in Microscopic Optical Dipole Traps*, *Phys. Rev. Lett.* **89**, 023005 (2002)
- [105] D. D. Yavuz *et al.*, *Fast ground state manipulation of neutral atoms in microscopic optical traps*, *Phys. Rev. Lett.* **96**, 063001 (Feb 2006), <https://link.aps.org/doi/10.1103/PhysRevLett.96.063001>
- [106] M. Reetz-Lamour, T. Amthor, J. Deiglmayr, and M. Weidemüller, *Rabi Oscillations and Excitation Trapping in the Coherent Excitation of a Mesoscopic Frozen Rydberg Gas*, *Phys. Rev. Lett.* **100**, 253001 (2008)
- [107] T. A. Johnson *et al.*, *Rabi Oscillations between Ground and Rydberg States with Dipole-Dipole Atomic Interactions*, *Phys. Rev. Lett.* **100**, 113003 (2008)
- [108] E. Urban *et al.*, *Observation of Rydberg blockade between two atoms*, *Nature Phys.* **5**, 110 (2009)
- [109] A. Gaëtan *et al.*, *Observation of collective excitation of two individual atoms in the Rydberg blockade regime*, *Nature Phys.* **5**, 115 (2009)
- [110] T. Wilk *et al.*, *Entanglement of Two Individual Neutral Atoms Using Rydberg Blockade*, *Phys. Rev. Lett.* **104**, 010502 (2010)
- [111] A Gaëtan *et al.*, *Analysis of the entanglement between two individual atoms using global Raman rotations*, *New J. Phys.* **12**, 065040 (2010)

- [112] L. Isenhower *et al.*, *Demonstration of a Neutral Atom Controlled-NOT Quantum Gate*, [Phys. Rev. Lett.](#) **104**, 010503 (2010)
- [113] X. L. Zhang *et al.*, *Deterministic entanglement of two neutral atoms via Rydberg blockade*, [Phys. Rev. A](#) **82**, 030306 (2010)
- [114] Yong Zeng *et al.*, *Entangling Two Individual Atoms of Different Isotopes via Rydberg Blockade*, [Phys. Rev. Lett.](#) **119**, 160502 (2017)
- [115] I. I. Beterov and M. Saffman, *Rydberg blockade, Förster resonances, and quantum state measurements with different atomic species*, [Phys. Rev. A](#) **92**, 042710 (2015)
- [116] L. Isenhower, M. Saffman, and K. Mølmer, *Multibit  $C_k$ -NOT quantum gates via Rydberg blockade*, [Quantum Information Processing](#) **10**, 755 (2011)
- [117] H. Levine *et al.*, *Parallel implementation of high-fidelity multi-qubit gates with neutral atoms*, [Phys. Rev. Lett.](#) **123**, 170503 (2019)
- [118] Xiao-Feng Shi, *Rydberg Quantum Gates Free from Blockade Error*, [Phys. Rev. Applied](#) **7**, 064017 (2017)
- [119] Klaus Mølmer, Larry Isenhower, and Mark Saffman, *Efficient Grover search with Rydberg blockade*, [J. Phys. B](#) **44**, 184016 (2011)
- [120] David Petrosyan, Mark Saffman, and Klaus Mølmer, *Grover search algorithm with Rydberg-blockaded atoms: quantum Monte Carlo simulations*, [J. Phys. B](#) **49**, 094004 (2016)
- [121] James M. Auger, Silvia Bergamini, and Dan E. Browne, *Blueprint for fault-tolerant quantum computation with Rydberg atoms*, [Phys. Rev. A](#) **96**, 052320 (2017)
- [122] Y.-Y. Jau *et al.*, *Entangling atomic spins with a Rydberg-dressed spin-flip blockade*, [Nat. Phys.](#) **12**, 71 (2016)
- [123] C. J. Picken, R. Legaie, K. McDonnell, and J. D. Pritchard, *Entanglement of neutral-atom qubits with long ground-Rydberg coherence times*, [Quantum Sci. Technol.](#) **4**, 015011 (2019)

- [124] Sylvain de Léséleuc *et al.*, *Analysis of imperfections in the coherent optical excitation of single atoms to Rydberg states*, *Phys. Rev. A* **97**, 053803 (2018)
- [125] H. Levine *et al.*, *High-fidelity control and entanglement of Rydberg atom qubits*, *Phys. Rev. Lett.* **121**, 123603 (2018)
- [126] H. J. Kimble, *The quantum internet*, *Nature* **453**, 1023 (2008)
- [127] A. Wallraff *et al.*, *Strong coupling of a single photon to a superconducting qubit using circuit quantum electrodynamics*, *Nature* **431**, 162 (2004)
- [128] J. Majer *et al.*, *Coupling superconducting qubits via a cavity bus*, *Nature* **449**, 443–447 (2007)
- [129] Austin Fowler, Matteo Mariantoni, John Martinis, and Andrew Cleland, *Surface codes: Towards practical large-scale quantum computation*, *Phys. Rev. A* **86**, 032324 (2012)
- [130] Y. Tomita and K. M. Svore, *Low-distance surface codes under realistic quantum noise*, *Phys. Rev. A* **90**, 062320 (2014)
- [131] J. Kelly *et al.*, *State preservation by repetitive error detection in a superconducting quantum circuit*, *Nature* **519**, 66 (2015)
- [132] Yang Wang, Aishwarya Kumar, Tsung-Yao Wu, and David S. Weiss, *Single-qubit gates based on targeted phase shifts in a 3D neutral atom array*, *Science* **352**, 1562 (2016)
- [133] D. I. Schuster *et al.*, *High-Cooperativity Coupling of Electron-Spin Ensembles to Superconducting Cavities*, *Phys. Rev. Lett.* **105**, 140501 (2010)
- [134] Y. Kubo *et al.*, *Hybrid Quantum Circuit with a Superconducting Qubit Coupled to a Spin Ensemble*, *Phys. Rev. Lett.* **107**, 220501 (2011)
- [135] A. Andre *et al.*, *A coherent all-electrical interface between polar molecules and mesoscopic superconducting resonators*, *Nature Phys.* **2**, 636 (2006)

- [136] Bushev, P. and Feofanov, A. K. and Rotzinger, H. and Protopopov, I. and Cole, J. H. and Wilson, C. M. and Fischer, G. and Lukashenko, A. and Ustinov, A. V., *Ultralow-power spectroscopy of a rare-earth spin ensemble using a superconducting resonator*, *Phys. Rev. B* **84**, 060501 (2011)
- [137] Brune, M. and Haroche, S. and Raimond, J. M. and Davidovich, L. and Zagury, N., *Manipulation of photons in a cavity by dispersive atom-field coupling: Quantum-nondemolition measurements and generation of “Schrödinger cat” states*, *Phys. Rev. A* **45**, 5193–5214 (1992)
- [138] S. Bernon *et al.*, *Manipulation and coherence of ultra-cold atoms on a superconducting atom chip*, *Nature Comms.* **4**, 2380 (2013)
- [139] D. A. Steck, *Rubidium 87 D Line Data* (2007), <http://steck.us/alkalidata/rubidium87numbers.pdf>
- [140] T. F. Gallagher, *Rydberg Atoms* (CUP, New York, 2005)
- [141] L. Sárkány, J. Fortágh, and D. Petrosyan, *Long-range quantum gate via rydberg states of atoms in a thermal microwave cavity*, *Phys. Rev. A* **92**, 030303 (2015)
- [142] S. D. Hogan *et al.*, *Driving Rydberg-Rydberg Transitions from a Coplanar Microwave Waveguide*, *Phys. Rev. Lett.* **108**, 063004 (2012), <http://link.aps.org/doi/10.1103/PhysRevLett.108.063004>
- [143] J. D. Pritchard, K. J. Weatherill, and C. S. Adams, *Non-linear optics using cold Rydberg atoms*, *Ann. Rev. Cold. Atoms and Mol.* **1**, 301 (2013)
- [144] M. A. Beck *et al.*, *Optimized coplanar waveguide resonators for a superconductor–atom interface*, *App. Phys. Lett.* **109**, 092602 (2016)
- [145] Bryan T. Gard, Kurt Jacobs, R. McDermott, and M. Saffman, *Microwave-to-optical frequency conversion using a cesium atom coupled to a superconducting resonator*, *Phys. Rev. A* **96**, 013833 (2017)
- [146] D. Petrosyan *et al.*, *Reversible state transfer between superconducting qubits and atomic ensembles*, *Phys. Rev. A* **79**, 040304 (2009)

- [147] L. Sárkány, J. Fortágh, and D. Petrosyan, *Faithful state transfer between two-level systems via an actively cooled finite-temperature cavity*, *Phys. Rev. A* **97**, 032341 (2018)
- [148] T. F. Gallagher, *Rydberg Atoms*, *Rep. Prog. Phys.* **51**, 143 (1988)
- [149] J. D. Pritchard, *Cooperative Optical Non-Linearity in a Blockaded Rydberg Ensemble* (Springer-Verlag, Berlin, 2012)
- [150] N. Bohr, *On the Constitution of Atoms and Molecules*, *Phil. Mag.* **26**, 1 (1913)
- [151] P. J. Mohr, D. B. Newell, and B. N. Taylor, *Codata recommended values of the fundamental physical constants: 2014*, *Rev. Mod. Phys.* **88**, 035009 (2016)
- [152] Johannes Deiglmayr *et al.*, *Precision measurement of the ionization energy of Cs  $i$* , *Phys. Rev. A* **93**, 013424 (2016)
- [153] K.-H. Weber and Craig J. Sansonetti, *Accurate energies of  $nS$ ,  $nP$ ,  $nD$ ,  $nF$ , and  $nG$  levels of neutral cesium*, *Phys. Rev. A* **35**, 4650–4660 (1987)
- [154] P. Goy, J. M. Raimond, G. Vitrant, and S. Haroche, *Millimeter-wave spectroscopy in cesium rydberg states. quantum defects, fine- and hyperfine-structure measurements*, *Phys. Rev. A* **26**, 2733 (1982)
- [155] C. J. Lorenzen and K. Niemax, *Precise quantum defects of  $nS$ ,  $nP$  and  $nD$  Levels in Cs I*, *Z. Phys. A* **315**, 127 (1984), <http://dx.doi.org/10.1007/BF01419370>
- [156] E. Schrödinger, *An Undulatory Theory of the Mechanics of Atoms and Molecules*, *Phys. Rev.* **28**, 1049 (1926)
- [157] M. Saffman, *Quantum computing with atomic qubits and Rydberg interactions: progress and challenges*, *J. Phys. B* **49**, 202001 (2016)
- [158] M. Müller *et al.*, *Mesoscopic Rydberg Gate Based on Electromagnetically Induced Transparency*, *Phys. Rev. Lett.* **102**, 170502 (2009)
- [159] I. I. Beterov, I. I. Ryabtsev, D. B. Tretyakov, and V. M. Entin, *Quasiclassical calculations of blackbody-radiation-induced depopulation rates and effective*

- lifetimes of Rydberg  $nS$ ,  $nP$ , and  $nD$  alkali-metal atoms with  $n \leq 80$* , *Phys. Rev. A* **79**, 052504 (2009)
- [160] D. A. Steck, *Cesium D Line Data*, <http://steck.us/alkalidata>
- [161] T. G. Walker and M. Saffman, *Consequences of Zeeman degeneracy for the van der Waals blockade between Rydberg atoms*, *Phys. Rev. A* **77**, 032723 (2008)
- [162] W. R. Anderson, J. R. Veale, and T. F. Gallagher, *Resonant Dipole-Dipole Energy Transfer in a Nearly Frozen Rydberg Gas*, *Phys. Rev. Lett.* **80**, 249 (1998)
- [163] I. Mourachko *et al.*, *Many-Body Effects in a Frozen Rydberg Gas*, *Phys. Rev. Lett.* **80**, 253 (1998)
- [164] Sylvain Ravets *et al.*, *Measurement of the angular dependence of the dipole-dipole interaction between two individual rydberg atoms at a förster resonance*, *Phys. Rev. A* **92**, 020701 (2015)
- [165] S. Ravets, *Development of tools for quantum engineering using individual atoms : optical nanofibers and controlled Rydberg interactions*, Ph.D. thesis, Institut d'Optique Graduate School (2014)
- [166] J. D. Pritchard *et al.*, *Cooperative Atom-Light Interaction in a Blockaded Rydberg Ensemble*, *Phys. Rev. Lett.* **105**, 193603 (2010)
- [167] L. Béguin *et al.*, *Direct measurement of the van der waals interaction between two rydberg atoms*, *Phys. Rev. Lett.* **110**, 263201 (2013)
- [168] K. Singer, J. Stanojevic, M. Weidemüller, and R. Coté, *Long-range interactions between alkali Rydberg atom pairs correlated to the  $ns$ - $ns$ ,  $np$ - $np$  and  $nd$ - $nd$  asymptotes*, *J. Phys. B* **38**, S295 (2005)
- [169] M. Weissbluth, *Atoms and Molecules* (Academic Press, 1978)
- [170] M. L. Zimmerman, M. G. Littman, M. M. Kash, and D. Kleppner, *Stark structure of the Rydberg states of alkali-metal atoms*, *Phys. Rev. A* **20**, 2251 (1979)

- [171] Y. O. Dudin and A. Kuzmich, *Strongly Interacting Rydberg Excitations of a Cold Atomic Gas*, [Science](#) **336**, 887 (2012)
- [172] M. Müller, I. Lesanovsky, and P. Zoller, Private Communication (2008)
- [173] L. Allen and J. H. Eberly, *Optical resonance and two-level atoms* (Dover Publications, New York, 1987)
- [174] C. Cohen-Tannoudji, J. Dupont-Roc, and G. Grynberg, *Atom-Photon Interactions* (Wiley-Interscience, New York, 1998)
- [175] I. I. Rabi, *Space Quantization in a Gyration Magnetic Field*, [Phys. Rev.](#) **51**, 652 (1937)
- [176] A. Ashkin, *Trapping of Atoms by Resonance Radiation Pressure*, [Phys. Rev. Lett.](#) **40**, 729 (1978)
- [177] R. Grimm, M. Weidemüller, and Y. B. Ovchinnikov, *Optical dipole trap for neutral atoms*, [Adv. At. Mol. Opt. Phys.](#) **42**, 170 (2000)
- [178] J. Dalibard and C. Cohen-Tannoudji, *Dressed-atom approach to atomic motion in laser light: the dipole force revisited*, [J. Opt. Soc. Am. B](#) **2**, 1707 (1985)
- [179] G. Lindblad, *On the generators of quantum dynamical semigroups*, [Comm. Math. Phys.](#) **48**, 119 (1976)
- [180] K. Mølmer and Y. Castin, *Monte Carlo wavefunctions in quantum optics*, [Quantum Semiclass. Opt.](#) **8**, 49 (1996)
- [181] J. Gea-Banacloche, Y. Li, S. Jin, and M. Xiao, *Electromagnetically induced transparency in ladder-type inhomogeneously broadened media: Theory and experiments*, [Phys. Rev. A](#) **51**, 576 (1995)
- [182] S. H. Autler and C. H. Townes, *Stark Effect in Rapidly Varying Fields*, [Phys. Rev.](#) **100**, 703 (1955)
- [183] B. K. Teo *et al.*, *Autler-Townes spectroscopy of the  $5S_{1/2} - 5P_{3/2} - 44D$  cascade of cold  $85\text{Rb}$  atoms*, [Phys. Rev. A](#) **68**, 053407 (2003)

- [184] M. Fleischhauer, A. Imamoglu, and J. Marangos, *Electromagnetically induced transparency: Optics in coherent media*, [Rev. Mod. Phys.](#) **77**, 633 (2005)
- [185] *Exploring the Quantum: Atoms, Cavities and Photons* (Oxford University Press, Oxford, 2006)
- [186] C. Liu, Z. Dutton, C. H. Behroozi, and L. V. Hau, *Observation of coherent optical information storage in an atomic medium using halted light pulses*, [Nature](#) **409**, 490 (2001)
- [187] S. E. Harris, J. E. Field, and A. Imamoglu, *Nonlinear optical processes using electromagnetically induced transparency*, [Phys. Rev. Lett.](#) **64**, 1107 (1990)
- [188] E. Brion, L. H. Pedersen, and K. Mølmer, *Adiabatic elimination in a lambda system*, [J. Phys. A](#) **40**, 1033 (2007)
- [189] Richard W. Fox, *Temperature analysis of low-expansion Fabry-Perot cavities*, [Opt. Express](#) **17**, 15023–15031 (2009)
- [190] M. J. Martin and J. Ye, *Optical Coatings and Thermal Noise in Precision Measurement* (CUP, 2012) Chap. 15, p. 237
- [191] B. J. Bloom *et al.*, *An optical lattice clock with accuracy and stability at the  $10^{-18}$  level*, [Nature](#) **506**, 71 (2014)
- [192] S. L. Campbell *et al.*, *A Fermi-degenerate three-dimensional optical lattice clock*, [Science](#) **358**, 90 (2017)
- [193] J. Alnis *et al.*, *Subhertz linewidth diode lasers by stabilization to vibrationally and thermally compensated ultralow-expansion glass Fabry-Pérot cavities*, [Phys. Rev. A](#) **77**, 053809 (2008)
- [194] G. Cappellini *et al.*, *A compact ultranarrow high-power laser system for experiments with 578 nm ytterbium clock transition*, [Rev. Sci. Instr.](#) **86**, 073111 (2015)
- [195] I R Hill *et al.*, *A low maintenance Sr optical lattice clock*, [J. Phys. Conf. Series](#) **723**, 012019 (2016)

- [196] Christian Hagemann *et al.*, *Ultrastable laser with average fractional frequency drift rate below  $5 \times 10^{19}/s$* , *Opt. Lett.* **39**, 5102–5105 (2014)
- [197] D. G. Matei *et al.*, *1.5  $\mu\text{m}$  Lasers with Sub-10 mHz Linewidth*, *Phys. Rev. Lett.* **118**, 263202 (2017)
- [198] R. Legaie, C. J. Picken, and J. D. Pritchard, *Sub-kHz excitation lasers for Quantum Information Processing with Rydberg atoms*, *J. Opt. Soc. Am. B* **35**, 892 (2018)
- [199] A. S. Arnold, J. S. Wilson, and M. G. Boshier, *A simple extended-cavity diode laser*, *Rev. Sci. Instr.* **69**, 1236–1239 (1998)
- [200] A. Hemmerich, D. H. McIntyre, C. Zimmermann, and T. W. Hänsen, *Second-harmonic generation and optical stabilization of a diode laser in an external ring resonator*, *Opt. Lett.* **15**, 372 (1990)
- [201] G. D. Boyd and D. A. Kleinman, *Parametric Interaction of Focused Gaussian Light Beams*, *J. App. Phys.* **39**, 3597 (1968)
- [202] T.W. Hansch and B. Couillaud, *Laser frequency stabilization by polarization spectroscopy of a reflecting reference cavity*, *Opt. Comm.* **35**, 441 (1980)
- [203] A. G. White *et al.*, *Classical and quantum signatures of competing  $\chi^{(2)}$  nonlinearities*, *Phys. Rev. A* **55**, 4511 (1997)
- [204] Iolanda Ricciardi *et al.*, *Cavity-enhanced generation of 6 W cw second-harmonic power at 532 nm in periodically-poled MgO:LiTaO<sub>3</sub>*, *Opt. Express* **18**, 10985 (2010)
- [205] R. Le Targat, J.-J. Zondy, and P. Lemonde, *75%-Efficiency blue generation from an intracavity PPKTP frequency doubler*, *Opt. Comm.* **247**, 471 (2005)
- [206] Kaye & Laby, *Table of Physical & Chemical Constants : 2.5.7 Refractive index of gases*, Online : [http://www.kayelaby.npl.co.uk/general\\_physics/2\\_5/2\\_5\\_7.html](http://www.kayelaby.npl.co.uk/general_physics/2_5/2_5_7.html)
- [207] Y. Jiang *et al.*, *Making optical atomic clocks more stable with  $10^{-16}$  level laser stabilisation*, *Nature Photon.* **5**, 158–161 (2011)

- [208] S. Häfner *et al.*,  $8 \times 10^{-17}$  fractional laser frequency instability with a long room-temperature cavity, *Opt. Lett.* **40**, 2112–2115 (2015)
- [209] Lisheng Chen *et al.*, Vibration-induced elastic deformation of Fabry-Perot cavities, *Phys. Rev. A* **74**, 053801 (2006)
- [210] Eric D. Black, *An introduction to Pound–Drever–Hall laser frequency stabilization*, *Am. J. Phys.* **69**, 79–87 (2001)
- [211] R. W. P. Drever *et al.*, *Laser phase and frequency stabilization using an optical resonator*, *App. Phys. B* **31**, 97 (1983)
- [212] R. W. Fox, C. W. Oates, and L. W. Hollberg, *Stabilizing diode lasers to high-finesse cavities*, *Experimental Methods in the Physical Sciences* **40**, 1 (2003)
- [213] J. I. Thorpe, K. Numata, and J. Livas, *Laser frequency stabilization and control through offset sideband locking to optical cavities*, *Opt. Express* **16**, 15980 (2008)
- [214] P D Gregory *et al.*, *A simple, versatile laser system for the creation of ultracold ground state molecules*, *N. J. Phys.* **17**, 055006 (2015)
- [215] G. Rempe, R. Lalezari, R. J. Thompson, and H. J. Kimble, *Measurement of ultralow losses in an optical interferometer*, *Opt. Lett.* **17**, 363 (1992)
- [216] E. M. Bridge, *Towards a Strontium Optical Lattice Clock*, Ph.D. thesis, University of Oxford (2012)
- [217] T. Okoshi, K. Kikuchi, and A. Nakayama, *Novel method for high resolution measurement of laser output spectrum*, *Elec. Lett.* **16**, 630 (1980)
- [218] M. Saffman and T. G. Walker, *Entangling single- and  $N$ -atom qubits for fast quantum state detection and transmission*, *Phys. Rev. A* **72**, 042302 (2005)
- [219] M. G. Tarallo, *Development of a Strontium optical lattice clock*, Ph.D. thesis, Università degli studi di Pisa (2009)
- [220] N. Akerman *et al.*, *Universal gate-set for trapped-ion qubits using a narrow linewidth diode laser*, *New J. Phys.* **17** (2015)

- [221] C. J. Picken, *Experimental demonstration of high-fidelity entanglement via Rydberg blockade*, Ph.D. thesis, University of Strathclyde (2019)
- [222] J. Halbritter, *On the oxidation and on the superconductivity of niobium*, *Applied Physics A* **43**, 1–28 (May 1987), ISSN 1432-0630, <https://doi.org/10.1007/BF00615201>
- [223] W. S. Bakr *et al.*, *A quantum gas microscope for detecting single atoms in a Hubbard-regime optical lattice*, *Nature* **462**, 74 (2009)
- [224] J. Sherson *et al.*, *Single-atom-resolved fluorescence imaging of an atomic Mott insulator*, *Nature* **467**, 68 (2010)
- [225] A. Tauschinsky *et al.*, *Spatially Resolved Excitation of Rydberg Atoms and Surface Effects on an Atom Chip*, *Phys. Rev. A* **81**, 063411 (2010)
- [226] R. P. Abel, C. Carr, U. Krohn, and C. S. Adams, *Electrometry near a dielectric surface using Rydberg electromagnetically induced transparency*, *Phys. Rev. A* **84**, 023408 (2011)
- [227] J. D. Pritchard, J. A. Isaacs, and M. Saffman, *Long working distance objective lenses for single atom trapping and imaging*, *Rev. Sci. Instr.* **87**, 073107 (2016)
- [228] Y. R. P. Sortais *et al.*, *Diffraction-limited optics for single-atom manipulation*, *Phys. Rev. A* **75**, 013406 (2007)
- [229] Henning Labuhn *et al.*, *Single-atom addressing in microtraps for quantum-state engineering using rydberg atoms*, *Phys. Rev. A* **90**, 023415 (2014)
- [230] L. Beguin, *Measurement of the van der Waals interaction between two Rydberg atoms*, Ph.D. thesis, Institut d’Optique Graduate School (2013)
- [231] C. S. Adams and E. Riis, *Laser Cooling and trapping of neutral atoms*, *Prog. Quant. Electron.* **21**, 1 (1997)
- [232] H. J. Metcalf and P. van der Straten, *Laser Cooling and Trapping* (Springer-Verlag, 2002)

- [233] Paul D. Lett *et al.*, *Observation of atoms laser cooled below the doppler limit*, *Phys. Rev. Lett.* **61**, 169–172 (Jul 1988), <https://link.aps.org/doi/10.1103/PhysRevLett.61.169>
- [234] J. Dalibard and C. Cohen-Tannoudji, *Laser cooling below the Doppler limit by polarisation gradients: simple theoretical models*, *J. Opt. Soc. Am. B* **6**, 2023 (1989)
- [235] C. G. Townsend *et al.*, *Phase-space density in the magneto-optical trap*, *Phys. Rev. A* **52**, 1423 (1995)
- [236] M. L. Harris *et al.*, *Polarization spectroscopy in rubidium and cesium*, *Phys. Rev. A* **73**, 062509 (2006)
- [237] W. Ketterle, D. S. Durfee, and D. M. Stamper-Kurn, *Making, probing and understanding Bose-Einstein condensates* (1999), <http://www.citebase.org/abstract?id=oai:arXiv.org:cond-mat/9904034>
- [238] T. Grunzweig, A. Hilliard, M. McGovern, and M. F. Andersen, *Near deterministic preparation of a single atom in an optical microtrap*, *Nat. Phys.* **6**, 951–954 (2010)
- [239] John Weiner, Vanderlei S. Bagnato, Sergio Zilio, and Paul S. Julienne, *Experiments and theory in cold and ultracold collisions*, *Rev. Mod. Phys.* **71**, 1–85 (1999)
- [240] C. D. Wallace *et al.*, *Measurements of temperature and spring constant in a magneto-optical trap*, *J. Opt. Soc. Am. B* **11**, 703 (1994)
- [241] Steven Chu, J. E. Bjorkholm, A. Ashkin, and A. Cable, *Experimental Observation of Optically Trapped Atoms*, *Phys. Rev. Lett.* **57**, 314 (1986)
- [242] S. Friebel *et al.*, *CO<sub>2</sub>-laser optical lattice with cold rubidium atoms*, *Phys. Rev. A* **57**, R20 (1998)
- [243] C. J. Picken, R. Legaie, and J. D. Pritchard, *Single atom imaging with an sCMOS camera*, *App. Phys. Lett.* **111**, 164102 (2017)

- [244] S. Kuhr *et al.*, *Analysis of dephasing mechanisms in a standing-wave dipole trap*, *Phys. Rev. A* **72**, 023406 (Aug 2005), <https://link.aps.org/doi/10.1103/PhysRevA.72.023406>
- [245] C. Tuchendler *et al.*, *Energy distribution and cooling of a single atom in an optical tweezer*, *Phys. Rev. A* **78**, 033425 (2008)
- [246] H. Engler *et al.*, *Very long storage times and evaporative cooling of cesium atoms in a quasielectrostatic dipole trap*, *Phys. Rev. A* **62**, 031402 (2000)
- [247] Alda Arias *et al.*, *Versatile, high-power 460 nm laser system for Rydberg excitation of ultracold potassium*, *Opt. Express* **25**, 14829 (2017)
- [248] A. K. Mohapatra, T. R. Jackson, and C. S. Adams, *Coherent Optical Detection of Highly Excited Rydberg States Using Electromagnetically Induced Transparency*, *Phys. Rev. Lett.* **98**, 113003 (2007)
- [249] Löw R. *et al.*, *An experimental and theoretical guide to strongly interacting Rydberg gases*, *J. Phys. B* **45**, 113001 (2012)
- [250] P. Siddons, C. S. Adams, C. Ge, and I. G. Hughes, *Absolute absorption on rubidium D lines: comparison between theory and experiment*, *J. Phys. B* **41**, 155004 (2008)
- [251] B. V. Numerov, *A method of extrapolation of perturbations*, *MNRAS* **84**, 592 (1924)
- [252] B. V. Numerov, *Note on the numerical integration of  $d^2x/dt^2 = f(x, t)$* , *Astronomische Nachrichten* **230**, 359 (1927)
- [253] B. H. Bransden and C. J. Joachain, *Physics of atoms and molecules* (Longman Scientific and Technical, 1983)
- [254] A. L. Migdall *et al.*, *First Observation of Magnetically Trapped Neutral Atoms*, *Phys. Rev. Lett.* **54**, 2596 (1985)
- [255] W. Wing, *On neutral particle trapping in quasistatic electromagnetic fields*, *Prog. Quant. Electron.* **8**, 181 (1984)

- [256] Elizabeth M. Bridge *et al.*, *Tunable cw UV laser with  $< 35$  kHz absolute frequency instability for precision spectroscopy of Sr Rydberg states*, *Opt. Express* **24**, 2281 (2016)
- [257] Julius de Hond, Nataly Cisternas, Graham Lohead, and N. J. van Druten, *Medium-finesse optical cavity for the stabilization of Rydberg lasers*, *Appl. Opt.* **56**, 5436 (2017)
- [258] D. Jaksch *et al.*, *Entanglement of atoms via cold controlled collisions*, *Phys. Rev. Lett.* **82**, 1975–1948 (1999)
- [259] B.B. Blinov, D.L. Moehring, L.-M. Duan, and C. Monroe, *Observation of entanglement between a single trapped atom and a single photon*, *Nature* **428**, 153 (2004)
- [260] M. Dornseifer D. Haubrich and R. Wynands, *Lossless beam combiners for nearly equal laser frequencies*, *Rev. Sci. Instr.* **71**, 338 (2000)
- [261] I.I. Ryabtsev *et al.*, *Doppler- and recoil-free laser excitation of rydberg states via three-photon transition*, *Phys. Rev. A* **84**, 053409 (2011)
- [262] S. de Léséleuc, *Quantum simulation of spin models with assembled arrays of Rydberg atoms*, Ph.D. thesis, Institut d’Optique Graduate School (2018)
- [263] I I Beterov *et al.*, *Coherent control of mesoscopic atomic ensembles for quantum information*, *Laser Physics* **24**, 074013 (2014)
- [264] Calum MacCormick *et al.*, *Supraclassical measurement using single-atom control of an atomic ensemble*, *Phys. Rev. A* **93**, 023805 (2016)
- [265] I. I. Sobelman, *Atomic Spectra and Radiative Transitions* (Springer-Verlag, Berlin, 1979)
- [266] Texas Instrument, *Datasheet*, [www.ti.com](http://www.ti.com)